Engineering Field-Insensitive Clock Transitions for Symmetry-Violating New Physics Searches

Thesis by
Yuiki Takahashi

In Partial Fulfillment of the Requirements for the
Degree of
Doctor of Philosophy

CALIFORNIA INSTITUTE OF TECHNOLOGY
Pasadena, California

2026
Defended May 19, 2026

Yuiki Takahashi
ORCID: 0000-0003-0027-0556

Acknowledgements

First, I am deeply grateful to my advisor, Nick Hutzler, for giving me the scientific freedom to explore new ideas while also helping me turn them into real science and experiments. Your insight shaped the direction of the project, and your careful feedback improved every stage of the research and writing. Moreover, during my PhD, there were difficult times for me, but you were always willing to take the time to talk with me whenever I needed it, and that meant a lot to me. Thank you very much for all of your support. My PhD would not have been possible without you.

I would also like to thank my committee members, Professor Hiroshi Ooguri, Professor Brad Filippone, and Professor Ryan Patterson, for serving on my thesis committee despite your busy schedules and for all of your support and guidance throughout the process.

I would like to thank Professor Tim Steimle for teaching me so much about molecular spectroscopy and for all of the fun conversations. You always encouraged and cheered me up, which gave me great motivation for my PhD research. Thank you for always caring about me.

I want to thank my labmates for many helpful discussions and for their support with experiments, analysis, and day-to-day problem solving. In particular, I appreciate Chandler Conn and Phelan Yu for being wonderful cohortmates. Thanks, Chandler, for your input on experiments, from leak checks to designing machined parts, for helping me with tricky problems like removing stuck screws, for sitting at the next

desk for many years, for explaining a lot of American culture to me in a very funny way, and for countless funny jokes, which not only made my lab life much more fun but also helped me greatly, especially during difficult times. Thanks, Phelan, for helping maintain lab safety and facilities, for occasionally assisting with our experiments, and for all of the highly technical scientific discussions and detailed knowledge you shared across many topics, which greatly improved my knowledge and scientific perspective and was important for my growth as a scientist.

I want to thank Madison Howard for bringing a great culture into the whole lab, making me and everyone smile and laugh, having ramen dinners and mochi ice-cream trips, and, most importantly, being my bestie. I cannot remember how many times you made me smile and feel happy, even when I was stressed out. I always truly wish I could carry your happy vibe, and I really respect you as a person. Next time you are planning a trip to Japan, I would be happy to show you around. Thank you, Yuxi Yang, for working with me for about the last 10 months of my PhD. We were fortunate to observe together one of the really exciting moments in the YbOH project: the Ramsey demonstration in ^{173}YbOH and the observation of Ramsey fringes with a 1 ms coherence time. I am really glad to have had your enthusiasm and willingness to learn the experiment and to stay with me while working on it. Good luck with the rest of your PhD, and I am sure you will have a successful outcome at the end.

I also want to thank all of the new lab members, Jonathan Bright, Xukun Lin, Olivia Rosenstein, and Roy Ready, for all of the fun conversations we had. I also want to thank the past lab members, especially Harish Ramachandran, for bringing everything necessary to conduct the precision measurement: insightful ideas, sharp observations, enthusiasm and momentum to make real progress on the experiment, and critical thinking to assess and identify issues. You are definitely one of the greatest scientists I have ever seen, and there is no doubt that you accelerated the

progress of the YbOH project. I really enjoyed working with you for about 14 months, and I am sure you will have a great time at Johns Hopkins too. I want to thank Adele Basturk and Zitian Ye for working with me during the SURF program and also after SURF. I did not expect that we would become this close before I was asked to mentor SURF students, and I am very happy to see both of you doing fantastic in Cambridge. Thanks, Adele, for being willing to chat with me on the 4th floor of Downs when you were clearly busy with a lot of assignments, and for bringing me interesting ideas from a different angle, which enriched my perspective a lot. Thanks, Zitian, for working with me on the metastable helium project, which was my first mentoring project. I will probably never forget the night when we worked on the minifridge and (I) accidentally introduced too much helium, but looking back now, it is a good memory from my PhD. I also learned a lot from your humble and diligent attitude and enjoyed many conversations we had about life and science. I also want to thank Chi Zhang for working with me on the same project for a few years, and all other past lab members with whom I overlapped.

I also want to thank everyone in Manuel Endres's group for sometimes lending us optics and electronics, and also for the many fun conversations we had. Thank you, Gyohei Nomura, for so many hours of conversations, discussions about quantum and AI, and the huge number of messages we exchanged during the PhD. I also want to thank Kon Leung and Xiangkai Sun for all the random chats we had, as well as everyone else in the Endres group.

I also want to thank the people at Okayama University, especially Professor Yuki Miyamoto, for welcoming me as a visiting student in his project for almost one year when I was back in Japan during COVID-19 and for teaching me so much about experiments and molecular spectroscopy. I also want to thank Professor Yoshimura, Professor Uetake, Ayami Hiramoto, and everyone else in the Okayama group for many scientific discussions and conversations. I also want to thank Professor John

Doyle, Professor Amar Vutha, Professor Xing Fan, and Professor Rana Adhikari for all of the insightful scientific discussions and very helpful career advice, which helped my career decisions a lot. I also want to thank people in the Doyle group at Harvard for chatting with me when I visited, especially Hiromitsu Sawaoka for all the fun conversations.

I also want to thank all of my friends for spending time with me and hanging out with me during my PhD, especially Ryoto Sekine, Aki Park, and Masami Hazu, for being fantastic cohortmates and for having dinner with me so many times with lots of conversation. Special thanks to Ryoto for going out to dinner with me so many times and having deep conversations about everything, which shaped my career views. Thank you to everyone in the Japanese Student Association for hanging out with me at various events and going out together, especially Sayaka Kozuki, Honami Tanaka, Gohta Aihara, Koki Yoshioka, Son-san, Ikeda-kun, Hayakawa-san, Hao-san, Rui-san, Kawate-san, Kensuke-kun, Hayato-kun, Sota-kun, Nakano-san, Noguchi-san, and everyone else. I also want to thank my friends Chun-ju, Tasuku, Sky, Jaeha, Shungo, Sepehr, Chuankun, Shanto, Xiaowei, Taniguchi-san, Sahil, Yufeng, Chris, Vincent, Jerry, Aike, Anthony, and all other friends I met during my PhD.

Last, and most importantly, I thank my whole family and my grandparents for raising me, for their constant encouragement, and for giving me the support and environment that allowed me to focus on research. Even when I was far from home, your care, patience, and belief in me gave me strength during difficult times and helped me keep moving forward. This thesis would not have been possible without your love and support.

Abstract

Heavy polar molecules are powerful quantum sensors for tests of fundamental symmetries and searches for physics beyond the Standard Model. Their internal electromagnetic environment can provide exceptional sensitivity to symmetry-violating effects, but they also create significant challenges for achieving high precision and accuracy in measurement. In addition, their rich internal structure significantly complicates quantum state preparation, coherent control, and readout. This thesis addresses these challenges by devising and demonstrating a general approach for engineering field-insensitive "clock" transitions that suppress sensitivity to external fields while preserving strong sensitivity to new physics. This approach is broadly applicable to a wide range of experimental systems, including species with complex, deformed nuclei and systems compatible with state-of-the-art cooling and trapping techniques, offering the potential to significantly improve sensitivity to various new physics while expanding the experimental design space for quantum sensing.

A central result of this work is the conceptualization and demonstration of field-insensitive clock transitions for symmetry-violation searches. Uncontrolled external electromagnetic fields are a major obstacle to precise and accurate measurements. Minimizing sensitivity to such fields is therefore essential and has played a key role in all precision experiments of this kind. Here, we devise and demonstrate clock transitions engineered to enable robust symmetry-violation searches in YbOH. Sensitivities to external electric and magnetic fields are suppressed by orders of magnitude while maintaining strong sensitivity to the electron electric dipole moment

(eEDM). Using Ramsey measurements on these clock transitions, we observe suppression of electric- and magnetic-field sensitivities by at least factors of 700 and 200, respectively, and demonstrate robust spin coherence in the presence of large electromagnetic-field fluctuations. We also identify and employ selected quantum states for sensitive measurements of external magnetic and electric fields, another capability that is critical for high-accuracy experiments.

This thesis also establishes and demonstrates the quantum-control toolkit required for symmetry violation searches in the isotopologue ^{173}YbOH, which is of particular interest because of its large nuclear spin ($I = 5/2$) and quadrupole-deformed nucleus. These features make it a promising candidate for searches for hadronic symmetry-violating effects, including those arising from the nuclear magnetic quadrupole moment (MQM). Realizing an MQM measurement in ^{173}YbOH, however, requires quantum state control within highly complex hyperfine manifolds. Here, we demonstrate state preparation, coherent control, and readout for Ramsey interferometry on MQM-sensitive transitions in ^{173}YbOH with magnetic-field sensitivity suppressed by more than an order of magnitude. We also demonstrate a "co-magnetometer" protocol that disentangles a potential MQM signature from systematic backgrounds. These results establish the essential quantum-control toolkit for precision measurements in systems with the intricate hyperfine structure commonly encountered in searches for nuclear symmetry violation, and show that it is possible to take advantage of the suppressed field sensitivities in these complicated systems.

Together, these results show that molecular structure can be engineered and controlled to realize robust precision measurements in complex systems and that molecular complexity can be transformed from a challenge into a resource for robust symmetry-violation measurements.

Published Content and Contributions

[1] Yuiki Takahashi, David Shlivko, Gabriel Woolls, and Nicholas R. Hutzler. "Simulation of cryogenic buffer gas beams". In: *Phys. Rev. Research* 3 (2 Apr. 2021), p. 023018. DOI: 10.1103/PhysRevResearch.3.023018.
Y. T. wrote the simulation code, performed the simulation, analyzed the results, and wrote the manuscript.

[2] Yuiki Takahashi, Chi Zhang, Arian Jadbabaie, and Nicholas R. Hutzler. "Engineering Field-Insensitive Molecular Clock Transitions for Symmetry Violation Searches". In: *Phys. Rev. Lett.* 131 (18 Oct. 2023), p. 183003. DOI: 10.1103/PhysRevLett.131.183003.
Y. T. developed the concept, conceived the project, designed and built the experiment, performed the measurements, analyzed the data, and wrote the manuscript.

[3] Arian Jadbabaie, Yuiki Takahashi, Nickolas H Pilgram, Chandler J Conn, Yi Zeng, Chi Zhang, and Nicholas R Hutzler. "Characterizing the fundamental bending vibration of a linear polyatomic molecule for symmetry violation searches". In: *New Journal of Physics* 25.7 (July 2023), p. 073014. DOI: 10.1088/1367-2630/ace471.
Y. T. built the experiment, performed the measurements, analyzed the data, and wrote the manuscript.

[4] Yuiki Takahashi, Harish D. Ramachandran, Arian Jadbabaie, Yi Zeng, Chi Zhang, and Nicholas R. Hutzler. "Engineered Molecular Clock Transitions for Symmetry Violation Searches". In: *Phys. Rev. X* (2026). Accepted in Phys. Rev. X. DOI: 10.1103/4t7q-d58r. arXiv: 2508.06787 [physics.atom-ph].
Y. T. developed the concept, conceived the project, designed and built the experiment, performed the measurements, analyzed the data, and wrote the manuscript.

Table of Contents

List of Illustrations

List of Tables

Chapter 1

Introduction

1.1 Fundamental puzzles and the need for new physics

Modern physics is built on two extraordinarily successful frameworks: the Standard Model of particle physics and general relativity. Yet several central observations of our universe remain unexplained within this combined framework. Among the most prominent are the absence of a complete quantum theory of gravity, the existence of dark matter and dark energy, and the observed dominance of matter over antimatter on cosmological scales [1, 2]. These open problems strongly suggest the existence of new physics beyond the Standard Model.

Among these puzzles, the matter–antimatter asymmetry is interesting to explore because it is both tightly connected to fundamental symmetries and is quantitatively established. Observations indicate that the number of baryons (protons and neutrons) in the Universe is unequal to the number of antibaryons (antiprotons and antineutrons) and all large-scale structures that we observe—stars, galaxies, and clusters—appear to be composed of matter rather than antimatter. More specifically, the visible Universe is made of baryons and electrons, with no evidence for appreciable amounts of antibaryons or positrons [1]. In this thesis, the emphasis is placed on the baryon asymmetry in particular, rather than on a charged-lepton asymmetry, because the baryon excess is the quantity most directly established by

cosmological observations, while the charged-lepton asymmetry is largely tied to it by the requirement of overall charge neutrality [3]. A lepton asymmetry in the neutrino sector may also play an important role and, in leptogenesis scenarios can be partially converted into a baryon asymmetry, as discussed in Sec. 1.3. Nevertheless, the observed cosmic excess of ordinary matter is most directly and conventionally characterized as a baryon asymmetry.

If the early universe began with equal matter and antimatter abundances, then the observed baryon excess must have been generated dynamically through baryogenesis rather than having been simply built into the initial state of the Universe. By an "initial-conditions explanation," one means a scenario in which the universe is assumed to contain a tiny excess of baryons over antibaryons, without any later dynamical mechanism that creates the asymmetry. This possibility is generally regarded as highly implausible. It would require extreme fine-tuning—roughly 6,000,001 quarks for every 6,000,000 antiquarks—and any primordial asymmetry present before inflation would be exponentially diluted by the inflationary expansion [1]. Assuming instead a symmetric starting point, Standard Model physics alone predicts a present-day baryon density many orders of magnitude smaller than observed [2]. Explaining the observed asymmetry therefore requires new sources of symmetry violation together with nonequilibrium dynamics capable of generating a net excess of baryons, as we shall discuss in Sec. 1.2.

1.2 Baryon asymmetry and Sakharov conditions

The baryon asymmetry is conventionally parameterized by

$$\eta_B \equiv \frac{n_B - n_{\bar{B}}}{n_\gamma}, \tag{1.1}$$

where n_B, $n_{\bar{B}}$, and n_γ are baryon, antibaryon, and photon number densities, respectively. Cosmic microwave background and big-bang nucleosynthesis analyses

imply [2, 4]

$$\eta_B \simeq 6.1 \times 10^{-10}, \tag{1.2}$$

while Standard-Model-only estimates are typically in the range $\eta_B^{\rm SM} \sim 10^{-20}$–$10^{-18}$, far too small to explain observations [5, 1].

Sakharov identified three necessary ingredients for baryogenesis [5]. In conventional CPT-invariant scenarios, these are necessary—though not by themselves sufficient—for generating a baryon asymmetry from an initially symmetric state.

(i) Baryon-number violation. There must exist processes with

$$\Delta B \equiv B_{\rm final} - B_{\rm initial} \neq 0.$$

If all interactions conserve baryon number, then no net baryon excess can be generated.

(ii) Departure from thermal equilibrium. Thermal equilibrium is a time-translation-invariant state in which the expectation values of observables remain constant. A system that begins in equilibrium with $B = 0$ therefore cannot evolve to a state with $B \neq 0$ while remaining in equilibrium. Baryogenesis thus requires a departure from thermal equilibrium.

(iii) C and CP violation. Let B_R and B_L denote representative baryon-carrying final states, where the subscripts indicate chirality. If C and CP were exact symmetries, then every baryon-producing process would be accompanied by a C- and CP-conjugate antibaryon-producing process with the same rate. Consequently, particle and antiparticle decays into corresponding channels would occur equally often. In the schematic two-channel example,

$$\Gamma(X \to B_R) + \Gamma(X \to B_L) = \Gamma(\bar{X} \to \bar{B}_R) + \Gamma(\bar{X} \to \bar{B}_L). \tag{1.3}$$

Baryon and antibaryon production would therefore remain equal, so no net asymmetry could develop. Baryogenesis thus requires C- and CP-violating processes.

All three Sakharov ingredients are present, at least formally, in the Standard Model, yet their quantitative realization is insufficient to explain the observed baryon asymmetry. Baryon number is violated by the processes called sphalerons, which preserve $B - L$ but violate $B + L$ and obey

$$\Delta B = \Delta L = \pm 3. \tag{1.4}$$

These transitions are exponentially suppressed at zero temperature, but they can become efficient in the hot early universe [1].

The Standard Model also contains C violation in the weak interaction and CP violation through the Cabibbo–Kobayashi–Maskawa mechanism. However, the corresponding CP-violating effects, commonly characterized by the Jarlskog invariant, are far too small to account for the observed value of η_B [2, 1]. Additional sources of CP violation are therefore required.

A possible departure from thermal equilibrium arises at the electroweak phase transition. In electroweak baryogenesis, such nonequilibrium dynamics would be generated by interactions with expanding bubble walls during a first-order transition. For the measured Higgs-boson mass, however, the electroweak phase transition in the Standard Model is a second-order transition rather than a strongly first-order [1]. Thus, although the Standard Model contains the Sakharov ingredients in principle, it does not provide enough CP violation or a sufficiently strong nonequilibrium environment to produce the observed asymmetry. Viable baryogenesis scenarios therefore require physics beyond the Standard Model.

Several broad mechanisms have been proposed. In *GUT baryogenesis*, superheavy bosons decay out of equilibrium and directly generate a baryon asymmetry [1]. Although conceptually simple, this idea is constrained by proton-decay limits, which push the relevant scale very high and typically demand a high reheating temperature after inflation. Moreover, in many minimal models the asymmetry is stored in $B + L$

rather than $B - L$ and can later be erased by electroweak sphalerons.

In *leptogenesis*, heavy singlet Majorana neutrinos decay out of equilibrium and generate a lepton asymmetry, which sphalerons partially convert into a baryon asymmetry [1]. The same framework naturally links baryogenesis to neutrino mass generation through the seesaw mechanism, making leptogenesis one of the most compelling possibilities, as discussed in detail in sec 1.3.

In *electroweak baryogenesis*, the asymmetry is generated near the electroweak scale by CP-violating interactions at bubble walls during a strongly first-order electroweak phase transition [1]. Realizing this scenario requires extending the Standard Model. Examples include two-Higgs-doublet models and supersymmetric frameworks such as the minimal supersymmetric SM (MSSM). A particularly attractive feature is that the required new CP-violating interactions may be testable experimentally.

Among these possibilities, scenarios with new CP-violating phases near experimentally accessible scales are especially interesting. However, even a clear observation of new CP violation alone would establish only one of the Sakharov conditions. It would therefore not, by itself, identify the full mechanism of baryogenesis; one would still need to explain how the required departure from thermal equilibrium, and possibly baryon-number violation, are realized. Nonetheless, such a discovery would signal physics beyond the Standard Model, which would already be a major breakthrough, and could serve as a starting point for constructing the theoretical framework needed to explain the full baryogenesis mechanism.

1.3 What should we do to find new CP violation?

How, then, should we search for new CP violation? Historically, symmetry principles have repeatedly guided major advances in fundamental physics: Noether's theorem connects continuous symmetries to conservation laws; gauge symmetries underlie the electromagnetic, electroweak, and strong interactions; beta-decay ex-

periments revealed parity violation in weak interactions; CP violation in kaon and B-meson systems established the CKM picture of quark-sector CP violation; and electroweak symmetry breaking is realized through the Higgs mechanism.

The last example is especially instructive: the Higgs boson was discovered through direct production at the Large Hadron Collider (LHC) at CERN. Therefore, one natural strategy is direct production at the energy frontier. Proton-proton collisions at the LHC currently reach center-of-mass energies of up to 13.6 TeV and have been used to search extensively for new particles, including supersymmetric partners [6], but no new fundamental particle has been confirmed since the Higgs boson discovery in 2012. Supersymmetric frameworks remain conceptually attractive in the context of new CP violation sources because they naturally introduce many additional CP-violating phases and can assist baryogenesis mechanisms, but the absence of direct signals increasingly pushes viable parameter space toward higher masses or more tuned regions [7]. Pushing the collider's energy frontier substantially beyond its present reach is extremely challenging in practice since it requires facilities of exceptional scale, cost, and technical complexity. At the same time, the LHC program has increasingly emphasized the precision frontier, where subtle deviations from Standard Model predictions may provide indirect evidence for new physics.

A second route is to explore the neutrino sector. Long-baseline accelerator experiments probe leptonic CP violation by comparing the $\nu_\mu \to \nu_e$ and $\bar{\nu}_\mu \to \bar{\nu}_e$ appearance channels, thereby constraining the CP-violating phase δ_{CP} in the Pontecorvo-Maki-Nakagawa-Sakata (PMNS) matrix. These measurements are especially interesting because they connect to leptogenesis, the idea that the cosmic baryon asymmetry may originate from an earlier lepton asymmetry [1, 2]. Leptogenesis is based on the seesaw mechanism where the Standard Model is extended by heavy neutrinos in order to account for the observed smallness of neutrino masses. It provides new CP-violating phases and violates lepton number. The heavy neutrinos

can also decay out of thermal equilibrium in the early universe and produce a net lepton asymmetry. Electroweak sphaleron processes then partially convert that lepton asymmetry into a baryon asymmetry [1, 2]. In this sense, the seesaw framework naturally realizes all three Sakharov conditions and is particularly appealing because the same new physics invoked to explain neutrino masses can also provide a viable mechanism for baryogenesis [1, 2].

Recent measurements and analyses have raised the possibility of a nonzero CP-violating phase δ_{CP} in the PMNS matrix [8, 9], which is very exciting and could provide important clues about leptogenesis. Note that the Dirac phase δ_{CP} alone may not account for all of the CP violation required in the lepton sector for leptogenesis to explain the observed matter–antimatter asymmetry, since additional phases may also be relevant. Moreover, the interpretation of current results depends sensitively on the neutrino mass ordering: depending on whether the ordering is normal or inverted, the evidence for a nonzero phase can appear stronger or weaker [8, 9]. Standard leptogenesis also requires neutrinos to be Majorana particles, a possibility that ongoing neutrinoless double-beta decay experiments aim to test. Nonetheless, any observation of nonzero leptonic CP violation would be very important, since it would constitute the first evidence for CP violation in the lepton sector—and specifically in the neutrino sector—and would establish one of the Sakharov ingredients needed for leptogenesis. Future measurements of the neutrino mass ordering, the absolute neutrino mass scale, $0\nu\beta\beta$ decay, and cosmological observables may therefore provide further insight into the seesaw mechanism and the viability of leptogenesis scenarios.

Although these large-scale experimental programs have been extraordinarily successful in the history of fundamental physics, recent technological progress—especially in artificial intelligence and quantum computing—naturally raises the question of whether new search strategies are now possible. At present, however,

these tools are best understood as powerful enablers rather than stand-alone replacements for experimental probes of fundamental physics. Modern AI and LLM systems can already accelerate many cognitive tasks, including data analysis, control optimization, theoretical exploration, and more, but experimental fundamental physics still depends on building, operating, and, crucially, debugging delicate and complex hardware systems: ultra-high-vacuum and cryogenic infrastructure, reliable high-voltage systems, and stable laser systems. Quantum computing is similarly transformative yet complementary; beyond its potential impact on cryptography, quantum simulation, and chemistry calculations, and more, it does not by itself provide direct experimental verification of new particles or interactions. For these reasons, the development of physical sensors and sophisticated experiments remains central to the discovery of new fundamental physics, while these emerging technologies become extremely important in the design, control, and interpretation of such experiments. This statement may eventually even need to be revisited if sufficiently capable embodied AI or robotic laboratory systems become able to autonomously build, operate, and maintain highly sophisticated experimental apparatus—a possibility that, while still emerging, may not lie in the very distant future[1].

Returning to examples of experiments guided by fundamental symmetries, one modern example comes from searches for electric dipole moments (EDMs), particularly of the neutron. Increasingly stringent limits on the neutron EDM imply that the QCD vacuum angle θ_{QCD} is extraordinarily small, sharpening the strong CP problem and motivating the Peccei–Quinn mechanism and its associated axion, which is also a compelling dark-matter candidate [10, 11]. In this way, EDM searches and their resulting constraints do not merely bound new sources of CP violation; they also

[1] If such systems become truly capable of performing the physical tasks required for experimental construction, calibration, troubleshooting, and routine operation, then perhaps they can carry out nearly all of the tasks currently performed by humans, and we may face a serious existential crisis. It remains to be seen whether that will happen.

deepen our understanding of the symmetry structure of fundamental theory.

1.4 Quantum sensing of CP violation via EDM searches in atoms and molecules

Beyond neutron EDM searches, one can ask which systems offer the greatest leverage for detecting similarly tiny symmetry-violating effects. Atoms and molecules are especially powerful in this regard: as quantum sensors, they combine exquisite state control and long coherence times with strong enhancement mechanisms—including, in polar molecules, enormous internal effective electric fields. EDM searches in such systems, and in particular molecules, therefore provide a complementary and often extraordinarily sensitive approach to CP violation [12, 11, 13, 14]. Indeed, current eEDM experiments in ThO and HfF^+ molecules already constrain broad classes of CP-violating new physics at and beyond the multi-TeV scale, with favorable model dependence extending this reach much further, up to 50 TeV energy scale [15, 16, 17, 18].

How, in the first place, can new physics at a high energy scale manifest itself in low-energy observables of atoms and molecules? The basic idea is that unknown CP-violating new physics usually introduces some new particles and they first couple to ordinary particles such as electrons, quarks, and gluons. In the leptonic sector, these interactions between new particles and ordinary particles can generate an electron EDM and a scalar–pseudoscalar electron–nucleon interaction, parameterized by C_S. In the hadronic sector, they can generate the QCD angle $\bar{\theta}_{\mathrm{QCD}}$, quark EDMs, and quark chromo-EDMs. These hadronic sources can then induce proton and neutron EDMs, and CP-odd hadronic couplings such as the pion–nucleon couplings $\bar{g}_{\pi NN}$. These can further induce, within nuclei, collective CP-odd moments such as the nuclear Schiff moment (NSM) and the magnetic quadrupole moment (MQM), as well as semileptonic interactions. In practice, three experimentally central observables are [19, 12, 13, 14]:

Electron electric dipole moment (eEDM, d_e). An EDM of the electron, most strongly amplified in heavy paramagnetic atoms and molecules. Sensitivity to d_e requires nonzero electronic spin, $S > 0$, i.e., at least one unpaired electron. The electron EDM and the scalar–pseudoscalar electron–nucleon interaction C_S are often not experimentally distinguished, because they produce the same dependence on electron spin; they are therefore frequently discussed together under the label of an electron EDM.

Nuclear Schiff moment (NSM, S). A CP-odd electric multipole moment of the nucleus generated by hadronic CP violation. A nonzero Schiff moment requires nonzero nuclear spin, $I > 0$, and it is most cleanly probed in diamagnetic atoms or closed-shell molecules with $S = 0$, where sensitivity to the external magnetic field is suppressed.

Nuclear magnetic quadrupole moment (MQM, M). A CP-odd magnetic quadrupole moment of the nucleus generated by hadronic CP violation. A nonzero MQM requires $I > \frac{1}{2}$, and also nonzero electronic spin, $S > 0$ [20, 21].

Finally, these CP violating observables further induce the collective electric dipole moment in atoms and molecule, in a way that violates CP symmetry. Experimentally, to measure these symmetry violating electric dipole moments induced in atoms and molecules, one would apply external electric field to atoms and molecules and let the electric field interact with EDMs to extract their interaction as energy shifts.

The measurement principle is thus to convert tiny CP-violating (CPV) EDMs into energy shifts by applying an electric field:

$$\Delta E_{\mathrm{CPV}} = -\mathbf{d}_{\mathrm{CPV}} \cdot \mathcal{E}_{\mathrm{eff}}, \tag{1.5}$$

followed by correlated reversals of electric-field or internal-state orientation to isolate the CP-violating signal. This induced CP-violating dipole interaction is con-

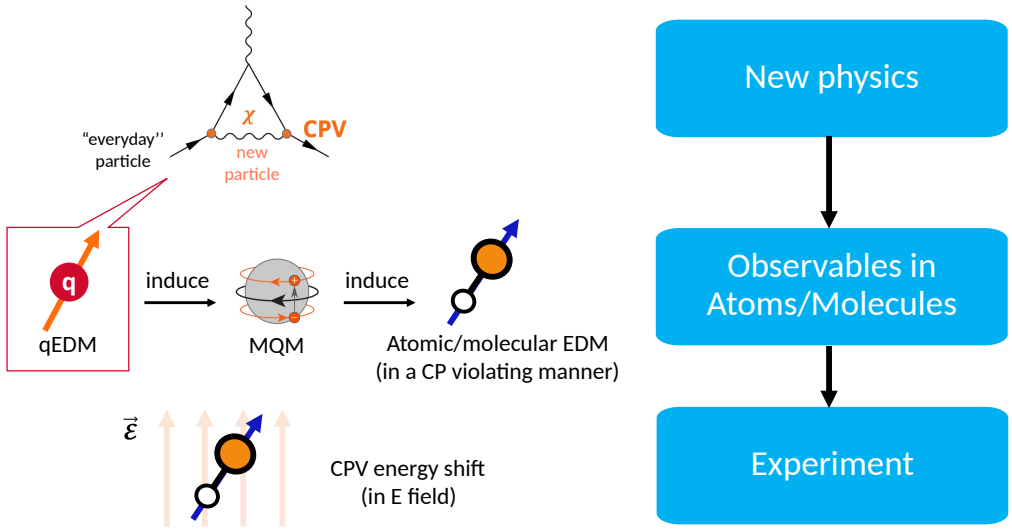

Figure 1.1: Schematic overview of the general flow from microscopic CP-violating new physics to measurable EDM signatures in atoms and molecules. The quark EDM (qEDM) and magnetic quadrupole moment (MQM) are shown here as representative examples of low-energy CP-odd observables used to illustrate this general pathway; other operators and moments can contribute in analogous ways. In precision experiments, such observables generate CP-odd energy shifts in atoms and molecules, which are measured by applying electric fields and comparing configurations related by field or internal-state reversal.

ceptually distinct from the ordinary molecular permanent dipole moment, which reflects static charge distribution in a bound state and does *not* violate CP symmetry.

Although many operator coefficients appear in the underlying effective field theory, eEDM, NSM, and MQM are especially experimentally useful observables because they produce distinct dependences on electronic and nuclear spins. This structure determines which species (paramagnetic molecules, diamagnetic atoms, polyatomics with parity doublets, nuclei with octupole or quadrupole collectivity, etc.) provide optimal sensitivity to different microscopic CP-violating sources.

A schematic overview of this chain, from microscopic CP-violating interactions to a measurable EDM signal in atoms and molecules, is shown in Fig. 1.1.

1.5 MQM searches

As discussed above, the two most sensitive eEDM searches, in ThO and HfF^+, have been remarkably successful, probing CP-violating new physics at effective energy scales of order 50 TeV (at one loop), well beyond the reach of current and near-term colliders. Whereas eEDM searches are primarily sensitive to CP-violating physics in the leptonic sector, NSM and MQM searches are especially sensitive to hadronic sources. For example, assuming the same frequency resolution, the sensitivity of the MQM in the polyatomic molecule YbOH to the underlying $\bar{\theta}_{\mathrm{QCD}}$ parameter is roughly 150 times greater than that of the eEDM in HfF^+. Experimentally, there is only one existing constraint on an MQM, and it comes from the Cs nucleus. That measurement was performed in 1989 using atoms rather than molecules, and therefore did not benefit from the molecular enhancement available in molecular MQM searches [22]. It is therefore particularly compelling to pursue MQM measurements in molecules and to explore nuclei with enhanced sensitivity to underlying CP-violating parameters such as $\bar{\theta}_{\mathrm{QCD}}$.

1.6 Design principles for precision EDM experiments

In a precision symmetry-violation experiment, the observable is typically a small frequency shift induced by underlying CP-violating sources. Schematically, one may write

$$\delta f = \frac{1}{h} \left(\beta_d \mathcal{E}_{\mathrm{eff}} d_e + \beta_M W_M M + \beta_S W_S S \right), \tag{1.6}$$

where d_e denotes the electron EDM, M the magnetic quadrupole moment (MQM), and S the nuclear Schiff moment (NSM). The coefficients $\mathcal{E}_{\mathrm{eff}}$, W_M, and W_S describe the intrinsic sensitivity of a given electronic state to these new-physics observables, while the factors β_d, β_M, and β_S encode how strongly a particular quantum state or transition within that electronic state responds to them. This decomposition is useful because it makes clear that improving sensitivity is not a single-parameter optimization problem: the reach of an EDM experiment is determined jointly by

frequency resolution, the chosen quantum states and transitions, and the molecular species and electronic state.

A convenient way to organize the problem is to separate the relevant design parameters into three categories. The first is *frequency resolution*, set by the measurement protocol and the total amount of acquired data. The second is the *intrinsic molecular sensitivity* to the targeted CP-violating observable, governed by quantities such as $\mathcal{E}_{\text{eff}}$, W_M, and W_S, which depend primarily on the electronic structure of the chosen species. The third is the *state-dependent sensitivity*, captured schematically by the β_i, which depends on the selected quantum states (e.g., Zeeman sublevels). From an experimental point of view, the first category is controlled largely by experimental design and implementation, the second by the choice of molecular species, and the third by the internal molecular structure.

In the shot-noise-limited regime, the statistical frequency resolution may be written schematically as

$$\delta f \sim \frac{1}{2\pi\tau\sqrt{f_{\text{rep}} N_{\text{shot}} T_{\text{DAQ}}}}, \tag{1.7}$$

where τ is the spin-precession or coherent interrogation time, f_{rep} is the experimental repetition rate, N_{shot} is the number of detected molecules per shot in the relevant state, and T_{DAQ} is the total data-acquisition time. This expression illustrates the basic statistical design principle: one seeks to maximize coherence time, repetition rate, and state-resolved molecule number while maintaining high detection efficiency and long-term stability. In practice, different platforms optimize different factors. Trapped-particle experiments can achieve long coherence times, whereas beam experiments often trade shorter τ for higher repetition rates or larger total flux.

The second major lever is the choice of molecule. Heavy polar molecules are especially attractive because relativistic effects in heavy nuclei and strong internal polarizing electric fields can produce large values of $\mathcal{E}_{\text{eff}}$, while these properties often also enhance sensitivity to hadronic CP-violating observables through W_M

and W_S. In this sense, molecular species selection directly determines how effectively a measured frequency shift can be converted into a bound on a fundamental new-physics parameter. Equally important is the choice of nucleus. Nuclear deformation can substantially enhance sensitivity to certain hadronic symmetry-violating moments, meaning that the sensitivity of NSM and MQM (S, M) to the underlying fundamental new-physics parameters is enhanced. In particular, quadrupole- and octupole-deformed nuclei can strongly enhance MQM and NSM effects, respectively. Thus, the optimal molecule is not merely a convenient spectroscopic system; it is one whose electronic and nuclear structure amplify the specific CP-violating interaction of interest.

The third lever is the internal molecular structure used to encode and read out the signal. Even if a molecule possesses large intrinsic values of $\mathcal{E}_{\text{eff}}$, W_M, or W_S, or large enhancement in sensitivity of d_e, S, M to the underlying fundamental new physics parameters, realized experimental sensitivity still depends on the angular momentum projections in the chosen states under electric and magnetic fields, how easily the population can be prepared in the chosen state, and how cleanly their relative phase can be prepared and detected. In this sense, molecular internal structure is not only a tool for characterizing the molecule but also a central part of the experimental design. The choice of parity doublets, hyperfine manifolds, and Zeeman sublevels can determine both the useful signal size and the degree of common-mode rejection against systematic shifts. The richest molecular structures therefore offer both opportunities and challenges: they provide more handles for engineering high sensitivity and suppressing noise and systematics, but they also make state preparation, control, and interpretation more complicated.

1.7 Polyatomic YbOH

These considerations are illustrated particularly well by YbOH, the molecule studied in our group, which provides an especially appealing case study for symmetry-

violation searches. As a heavy polar polyatomic molecule, YbOH offers large intrinsic sensitivity to CP-violating observables. In isotopes with nonzero nuclear spin, it also provides access to nuclear-spin-dependent effects, and the quadrupole-deformed ytterbium nucleus makes the system especially interesting for MQM studies. At the same time, YbOH is experimentally attractive for several practical reasons. Its polyatomic structure gives rise to closely spaced opposite-parity levels, or parity doublets, which allow strong polarization at electric fields much smaller than those typically required in diatomic molecules. This substantially relaxes the technical demands associated with high-field operation and can reduce electric-field-related systematic effects. In addition, YbOH is not radioactive, which simplifies handling and enables sustained laboratory development without the complications associated with radioactive species.

The main challenge is that these advantages do not automatically translate into the best statistical sensitivity, because the internal structure of polyatomic molecules with nonzero nuclear spin is extremely complicated. In a molecular-beam implementation, the coherent interrogation time is typically limited to the millisecond scale, and although the total molecular flux may be large, the number of molecules detected in any single science state can be relatively small because the population is distributed over many levels in the complex hyperfine structure, especially in odd isotopologues with large Yb nuclear spin. This makes the effective N_{shot} per addressed state a crucial bottleneck. Furthermore, the internal structure of polyatomic molecules is much richer than that of simpler diatomics, so the spectroscopy required for high-fidelity state preparation and readout can be experimentally demanding. Thus, the design problem is not simply to identify a molecule with large theoretical sensitivity coefficients, but rather to establish measurement schemes in which those coefficients can be exploited without sacrificing count rate, coherence, or control.

Another important factor to improve frequency resolution is state preparation and detection efficiency. In YbOH, recent advances in photon cycling and laser cooling point directly in this direction. Photon cycling in the odd isotopes enables more efficient optical state readout and can increase the usable molecule number per shot. Likewise, Doppler and Sisyphus cooling in YbOH can reduce transverse spread and improve phase-space density, thereby increasing both detection efficiency and interaction time. Implementing these techniques in odd isotopologues remains challenging because of their highly complex internal structure, but this appears to be a realistic target for future work.

From the perspective of experimental design, the central lesson is that an EDM experiment must be optimized simultaneously at the levels of molecular choice, internal structure, and experimental implementation. The best platform is not necessarily the one with the largest $\mathcal{E}_{\text{eff}}$, W_M, or W_S in isolation, nor the one with the longest coherence time alone, but rather the one that maximizes the overall product of intrinsic new-physics sensitivity and achievable frequency resolution while maintaining robust control of systematics. This thesis adopts that viewpoint throughout: the goal is to engineer and exploit molecular states that retain strong sensitivity to fundamental symmetry-violating interactions while also enabling favorable experimental operation, efficient readout, and robust suppression of systematic effects.

1.8 Scope of this thesis

This thesis develops and demonstrates general tools for symmetry-violation searches with enhanced robustness against experimental noise. The chapters that follow progress from source and beam technology to high resolution spectroscopy and engineered metrology protocols: simulation of cryogenic buffer-gas beams, spectroscopy of key YbOH bending-mode structure, development of field-insensitive clock transitions for symmetry violation searches, and an experimental demonstration of this clock-transition strategy. Together, these results establish a pathway

toward next-generation quantum sensors capable of probing CP-violating physics beyond the Standard Model.

Chapter 2

Simulation of Cryogenic Buffer Gas Beams

Portions of this chapter were published previously [23]. I also acknowledge David Shlivko and Gabriel Woolls for their contributions to this work.

2.1 Introduction

The cryogenic buffer-gas beam (CBGB) has emerged as a particularly powerful method for producing cold, slow, and intense beams of a variety of molecular species [24, 25]; it has been used for a range of spectroscopy [26, 27, 28, 29] and precision measurement experiments [15] and as the starting point for molecular laser cooling experiments [30, 31]. There are a number of established techniques to tailor CBGB properties to a particular application, such as hydrodynamic extraction [32] to create high-flux beams useful for precision measurements [33, 15], or two-stage "slowing" cells [32, 34] to create low-velocity beams suited to further slowing [35] and trapping [36]. These techniques often trade one feature for another; for example, two-stage cells benefit from reduced velocities but also have lower brightness, while hydrodynamically extracted beams have higher flux but are "boosted" to higher velocities.

It would be useful to be able to rely on computer simulation to optimize CBGB design for any given application. Direct simulation of buffer gas beams, however, is a computationally challenging problem. The difficulty lies in the density regimes of the buffer gas and molecular[1] species. CBGBs typically operate in the "intermediate" flow regime, where the mean free path between buffer gas collisions is not in the range of either the molecular or fluid limits [25]. Additionally, the species of interest often has a density orders of magnitude smaller than that of the buffer gas, which can cause out-of-equilibrium dynamics under typical operating parameters. Accurately capturing the behavior of CBGBs therefore requires not only a reliable model of intermediate-regime flows, but also of dynamics on the molecular level.

To overcome this difficulty, we utilize a two-step approach that explicitly incorporates these considerations to model a variety of CBGB implementations. First, we model the steady-state buffer gas flow using Direct Simulation Monte Carlo (DSMC) [37], which enables computationally tractable simulations of intermediate-regime flows. Second, we trace individual particles of the molecular species through the background buffer gas flow using a random collision model. By treating both the buffer gas flow and the molecular trajectories throughout the cell, aperture, and beam regions, this approach is able to reproduce nontrivial features of various CBGB designs [25], such as aerodynamic focusing and the effects of slowing cells and de Laval nozzles, that depend on the particular behavior of both the molecules and buffer gas. These results indicate that the two-step approach correctly models both the intermediate-density regime of the cell and the low-density regime of the beam itself, offering a robust tool for CBGB study and optimization across a wide range of applications.

Several previous works have modeled the behavior of molecules in a buffer gas cell using a variety of methods and their combinations, such as particle tracing with

[1] Though these sources are also useful for atoms, we shall refer to the species of interest as a molecule for simplicity.

random walk processes [24, 38], continuum fluid simulation [39, 40] in combination with diffusion [41], direct simulation Monte Carlo (DSMC) [42, 43], and Self-Consistent Mean Field DSMC (SCMFD) [44]. The last of these is most similar to the methods employed here, though all of these previous works share some similarities with our approach.

2.2 Methods

We shall focus on simulations of a CBGB source consisting of a cryogenic volume or "cell" with cm-scale dimensions connected to a buffer gas inlet tube and an opposing exit aperture, as shown in Fig. 2.1. In steady-state, the balance between flows through the inlet and aperture creates a roughly stagnant density of buffer gas in the cell. Hot atoms or molecules are introduced through ablation of a solid precursor or through a heated inlet, thermalizing with the cold buffer gas and exiting through the aperture as a molecular beam. Details of typical CBGB sources, along with relationships for quantities such as flow, density, diffusion, *etc.*, can be found in Ref. [25].

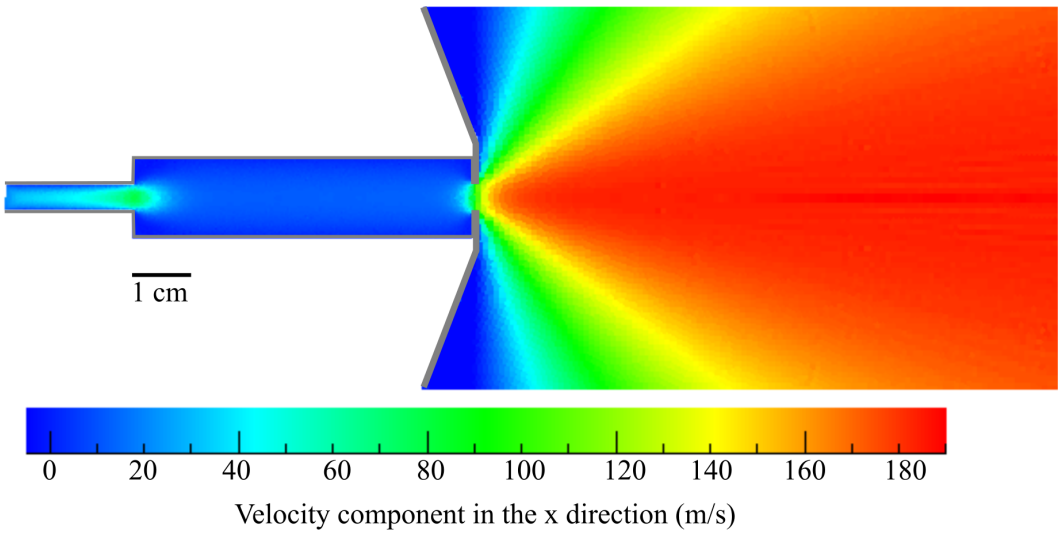

Figure 2.1: Spatial variation of the forward velocity of the 4 K He buffer gas at around 20 SCCM in a single-stage cell computed with DS2V. In this and all other cells, the buffer gas enters on the left and exits through a 5 mm diameter, 0.5 mm thick aperture before expanding into vacuum. Gray lines indicate 4 K surfaces.

we present a two-step approach to simulating the dynamics of the CBGB. The first step is a DSMC simulation that computes the properties of the buffer gas alone, including its equilibrium flow velocities, temperatures, and densities throughout the cell and beyond the aperture. The second step is a particle-by-particle simulation of the molecular species as it traverses the cell while interacting with the steady-state buffer gas and emerges as a beam.

Direct Simulation Monte Carlo

The DSMC method is a statistical technique for simulating gas dynamics via the Boltzmann equation [37]. DSMC is particularly useful for modeling the density regimes of typical cryogenic buffer gas beam experiments, where gases are too dilute for the Navier-Stokes Equations to be applicable, but too dense for a tractable computation of each atom's trajectory. In the DSMC algorithm, each simulated particle represents a large number of identical particles, so that the overall distribution in phase space is maintained but fewer computations must be made to recover an accurate description of the flow dynamics. These particles are grouped into "cells" (not to be confused with the cryogenic cell containing the buffer gas and species) and nearby particles within a cell are allowed to collide and exchange momentum. Beyond these general features, the mechanics of the DSMC algorithm are largely adjustable to best fit the context of a specific system.

The DSMC software we utilize in this work is DS2V [45]. We assume an axially symmetric flow to simulate a cylindrical buffer gas cell and allow the buffer gas to flow in through the inlet at rates between 1 and 130 SCCM (standard cubic centimeter per minute, or about 4.5×10^{17} atoms per second). Typical number densities and velocities of this flow are on the order of 10^{15} cm^{-3} and 10 m/s. The simulations produce detailed information about the properties of the buffer gas, such as temperature, number density, and flow velocity, on a mesh of points within the specified geometry of the buffer gas cell and the area beyond its aperture. The walls

of the cell in the simulation are kept at 4 K and are assumed to be diffuse reflectors for the buffer gas and perfect absorbers for the molecular species, since the latter has negligible vapor pressure at cryogenic temperatures. The cell is initially empty (vacuum), and the simulation runs until it converges to a steady state. The mass flow rate into the cell is explicitly calculated by integrating the flux over the surface of the inlet tube aperture. We model the helium-helium collisions as hard spheres with cross-section $\sigma_{b-b} = 2 \times 10^{-15}\text{cm}^2$ [46]. Though the true cross section depends on collision energy [47], we have varied the buffer gas collision cross-section by a factor of ∼5 in either direction and confirmed that the main features and trends are relatively unaffected. Future improvements of this technique could include more accurate collision models, but we find that the hard sphere approximation is sufficient for the present purpose.

Particle Tracing

Once the properties of the buffer gas have been determined by DSMC, we trace the paths of individual molecules as they move through the steady-state buffer gas flow. Because the density of the molecular species is significantly lower than that of the buffer gas in typical experiments, each molecule's path is traced independently of the others, and collisions occur only with the buffer gas. The general structure of the particle tracing algorithm is as follows:

1. *Specify the molecule's initial state.* The position $\mathbf{x}$ and velocity $\mathbf{v_s}$ of the molecular species (s) are either specified explicitly or drawn randomly from a desired distribution. The initial conditions used to generate our results in Section 2.3 will be stated and motivated therein.

2. *Compute the duration of the present time step.* We use a dynamic time step chosen[2] such that the probability of collision at every step is $p = 0.1$. To

[2]Taking smaller (more precise) time steps does not noticeably impact the results of these simulations, as long as the probability of a collision in a time step is $\lesssim 0.3$.

accomplish this, we compute the collision rate of the molecular species,

$$\Gamma = \sigma_{b-s} n \langle v_{\text{rel}} \rangle, \tag{2.1}$$

where the hard-sphere elastic collision cross section between the buffer gas (b) and the molecular species, σ_{b-s}, is set to a benchmark value of $3 \times 10^{-14}\text{cm}^2$ unless specified otherwise. The buffer gas number density $n = n(\mathbf{x})$ is interpolated from DSMC data at the molecule's position, and the mean velocity of buffer gas atoms relative to the molecular species $\langle v_{\text{rel}} \rangle$ is computed from the molecule's velocity and the interpolated buffer gas temperature and flow velocity at its position using Eq. (B1) in ref. [23]. The desired time step is then $\Delta t = p/\Gamma = 0.1/\Gamma$.

3. *Update the molecule position and velocity.* We first update the molecule's position given its current velocity, $\mathbf{x} \mapsto \mathbf{x} + \mathbf{v_s} \Delta t$. Next, if a collision occurs (which is decided at random with probability $p = 0.1$), we randomly choose a collision partner based on the local buffer gas properties and compute the resulting velocity change of the species. This process is described in detail in the appendices, but we provide a brief summary here.

   First, we randomly sample the thermal velocity $\mathbf{u}$ of a colliding buffer gas atom from the conditional distribution

$$f(\mathbf{u}|\text{coll}) \propto v_{\text{rel}} \times f_{\text{MB}}(\mathbf{u}), \tag{2.2}$$

   where

$$v_{\text{rel}} \equiv |\mathbf{v_s} - \mathbf{v_b}| = |\mathbf{v_s} - (\mathbf{u} + \mathbf{v}_{\text{flow}})| \tag{2.3}$$

   is the relative velocity between the molecule and the randomly chosen buffer gas atom, $f_{\text{MB}}(\mathbf{u})$ is the Maxwell-Boltzmann distribution, and $\mathbf{v}_{\text{flow}}$ is the buffer gas flow velocity extracted from DSMC. This weighted distribution accounts for the greater likelihood of collisions involving atoms with higher

relative velocities. The process by which we sample from this distribution is detailed in ref. [23] under "Bayesian Thermal Velocity Sampling."

Once a buffer gas atom velocity is determined, we employ a hard-sphere elastic collision model to compute the impulse felt by the molecule when colliding with this buffer gas atom with a random impact parameter. The process of sampling an impact parameter and computing the post-collision velocity of the molecule is detailed in ref. [23] under "Hard-Sphere Collision Mechanics."

4. *Repeat Steps 2-3 until the molecule reaches a wall or a specified finish line.* The simulation ends if the molecule hits a wall of the specified geometry (at which point it sticks to the surface) or reaches an end point of the simulation space.

Note that in this work we only examine the external degrees of freedom of the molecule. We do not consider the internal state of the molecule and therefore ignore the effects of inelastic collisions. The collisions are treated as an average over all relevant internal degrees of freedom, which we find is sufficient to track the molecule's external state. A future improvement would be to include the internal states for even more accurate and complete modeling [42, 43].

2.3 Results

The goal of this study is to model the qualitative behaviors of the CBGB in a number of different experimental configurations. We will begin with a single-stage cell fixed at typical experimental dimensions and add features incrementally, such as a second slowing stage and a de Laval nozzle. In this way, we can explore the direct effects of those changes on the beam. We will predominantly be simulating SrF molecules in a 4 K helium buffer gas [48] to model typical conditions of previous experiments, which range over both heavier and lighter species [25].

Single-stage cell

The single-stage buffer gas cell is the standard design for producing cold molecules using the CBGB method [24, 25]. The flow of the buffer gas is usually operated in the "hydrodynamic" enhancement regime, where hydrodynamic forces push the molecules out of the cell and into the beam before they have time to diffuse and stick to a cell wall [32].

Figure 2.1 shows the forward velocity of the 4 K He buffer gas with around 20 SCCM input flow in the single-stage cell used in this simulation. The cell is cylindrical with a 12.7 mm internal diameter and 53 mm length. 4 K helium gas flows into the cell through an inlet tube whose internal diameter is 4 mm and length is 20 mm. The exit aperture has a 5 mm diameter and 0.5 mm thickness.

Flow parameterization

In discussing our results, it is useful to relate several quantities to describe the buffer gas flow [25], such as the mean free path between buffer gas collisions λ and Knudsen number $\mathcal{K} = \lambda/d_{aperture}$. Another common parameter is the Reynolds number $\mathcal{R}$, which can be related [49, 25] to microscopic quantities via

$$\mathcal{M} \approx \frac{1}{2}\mathcal{K}\mathcal{R}, \tag{2.4}$$

where the Mach number $\mathcal{M}$ is the ratio of the buffer gas flow velocity to the local speed of sound. We compute λ and $\mathcal{M}$ using DSMC, which allows us to extract $\mathcal{R}$ using the equation above. $\mathcal{M}$ is typically estimated as being ≈ 1 at the aperture for these sources, which our DSMC simulations show to be reasonably accurate (see Fig. 2.2). However, the Mach number of the buffer gas varies by around an order of magnitude within a few diameters of the exit aperture, as expected for a free jet expansion [50]. The parameters $\mathcal{K}$ and $\mathcal{R}$ are frequently used to classify flows into the molecular ($\mathcal{R} \lesssim 1$), intermediate ($\mathcal{R} \approx 1 - 100$), and hydrodynamic ($\mathcal{R} \gtrsim 100$) limits [25].

We can use eq. (2.4) to extract a linear relationship [25] between flow f and Reynolds number $\mathcal{R}$ with slope $\mathcal{R}/(f/\text{SCCM}) \approx 0.8$, as shown in Fig. 2.2. Plots presented here are parameterized in terms of buffer gas flow, but we include this conversion as some CBGB papers use $\mathcal{R}$ instead.

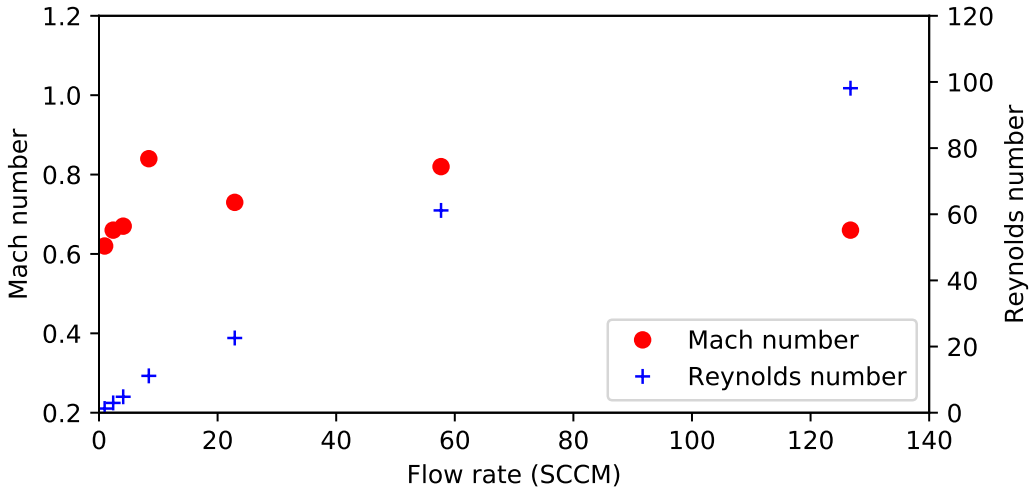

Figure 2.2: DSMC results for Mach Number $\mathcal{M}$ at the aperture, and corresponding Reynolds Number $\mathcal{R}$ (from Eq. 2.4), plotted against 4 K He flow (SCCM) for a single-stage cell.

Extraction

The extraction fraction is defined as the total number of molecules emitted into the beam divided by the total number of molecules initially present in the cell. For hydrodynamically extracted beams, this is typically 10-50% [32, 25]. This efficient extraction, combined with the buffer gas density being too low for appreciable losses from reactions or clustering, is one of the reasons why CBGB sources are so bright, especially for refractory and radical species. In the context of experiments where molecules are introduced into the cell through laser ablation, which is common for these types of challenging species, extraction will depend on complex ablation dynamics that set the initial spatial distribution of molecules [51, 52]. While our computational methods could be employed to investigate the post-ablation ther-

malization itself,[3] we choose in this thesis to focus on exploring the molecular dynamics post-thermalization. Under typical conditions, the thermalization process occurs rapidly and yields a fairly uniform distribution of molecules throughout the cell [51], making this a valid starting point for simulation.

We studied the dependence of extraction on initial spatial distribution by comparing simulations with three different initial conditions: a 1 cm diameter Gaussian ball (with standard deviation 0.33 cm), a 1 cm diameter uniform ball, and a uniform distribution over the entire cell. The molecule velocities are initialized to a 4 K thermal distribution with zero mean velocity. Figure 2.3 shows the extraction fraction for each of these three cases under various flow rates. While the extraction fraction itself depends on these initial conditions, we see that the qualitative behavior is consistent among all of them. This behavior can be understood by comparing the timescales of "pumpout" τ_{pump}, the time it takes for a typical buffer gas atom to exit the cell, against diffusion τ_{diff}, the time it takes for a typical molecule to diffuse to the walls [32, 25]. The ratio $\gamma_{cell} = \tau_{diff}/\tau_{pump}$ therefore characterizes the extraction behavior.

[3] Our simulations of the thermalization process indeed recovered the time constant estimated in [25].

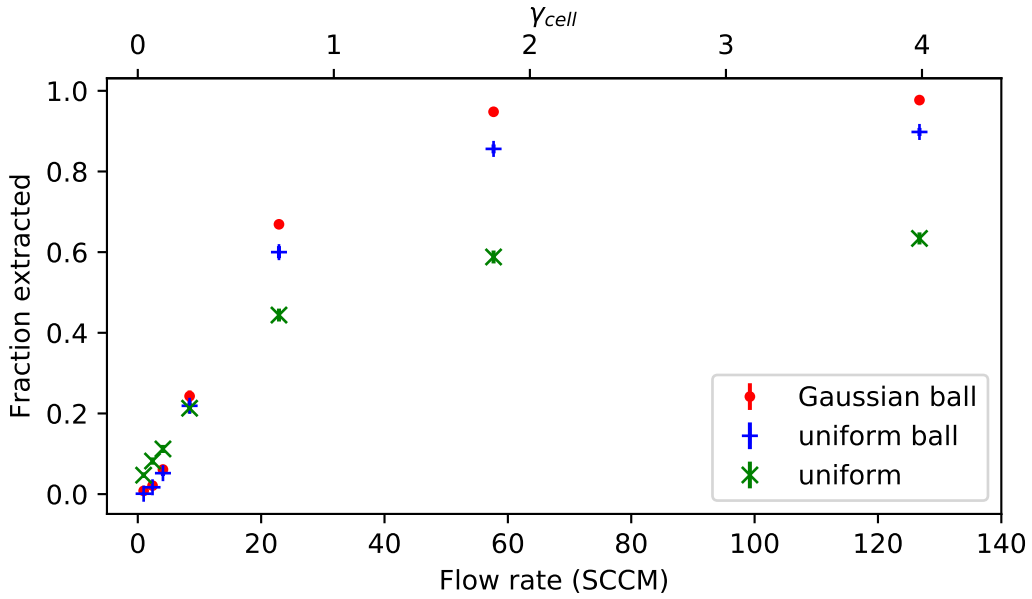

Figure 2.3: Extraction versus 4 K He flow (SCCM) with three initial conditions: 1 cm diameter Gaussian ball, 1 cm diameter uniform ball, and uniform distribution over the cell. The initial molecules are thermalized at 4 K. The error bars are calculated using binomial statistics.

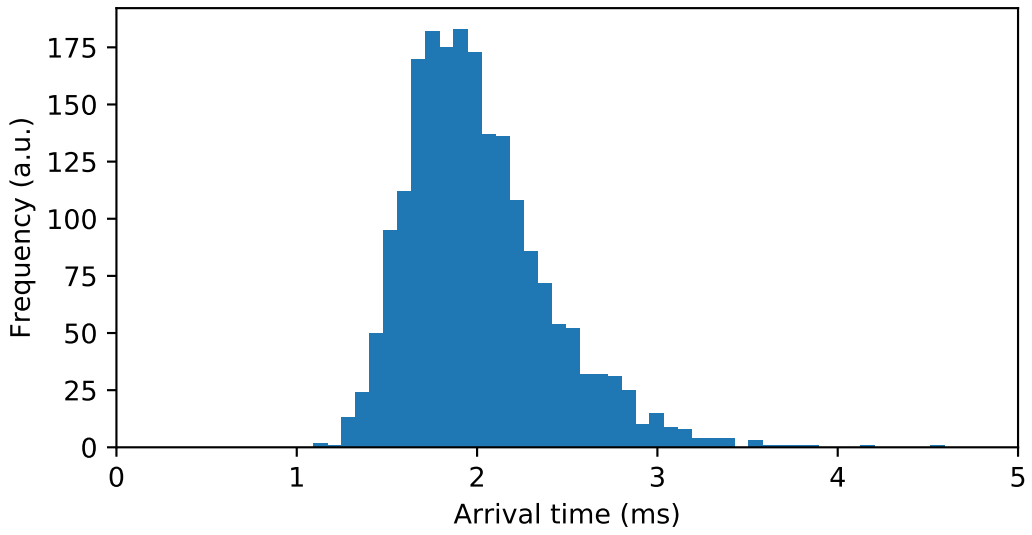

Figure 2.4: Histogram of pumpout times for a 20 SCCM helium flow, or equivalently instantaneous number density at the aperture versus time after the molecules are created. The initial spatial distribution of molecules is a 1 cm diameter Gaussian ball.

For $\gamma_{cell} \lesssim 1$, most molecules will diffuse to the cell walls and stick. However, for $\gamma_{cell} \gtrsim 1$, many of the molecules will be extracted from the cell, and the extraction

saturates to some maximum value for $\gamma_{cell} \gg 1$, as depicted in Fig. 2.3. Notice, however, that the maximum saturated values depend on the initial spatial distribution of molecules; this makes intuitive sense, as the fate of each molecule depends on its distance from a wall or the aperture. This spatial dependence contributes to the typical molecular beam pulse width of $\sim$ 1 ms at the exit aperture, as shown in Fig. 2.4, though it is possible to design and engineer cells to have shorter effective pumpout times to create narrower pulses [40].

The data for the initial conditions of Gaussian ball and uniform ball are similar since the variation of extraction efficiency over $\sim$ 1 cm length scales near the cell center is minor (as can be seen in Fig. 2.5) and correspondingly does not have significant impact on the total extraction efficiency. On the other hand, a distribution which is initially uniform across the entire cell has a lower extraction efficiency because it includes molecules that begin very close to a wall or a corner, where the extraction efficiency is low.

To further elucidate this spatial dependence, we can map out the extraction probability, pumpout time, and diffusion time within the cell. Figure 2.5 shows these quantities for a buffer gas flow rate of around 20 SCCM. Note that the extraction drops fairly rapidly as one approaches the "corner" (lower right), possibly due to vortex formation, as has been noted elsewhere [40, 39]. The diffusion time can be estimated [25] to be around 3.3 ms, which is close to our results near the interface with the buffer gas inlet tube.

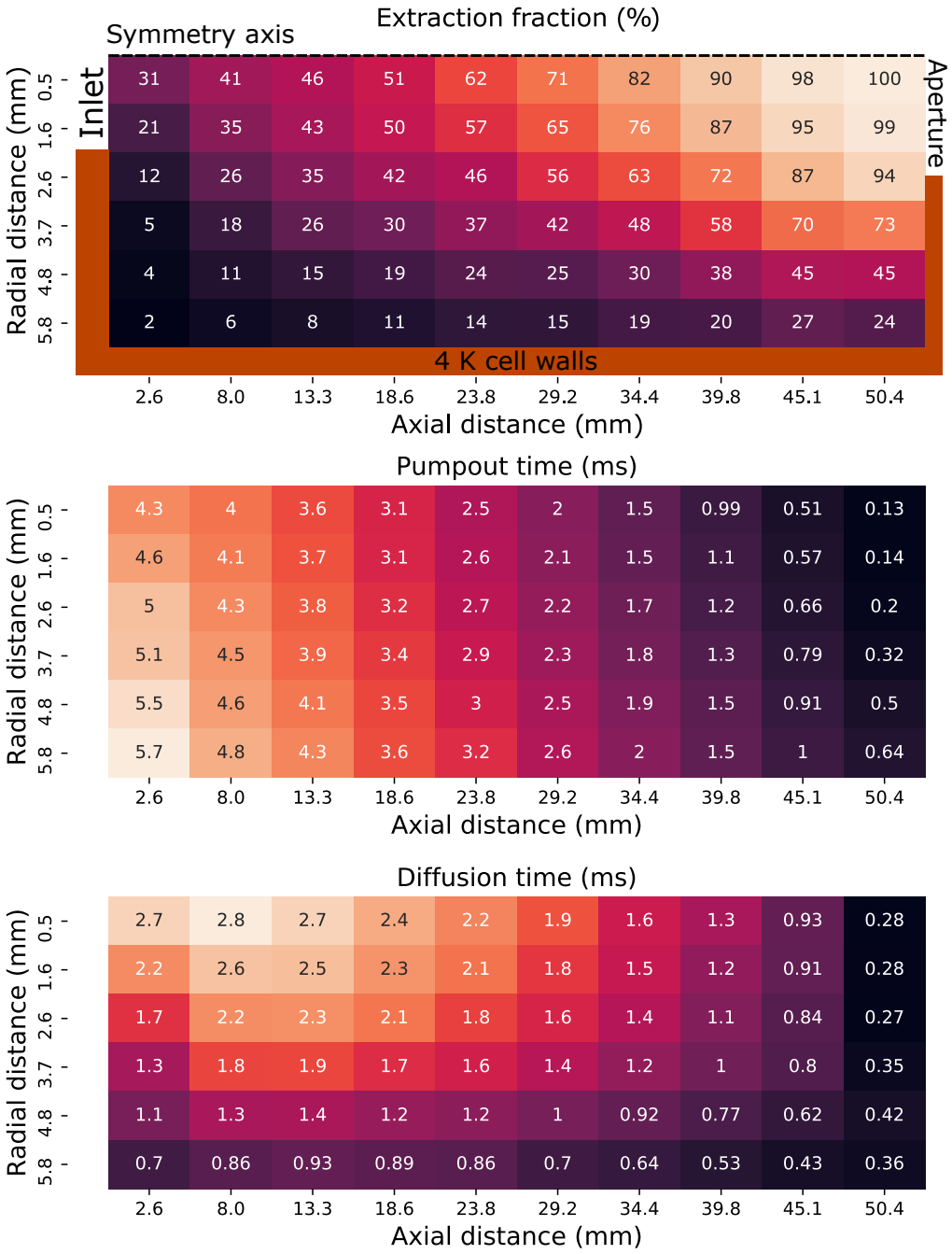

Figure 2.5: Heat map of extraction fraction (top), pumpout time (middle), and diffusion time (bottom) versus initial molecule position for a 20 SCCM buffer gas flow. The x-axis indicates the distance from the point where the buffer gas inlet tube ends (0 mm) and finishes at the exit aperture (53 mm). The y-axis indicates the radial distance from the central axis of the cell. Therefore, the top right (left) corresponds to the exit aperture (fill line), and the bottom left and right are interior corners. The top figure indicates the symmetry axis (dashed line), as well as the location of the buffer gas inlet, beam exit aperture, and the cell walls. Note that the x- and y- axes have different scales.

Velocity

Another critically important feature of the CBGB is the relatively low forward velocity of the molecular beam, typically $\lesssim 200$ m/s. This enables molecular beam experiments with long coherence times [53, 15] and efficient slowing of molecules to the capture velocity of magneto-optical traps [54, 30, 31]. Figure 2.6(a) shows the median forward velocities versus buffer gas flow rate with different cross section values $\sigma_{b-s} = \{3,\ 1,\ 0.3\}\times 10^{-14}$ cm^2. For all velocity plots, the reported values are measured 3 cm from the exit aperture. As the cross section value increases, the forward velocity also increases but its dependence on flow rate is the same, increasing linearly before saturating at some value. The behavior is consistent with results from experiments using a similar configuration [33, 48, 41], as well as theoretical expectations [25]. For low flow, the source is effectively effusive and we expect a velocity close to that of an effuse thermal source of molecules. At high flow, we expect the large collision rate to keep the molecules in equilibrium with the buffer gas, which approaches the supersonic velocity of ≈ 200 m/s for 4 K He. This increase of molecular forward velocity with increasing flow is typically called "boosting."

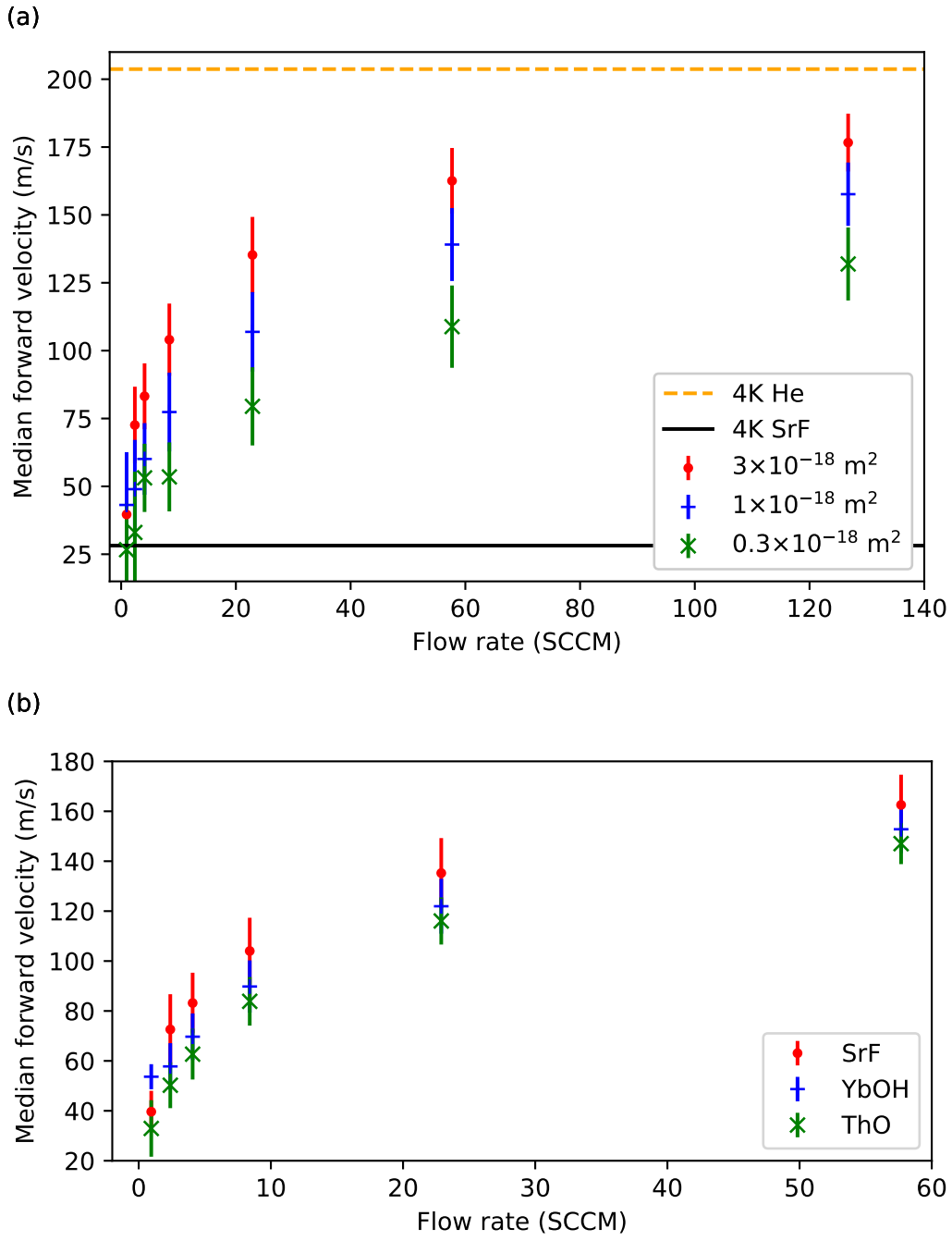

Figure 2.6: (a) Median forward velocities versus 4 K He flow (SCCM) for SrF mass and various cross sections σ_{b-s}. The dashed and solid lines indicate 4 K He supersonic mean velocity and 4 K SrF thermal velocity, respectively. (b) Median forward velocities versus 4 K He flow (SCCM) for cross section $\sigma_{b-s} = 3 \times 10^{-14}$ cm^2 and various molecular masses. The error bars indicate the standard deviation of the velocity distribution.

Our simulation results for all molecular masses (SrF, YbOH, ThO) show lower

velocity at low flows compared to experimental results for SrF [48] and ThO [33] but more closely match those for Yb [41]. This discrepancy could be explained by a number of factors, including imperfect thermalization at low densities or instantaneous changes in densities as buffer gas is desorbed from the cell walls by ablation. However, the higher flow behavior is consistent with the experimental data, particularly for the larger cross section value of 3×10^{-14} cm^2. Note that the cross section could be treated as a fit parameter if the goal is to match data from a particular experiment.

Figure 2.6(b) shows the median forward velocities versus He flow at 4 K for species of different mass: SrF, YbOH, and ThO. As the mass of the species decreases, the forward velocity increases while the general trend of velocity versus flow is maintained. However, the effect is not significant, which agrees with experimental data for species over this mass range [33, 48, 41]. Figure 2.7 shows the median forward velocities versus distance from the exit aperture for 4 K He with various flow rates. As the flow rate approaches $\sim$ 100 SCCM, the molecular velocities begin to saturate near the supersonic mean velocity of the helium buffer gas. The forward velocity saturates at around 1 cm from the exit aperture, similar to experimental data [48].

We explored the sensitivity of these simulated velocities to various parameters of the buffer gas cell configuration, such as the thickness of the exit aperture (by a factor of 5, up to 2.5 mm) and the initial distribution of molecules, but these did not have an appreciable effect on the results. We also ran these simulations with 16 K He and 16 K Ne buffer gas and found that the behavior scaled as expected with the thermal velocities and temperature of the buffer gas atoms, e.g. with the supersonic mean velocity scaling as $\sim \sqrt{T/m_b}$ [25] .

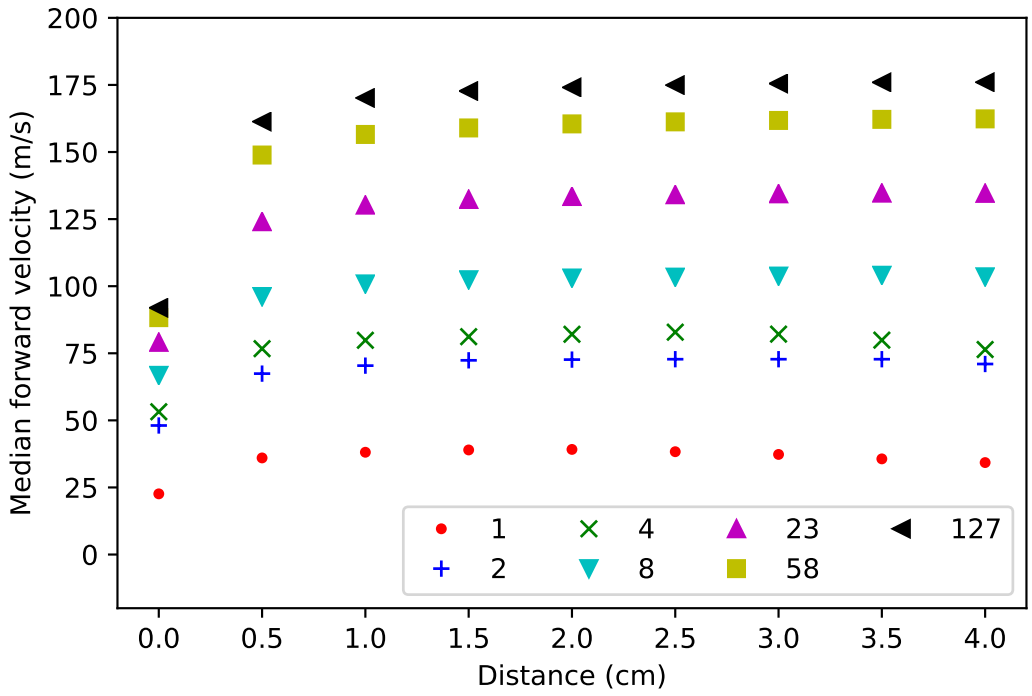

Figure 2.7: Median forward velocities versus distance from the exit aperture for 4 K He with various flow rates (SCCM). The legend indicates flow rate (SCCM) rounded to the nearest integer.

Beam divergence

A third key feature of CBGBs is low beam divergence. Molecules from a beam source are emitted into a finite solid angle, only a fraction of which can be used in an experiment, with the remainder leaving the beam line and striking a wall. Lower divergence results in higher density on the beam line, and therefore higher useful molecular flux. A common measure of beam divergence is given by [25]

$$\Delta\theta = 2\arctan\left(\frac{\Delta v_\perp}{2v_\parallel}\right), \tag{2.5}$$

where $\Delta v_\perp$ is the transverse velocity spread (FWHM) and $v_\parallel$ is the mean forward velocity. Since the transverse spread is set by the molecular species' thermal velocity, while the forward velocity is largely set by the buffer gas thermal velocity, we expect the angular spread to be narrower than that of an effusive or supersonic source, where $\Delta v_\perp \sim v_\parallel$. Figure 2.8 shows the beam divergence versus 4 K He flow for

a single-stage cell. The minimum arises from the fact that the transverse velocity spread continues to increase while the forward velocity begins to saturate. The value at this minimum can be estimated [32, 25, 41] to be $\Delta\theta \sim 1 - 2 \times \sqrt{m_b/m_s}$. For the case of SrF in He, this value ranges from $\approx 10 - 20°$, compared to the simulated minimum of $\approx 25°$.

Note, however, that the experimental data from different CBGB sources show differing behavior of divergence versus flow. For example, ThO and SrF in He buffer gas [33, 48] show a flat divergence versus flow relationship and at a larger than expected value, ThO in Ne [33] exhibits a minimum but at a larger than expected value, and Yb in He [41] has a minimum close to the expected value. As we shall discuss in section 2.3, the kinetics of the expansion depend on the specific geometry of the nozzle [41, 55], which was similar but not identical in these various experimental implementations.

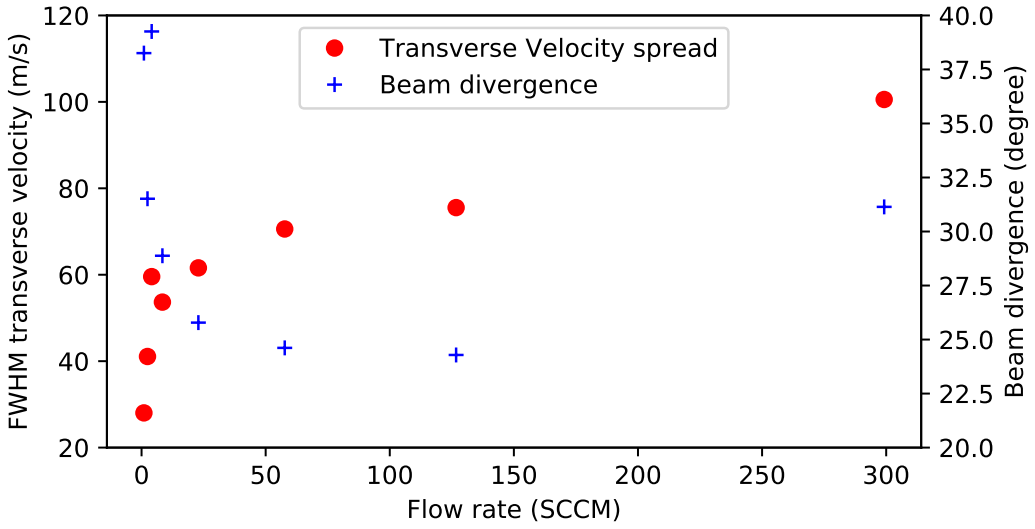

Figure 2.8: Transverse velocity FWHM and beam divergence versus 4 K He flow (SCCM). The slope of the transverse velocity FWHM at higher flow rates is roughly 0.2 m/s/$\mathcal{R}$, which is consistent with [33, 48].

Two-stage cell

We now move on to discussing some variations of the traditional CBGB design, with the first being the two-stage "slowing" cell. In these remaining sections, we focus only on the salient features of these variants compared to the single-stage cell.

The two-stage cell [32, 34] is designed to benefit from hydrodynamic extraction while producing a slower molecular beam than a traditional single-stage cell. The idea is to create a steady-state density of buffer gas at the aperture, thereby stifling the boosting effect through collisions with nearly stationary buffer gas atoms. Our simulated cell consists of the same single-stage buffer gas cell as described in the previous section, with the addition of a second slowing cell after a 4.7 mm gap, as shown in Fig. 2.9. This second cell has a 17 mm internal diameter and a length of 10 mm, with an exit aperture of 5 mm diameter and 0.5 mm thickness. Note that experimental implementations of this design use a variety of configurations, several of which were examined in [34].

Figure 2.10 shows the median forward velocities and the extraction fractions versus 2 and 4 K He flow with a single-stage cell and two-stage cell. Compared to a single-stage design, the two-stage cell reduces the forward velocity by a factor of $\sim$1.5 but simultaneously reduces the extraction by up to a factor of $\sim$ 10. This is consistent with observations in experimental implementations of two-stage cells [34]. Similarly, decreasing the temperature of the cell from 4 K to 2 K results in a reduction of the forward velocity by a factor of $\sim \sqrt{2}$, as expected. The boosted molecules at the first exit aperture experience several collisions with nearly-stationary buffer gas atoms and are slowed. The density of the buffer gas is also much lower in the second stage than the first stage (roughly by a factor of 10), so the boosting effect at the second aperture is weaker. Thus, the molecules exit the second aperture slower than in a traditional single stage cell.

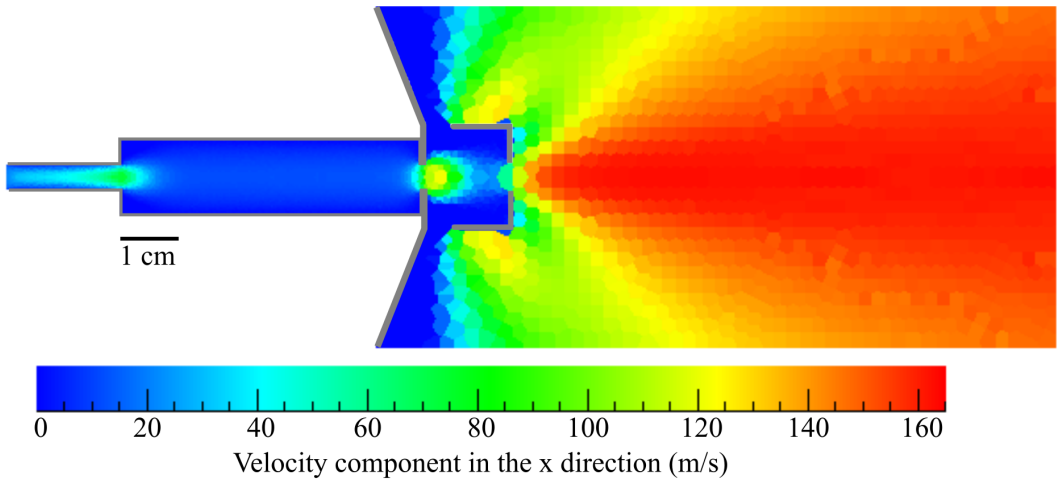

Figure 2.9: Spatial variation of the forward velocity of the 4 K He buffer gas at around 20 SCCM in a two-stage cell as computed with DS2V. It consists of the same single-stage buffer gas cell as the previous section with the addition of a slowing cell.

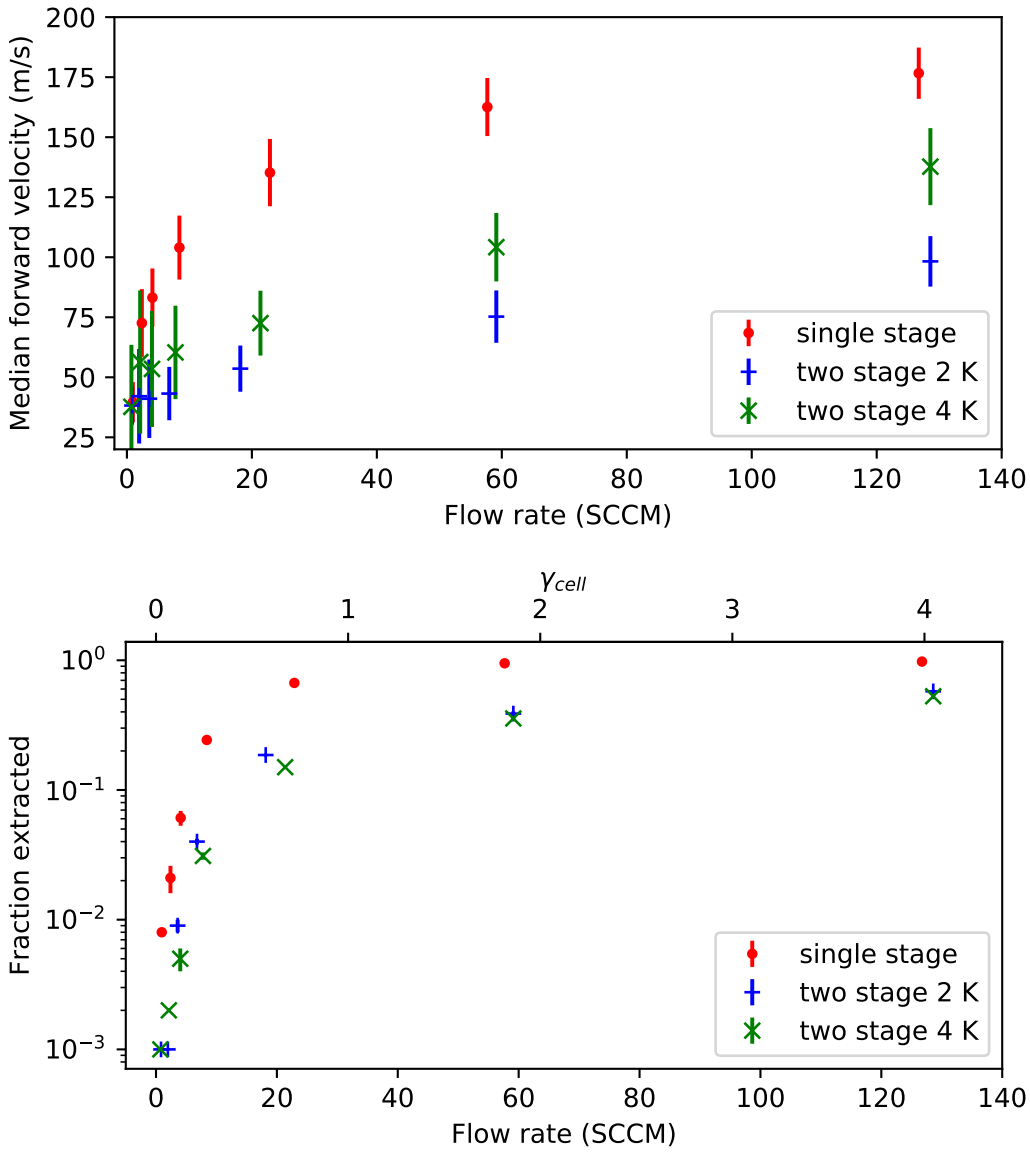

Figure 2.10: Median forward velocities (top) and extraction fraction (bottom) versus He flow (SCCM) for single-stage (4 K) and two-stage (2 K and 4 K) cells.

de Laval nozzle

A de Laval nozzle [50, 56, 57] is a converging-diverging nozzle designed to reduce the transverse velocity spread and beam divergence in high flow regimes without significantly reducing the overall extraction fraction. The de Laval cell is a modified single-stage buffer gas cell with a de Laval nozzle placed at the exit aperture [57], as shown in Fig. 2.11. We use the geometry of [57] but approximate the shape of

the nozzle with four straight lines. Figure 2.12 compares the beam divergence and transverse velocity spread for a traditional single-stage cell versus a cell with a de Laval aperture. The divergence of the molecular beam is reduced compared to the standard aperture at the high flow rates ($\gtrsim$ 50 SCCM), where the hydrodynamic effects of the de Laval nozzle are expected to be important, as seen in previous experimental results [57]. The reduction in divergence results almost entirely from the lower transverse velocity spread, as we find both in the simulations and the experimental data that the forward velocity is essentially unaffected.

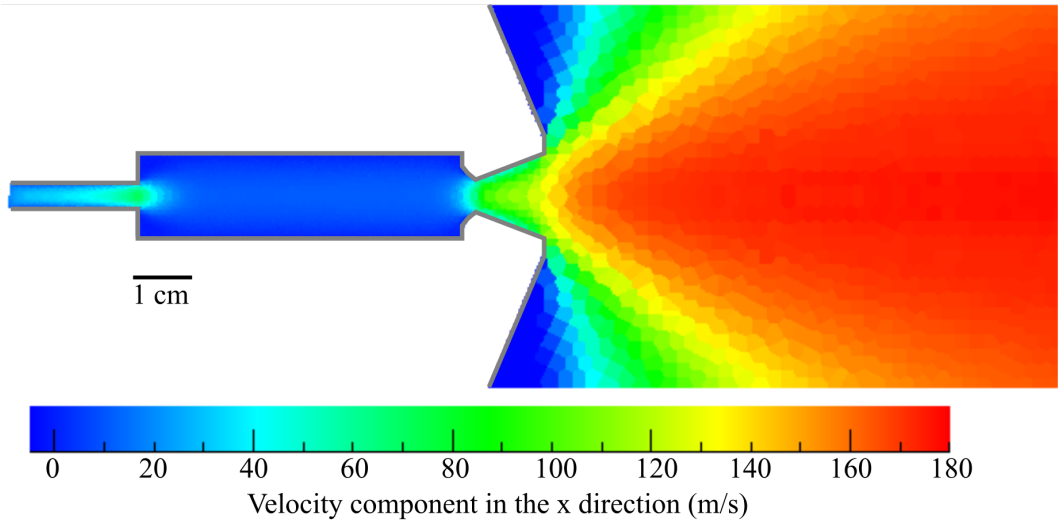

Figure 2.11: Spatial variation of the forward velocity of the 4 K He buffer gas at around 10 SCCM in a cell with a de Laval nozzle, as computed with DS2V.

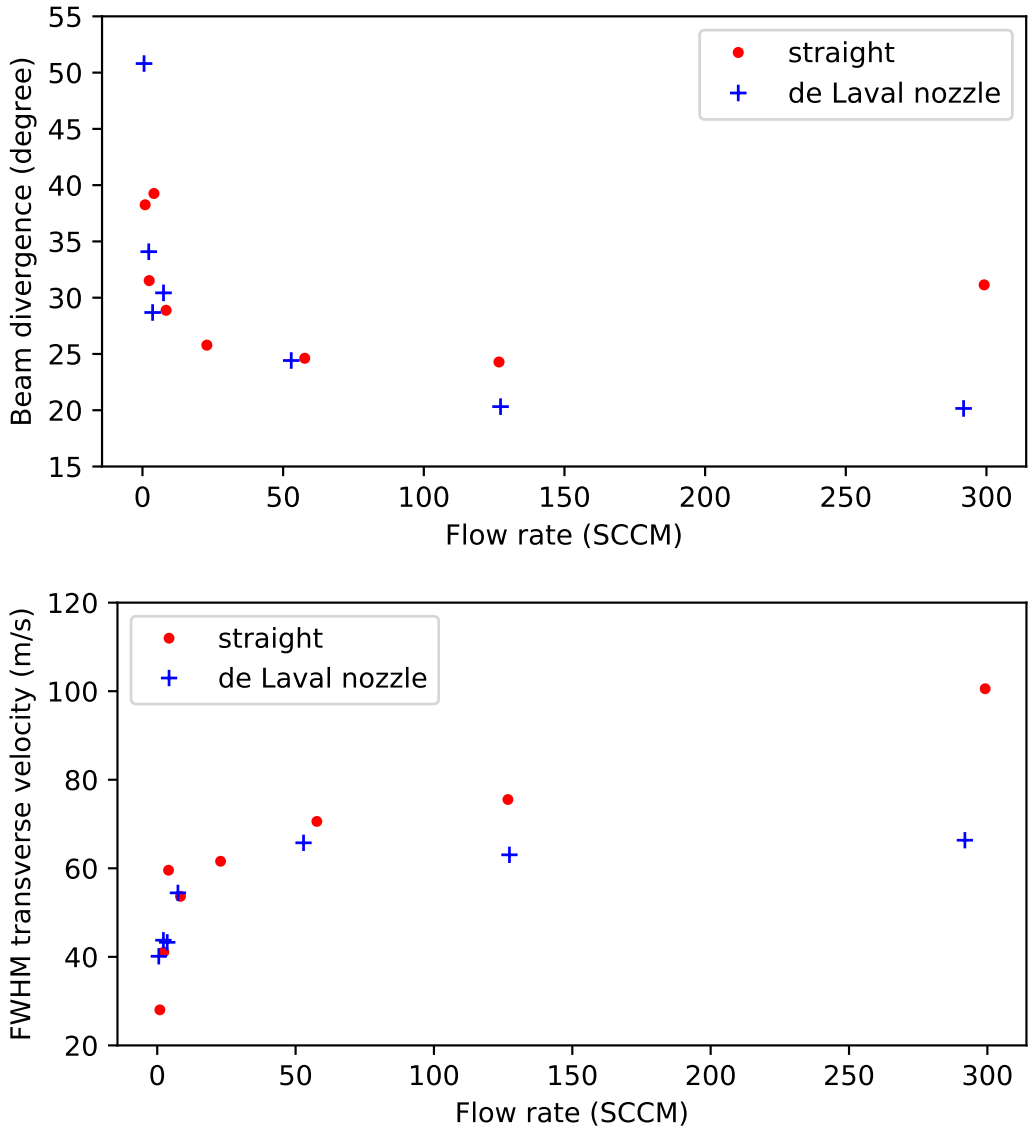

Figure 2.12: Beam divergence (top) and transverse velocity spread (bottom) versus 4 K He flow (SCCM) for the straight (standard single-stage) and de Laval apertures.

2.4 Outlook

We have implemented a two-step approach to simulating cryogenic buffer-gas beams and used it to demonstrate non-trivial features in a number of different geometries. While this thesis has focused on reproducing and understanding known behavior, the real utility of our work will be to numerically optimize geometries for a given purpose. Fluid dynamics simulations have already been used to successfully design

cells with enhanced properties such as extraction [40, 39], and we hope that the current approach will be especially useful for beam properties that depend critically on both high and low density regimes, such as beam divergence and forward velocity. Furthermore, the output particles can be fed into simulations of post-CBGB techniques, such as laser slowing and cooling [58], Stark [59] and Zeeman [60, 61] deceleration, guiding [32, 62], and beam loading [63, 64]. Future improvements of this method including treating the effect of inelastic collisions to calculate internal state distributions [43] and using more advanced collision models beyond simple hard sphere. The ability to numerically fine-tune buffer-gas cells for specific applications will enable rapid prototyping of CBGB implementations and open new directions in molecular quantum control.

Chapter 3

Spectroscopy of the vibrational bending mode in ^{171,173}YbOH

Portions of this chapter were published previously [65].

3.1 Introduction

As discussed in Chap. 1.7, YbOH is a particularly promising platform for symmetry-violation searches. The heavy ytterbium metal gives the molecule strong internal electric field and thus large intrinsic sensitivity to CP-violating physics. In isotopologues with nonzero nuclear spin, YbOH is also sensitive to nuclear-spin-dependent observables, including NSM, MQM, and nuclear-spin-dependent parity-violation effects. In addition, the quadrupole deformation of the ytterbium nucleus makes this system especially attractive for MQM studies.

YbOH also offers important experimental advantages. Its polyatomic structure supports a vibrational bending mode that produces closely spaced opposite-parity levels. As a result, the molecule can be strongly polarized in electric fields much smaller than those typically required for comparable diatomic species. This eases operation at high field and helps reduce electric-field-related noise and systematics. For these reasons, the vibrational bending mode of odd isotopologues of YbOH is

an especially attractive manifold for symmetry-violation measurements.

These advantages, however, come with significant challenges. In the odd isotopologues, the nonzero Yb nuclear spin generates a dense hyperfine structure, making the level structure far more congested than in the even isotopologues. As the number of internal states increases, the molecular population is distributed over many levels, so even a molecular beam with substantial total flux can yield only a small number of molecules in any one target state. The same complexity also leads to crowded spectra, making spectroscopic assignment of the observed lines extremely difficult. Because a firm understanding of the internal structure is essential for identifying and establishing state preparation and readout scheme, high-resolution spectroscopy of the bending mode in the odd isotopologues is a necessary step toward symmetry violation measurements.

We first performed high-resolution spectroscopy of the bending mode in ^{174}YbOH [66], which is the simplest isotopologue of the Yb isotopic series. Because ^{174}Yb has $I_{\mathrm{Yb}} = 0$, its spectrum is free of additional Yb hyperfine splitting and therefore provides a clean reference for the rotational, Stark, and Zeeman structure. From the field-free, Stark, and Zeeman spectra, we determined the rotational structure of the bending state, quantified its electric- and magnetic-field dependence, and extracted the molecule-frame dipole moment.

In this chapter, we extend that spectroscopy to the fundamental bending vibration in the electronic ground state of ^{171}YbOH and ^{173}YbOH. The overall approach follows the work on ^{174}YbOH, but the nonzero Yb nuclear spin introduces substantial hyperfine structure and greatly increases the spectral complexity. Studying the isotopologues in this order allows the simpler ^{174}YbOH case to serve as a useful reference for assigning and interpreting the more crowded spectra of the odd isotopologues. Overall, these results demonstrate the high degree of state control available in the vibrational bending mode of polyatomic molecules and support

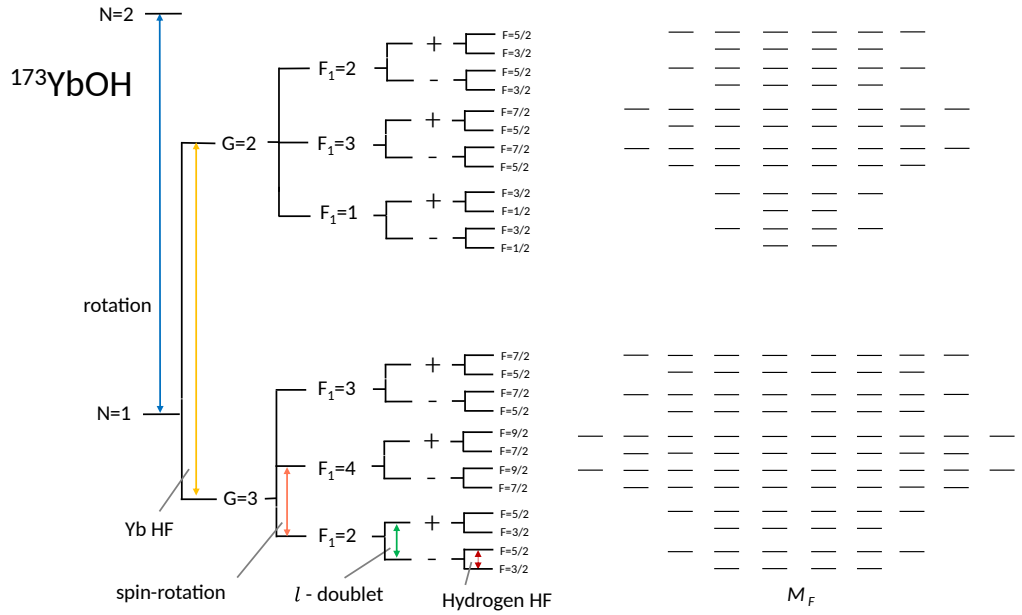

Figure 3.1: Splittings of the $\tilde{X}^2\Sigma^+(01^10)$ state in ^{173}YbOH for the low-lying rotational manifolds shown ($N = 1$) at zero applied electric and magnetic field. Starting from the rotational structure, the levels are further resolved by spin–rotation coupling, Yb hyperfine structure, l-doubling, and hydrogen hyperfine structure, yielding the dense set of parity- and hyperfine-resolved states labeled by G, F_1, and F. The large ^{173}Yb nuclear spin is responsible for the substantially greater complexity relative to ^{174}YbOH.

future symmetry-violation searches.

3.2 Structure of $\tilde{X}^2\Sigma^+(01^10)$ state in ^{171,173}YbOH

As shown in Fig. 3.1, the level structure of ^{173}YbOH is substantially more complicated than that of ^{174}YbOH because the large ytterbium nuclear spin, $I_{\mathrm{Yb}} = 5/2$, introduces extensive hyperfine splitting. The resulting manifold contains many closely spaced states and parity components, making transition assignments significantly more challenging than in the even isotopologue. To map out this internal structure, we must therefore perform high-resolution spectroscopy and compare the measured spectra with spectra predicted by the effective Hamiltonian.

In ^{173}YbOH, the ^{173}Yb nucleus has a nuclear spin of 5/2, and the hyperfine coupling between ^{173}Yb nuclear spin and an electron spin forms the angular momentum

$\boldsymbol{G} = \boldsymbol{I} + \boldsymbol{S}$. (Here, $\boldsymbol{S}$ and $\boldsymbol{I}$ are the electron and nuclear spin of Yb respectively.) $\boldsymbol{G}$ is then coupled to the rotational angular momentum $\boldsymbol{N}$, forming the angular momentum $\boldsymbol{F_1} = \boldsymbol{G} + \boldsymbol{N}$. Here, $\boldsymbol{N} = \boldsymbol{\Lambda} + \boldsymbol{\ell} + \boldsymbol{R}$ where $\boldsymbol{R}$ is the nuclei rotational angular momentum, $\boldsymbol{\Lambda}$ is the projection of electronic orbital angular momentum on the molecular axis, and $\boldsymbol{\ell}$ is the projection of vibrational angular momentum on the molecular axis. Finally, the total angular momentum $\boldsymbol{F}$ is formed from the coupling between $\boldsymbol{F_1}$ and $\boldsymbol{I_H}$, where $\boldsymbol{I_H}$ is the distant Hydrogen nuclear spin. The non Born-Oppenheimer interactions give rise to parity doublets of $|\mathcal{P} = \pm\rangle = \frac{1}{\sqrt{2}}(|N, \ell\rangle \pm (-1)^{N-\ell-\Lambda}|N, -\ell\rangle)$.

The total effective molecular Hamiltonian for $\tilde{X}^2\Sigma^+(01^10)$ state of ^{171,173}YbOH used in the numerical diagonalization is given by [67]:

$$\begin{aligned} H_{\tilde{X}(010)} = H_{Rot} + H_{SR} + H_{aSR} + H_{b_F(\mathrm{Yb})} + H_{c(\mathrm{Yb})} + H_{b_F(\mathrm{H})} \\ + H_{c(\mathrm{H})} + H_Q + H_{q_G} + H_{p_G} + H_{Stark} + H_{Zeeman}, \end{aligned} \tag{3.1}$$

where

$$H_{Rot} = B(N^2 - \ell^2) \tag{3.2a}$$

$$H_{SR} = \gamma(N \cdot S - N_z S_z) \tag{3.2b}$$

$$H_{aSR} = \gamma_G N_z S_z \tag{3.2c}$$

$$H_{b_F(\mathrm{Yb})} = b_F(^{171,173}\mathrm{Yb}) I \cdot S \tag{3.2d}$$

$$H_{c(\mathrm{Yb})} = c(^{171,173}\mathrm{Yb})(I_z S_z - \frac{1}{3} I \cdot S) \tag{3.2e}$$

$$H_{b_F(\mathrm{H})} = b_F(\mathrm{H}) I \cdot S \tag{3.2f}$$

$$H_{c(\mathrm{H})} = c(\mathrm{H})(I_z S_z - \frac{1}{3} I \cdot S) \tag{3.2g}$$

$$H_Q = e^2 Q q_0(^{173}\mathrm{Yb}) \frac{3I_z^2 - I^2}{4I(2I-1)} \tag{3.2h}$$

$$H_{q_G} = -\frac{q_G}{2}(N_+^2 e^{-i2\phi} + N_-^2 e^{i2\phi}) \tag{3.2i}$$

$$H_{p_G} = \frac{p_G}{2}(N_+ S_+ e^{-i2\phi} + N_- S_- e^{i2\phi}) \tag{3.2j}$$

$$H_{Stark} = -D_{\tilde{\mathrm{X}}} \cdot E \tag{3.2k}$$

$$H_{Zeeman} = g_S \mu_B S_Z B_Z. \tag{3.2l}$$

ϕ is the azimuthal angle of the bending nuclear framework, $D_{\tilde{\mathrm{X}}}$ is the dipole moment of $\tilde{X}^2\Sigma^+(01^10)$ state in the molecule frame, +/– and z subscripts refer to the molecule frame projections, and Z refers to the lab-frame projection. The total Hamiltonian consists of rotation (H_{Rot}), spin-rotation (H_{SR}), axial spin-rotation (H_{aSR}), Fermi contact (Yb) ($H_{b_F(\mathrm{Yb})}$), dipolar (Yb) ($H_{c(\mathrm{Yb})}$), Fermi contact (Hydrogen) ($H_{b_F(\mathrm{H})}$), dipolar (Hydrogen) ($H_{c(\mathrm{H})}$), quadrupole (H_Q), ℓ-doubling q_G (H_{q_G}), ℓ-doubling p_G (H_{p_G}), Stark (H_{Stark}), and Zeeman (H_{Zeeman}) terms. The quadrupole term only exists for ^{173}YbOH. Subtraction of $N_z S_z$ in spin-rotation term and sign convention for ℓ-doubling term are detailed in ref. [66].

B, γ, γ_G, b_F(Yb), c(Yb), e^2Qq_0, q_G, and p_G are spectroscopic constants for each term and determined by spectroscopy on $\tilde{A}^2\Pi_{1/2}(000) - \tilde{X}^2\Sigma^+(01^10)$ band. b_F(H) and c(H) are measured to be 0.000160 and 0.000082 cm^{-1} in the previous

microwave study in ^{174}YbOH [66]. $D_{\tilde{X}}$ and g_S are also measured to be 2.16 D and 2.07 respectively in ^{174}YbOH.

The Hamiltonian terms above are represented in the spherical tensor notation in the following way:

$$H_{Rot} = B(N^2 - \ell^2) \tag{3.3a}$$

$$H_{SR} = \gamma \left(T^1(N) \cdot T^1(S) - T^1_{q=0}(N) T^1_{q=0}(S) \right) \tag{3.3b}$$

$$H_{aSR} = \gamma_G T^1_{q=0}(N) T^1_{q=0}(S) \tag{3.3c}$$

$$H_{b_F(\mathrm{Yb})} = b_F(^{171,173}\mathrm{Yb}) T^1(I) \cdot T^1(S) \tag{3.3d}$$

$$H_{c(\mathrm{Yb})} = c(^{171,173}\mathrm{Yb}) \frac{\sqrt{6}}{3} T^2_{q=0}(I, S) \tag{3.3e}$$

$$H_{b_F(\mathrm{H})} = b_F(\mathrm{H}) T^1(I) \cdot T^1(S) \tag{3.3f}$$

$$H_{c(\mathrm{H})} = c(\mathrm{H}) \frac{\sqrt{6}}{3} T^2_{q=0}(I, S) \tag{3.3g}$$

$$H_Q = e^2 Q q_0(^{173}\mathrm{Yb}) \frac{\sqrt{6}}{4I(2I-1)} T^2_{q=0}(I, I) \tag{3.3h}$$

$$H_{q_G} = -q_G \sum_{q=\pm 1} e^{-2iq\phi} T^2_{2q}(N, N) \tag{3.3i}$$

$$H_{p_G} = p_G \sum_{q=\pm 1} e^{-2iq\phi} T^2_{2q}(N, S) \tag{3.3j}$$

$$H_{Stark} = -T^1_{p=0}(D_{\tilde{X}}) T^1_{p=0}(E) \tag{3.3k}$$

$$H_{Zeeman} = g_S \mu_B T^1_{p=0}(S) T^1_{p=0}(B) \tag{3.3l}$$

Note that $p(q)$ labels space-fixed (molecule-fixed) spherical tensor coordinates.

3.3 Spectroscopy of $\tilde{X}^2\Sigma^+(01^10)$ state in ^{171,173}YbOH

To conduct high-resolution spectroscopy on $\tilde{A}^2\Pi_{1/2}(000) - \tilde{X}^2\Sigma^+(01^10)$ band in ^{171,173}YbOH, we used the same experimental technique and apparatus employed in ^{174}YbOH [66].

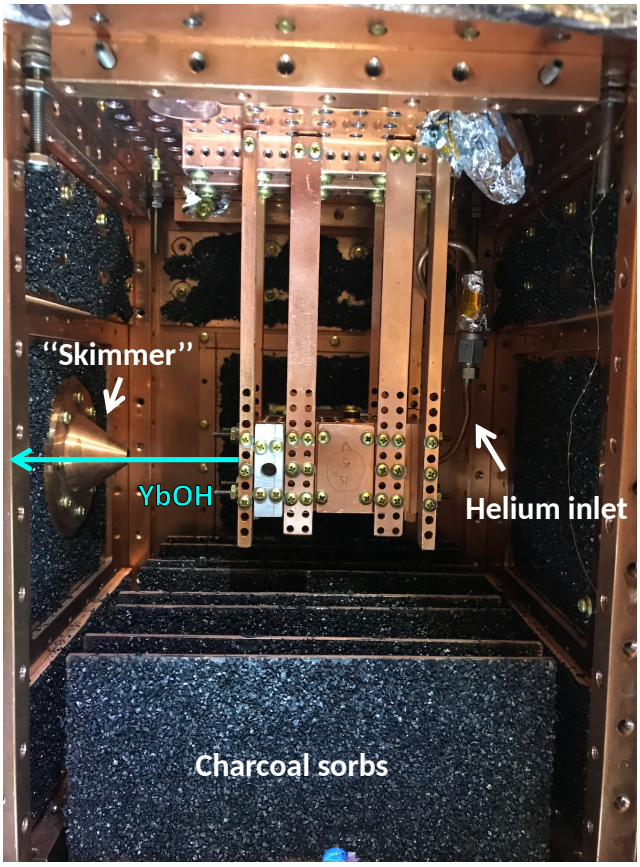

Figure 3.2: Photograph of the cryogenic buffer gas beam (CBGB) source used for spectroscopy of YbOH. Visible are the helium inlet on the right, the skimmer at the beam exit on the left, and the activated-charcoal cryosorption surfaces used to pump helium. The YbOH production region inside the cell is also indicated.

Briefly, a YbOH molecular beam from the cryogenic buffer-gas beam (CBGB) source enters a laser-induced fluorescence (LIF) detection region where the molecules can experience electric and magnetic fields from ITO-coated glass electrodes and magnetic field coils, respectively. The photo of the CBGB setup is in Fig. 3.2.

By utilizing the isotopologue-specific enhancement technique ^{173}YbOH spectra are disentangled from different isotopologues even in spectral regions where they are significantly overlapped.

The effective molecular Hamiltonian for the $\tilde{A}^2\Pi_{1/2}(000)$ state used to model the spectrum without Stark and Zeeman terms is detailed in ref. [67]. It includes spin-orbit (A_{SO}), rotation (B), centrifugal distortion (D), Λ-doubling ($p+2q$), quadrupole

(e^2Qq_0), and hyperfine a and d terms (a, d).

The Stark and Zeeman terms for the $\tilde{A}^2\Pi_{1/2}(000)$ state are given by:

$$\begin{aligned} H_{Stark} &= -D_{\tilde{\mathrm{A}}} \cdot E \\ H_{Zeeman} &= g'_S \mu_B S_Z B_Z + g_L L_Z B_Z + g'_l \mu_B (e^{-2i\theta} S_+ B_+ + e^{2i\theta} S_- B_-), \end{aligned} \tag{3.4}$$

where $D_{\tilde{\mathrm{A}}}$ is the dipole moment of $\tilde{A}^2\Pi_{1/2}(000)$ state in the molecule frame, and θ is the electronic azimuthal coordinate. $D_{\tilde{\mathrm{A}}}$ has been previously measured to be 0.43 D [68]. For g'_S, g_L, and g'_l. we use the values from Ref. [69], fixing $g'_S = 1.860$, $g_L = 1.0$, and $g'_l = -0.724$.

The effective Hamiltonian for $\tilde{X}^2\Sigma^+(01^10)$ for ^{171,173}YbOH is described in the next section. Again, it includes rotation (B), spin-rotation (γ), axial spin-rotation (γ_G), Fermi contact (Yb) (b_F(Yb)), dipolar (Yb) (c(Yb)), quadrupole (e^2Qq_0), ℓ-doubling q_G (q_G), and ℓ-doubling p_G (p_G) terms.

The hyperfine structure from the distant Hydrogen nuclear spin I_H is neglected in the spectroscopy analysis since it is optically unresolved [66]. However, in the main analysis, we included the hyperfine structure and set b_F(H) and c(H) to 0.000160 and 0.000082 cm^{-1}, which were previously determined for ^{174}YbOH [70].

Since the spectroscopic constants B, γ, and q_G of the $\tilde{X}^2\Sigma^+(01^10)$ state in ^{174}YbOH are measured, those of ^{171,173}YbOH can be initially guessed with high accuracy using mass scaling. The spectroscopic constants A_{SO}, B, D, $p + 2q$, e^2Qq_0, a, and d of $\tilde{A}^2\Pi_{1/2}(000)$ and b_F, c, and e^2Qq_0 of the $\tilde{X}^2\Sigma^+(000)$ state in ^{171,173}YbOH are also determined from the previous work [67]. By combining all the information, the spectrum can be predicted with high accuracy and directly compared against the observed spectrum to assign the observed lines.

Since this band is forbidden in E1 approximation, the intensities arise from the perturbations in the electronic excited state. The study of ^{174}YbOH modeled the intensity borrowing and their prediction agrees well with the observed intensities [66].

The similar intensity borrowing coefficients of $(c_\mu, c_\kappa, c_B) = (0.20, -0.40, 0.89)$ are used to predict the intensities in ^{171,173}YbOH to assist the line assignments and they showed good agreement with the observed spectrum. For the lines that are close and overlapped each other, they are assigned to the same feature. As a result, in total, 37 and 61 transitions are assigned in ^{171}YbOH and ^{173}YbOH, respectively.

We obtained the spectroscopic constants by fitting the assigned lines. For the overlapped lines that are assigned to the same feature, they are weighted according to the peak width in the fitting. All the observed transition frequencies are given in Tables 3.3 and 3.2 for ^{171}YbOH and ^{173}YbOH, respectively, along with the prediction calculated from the obtained spectroscopic constants.

As expected from the mass scaling, the rotational constant decreases as the mass of the Yb nucleus increases. The parameters associated with ℓ-doubling (q_G, p_G, and γ_G) are the same within their errors, which are also expected due to the small dependence on the mass. The hyperfine and quadrupole constants (b_F, c, and e^2Qq_0) are the same as or close to the measured values for $\tilde{X}^2\Sigma^+(000)$ within the errors [67]. The relatively large errors on c and e^2Qq_0 are presumably due to the large errors on the excited $\tilde{A}^2\Pi_{1/2}(000)$ state parameters. Nevertheless, our fit residuals on the assigned lines are smaller than the previous spectroscopy work on $\tilde{A}^2\Pi_{1/2}(000) - \tilde{X}^2\Sigma^+(000)$ band in ^{171,173}YbOH by a factor of few [67].

The Stark and Zeeman spectra under the DC electric and magnetic fields were also measured and compared against the prediction with the molecular dipole moment and g_S fixed at 2.16 D and 2.07 respectively, which were measured for ^{174}YbOH [66]. The electric and magnetic fields lift the Zeeman sublevel degeneracy, resulting in the significantly congested spectra. However, both the overall structure and the shift of the strong features agree with the prediction at each field value, confirming that the dipole moment of ^{171,173}YbOH is roughly the same as ^{174}YbOH, which is expected. We do not report a measured value of the dipole moments, but instead

Table 3.1: Spectroscopic parameters for the $\tilde{X}^2\Sigma^+(01^10)$ state of YbOH.

Parameter		^{171}YbOH	^{173}YbOH	^{174}YbOH [66]
T_0/cm^{-1}	Origin energy	319.90861(6)	319.90932(6)	319.90901(6)
B/MHz	Rotation	7340.9(3)	7334.1(4)	7,328.64(15)
γ/MHz	Spin-rotation	–90(2)	–87(3)	–88.7(9)
γ_G/MHz	Axial spin-rotation	12(6)	14(4)	16(2)
q_G/MHz	ℓ-doubling	–12.6(3)	–12.5(5)	–12.0(2)
p_G/MHz	P-odd ℓ-doubling	–11(3)	–13(5)	–11(1)
b_F/MHz	Fermi contact	6795(3)	–1881.0(8)	–
c/MHz	Spin dipolar	281(21)	–92(10)	–
e^2Qq_0/MHz	Quadrupolar	–	–3322(27)	–

use our measurements as a check that our assumption of their similarity between isotopologues to be accurate, and fix the moments at the values measured for ^{174}YbOH. A more comprehensive analysis of Stark and Zeeman spectrum would require higher resolution via microwave, RF, or optical Raman transitions to resolve the small splittings between different Zeeman sublevels.

Table 3.2: Ground states quantum numbers (N", G", F_1", $\mathcal{P}'$), excited states quantum numbers (J', F_1', $\mathcal{P}'$), observed positions, and residuals of $\tilde{A}^2\Pi(000)$ – $\tilde{X}^2\Sigma^+(01^10)$ band of ^{173}YbOH. There are in total 61 lines assigned. The fit residual is 9.0 MHz.

$N^{''}, G^{''}, F_1^{''}, \mathcal{P}$	$J', F_1^{'}, \mathcal{P}$	Obs. (cm^{-1})	Obs. – Calc. (MHz)
1, 2, 1, +	1.5, 2, –	17004.7905	–10.0
1, 2, 2, +	1.5, 2, –	17004.7757	10.8
1, 2, 2, +	1.5, 1, –	17004.7823	5.4
1, 2, 3, +	1.5, 3, –	17004.7831	–5.1
1, 2, 3, +	1.5, 2, –	17004.7841	–6.8
1, 2, 3, +	1.5, 4, –	17004.7993	–9.3
1, 2, 1, –	2.5, 2, +	17006.2784	27.4
1, 2, 2, –	2.5, 3, +	17006.2589	–4.8
1, 2, 2, –	2.5, 2, +	17006.2618	–8.7
1, 2, 2, –	0.5, 2, +	17003.7993	–2.0
1, 2, 2, –	0.5, 3, +	17003.8045	–7.2
1, 2, 3, –	2.5, 3, +	17006.2684	3.3
1, 2, 3, –	2.5, 4, +	17006.2719	2.6
1, 2, 3, –	0.5, 2, +	17003.8090	15.7
1, 2, 3, –	0.5, 3, +	17003.8142	7.1
1, 3, 2, +	1.5, 3, –	17004.9761	–8.8
1, 3, 2, +	1.5, 1, –	17004.9842	–3.5
1, 3, 2, +	1.5, 2, –	17004.9772	–9.4
1, 3, 3, +	1.5, 4, –	17004.9772	11.9
1, 3, 4, +	2.5, 5, –	17005.1454	10.5
1, 3, 4, +	1.5, 3, –	17004.9736	–1.4
1, 3, 4, +	1.5, 4, –	17004.9898	–5.8
1, 3, 2, –	2.5, 3, +	17006.4619	8.6
1, 3, 2, –	0.5, 3, +	17004.0075	8.3
1, 3, 3, –	2.5, 3, +	17006.4452	–7.0
1, 3, 3, –	2.5, 4, +	17006.4487	–6.3
1, 3, 3, –	0.5, 2, +	17003.9861	13.4
1, 3, 3, –	0.5, 3, +	17003.9910	–2.8
1, 3, 4, –	2.5, 4, +	17006.4619	1.3
1, 3, 4, –	2.5, 5, +	17006.4786	–6.3
1, 3, 4, –	2.5, 5, +	17006.4786	–6.9

Table 3.2: Ground states quantum numbers (N", G", F_1", $\mathcal{P}'$), excited states quantum numbers (J', $F_1^{'}$, $\mathcal{P}'$), observed positions, and residuals of $\tilde{A}^2\Pi(000)$ – $\tilde{X}^2\Sigma^+(01^10)$ band of ^{173}YbOH (continued).

$N^{''}, G^{''}, F_1^{''}, \mathcal{P}$	$J', F_1^{'}, \mathcal{P}$	Obs. (cm^{-1})	Obs. – Calc. (MHz)
2, 2, 4, +	0.5, 3, –	17002.3808	17.5
2, 2, 2, –	2.5, 1, +	17005.2973	0.5
2, 2, 2, –	2.5, 2, +	17005.2923	–6.1
2, 2, 3, –	2.5, 3, +	17005.2923	12.9
2, 2, 3, –	2.5, 2, +	17005.2951	5.4
2, 2, 4, –	2.5, 4, +	17005.2845	–7.0
2, 2, 4, –	2.5, 5, +	17005.3013	–13.6
2, 3, 2, +	0.5, 2, –	17002.5933	–14.2
2, 3, 3, +	3.5, 4, –	17007.4713	–10.3
2, 3, 4, +	3.5, 5, –	17007.4800	–6.0
2, 3, 5, +	3.5, 5, –	17007.4713	–1.6
2, 3, 5, +	3.5, 6, –	17007.4883	4.8
2, 3, 1, –	2.5, 1, +	17005.4683	1.7
2, 3, 1, –	2.5, 2, +	17005.4634	–1.7
2, 3, 1, –	2.5, 0, +	17005.4719	14.6
2, 3, 2, –	2.5, 3, +	17005.4689	3.7
2, 3, 2, –	2.5, 2, +	17005.4719	1.8
2, 3, 3, –	2.5, 4, +	17005.4814	5.7
2, 3, 4, –	2.5, 5, +	17005.5018	3.4
2, 3, 4, –	2.5, 5, +	17005.5018	4.1
2, 3, 4, –	2.5, 4, +	17005.4849	6.8
2, 3, 5, –	2.5, 5, +	17005.4930	–4.3
2, 3, 5, –	2.5, 5, +	17005.4930	–2.9
3, 2, 2, –	4.5, 3, +	17008.3141	9.7
3, 2, 3, –	4.5, 4, +	17008.3179	–7.3
3, 2, 4, –	4.5, 5, +	17008.3179	–22.8
3, 3, 4, +	3.5, 5, –	17006.0102	5.7
3, 3, 5, +	3.5, 6, –	17006.0278	–1.8

Table 3.3: Ground states quantum numbers (N", G", F_1", $\mathcal{P}'$), excited states quantum numbers (J', F_1', $\mathcal{P}'$), observed positions, and residuals of $\tilde{A}^2\Pi(000)$ – $\tilde{X}^2\Sigma^+(01^10)$ band of ^{171}YbOH. There are in total 37 lines assigned. The fit residual is 6.9 MHz.

$N^{''}, G^{''}, F_1^{''}, \mathcal{P}$	$J', F_1^{'}, \mathcal{P}$	Obs. (cm^{-1})	Obs. – Calc. (MHz)
1, 0, 1, +	1.5, 2, –	17005.0986	10.2
1, 0, 1, +	1.5, 1, –	17005.1126	–3.9
1, 0, 1, –	2.5, 2, +	17006.5996	–6.1
1, 1, 0, +	1.5, 1, –	17004.8826	–12.7
1, 1, 1, +	1.5, 2, –	17004.8721	14.5
1, 1, 2, +	1.5, 2, –	17004.8721	–2.4
1, 1, 2, +	1.5, 1, –	17004.8863	–11.5
1, 1, 0, –	0.5, 1, +	17003.8918	9.5
1, 1, 1, –	0.5, 1, +	17003.8945	3.6
1, 1, 1, –	2.5, 2, +	17006.3733	–1.6
1, 1, 1, –	1.5, 2, +	17004.0096	1.9
1, 1, 1, –	0.5, 0, +	17003.9077	–9.1
1, 1, 2, –	0.5, 1, +	17003.8945	–2.5
1, 1, 2, –	2.5, 3, +	17006.3588	4.7
1, 1, 2, –	2.5, 2, +	17006.3737	5.9
1, 1, 2, –	1.5, 2, +	17004.0096	–4.2
2, 0, 2, +	3.5, 3, –	17007.6141	–0.2
2, 0, 2, –	2.5, 2, +	17005.6182	–14.1
2, 1, 2, +	3.5, 3, –	17007.3854	–3.4
2, 1, 2, +	1.5, 2, –	17003.8918	–3.3
2, 1, 3, +	3.5, 4, –	17007.3750	7.4
2, 1, 1, –	2.5, 2, +	17005.3888	–0.3
2, 1, 2, –	2.5, 3, +	17005.3752	8.9
2, 1, 2, –	2.5, 2, +	17005.3897	–4.4
2, 1, 3, –	3.5, 4, +	17005.6326	–11.2
2, 1, 3, –	2.5, 3, +	17005.3802	8.2
2, 1, 3, –	2.5, 2, +	17005.3947	–4.0
3, 0, 3, +	3.5, 3, –	17006.1412	–0.9
3, 0, 3, –	4.5, 4, +	17008.6462	6.8
3, 1, 3, +	3.5, 4, –	17005.8967	2.4
3, 1, 4, +	3.5, 4, –	17005.9044	9.2
3, 1, 2, –	2.5, 2, +	17003.9224	–0.8
3, 1, 3, –	4.5, 4, +	17008.4166	–2.0
3, 1, 3, –	2.5, 3, +	17003.9093	6.3
3, 1, 4, –	4.5, 5, +	17008.4085	–8.4
4, 1, 3, –	4.5, 4, +	17006.4469	–1.7
4, 1, 5, –	4.5, 5, +	17006.4453	–2.8

Chapter 4

Field-insensitive clock transitions for symmetry violation searches

Portions of this chapter were published previously [65].

4.1 Introduction

As mentioned in Chapter 1, searches for the electron's electric dipole moment (eEDM) in ThO and HfF^+ have been extremely powerful tools for probing charge-parity (CP) violating new physics at TeV energy scales [15, 71, 72]. Their high sensitivities rely on the enhancement of CP-violating observables in the internal molecular electromagnetic environment, combined with the advantageous experimental features arising from their unique molecular structures. The sensitivity of these molecular CP-violation (CPV) searches will continue to improve as new methods such as laser cooling are developed to increase count rates and coherence times [12, 13, 17].

The two most sensitive eEDM experiments [15, 71, 72] rely on a particular molecular structure ($^3\Delta_1$ state) which offers two critical features: a small magnetic moment, and "internal co-magnetometers." The small magnetic moment of these states makes them largely insensitive to uncontrolled magnetic fields, which are a major

challenge for EDM experiments with atoms [73] and neutrons [74]. Internal co-magnetometers give the ability to reverse the desired CPV energy shifts without changing lab fields, resulting in robustness against systematic effects arising from the applied electric and magnetic fields.

However, molecules which are sensitive to CPV and have this molecular structure are not laser coolable – a feature which would be advantageous for improving sensitivity through advanced quantum control. Polyatomic molecules offer internal co-magnetometers generically, including molecules which can be laser-cooled [75, 13]. Laser-coolable, eEDM sensitive molecules have a single, metal-centered s-type valence electron [76, 77], which means that they have magnetic moments on the order of the Bohr magneton μ_B; this is $\gtrsim$ 100 times larger than $^3\Delta_1$ states, and correspondingly more sensitive to magnetic fields. A recent demonstration [78] showed that it is possible to tune the magnetic sensitivity in polyatomic molecules to very low values while still maintaining eEDM sensitivity. Another proposal to reduce field sensitivity is to use magnetically-insensitive "clock" transitions, which occur in many molecules [79].

In this chapter, we discuss a new generic method to engineer "clock" transitions which have reduced sensitivity to both magnetic *and* electric fields while maintaining large sensitivity to CPV in molecules. The basic idea behind these CPV-sensitive field-insensitive transitions (EDM-clock transitions) is similar to magic conditions in atomic clocks [80, 81] and precision spectroscopy in molecules [82]. We find EDM-clock transitions in a wide range of polyatomic and diatomic molecules with applications to search for the eEDM, nuclear Schiff moments (NSM), and nuclear magnetic quadrupole moments (MQM). This technique is particularly useful for molecules with large nuclear spins and complicated hyperfine structure for nuclear CPV searches. Furthermore, because EDM-clock transitions do not involve traditional $M = 0 \rightarrow 0$ clock transitions, where M is the angular momentum projection

quantum number, driving the same transitions with the opposite signs of M provides a co-magnetometry method to reject systematic errors. Finally, since the states involved have static energy shifts sensitive to CPV, they can be probed with traditional Ramsey spectroscopy using RF, microwaves, or lasers.

4.2 Mechanism of EDM-clock transitions

The Hamiltonian governing the CPV energy shifts [20] in a molecule interacting with external fields is

$$H = -D\boldsymbol{n}\cdot\boldsymbol{\mathcal{E}} - g\mu_B\boldsymbol{S}\cdot\boldsymbol{\mathcal{B}} + W_d d_e \boldsymbol{S}\cdot\boldsymbol{n} + W_Q\frac{Q}{I}\boldsymbol{I}\cdot\boldsymbol{n} - W_M\frac{M}{2I(2I-1)}\boldsymbol{S}\hat{\boldsymbol{T}}\boldsymbol{n}. \quad (4.1)$$

The first line is the external field interaction; D is the molecular dipole moment, $\boldsymbol{n}$ is a unit vector along the molecular axis, g is the magnetic g-factor, and $\boldsymbol{S}$ is the effective electron spin. Here we define the molecular axis as the symmetry axis, along which the dipole moment lies. The second line is the CPV effects; d_e is the eEDM, Q is the NSM, $\boldsymbol{I}$ is the nuclear spin, M is the MQM, and $\boldsymbol{T}$ is the rank 2 tensor operator $T_{ij} = I_iI_j + I_jI_i - \frac{2}{3}\delta_{ij}I(I+1)$. W_d, W_Q, and W_M are sensitivities to eEDM, NSM, and MQM, which are determined by electronic structure, and are the same within the same electronic state to good approximation. On the other hand, $P_d \equiv \langle\boldsymbol{S}\cdot\boldsymbol{n}\rangle$, $P_Q \equiv \frac{1}{I}\langle\boldsymbol{I}\cdot\boldsymbol{n}\rangle$, $P_M \equiv \frac{1}{2I(2I-1)}\langle\boldsymbol{S}\hat{\boldsymbol{T}}\boldsymbol{n}\rangle$ are measures of the eEDM, NSM, and MQM sensitivities which depend on each particular quantum state, and in general have different orientations of $\boldsymbol{S}, \boldsymbol{I}$, and $\boldsymbol{n}$. In this chapter, we refer to these state-dependent sensitivities P_d, P_Q, and P_M as "CPV sensitivities" as we shall restrict our discussion to transitions within a given electronic state.

The existence of EDM-clock transitions – pairs of states having similar electric and magnetic field sensitivities but different CPV sensitivities – can be intuitively understood as arising from the ability to access different orientations of the molecular

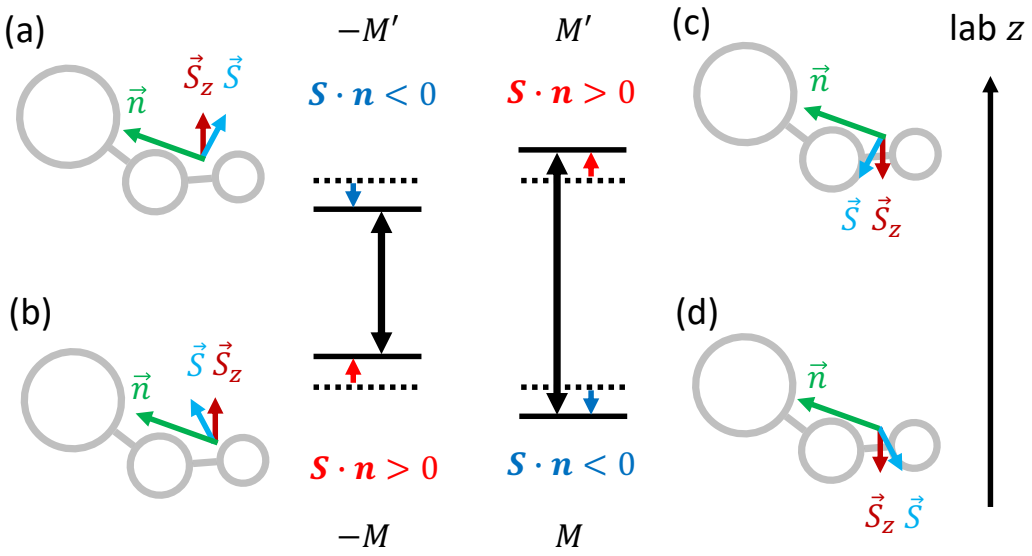

Figure 4.1: The EDM-clock transitions with eEDM sensitivity in partially polarized molecules where the molecule axis $\boldsymbol{n}$ and the lab z axis are not fully aligned. States (a) and (b) have the same orientation of $\boldsymbol{n}$ with respect to z as well as the same projection S_z of $\boldsymbol{S}$ on z, and thus have the same response to electric and magnetic fields. On the other hand, they have different orientations of S on $\boldsymbol{n}$, and thus different eEDM energy shifts (short arrows). This results in transitions (long arrows) sensitive to eEDM interactions but highly insensitive to electric and magnetic fields. The transition connecting states (c) and (d) is similar though it has the opposite eEDM shift, serving as an internal co-magnetometer. The same mechanism works for EDM-clock transitions with NSM and MQM sensitivity.

$\boldsymbol{n}$ and lab z axes. Figure 4.1 shows a time-reversed pair of two EDM-clock transitions in a partially polarized molecule where $\boldsymbol{n}$ and the lab z axis are not fully aligned. The field sensitivities arise from the projections of $\boldsymbol{n}$ and $\boldsymbol{S}$ on the *lab* axis whereas the CPV sensitivities arise from the projections of $\boldsymbol{S}$ and $\boldsymbol{I}$ on the *molecular* axis. The interactions between $\boldsymbol{S}$, $\boldsymbol{I}$, and the angular momentum associated with the molecular axis (e.g., spin-rotation interaction), all of which generically exist in species with non-zero electron and nuclear spin, offer different orientations of $\boldsymbol{S}$ and $\boldsymbol{I}$ with respect to $\boldsymbol{n}$. Thus, when molecules are partially polarized, states with the same projections of $\boldsymbol{n}\cdot z$ and $\boldsymbol{S}\cdot z$ (field sensitivities) can have different projections of $\boldsymbol{S}\cdot\boldsymbol{n}$, $\boldsymbol{I}\cdot\boldsymbol{n}$, and $\boldsymbol{S}\hat{\boldsymbol{T}}\boldsymbol{n}$ (CPV sensitivities).

As the molecular Stark shifts begin to approach the magnitude of other splittings in

the molecule, the coupling of the spins and dipole moment can transition from being molecule-quantized to lab-quantized, resulting in changes to the behavior of Stark and Zeeman shifts, including the appearance of pairs of states with the same absolute or differential ("magic") field sensitivity. This has been observed in molecules [82, 66], and is, for example, the intuitive reason behind magnetically-insensitive states and transitions [83] in alkali atoms. In this thesis, we show that these exist rather generically, and that we can find transitions that have large CPV-sensitivity.

Although this mechanism is similar to what gives rise to eEDM-sensitive, magnetically-insensitive states in polyatomic molecules [75, 78], here we are exploring *transitions* between states which may have large electromagnetic field sensitivity, but whose shifts are similar, making transition frequencies largely insensitive to electromagnetic fields while still sensitive to CPV. Similar types of field-insensitive transitions in atoms and molecules have been explored in other contexts, including for clocks [84], quantum computing [85], searches for ultralight dark matter [86], and precision spectroscopy of polyatomic molecules [82], and in the latter case have proven their experimental power.

A time-reversed pair of EDM-clock transitions (that is, transitions between $M \leftrightarrow M'$ and $-M \leftrightarrow -M'$, see Figs. 4.1 and 4.2a) are degenerate in the absence of a magnetic field (and CPV), and have exactly the same projection $\boldsymbol{n} \cdot z$, but opposite projections of $\boldsymbol{S}$ and $\boldsymbol{I}$ on $\boldsymbol{n}$ – that is, opposite CPV sensitivity. By comparing these two transition frequencies without changing lab fields, shifts due to the electric field are canceled while CPV energy shifts are not. Therefore, this scheme provides an opportunity for internal co-magnetometry, even for species and states without parity doublet structures. As we discuss in the next section, other potentially more powerful co-magnetometry approaches are also available via "field-sensing" transitions.

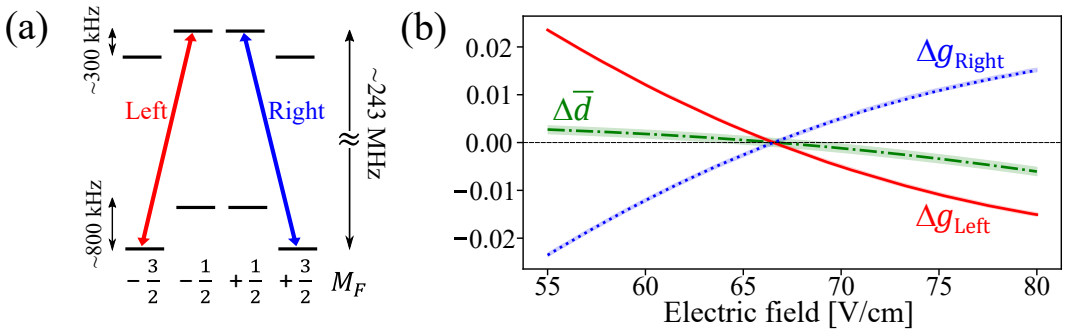

Figure 4.2: An example EDM-clock transition where both $\Delta\bar{d}$ and Δg cross zero near 66.7 V/cm. (a): Level diagram of states and transitions involved. (b): $\Delta\bar{d}$ and Δg as a function of the electric field. The shaded regions indicate the uncertainties from the measurement uncertainties of the spectroscopic parameters.

4.3 Example EDM-clock transitions in ^{173}YbOH

As a specific example, we examine EDM-clock transitions in the ^{173}YbOH metastable bending mode of the electronic ground state, $\tilde{X}^2\Sigma^+_{1/2}(010)$. The combination of parity doublets from the mechanical bending vibration and the heavy, quadrupole-deformed ^{173}Yb($I = 5/2$) nucleus offers good sensitivity to the eEDM, MQM, and NSM [75, 87, 88]. We shall find EDM-clock transitions in this molecule, as well as a number of others.

We diagonalize the molecular effective Hamiltonian [67, 66] including Stark and Zeeman terms to compute quantum state energy levels and magnetic, electric, eEDM, NSM, and MQM sensitivities at each electric field, as described in detail in Chapter 3. The nuclear spin and rotational Zeeman terms are neglected since their contributions are expected to be smaller by around three orders of magnitude than the electron spin term [90, 91]. To represent the magnetic and electric sensitivity, the g-factor and dipole moment are computed by taking the first derivative of energies as a function of magnetic and electric fields, respectively.

We are able to find many values of the electric field supporting EDM-clock transitions – pairs of states which have large CPV sensitivity, small g-factor and dipole moment, and which differ by $\Delta M \leq 2$, which makes them easier to drive in the

laboratory. Table 4.1 lists several examples in ^{173}YbOH, and Figure 4.2 shows one in detail. We characterize these transitions in this and other molecules by computing the differential g-factor between the two states, $\Delta g = g_1 - g_2$, the differential dipole moment $\Delta\bar{d} = (d_1 - d_2)/D$, normalized to the molecular dipole moment, and the differential CPV sensitivities. For ease of comparison, we typically display normalized CPV sensitivities, for example $\bar{P}_d$, defined to be P_d divided by the value to which P_d saturates in the limit of full mixing of the parity doublets. Note that these values can be larger than 1 since there can be local maxima in sensitivity, as has been observed elsewhere [92, 78], and because the transitions are between two states, which can have additive sensitivity greater than that of a single state. There are more than 250 other EDM-clock transitions in ^{173}YbOH where both $|\Delta\bar{g}|$ and $|\Delta\bar{d}|$ are < 0.01 and $|\Delta\bar{P}_M| > 30\%$. More EDM-clock transitions can be found when one or two of the three requirements for $|\Delta g|$, $|\Delta\bar{d}|$, and CPV sensitivity are relaxed. There are also transitions with large field sensitivity and small CPV sensitivity, providing further opportunities for robust systematic error detection and rejection. Furthermore, these transitions have different relative sensitivities to the eEDM, NSM, and MQM, which is important for disentangling their observable effects.

To quantify the reduction of electromagnetic sensitivity, we calculate decoherence times τ_{EM} due to inhomogeneous field fluctuations $\delta\mathcal{E}$ ~1 mV/cm and $\delta\mathcal{B} \sim 1$ μG across the molecular sample, which are typical experimental values [93]. Note the experimental coherence time may be limited to smaller values by several factors, including radiative decay of the bending state, which is estimated to be around 800 ms [94].

Here, we briefly show the steps to compute the coherence time. The frequency of the transition is shifted by the electric and magnetic field in the following way:

Table 4.1: Example EDM-clock transitions in ^{173}YbOH. The top eight transitions have good CPV sensitivity and low field sensitivity (EDM-clock transitions). The bottom two transitions have either large electric or magnetic field sensitivity, but small CPV sensitivity. Note that our uncertainty on Δg is $\sim 10^{-3}$

$\mathcal{E}$	f	$\lvert\Delta g\rvert$	$\lvert\Delta\bar{d}\rvert$	$\lvert\Delta\bar{P}_d\rvert$	$\lvert\Delta\bar{P}_Q\rvert$	$\lvert\Delta\bar{P}_M\rvert$
V/cm	MHz			%	%	%
194.98	58	1×10^{-3}	0	24	39	40
194.48	58	0	3×10^{-4}	24	39	40
66.71	243	2×10^{-3}	0	31	42	42
66.55	243	0	5×10^{-5}	31	42	42
143.1	5,132	3×10^{-3}	0	112	117	141
238.1	23,754	3×10^{-4}	0	93	48	95
533.91	29,520	2×10^{-4}	0	56	86	84
533.97	29,520	0	2×10^{-4}	56	86	84
23.3	5,597	1.1	0	1.0	0.4	0.1
650.6	28,550	0	0.7	0.1	0.2	0.2

$$f = D\Delta\bar{d}\cdot\mathcal{E} + \mu_B\Delta g\cdot\mathcal{B} \tag{4.2a}$$

The broadening of the transition due to inhomogeneous electric and magnetic field fluctuation is thus given by:

$$\delta f_{\delta\mathcal{E}} = D\left\{\Delta\bar{d}\cdot\delta\mathcal{E} + \frac{\mathrm{d}\Delta\bar{d}}{\mathrm{d}\mathcal{E}}\cdot(\delta\mathcal{E})^2 + \frac{\mathrm{d}\Delta\bar{d}}{\mathrm{d}\mathcal{B}}\cdot\delta B\cdot\delta\mathcal{E}\right\} \tag{4.3a}$$

$$\delta f_{\delta\mathcal{B}} = \mu_B\left\{\Delta g\cdot\delta\mathcal{B} + \frac{\mathrm{d}\Delta g}{\mathrm{d}\mathcal{E}}\cdot\delta\mathcal{E}\cdot\delta\mathcal{B} + \frac{\mathrm{d}\Delta g}{\mathrm{d}\mathcal{B}}\cdot(\delta\mathcal{B})^2\right\} \tag{4.3b}$$

The electromagnetic decoherence time τ_{EM} is thus given by:

$$\tau_{\mathrm{EM}} = \frac{1}{\delta f_{\delta\mathcal{E}} + \delta f_{\delta\mathcal{B}}} \tag{4.4a}$$

An example of an EDM-clock transition shown in Fig. 4.2 has τ_{EM} ~2900 s at ~66.7 V/cm. Both Δg and $\Delta\bar{d}$ are suppressed to below 0.001, and therefore have $\tau_{\mathrm{EM}} \gtrsim 4$ s over a 1.2 V/cm range of applied field. Typical, non-field-insensitive transitions have $|\Delta g|, |\Delta\bar{d}| \sim \mathcal{O}(1)$, which would result in $\tau_{\mathrm{EM}} \lesssim 1$ ms. At the same time, the magnitude of the normalized CPV sensitivity maintains reasonably large values of $|\Delta\bar{P}_M| \approx 42\%$, $|\Delta\bar{P}_d| \approx 31\%$, and $|\Delta\bar{P}_Q| \approx 42\%$.

Since there is field dependence of Δg and $\Delta\bar{d}$, there will be residual electromagnetic sensitivity in the presence of any field imperfections or noise, though it is also suppressed. We find $(\mathrm{d}\Delta g/\mathrm{d}\mathcal{E}) \sim 2 \times 10^{-4}$/(V/cm) and $(\mathrm{d}\Delta\bar{d}/\mathrm{d}\mathcal{E}) \sim 1 \times 10^{-3}$/(V/cm), indicating that high suppression of Δg and $\Delta\bar{d}$ is maintained over more than a few V/cm electric field range and therefore the EDM-clock transition is robust against the fields gradients and fluctuations. The dependencies of Δg and $\Delta\bar{d}$ on the electric (magnetic) field are linear over a few V/cm (Gauss) around the zero crossing point, so the differential energy shifts are mostly quadratic. Note that this dependence is factored in when calculating τ_{EM}.

An applied magnetic field parallel (or anti-parallel) to the electric field can also be utilized to further tune Δg and $\Delta\bar{d}$. For instance, with an EDM-clock transition where $\Delta\bar{d}$ crosses zero but Δg does not, Δg can be further suppressed or even tuned to zero. An example of this exists at an electric field of ~143 V/cm and a magnetic field of ~106 mG in ^{173}YbOH, where both the electric and magnetic sensitivities vanish. Note that by applying a magnetic field, the exact cancellation of $\Delta\bar{d}$ and the frequency between time-reversed transitions is lost; however, $\Delta\bar{d}$ only changes by $\sim 1 \times 10^{-5}$. Although here we only consider magnetic fields parallel (or anti-parallel) to the electric field, applying a magnetic field at a different angle relative to the electric field, or even to the polarization of an optical dipole trap [95, 96], may provide further tuning of field sensitivities.

4.4 Examples of EDM-clock transitions in various species

While EDM-clock transitions exist quite generically, their location and properties depend strongly on the molecular structure. To understand these transitions in ^{173}YbOH, we performed high-resolution spectroscopy on the $\tilde{X}^2\Sigma^+(01^10)$ bending mode in ^{173}YbOH and ^{171}YbOH to accurately determine the molecular constants, which are detailed in chap. 3. We studied the $\tilde{A}^2\Pi_{1/2}(000) - \tilde{X}^2\Sigma^+(01^10)$ band with the same experimental technique and apparatus employed in ^{174}YbOH (Chap. 3). Briefly, a cryogenic buffer gas beam is used to perform laser-induced fluorescence spectroscopy under electric and magnetic fields. The chemical enhancement enables identification of each isotopologue's spectral features [67]. We fit the features to an effective Hamiltonian including Stark, Zeeman, rotation, spin-rotation, ℓ-doubling, and hyperfine terms, which are shown in table 3.1. Further details can be found in chap. 3.

To understand the effect of spectroscopic parameter variation on the position and qualities of the EDM-clock transitions, we varied each individual spectroscopic parameter of ^{173}YbOH by its fit error, as shown in Fig. 4.2. Many of the parameters do not have a significant impact on the quality of the EDM-clock transitions and they simply slightly shift the electric field value for the EDM-clock transition. Despite the relatively large errors on b_F and c, they only shift $\Delta\bar{d}$ slightly by $\ll$0.001. e^2Qq_0 has also large error of ~27 MHz and q_G and p_G are the parameters sensitive to the parity doublet structure. Nonetheless, variation of e^2Qq_0 and p_G only give rise to the uncertainty of $\Delta\bar{d}$ of <0.001. Variation of q_G has the biggest impact on the EDM-clock transition, leading to the uncertainty of $\Delta\bar{d}$ and Δg on the order of ~0.002 and ~0.0005 respectively. Note that Δg ~0.0005 is comparable to or below the expected contribution of Δg ~0.001 from nuclear spin and rotational Zeeman terms.

Combining all of the above, it is fair to claim that optical spectroscopy would be suf-

ficient to identify the candidates of EDM-clock transitions and predict their qualities with reasonably good accuracy. Therefore, EDM-clock transitions of a particular species can be understood with only moderate uncertainty on spectroscopic parameters, and exist quite generally without reliance on finely-tuned properties. Their qualities or positions can be confirmed in the subsequent experiment with higher precision such as microwave, RF, or two-photon Raman.

We then calculated EDM-clock transitions in several species which are candidates for CPV searches and whose spectroscopic parameters have been measured or calculated, such as ^{137}BaOH [87, 97, 98], ^{173}YbF [21, 99, 100], ^{171}YbF [101, 100], ^{171}YbOH (measured here), ^{174}YbOH [66], ^{88}SrOH [97, 102], ^{175}LuOH$^+$ [103, 104], ^{225}RaF [105, 106], and ^{232}ThF$^+$ [107, 108, 109], as shown in table 4.2. We find EDM-clock transitions in all of these species, indicating that they appear to exist quite generally. However, for species without parity doublets, the electric fields required are orders of magnitude higher than those with parity doublets; this is expected as appreciable mixing of the rotational levels must occur for appreciable CPV sensitivity.

Table 4.2: Examples of EDM-clock transitions in other species.

Species	I	State/Transition[a]	Frequency MHz	$M_{F''}, M_{F'}$	E field [V/cm]	$\lvert\bar{P}_d\rvert$[b] ‰	$\lvert\bar{P}_Q\rvert$[b] ‰	$\lvert\bar{P}_M\rvert$[b] ‰	$\lvert\Delta\bar{d}\rvert$	$\lvert\Delta g\rvert$	τ_{EM} sec
$^2\Sigma^+(01^10)$ states											
^{137}BaOH[c]	3/2	$N = 1$	21.0	3/2, 3/2	45.76	69	117	173	zero crossing	9.0×10^{-4}	729
					45.74	69	117	173	9.3×10^{-4}	zero crossing	1.0
^{171}YbOH	1/2	$N = 1$	6.8	3/2, 3/2	226.3	81	81	–	zero crossing	1.6×10^{-3}	435
^{88}SrOH[d]	0	$N = 2$	120.46	2, 1	223.10	94	–	–	zero crossing	1.0×10^{-2}	70
					223.12	94	–	–	3.8×10^{-3}	zero crossing	0.2
^{174}YbOH	0	$N = 1 \rightarrow 2$	29196	1, 1	57.9	136	–	–	zero crossing	5.4×10^{-2}	13
^{175}LuOH$^+$	7/2	$N = 1$	32895	1/2, –3/2	519	38	151	98	zero crossing	3.3×10^{-3}	216
$^2\Sigma^+(v = 0)$ states											
^{173}YbF[e]	5/2	$N = 1$	5375.9	1/2, –3/2	29973	18	41	33	zero crossing	3.9×10^{-2}	18.1
^{171}YbF[f]	1/2	$N = 0$	7312.8	1/2, –3/2	28170	27	27	–	5.0×10^{-6}	zero crossing	185
^{225}RaF[g]	1/2	$N = 1$	121.9	1/2, 3/2	10215	44	44	–	zero crossing	9.6×10^{-2}	7.4
^{225}RaF[g]	1/2	$N = 1$	215.9	1/2, –3/2	24569	43	43	–	zero crossing	4.8×10^{-3}	148
					24577	43	43	–	5.9×10^{-3}	zero crossing	0.2
$^3\Delta_1(v = 0)$ states											
^{232}ThF$^+$[h]	0	$J = 1 \rightarrow 2$	29085	1/2, 1/2	18.6	56	–	–	zero crossing	1.1×10^{-4}	6656

Notes for Table 4.2. [a] For the EDM-clock transitions with relatively large electric fields of $\gtrsim$1 kV/cm, the rotational quantum number shown is that which

constitutes the largest admixture as N is no longer a good quantum number. [b] For ^{137}BaOH, ^{171}YbOH, ^{88}SrOH, ^{174}YbOH, and ^{232}ThF$^+$, sensitivities are normalized to the value to which $|\bar{P}|$ saturates in the limit of full mixing of the parity doublets. For ^{173}YbF, ^{171}YbF, and ^{225}RaF, sensitivities are normalized to their maximum sensitivity obtained over all N = 0–2 states in 0–50 kV/cm electric field range. [c] Spectroscopic parameters are taken from ref. [87, 98]. Since there is no direct measurement of $^2\Sigma^+(010)$ state, we assumed that the spectroscopic parameters and molecular dipole moment are the same as $^2\Sigma^+(000)$ state. The q_G parameter is assumed to be the same as ^{138}BaOH [97]. [d] Parameters are taken from ref. [97, 110]. The molecular dipole moment is assumed to be the same as $^2\Sigma^+(000)$ state. [e] Spectroscopic parameters are taken from ref. [99, 100]. The molecular dipole moment is assumed to be the same as ^{174}YbF. [f] Spectroscopic parameters are taken from ref. [101, 100]. The molecular dipole moment is assumed to be the same as ^{174}YbF. [g] Spectroscopic parameters are taken from ref. [105]. The hyperfine parameters from fluorine and molecular dipole moment are taken from the theoretical calculation results [106]. [h] Spectroscopic parameters are taken from ref. [107, 108]. The effective Hamiltonian and its matrix element in $^3\Delta_1$ state are taken from ref. [109]. Here, we neglected transverse magnetic and electric fields. The g-factor is assumed to be the same for all states as the J = 1, F = 3/2 state g-factor. Because the spin-orbit interaction in $^3\Delta_1$ state couples Σ and Λ and aligns them in anti-parallel, the orbital and electron magnetic moments nearly cancel each other, offering highly suppressed g-factor [89]. Thus, Δg is generally small in most transitions. This is in contrast with $^2\Sigma^+$ state where there is no cancellation due to spin-orbit interaction. Note also that the contributions from the nuclear and rotational Zeeman terms are neglected. [i] For ion species (LuOH$^+$ and ThF$^+$), transverse magnetic and electric fields in the rotating frame are neglected. [j] Hyperfine constants from hydrogen nuclear spin are assumed to be the same as ^{174}YbOH. [k] For all species except YbOH and ThF$^+$, the effective g-factor is assumed

to be the same as the electron g-factor g_S.

4.5 Practical considerations in EDM-clock transitions

Implementing a CPV measurement utilizing these EDM-clock transitions has the advantage of being immediately compatible with Ramsey methods used, for example, by ACME [15] and demonstrated in CaOH [78], which use either coherent population trapping or microwave pulses, respectively, to create and read out the necessary superpositions. There are many EDM-clock transitions having $\Delta M \leq 2$ (which is a restriction we impose on the EDM-clock transitions considered here), and the transition dipole moment of the two EDM-clock transitions shown in Fig. 4.2, for instance, is ~0.2 Debye, meaning that it can be easily driven with the aforementioned methods. Reversing the signs of the applied fields, polarizations, etc. can be used to isolate the CPV and non-CPV signals. The same measurement could be performed on the time-reversed pair to make use of the internal co-magnetometer feature; simultaneous measurement of both transitions could provide very strong robustness.

While the ability to suppress the effects of electromagnetic fields is valuable, any CPV measurement requires a careful and thorough consideration of systematic effects, which will be unique to each system. Here we mention two example relevant effects.

First, the residual, quadratic field sensitivity mentioned earlier will result in false EDMs due to non-reversing (nr) background fields [93], which can be estimated to be $\{\mu_B \frac{\mathrm{d}\Delta g}{\mathrm{d}\mathcal{E}} + D\frac{\mathrm{d}\Delta \bar{d}}{\mathrm{d}\mathcal{B}}\}\mathcal{E}_{nr}\mathcal{B}_{nr}$ ~0.3 μHz, or $\lesssim 10^{-31}$ e cm, using $\mathcal{E}_{nr} = 1$ mV/cm and $\mathcal{B}_{nr}$ =1 μG, and can be suppressed by using the internal co-magnetometers. Furthermore, there are different EDM-clock transitions where $\frac{\mathrm{d}\Delta g}{\mathrm{d}\mathcal{E}}/\Delta P_{CPV}$ differs by a factor of ~100. This means that the false vs. true CPV signals will be different for these transitions. Note that molecules in optical traps will have tensor AC Stark

residual moments as well, as was observed in CaOH [78], which could be addressed using the same methods discussed therein.

Second, transverse magnetic fields will introduce coupling between different M_F states and cause unwanted precession and dephasing. These states are typically split by $\delta \gtrsim 100$ kHz due to fine and hyperfine structure, so a transverse field of $\sim \mu$G will give rise to a transverse coupling of $\Omega \sim 1$ Hz and second order shift on the order of $\frac{\Omega^2}{4\delta} \sim \frac{(1\text{Hz})^2}{4(100\text{kHz})} \sim \mu$Hz. Transitions involving $|M_F| = 1/2$ states will have a degenerate partner state directly coupled by a transverse field; such a degeneracy could be lifted by applying a small bias field, with ∼1 mG giving rise to a second order shift of $\lesssim$mHz. More specifically, $|M_F| = 1/2$ states are degenerate in the absence of a B_z field and can be coupled by transverse fields at first order, whereas $|M_F| \neq 1/2$ states are typically split by more than 100 kHz due to fine and hyperfine structure and thus at second or higher order. The application of a small bias field would lift the degeneracy of $|M_F| = 1/2$ states to suppress the coupling between the states. For instance, with a bias field of 1 mG, $M_F = \pm 1/2$ states are split by ∼kHz, and therefore there is a quadratic sensitivity to transverse fields of $\ll$ mG. This will break the perfect symmetry of the internal co-magnetometry, but by a small amount; for example in the transition shown in figure 2 in ^{173}YbOH, $\Delta\bar{d}$, Δg, and the transition frequencies change by $\sim 1\times10^{-6}$, $\sim 3\times10^{-5}$, and ∼Hz respectively. The frequency difference between the *left* and *right* transition can be exactly canceled out by reversing the E_z or B_z field individually.

4.6 Conclusion

In summary, we show that we can find transitions in molecules with electric and magnetic field sensitivity suppressed by over a hundred-fold while maintaining good sensitivity to CP-violation. These transitions offer internal co-magnetometry, and can be driven with RF, microwave, or two-photon transitions, and are therefore compatible with Ramsey measurements in both beams and traps. It is also suitable for

systems with large angular momentum commonly found in nuclear CPV searches where hyperfine structure increases the internal complexity and congestion. No particular molecular structure is required, though in species with parity doublets the transitions exist at moderate electric fields $\lesssim$1 kV/cm. It is likely that similar transitions exist in a wide range of species, including atoms [111], and both symmetric and asymmetric tops. They may also be compatible with spin-squeezing methods to decrease the noise limit. Finally, the ability to polarize molecules while suppressing decoherence from electromagnetic field noise with these transitions can be of great interest in other fields including quantum simulation, where a long-range dipole-dipole interaction with a long interaction time is extremely advantageous [112, 113, 114].

Chapter 5

Demonstration of engineering field-insensitive clock transitions

Portions of this chapter were published previously [115].

5.1 Introduction

As discussed in the previous chapter, engineering field-insensitive transitions could substantially improve molecular CP-violation measurements by suppressing electric- and magnetic-field-induced systematics while preserving strong EDM sensitivity. In this chapter, we discuss experimental demonstration of field-insensitive yet EDM-sensitive clock transitions in paramagnetic species, while simultaneously engineering transitions to sense external fields. The concept of tuning parameters to magic values to suppress some unwanted effect has been successfully applied in a wide range of experiments [80, 81, 116, 117, 95, 96, 118], and is for example a critical ingredient for the high precision and accuracy of modern atomic clocks [119]. We demonstrate this using the YbOH molecule, and show that at particular "magic" values of applied electromagnetic fields, certain transitions exhibit orders-of-magnitude suppression of electric *and* magnetic field sensitivities while maintaining a large (differential) internal effective electric field of $\mathcal{E}_{eff} \approx 22$ GV/cm. Here we provide its

first experimental realization in a heavy polyatomic molecule at the requisite level of quantum control, including all requisite external parameters and their control via experimental "switches" to isolate the desired signal from background noise or systematic errors [93]. The observed suppression of the field sensitivities is measurement statistics-limited. This clock transition exhibits simultaneous zero-crossings of electric ($\boldsymbol{\mathcal{E}}$) and magnetic ($\boldsymbol{\mathcal{B}}$) field sensitivities at a particular electromagnetic field point (up to measurement precision), though the sensitivities are also considerably reduced over a broad range of electromagnetic field values. We perform Ramsey measurements and show that coherence is maintained under large external electric and magnetic field fluctuations. We further introduce and experimentally demonstrate a new measurement protocol that utilizes both "EDM-clock" (field-insensitive) and "field-sensing" (field-sensitive) transitions to significantly suppress systematic errors in EDM experiments.

As already discussed in chap. 4, this approach does not rely on a particular electronic state (e.g., a $^3\Delta_1$ state), and such magic conditions can be found in a wide range of molecules [65]. Realizing such magic conditions requires (i) sufficient internal complexity to enable complicated mixing among nearby internal states to allow accidental cancellations of field sensitivities, and (ii) mixing of opposite-parity states to acquire substantial EDM sensitivity. Since polyatomic molecules generically have suitable opposite parity states with sufficient internal complexity within ~10 MHz of each other [75], these magic conditions can be typically achieved with easily accessible laboratory fields ($\mathcal{E} \lesssim$100 V/cm.) Diatomics without parity doublets, such as those in $^2\Sigma$ states, generally require nonzero nuclear spin for magic conditions to emerge from their complex hyperfine structure, and large electric fields to mix rotational levels ($\gtrsim$ 10 kV/cm). Given the generic applicability of the approach, it should be useful for the study of a broad range of new physics observables including eEDM, nuclear Schiff moments (NSM), nuclear magnetic quadrupole moments

(MQM) [65], as well as for dark matter searches over many orders of magnitude in mass [120, 121]. The basic idea is to identify pairs of states whose electric and magnetic sensitivities can be tuned with external fields to a point where they have vanishing differential Stark and Zeeman shifts, yet retain large differential CP-violation sensitivity. The approach can use states that have a small difference in projection of total angular momentum (M_F), making state preparation and readout schemes straightforward. These methods are particularly useful for species with heavy spinful nuclei, which are needed for NSM and MQM searches, and which typically have complex hyperfine structure.

In this chapter, we shall focus on the eEDM-sensitive molecule ^{174}YbOH [75, 122, 123]. As discussed in an earlier work [65], apart from experimental parameter differences like electric/magnetic field values and laser frequencies, this approach should be very similar in other species, especially polyatomics for which these magic conditions generally appear at comparable field values. The energy shifts induced by the eEDM in a molecule under external fields are governed by the Hamiltonian [20]

$$H = -D\,\hat{\boldsymbol{n}} \cdot \boldsymbol{\mathcal{E}} - g\mu_B \boldsymbol{S} \cdot \boldsymbol{\mathcal{B}} + d_e \mathcal{E}_{eff}\,\hat{\boldsymbol{S}} \cdot \hat{\boldsymbol{n}}. \tag{5.1}$$

Note that this is a minimal effective Hamiltonian included to highlight the field- and eEDM-dependent contributions relevant for the engineered-transition concept; additional terms (e.g., hyperfine and spin-rotation) are included in the full model used for quantitative predictions. Here, D is the molecular-frame dipole moment, $\hat{\boldsymbol{n}}$ is a unit vector along the molecular (symmetry) axis, g denotes the magnetic g-factor, $\hat{\boldsymbol{S}}$ is the unit vector along the electron spin, d_e is the electron EDM, and $\mathcal{E}_{eff}$ is the internal effective field experienced by the electron. The relative orientation of $\hat{\boldsymbol{S}}$ and $\hat{\boldsymbol{n}}$, defined as $P \equiv \langle \hat{\boldsymbol{S}} \cdot \hat{\boldsymbol{n}} \rangle$, serves as a quantum-state-specific measure of the eEDM sensitivity. In this chapter we refer to $\mathcal{E}_{eff}P$ as the “eEDM sensitivity" since each state may have a different value of P.

5.2 Experimental overview

A schematic representation of the experiment is shown in Fig. 5.1(a). Here we briefly outline the experiment and then discuss the details below. YbOH molecules are produced via laser ablation of pressed targets in a 4 K cryogenic buffer-gas cell and extracted as a cryogenic buffer gas beam (CBGB) with forward velocity $v \approx 200$ m/s. After state preparation via 567 nm optical pumping into the "science state" $|\tilde{X}(010), N'' = 1, p = +\rangle$ manifold, a Ramsey measurement on the transition of interest, denoted by the states $|0\rangle$ and $|1\rangle$, is performed via two-photon Raman pulses in a region of controllable electric and magnetic fields generated by indium-tin-oxide (ITO) coated glass plates and wire coils, respectively. Here N denotes the molecular angular momentum not including spin, p is the parity, and (010) means that the molecule has one quanta of bending vibration. This bending motion leads to parity doubling, making this state useful as the science state for EDM measurements [75]. $\tilde{X}$ denotes the ground electronic state. There are additional few-meter-scale three pairs of coils which null ambient magnetic fields to the mG level. Zeeman spectroscopy confirms that field uncertainties are $\sim$ 1 mG and therefore have negligible impact on our extraction of the field sensitivities.

YbOH molecules in the beam experience two Ramsey pulses. The first $\pi/2$-pulse creates a superposition $|\psi\rangle \propto |0\rangle + |1\rangle$. For conceptual clarity we describe an ideal model with a perfect $\pi/2$-pulse, though our analysis includes imperfections in the pulses. The state then evolves into $|\psi\rangle \propto |0\rangle + e^{i\varphi}|1\rangle$ in the applied fields for a time $\tau \approx 25$ μs over a distance of ≈ 5 mm. Here the phase φ contains all physical phase accumulation, including the Stark and Zeeman shifts, the eEDM, and more [93]. The second $\pi/2$-pulse projects φ onto the populations in $|0\rangle$ and $|1\rangle$, yielding $|\psi\rangle \propto \cos(\varphi/2)|0\rangle + i\sin(\varphi/2)|1\rangle$. Finally, φ is read out by laser-induced fluorescence to form an asymmetry signal $\mathcal{A} = (N_0 - N_1)/(N_0 + N_1)$ and suppress unwanted effects arising from beam yield fluctuations both within a single pulse

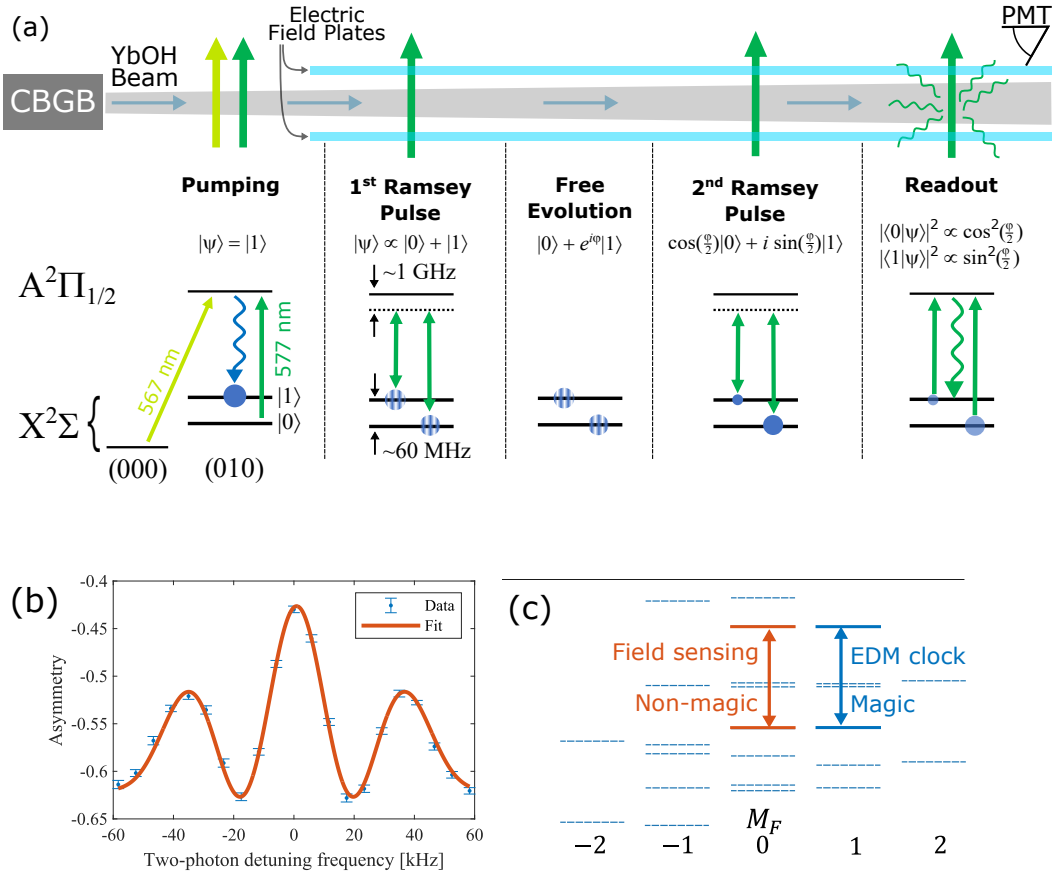

Figure 5.1: (a) A schematic representation of the experiment. A beam of YbOH molecules is directed through a series of lasers. The first lasers optically pump from the ground, non-vibrating (000) state to populate the $|1\rangle$ level in the (010) bending mode "science state." Next, a two-photon pulse creates a coherent superposition of $|0\rangle$ and $|1\rangle$. During spin precession, a phase φ is accumulated. A second two-photon pulse then maps the relative phase onto populations of $|0\rangle$ and $|1\rangle$. (The second Ramsey pulse is derived from the same laser but delivered downstream along a separate beam path.) Finally, state populations are determined by state-selective laser-induced fluorescence detected on a photomultiplier tube (PMT). (b) An example Ramsey fringe taken with $\mathcal{E} = 10.93$ V/cm and $\mathcal{B} = 0.30$ G as a function of two-photon frequency. Blue points indicate measured data with 1σ error bars, and the red curve is a fit to $\mathcal{A}(\delta)$, whose full expression is given in section 5.2. (c) Level diagrams of the $N'' = 1$, $\tilde{X}(010)$ state in ^{174}YbOH at $\mathcal{E} = 39.60$ V/cm and $\mathcal{B} = 12.15$ G, highlighting the EDM-clock transition that suppresses both electric and magnetic field sensitivities and nearby field-sensing transition used for field-sensing.

and between different pulses. Both populations of states $|0\rangle$ and $|1\rangle$ are measured via fast frequency switching [124] (see sec 5.2). A representative Ramsey fringe is shown in Fig. 5.1(b). Note that imperfect optical pumping leaves populations in states close in energy to $|0\rangle$ and $|1\rangle$, and their fluorescence adds background ($\mathcal{A}_0$) and reduces the Ramsey contrast (C).

Details of the experimental apparatus

In the experiment, YbOH molecules are produced by laser ablation of pressed powder targets at a ∼1 Hz repetition rate and subsequently thermalized by collisions with ∼4 K He buffer gas atoms in a cryogenic buffer gas cell. By resonantly driving the $^1S_0 \rightarrow {}^3P_1$ transition of ^{174}Yb, the ^{174}YbOH yield is increased by around an order of magnitude [125]. YbOH is extracted through the cell aperture as a rotationally and translationally cold beam [25, 23]. The YbOH beam travels at ∼ 200 m/s through a room-temperature chamber where YbOH is optically pumped from $|\tilde{X}(000), N'' = 0, p = +\rangle$ to $|\tilde{X}(010), N'' = 1, p = +\rangle$ through the $|\tilde{A}(010), p = -\rangle$ excited state using a laser at 567 nm [126]. There are no applied electric or magnetic fields in this region so the parity selection rules hold. A combined top and side view of this optical-pumping region is shown in Fig. 5.2. These views illustrate the field-free pumping region located between the cryogenic source and the science chamber, where the YbOH beam is optically pumped into the bending-mode science manifold.

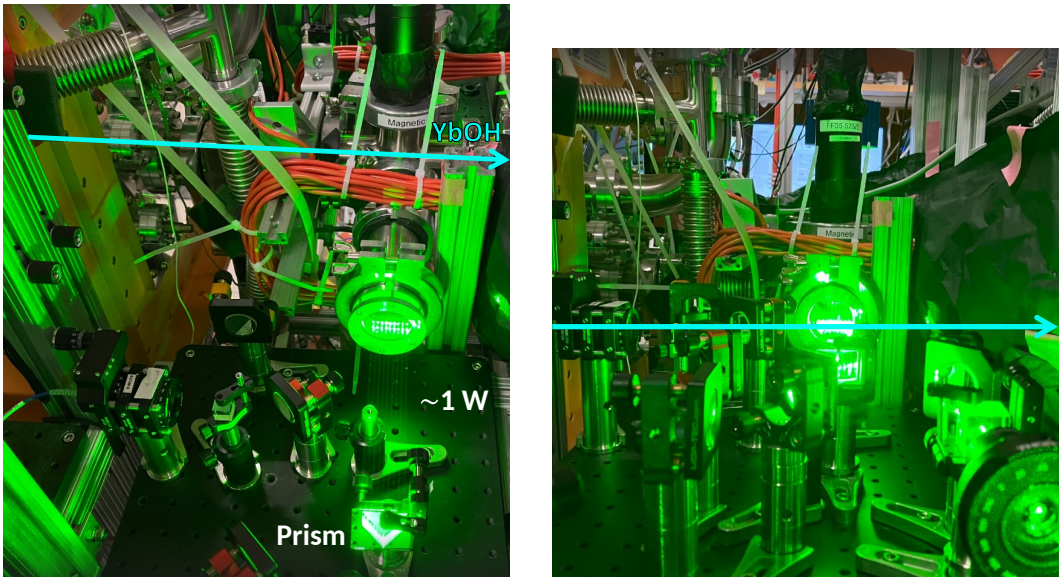

Figure 5.2: Top and side views of the optical-pumping region. The left panel shows the room-temperature section of the beamline where the YbOH molecular beam is illuminated with the 567 nm optical-pumping light before entering the science chamber; the prism used to direct the optical-pumping beam and the molecular-beam path are indicated. The right panel highlights the beamline geometry in the field-free region used for state preparation upstream of the science chamber, where the optical-pumping light intersects the YbOH beam prior to the Ramsey-interrogation region.

The YbOH molecules then enter the "science chamber" located ~112 cm downstream from the cell where the Ramsey measurement and laser-induced fluorescence (LIF) detection are performed. Inside the science chamber, two indium tin oxide (ITO) coated glass plates separated by 1 inch apply a uniform electric field in the vertical direction, which defines the lab $\hat{\boldsymbol{Z}}$ axis. Since the electric field applied in this work remains below the regime of full parity-doublet mixing [66, 65], a substantial fraction of the population in $|N'' = 1, p = +\rangle$ is transferred to the science states used in this work, such as $|0\rangle$ and $|1\rangle$, under the electric field in the science chamber. This allows us to optically pump from $|\tilde{X}(000), N'' = 0, p = +\rangle$ to $|\tilde{X}(010), N'' = 1, p = +\rangle$ before the YbOH beam enters the electric-field region in the science chamber, as can be seen from Fig.5.1 (a). This configuration is advantageous because it significantly reduces scattered light from the high-power optical

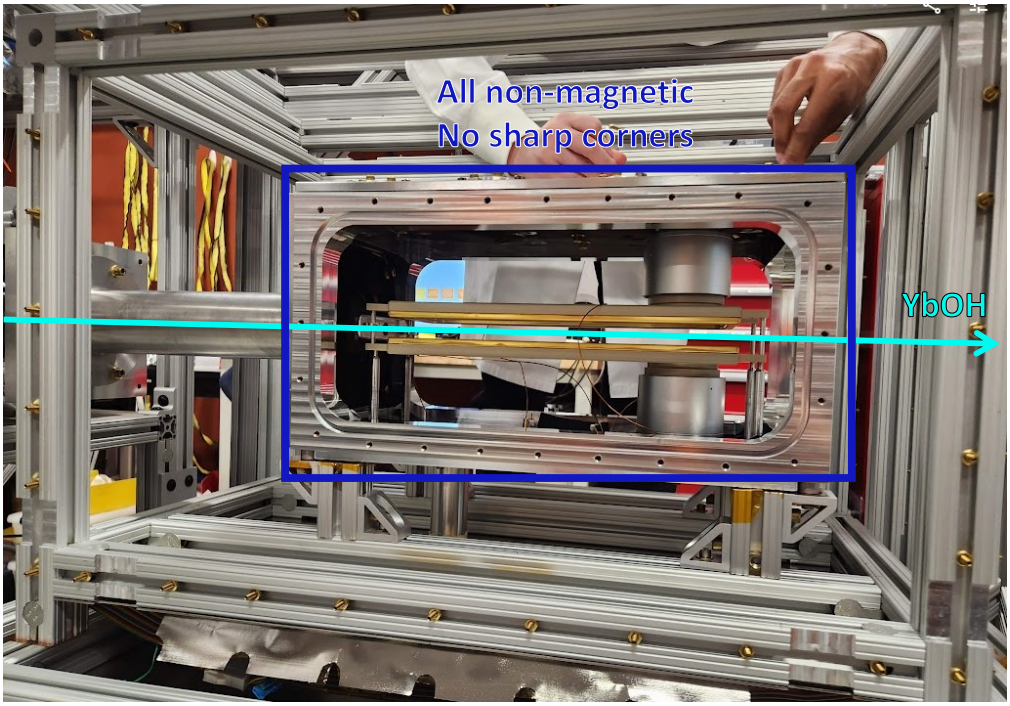

Figure 5.3: Photograph of the science chamber assembly. The cyan line indicates the YbOH beam path through the chamber. The chamber and surrounding support structure are designed to be nonmagnetic and to avoid sharp corners, helping to reduce magnetic contamination and unwanted electric-field enhancement near the interaction region.

pumping lasers reaching the final detector, thereby lowering the background signal. A photograph and a cutaway schematic of the science chamber are shown in Figs. 5.3 and 5.4. The photograph highlights the chamber assembly and the molecular-beam path through the interaction region, while the schematic identifies the principal internal components used for electric-field generation, Ramsey interrogation, and fluorescence collection.

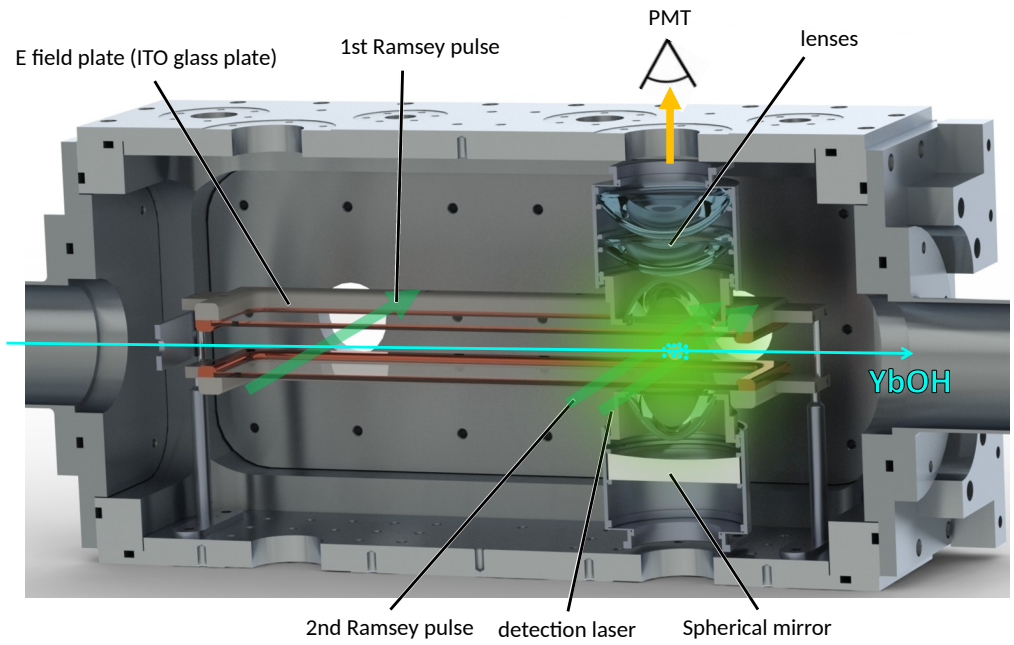

Figure 5.4: Cutaway schematic of the science chamber. Two ITO-coated glass plates generate the electric field in the interaction region traversed by the YbOH beam. The first and second Ramsey pulses intersect the beam upstream and downstream of the free-precession region, respectively. Fluorescence from the detection region is collected with spherical mirrors and lenses and directed onto a photomultiplier tube (PMT). In the implementation used in the present work, however, the second Ramsey pulse is delivered through the same chamber window as the first rather than through the downstream window shown schematically. Although we have demonstrated Ramsey interferometry in the geometry illustrated here at zero applied electric field as shown in Fig. 6.9, at finite electric field this configuration still suffers from decoherence caused by electric-field inhomogeneity. This is why the measurements reported here use the same-window delivery for both Ramsey pulses. In future work, we plan to improve the homogeneity of the electric-field plates and operate in the configuration illustrated in this schematic.

In the science chamber, YbOH molecules are illuminated with multiple lasers at 577 nm to perform Ramsey spin precession measurements. Note that the lasers are always on, and the motion of the molecules through the fixed laser beams results in their experiencing temporal pulses. Here the transitions of interest consist of $|0\rangle$ and $|1\rangle$ in $|\tilde{X}(010), N'' = 1, p = +\rangle$, roughly separated by ~60 MHz. To be clear, depending on the measurement these may be different states. The states used for the $\hat{\mathcal{M}}$ switch (changing between the EDM-clock transition and field-sensing transition) demonstration are shown in Fig. 5.1(c). The first laser optically pumps from $|0\rangle$ to $|1\rangle$ through a $|\tilde{A}(010), p = -\rangle$ excited state with $\hat{Z}$ polarization. Next the YbOH beam sees two Ramsey pulses. Note that we describe an ideal model with a perfect $\pi/2$-pulse for conceptual clarity, though our quantitative analysis uses a fit function that incorporates measured deviations from a perfect $\pi/2$-pulse. The first is a $\pi/2$-pulse with a two-photon laser phase θ to create a superposition $|\psi(0)\rangle \propto |0\rangle + e^{i\theta}|1\rangle$. This state then evolves into $|\psi(\tau)\rangle \propto |0\rangle + e^{i(\varphi+\theta)}|1\rangle$ under the applied fields for a time $\tau \approx 25$ μs over a distance of ≈5 mm with ~ 200 m/s molecular beam forward velocity. Note that this distance is between the center of two Ramsey pulse lasers. The laser beam for the Ramsey pulses is elliptical, with the major axis oriented vertically. The measured second moment width of the Gaussian fit along the horizontal (molecular beam) axis is 2.88 mm. The phase accumulation occurs during the Ramsey pulse as well so the Ramsey fringe period is $\tau \sim \tau_{\text{free}} + T$. The second Ramsey pulse projects the phase φ onto the populations in $|0\rangle$ and $|1\rangle$. Note that the second Ramsey pulse is derived from the same laser but delivered downstream along a separate beam path, and therefore has a constant two-photon laser phase offset $\delta\theta$ from the first pulse, up to the fluctuation of the path length difference. The phase φ contains all physical phase accumulation, including the Stark and Zeeman shifts, the eEDM, and more [93]. The Ramsey pulses are realized via two-photon Raman transitions with the driving laser detuned by approximately 0.5 GHz from the optical resonance between $|\tilde{X}(010)\rangle$ and $|\tilde{A}(010)\rangle$. (For some

field-sensing transitions, the detuning was set to 1 GHz.) A double-passed acousto-optic modulator (AOM) generates a single sideband with the carrier, and their beats address the EDM-clock transitions and field-sensing transitions of interest. Note that the Ramsey pulse beams are frequency-shifted using AOMs in a double-pass configuration, such that the resulting optical frequency shift is twice the applied RF frequency; unless otherwise stated, all frequency shifts quoted in this work refer to the corresponding optical (two-photon) frequencies. Finally, the last laser drives from $|0\rangle$ or $|1\rangle$ to $|\tilde{A}(010), p = -\rangle$, and the resulting laser-induced fluorescence (LIF) from decays to $|\tilde{X}(010), p = +\rangle$ at 577 nm is collected to give state populations from which φ is inferred. All laser frequencies are locked to a wavemeter.

Measurement of asymmetry

When we calculate the asymmetry, we form the background-subtracted asymmetry

$$\mathcal{A} = \frac{(M_0 - B_0) - (M_1 - B_1)}{(M_0 - B_0) + (M_1 - B_1)} = \frac{N_0 - N_1}{N_0 + N_1}, \tag{5.2}$$

where $M_{0,1}$ are the raw detected photon counts in the $|0\rangle$ and $|1\rangle$ detection channels, $B_{0,1}$ are the laser-scatter backgrounds measured $\sim$ 30 ms after the ablation where there is no molecular signal, and $N_i \equiv M_i - B_i$ are the background-subtracted signals. Assuming the photon shot noise,

$$\mathrm{Var}(N_i) \sim (N_i + B_i) + B_i = N_i + 2B_i. \tag{5.3}$$

Propagating uncertainties for $\mathcal{A} = (N_0 - N_1)/(N_0 + N_1)$ yields

$$\begin{aligned} \Delta\mathcal{A}^2 &= \left(\frac{\partial \mathcal{A}}{\partial N_0}\right)^2 \mathrm{Var}(N_0) + \left(\frac{\partial \mathcal{A}}{\partial N_1}\right)^2 \mathrm{Var}(N_1) \\ &= \left(\frac{2N_1}{(N_0 + N_1)^2}\right)^2 \mathrm{Var}(N_0) + \left(\frac{2N_0}{(N_0 + N_1)^2}\right)^2 \mathrm{Var}(N_1). \end{aligned} \tag{5.4}$$

Using representative values $N_0 \simeq 4500$, $N_1 \simeq 2500$, and $B_0 \simeq B_1 \simeq 6000$ photons, Eq. (5.3) gives $\mathrm{Var}(N_0) = N_0 + 2B_0 = 16500$ and $\mathrm{Var}(N_1) = N_1 + 2B_1 = 14500$. Substituting into eq. (5.4) yields $\Delta\mathcal{A} \simeq 0.026$ per shot.

To normalize against molecular yield variations from pulse-to-pulse and the non-uniform temporal shape of the molecular pulse within each pulse we employ fast switching [124] of the detection laser frequency to alternate the LIF detection between $|0\rangle$ and $|1\rangle$ at 50 kHz. With this approach, we can construct the asymmetry $\mathcal{A} = (N_0 - N_1)/(N_0 + N_1)$ within a single ablation pulse, which significantly reduces unwanted effects arising from pulse-to-pulse fluctuations and allows us to approach shot-noise-limited measurements. The observed $N_0 \sim 4500$ and $N_1 \sim 2500$ population imbalance is incidental and arises from imperfect state preparation and residual population in nearby levels that are not optically resolved. This mainly reduces the asymmetry fringe contrast, but does not alter the operating principle of the protocol. Note that imperfect optical pumping leaves populations in states close in energy to $|0\rangle$ and $|1\rangle$, and the measured N_0 and N_1 include background signals from the population in these nearby states.

The measured asymmetry can be influenced by several effects related to the optical readout process. These can be separated into three mechanisms. First, changes in detection efficiency of each state ($|0\rangle$ and $|1\rangle$) can modify the measured asymmetry. In particular, small variations in the detection laser power can lead to unequal detection efficiencies. In the present experiment, the $|0\rangle \leftrightarrow A$ and $|1\rangle \leftrightarrow A$ transitions are separated by only ≈ 60 MHz. To avoid power broadening and spectral overlap, which would significantly reduce the Ramsey fringe contrast, the readout lasers are operated near or below saturation. Operating in this regime increases the susceptibility of the asymmetry to laser power drifts. Moreover, the absolute saturation behavior is difficult to characterize due to possible photon cycling and mixing among excited electronic states, which limits precise knowledge of the relevant transition dipole moments. Note that the transition frequency is extracted from differential measurements in which the electric and/or magnetic fields are switched at ≈ 1 Hz and asymmetry differences are taken. This procedure strongly suppresses sensitivity

to slow drifts in detection efficiency and ensures that the extracted frequencies are not biased by such effects at the present level of precision.

To briefly estimate the sensitivity of the asymmetry $\mathcal{A} = (N_0 - N_1)/(N_0 + N_1)$ to changes in detection efficiency, we consider a fractional change $N_0 \to (1 + a)N_0$, yielding

$$\Delta\mathcal{A} \simeq \frac{2N_0N_1}{(N_0 + N_1)^2}\, a. \tag{5.5}$$

For typical values $N_0 \approx 4500$ and $N_1 \approx 2500$, this corresponds to $\Delta\mathcal{A} \approx 0.46a$. Since the typical laser power drift at relevant time scale (1 s) is below 5%, single shot fluctuations in the asymmetry due to detection-efficiency variations are below those arising from photon shot noise in the total detected signal ($\Delta\mathcal{A} \approx 0.026$). No statistically significant systematic effect associated with this mechanism is observed at the current precision.

Second, population excited to the $A(010)$ state can decay back into the originally addressed state during detection (e.g., $|0\rangle \to A(010) \to |0\rangle$). This photon cycling contributes to the effective detection efficiency of each state, but does not introduce a qualitatively new bias to the extracted asymmetry or transition frequency beyond a possible modification of the detection efficiency.

Third, decay from the A state can repopulate the other state during detection (e.g., $|0\rangle \to A(010) \to |1\rangle$). This process modifies the Asymmetry and reduces the observed Ramsey fringe contrast by partially washing out population differences between $|0\rangle$ and $|1\rangle$. As mentioned above, detection alternates between the two states at 50 kHz, with a 10 μs integration window for each state. This timescale is comparable to the interaction time of a molecule with the detection laser, given the laser beam diameter (few mm) and molecular beam velocity ($\sim$ 200 m/s). As a result, population transferred into another state may be detected in a subsequent channel, but cannot be repumped back to the original state and detected again before the molecule exits the detection region.

To see how these affect the asymmetry, we model the measured counts as a sum of the "direct" fluorescence contributions and cross-talk contributions,

$$N_0 = S_0 + x_0, \qquad N_1 = S_1 + x_1, \tag{5.6}$$

where

$$S_0 \equiv e_0 n_0, \qquad S_1 \equiv e_1 n_1 \tag{5.7}$$

are the direct signals (with $e_{0,1}$ effective detection efficiencies and $n_{0,1}$ the true state populations), and where cross-talk arises from excitation in one channel followed by decay into the opposite state and subsequent detection. We therefore write

$$x_0 = e_0 \eta_{10}\, e_1 n_1, \qquad x_1 = e_1 \eta_{01}\, e_0 n_0, \tag{5.8}$$

where η_{10} (η_{01}) is the branching probability for decay from A into $|0\rangle$ ($|1\rangle$). By construction $0 \leq \eta_{10}, \eta_{01} < 1$. Note that these branching probabilities (η_{10} η_{01}) are the stable properties of the molecule and constants that do not depend on the experimental parameters. For small fractional drifts $\delta e_0/e_0 = a$ and $\delta e_1/e_1 = b$, we have

$$\delta S_0 = a S_0, \quad \delta S_1 = b S_1, \quad \delta x_0 = (a+b) x_0, \quad \delta x_1 = (a+b) x_1. \tag{5.9}$$

Using eq. (5.4), one finds to first order

$$\delta \mathcal{A} = \frac{2}{(S_0 + S_1 + x_0 + x_1)^2} \left[(a-b) S_0 S_1 + a S_1 x_0 - b S_0 x_1 \right] \tag{5.10}$$

where $\delta N_0 = \delta S_0 + \delta x_0$ and $\delta N_1 = \delta S_1 + \delta x_1$.

As shown in Eq. (5.10), cross-talk modifies the sensitivity of the measured asymmetry to detection-efficiency fluctuations through two competing effects. First, the appearance of $(x_0 + x_1)$ in the denominator, $(S_0 + S_1 + x_0 + x_1)$, reduces the response of $\mathcal{A}$ to small changes in e_0 and e_1. Second, the additional terms proportional to $a S_1 x_0$ and $-b S_0 x_1$ can increase the sensitivity relative to the no–cross-talk case, depending on the relative signs and magnitudes of a and b. From measurements in

which we estimated the cross-talk contributions by comparing photon counts with and without upstream depletion of $|0\rangle$ ($|1\rangle$) prior to the downstream detection of $|1\rangle$ ($|0\rangle$), we find cross-talk at the $\sim$ 10% level: $x_0 \simeq 0.1S_0$ and $x_1 \simeq 0.1S_1$. We therefore do not expect cross-talk to significantly change the overall sensitivity of the measured asymmetry to detection-efficiency drifts compared with the no–cross-talk case.

For future EDM experiments employing similar readout schemes, these effects must be carefully considered. In particular, operating the detection transitions in a clearly saturated regime where possible, and quantitatively characterizing any detection-efficiency changes and its correlations with experimental switches, will be important for minimizing and bounding associated systematic effects.

Extraction of field sensitivities

As discussed in section 5.2, we perform Ramsey measurements to conduct Stark and Zeeman spectroscopy and extract the field sensitivities. First, we set the two-photon frequency to lie within the linear portion of the Ramsey fringe (the region highlighted by the orange line in Fig. 5.5 where the asymmetry varies approximately linearly with two-photon detuning and the slope is near maximal), and fit the linear portion of the fringe with a linear function to obtain the slope $\mathcal{A}/f$. Next, we vary the fields and record the asymmetries. As an example, we consider two asymmetry data points, $\mathcal{A}(\mathcal{E}_0, \mathcal{B}_0)$ and $\mathcal{A}(\mathcal{E}_1, \mathcal{B}_0)$, taken at $\mathcal{E} = \mathcal{E}_0, \mathcal{B} = \mathcal{B}_0$ and $\mathcal{E} = \mathcal{E}_1, \mathcal{B} = \mathcal{B}_0$, respectively, to extract the electric field sensitivity Δd_{eff}. Note that when we change the applied electric and magnetic fields, we correspondingly choose the two-photon detuning so that it remains on the linear portion of the Ramsey fringe. We then take differences $\mathcal{A}(\mathcal{E}_0, \mathcal{B}_0) - \mathcal{A}(\mathcal{E}_1, \mathcal{B}_0)$ and divide it by the slope $\mathcal{A}/f$ to convert it into a frequency difference $f(\mathcal{E}_0, \mathcal{B}_0) - f(\mathcal{E}_1, \mathcal{B}_0)$. The corresponding fit errors of the slope $\mathcal{A}/f$ are propagated. Finally, this frequency difference is divided by $\mathcal{E}_0 - \mathcal{E}_1$ to obtain the field sensitivity $\Delta d_{\text{eff}}(\frac{\mathcal{E}_0+\mathcal{E}_1}{2}, \mathcal{B}_0) = \frac{f(\mathcal{E}_0,\mathcal{B}_0)-f(\mathcal{E}_1,\mathcal{B}_0)}{\mathcal{E}_0-\mathcal{E}_1}$. We report the

field sensitivities at the midpoint ($\frac{\mathcal{E}_0+\mathcal{E}_1}{2}$) of two field points ($\mathcal{E}_0$ and $\mathcal{E}_1$), which is valid if the energy shift near the zero-crossing point is quadratic – a behavior that is consistent with both our predictions and the observed data. Nonetheless, around the zero-crossing points, we have $|\mathcal{E}_0 - \mathcal{E}_1| \lesssim 0.5$ V/cm and $|\mathcal{B}_0 - \mathcal{B}_1| \lesssim 0.07$ G. ($|\mathcal{E}_0 - \mathcal{E}_1|$ and $|\mathcal{B}_0 - \mathcal{B}_1|$ are different for different data points depending on their frequency shifts.) We repeat this measurement at various electric and magnetic fields to measure the field sensitivities Δd_{eff} and $\Delta\mu_{\text{eff}}$.

The uncertainties in Δd_{eff} and $\Delta\mu_{\text{eff}}$ are obtained by propagating the statistical uncertainties of the measured fluorescence signals. In particular, we repeat the measurements on N_0 and N_1 under certain experimental conditions and take the standard deviation of the resulting distributions as the corresponding statistical uncertainties. These uncertainties are then propagated sequentially from N_0 and N_1 to the asymmetry $\mathcal{A}$, from $\mathcal{A}$ to the extracted transition frequency f, and finally to the field sensitivities Δd_{eff} and $\Delta\mu_{\text{eff}}$, using standard error propagation. As mentioned earlier, the fit uncertainties of the slope $\mathcal{A}/f$ are also propagated. As explained later in section 5.2, uncertainties in the electric and magnetic field values are likewise propagated and found to be negligible. We assume these uncertainties are uncorrelated.

Note again that, although we show fits of the observed Ramsey fringes to the expected fringe shape in Fig. 5.1 as a guide to the eye, the extracted transition frequencies and field sensitivities do not depend on assumptions about the detailed fringe shape. The expected Ramsey fringe shape is given by

$$\begin{aligned}\mathcal{A}(\delta) = C\frac{\Omega^2}{\Omega_g^2}\sin^2\left(\frac{\Omega_g T}{2}\right)\Bigg[\cos\left(\frac{\Omega_g T}{2}\right)\cos\left(\frac{\delta\tau_{\text{free}}}{2}\right) \\ -\frac{\delta}{\Omega_g}\sin\left(\frac{\Omega_g T}{2}\right)\sin\left(\frac{\delta\tau_{\text{free}}}{2}\right)\Bigg]^2 + A_0\end{aligned} \tag{5.11}$$

where $\delta = 2\pi(f - f_{\text{res}})$ is the two-photon detuning, f_{res} is the resonant transition frequency, C is the Ramsey contrast, τ_{free} is the free evolution time between two

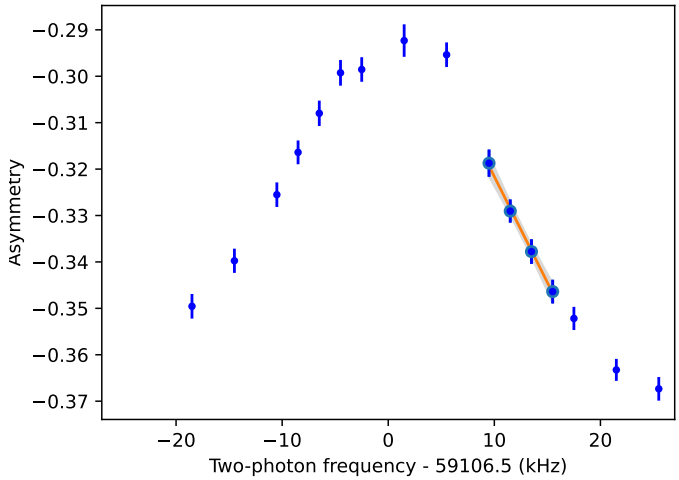

Figure 5.5: Ramsey fringe of the EDM-clock transition as a function of two-photon frequency. The Blue points represent measurements with their 1σ errors, while the orange solid line is a linear fit to the linear portion of the fringe. The shaded regions indicate the uncertainty of the fit. Note that the data here is taken on a different transition and at different field values from Fig. 5.1 (b). The transition in Fig. 5.1 (b) was chosen as an example with particularly good SNR.

pulses, T is the pulse duration, Ω is the two-photon Rabi frequency, $\Omega_g = \sqrt{\Omega^2 + \delta^2}$ is the generalized two-photon Rabi frequency, and $\mathcal{A}_0$ is the asymmetry offset. We incorporate a Gaussian distribution of molecular beam forward velocities which leads to a spread in τ_{free} and T. The phase accumulation occurs during the Ramsey pulse as well so the Ramsey fringe period is $\tau \sim \tau_{\text{free}} + T$ in our case. The fitted value of τ_{free} and T in Fig. 5.1 are (15 ± 2) and (10 ± 1) μs, respectively. Note that the demonstrated Ramsey free evolution time is currently limited by the available spatial separation between the two Ramsey pulses, which is limited by scattered light from the second Ramsey pulse beam reaching the final detector when it is moved closer to the detection optics. These are technical constraints rather than intrinsic limits of this protocol itself. With improved stray-light suppression and/or modified beam geometry, substantially longer interrogation times should be achievable.

To suppress the effect of any possible drift of the overall asymmetry offset (e.g., due to the drift of the power balance between two frequency components in the fast

switching of the detection laser), we alternate the two-photon frequency between red and blue side of the linear portion of the central Ramsey fringe. By taking the difference of the asymmetries at these two two-photon frequencies, we can cancel out the slow drift of the overall asymmetry offset. For the experimental data where we extract the bounds on the electric and magnetic field sensitivities at magic fields (i.e., the data at $\mathcal{E}$ = 39.60 V/cm and $\mathcal{B}$ = 12.15 G in Fig. 5.7), we have taken additional precautions to measure the frequency shift accurately. First, instead of employing the switch mentioned above, we alternate the two electric and magnetic field values around the magic field values. This cancels out the systematic effect more directly. Additionally, although narrowing the detection time window can reduce sensitivity to the velocity spread within a single molecular pulse, it may increase sensitivity to shot-to-shot variations in the overall temporal pulse shape. In particular, changes in the ablation spot on the target could modify the temporal profile and effective exit-time distribution of molecules from the buffer-gas cell, which may imprint on the measured asymmetry. To reduce sensitivity to such pulse-shape variations, we integrate over a larger time window (~4 ms out of ~10 ms), at the cost of reduced contrast, though we do not observe conclusive evidence of this effect in the present data set. Finally, as explained in the next paragraph, we stabilize the two-photon laser power to suppress the effects of laser power drift to well below our measurement uncertainty.

Laser power stabilization

For the two-photon transitions, the excitation pulses themselves can cause a frequency shift of the EDM-clock transition (probe light shift). To investigate this effect, we measure the transition frequency shift via Ramsey measurements at different two-photon laser powers. We change the laser power by 5% with laser power stabilization. The stabilization is done by adjusting the RF amplitude fed into an AOM with an active feedback loop. The measured energy shifts are (0.8 ± 0.8) kHz

for the EDM-clock transition and (1.2 ± 0.5) kHz for the field-sensing transition. The laser power drift without power stabilization is typically less than 2% over the experimentally relevant timescale of $\sim$ 5–10 minutes. This is the time needed to record a typical $\sim$ 500 shots at one electromagnetic field point, since the power can be measured and adjusted between field points. Thus, even without active feedback, any frequency shifts arising from laser power drift are smaller than the 1σ errors of this work. Nevertheless, we stabilize the two-photon laser power to make sure the laser power drift (and fluctuation) is well below 1% and thus is negligible for the experimental data where we extract the bounds on the electric and magnetic field sensitivities at magic fields (i.e., the data at $\mathcal{E} = 39.60$ V/cm and $\mathcal{B} = 12.15$ G in Fig. 5.7). Note that the 1σ errors of the switch channel frequency shifts (f^s) shown in Fig. 5.10 are $\sim 2\sqrt{2}$ times smaller than that of the transition frequency shifts $f\left(\hat{\mathcal{M}}, \hat{\mathcal{E}}|\mathcal{E}|, \hat{\mathcal{B}}|\mathcal{B}|\right)$ because of the way the switch channels are defined in Sec. 5.6. Therefore, any possible shift due to the laser power drift is smaller than the 1σ errors shown in Fig. 5.10 as well. The probe light AC Stark shift can also be categorized into switch channels and systematically characterized. This effect is well understood and characterized in atomic and molecular clocks, and there are methods to suppress and mitigate it via tailored pulse sequences [127, 128, 129, 130, 131] if needed, but also simply by measuring the relationship between laser power and the probe light shift [118]. Nonetheless, we can make the brief orders-of-magnitude estimate the magnitude of the several systematic effects that can arise from the combination of the non-reversing fields and probe light shifts. To simplify the estimation, we take the typical value of the one-photon detuning $\Delta \sim 2\pi \times 1$ GHz. The relevant probe-light shift for the present measurement is the *differential* AC Stark shift of the transition, i.e., the difference between the probe-induced light shifts of the upper and lower states. We denote this differential shift by $\Delta f_{\mathrm{LS}}(\Delta)$. The non-reversing fields of $\mathcal{E}_{nr} \sim 1$ mV/cm and $\mathcal{B}_{nr} \sim 1$ mG can cause a shift of the one-photon detuning by $\delta \sim 1$ kHz, which correlates with the $\hat{\mathcal{E}}$ and $\hat{\mathcal{B}}$ switches, respectively. For $\delta \ll \Delta$,

the resulting switch-correlated change in the differential light shift is, to first order,

$$\delta(\Delta f_{\mathrm{LS}}) \simeq \left|\frac{\partial \Delta f_{\mathrm{LS}}}{\partial \Delta}\right| \delta. \tag{5.12}$$

For far-detuned coupling, $\Delta f_{\mathrm{LS}}(\Delta)$ scales approximately as $1/\Delta$, so that

$$\delta(\Delta f_{\mathrm{LS}}) \approx |\Delta f_{\mathrm{LS}}| \, \frac{\delta}{\Delta}. \tag{5.13}$$

Using our experimentally determined bound on the differential probe-light shift, $|\Delta f_{\mathrm{LS}}| \lesssim 1$ kHz, we obtain $\delta(\Delta f_{\mathrm{LS}}) \lesssim 10^{-3}$ Hz (~ 1 mHz).

Magnetic fields

A several meter-scale set of square coil pairs outside of the science chamber cancel background magnetic fields down to the ~mG level in three axes. Another smaller pair of square coils applies a magnetic field of 0-20 G in the Ramsey region along the $\hat{\boldsymbol{Z}}$ axis. We calibrated the magnetic field in the Ramsey measurement region by measuring the Zeeman shift of a magnetically sensitive transition in YbOH using two-photon spectroscopy. The uncertainty in this Zeeman shift measurement was found to be negligible for the final uncertainty of the obtained field sensitivities. Temporal fluctuations of the magnetic and electric fields are roughly 1 mG and 1 mV/cm (on the timescale of a second), respectively, and found to be negligible for the final results.

Transverse fields can arise from misalignments between the electric field, magnetic field, and laser polarization axis. Similar to other EDM experiments [93], these effects do not directly give rise to false EDMs but can couple in at higher orders. Therefore, these effects can also be categorized into switch channels and systematically characterized. To suppress the transverse fields, additional magnetic coils in the $\hat{\boldsymbol{X}}$ and $\hat{\boldsymbol{Y}}$ axis can be installed and magnetic field stabilization can be applied, as demonstrated elsewhere [132]. The $\hat{\boldsymbol{X}}$- and $\hat{\boldsymbol{Y}}$-axis-coils could also be useful for more precise control of the magnetic field orientation or for the investigation of systematic errors arising from transverse fields.

5.3 Engineering field-insensitive molecular clock transitions for eEDM in ^{174}YbOH

Here we focus on a specific set of transitions in ^{174}YbOH that fall into two classes: an EDM-clock transition, whose sensitivities to both electric and magnetic fields are tuned to be simultaneously suppressed while maintaining high eEDM sensitivity, and a field-sensing transition, which retains high sensitivity to electric and magnetic fields. These two classes of transitions are employed in different experimental contexts throughout this work. Figure 5.1 (c) shows an EDM-clock transition and a field-sensing transition operated at the same electric and magnetic fields to demonstrate the switching protocol. The field-sensing transition used in the noise-robustness measurements of Fig. 5.8 is a different field-sensing transition, chosen at different field values to enhance sensitivity to applied field fluctuations.

Besides the EDM-clock transition and field-sensing transition, there are numerous transitions with different sensitivities to the electric field, magnetic field, and eEDM [65]. We have indeed found other transitions experimentally, including ones with suppressed sensitivity to electric fields and high sensitivities to magnetic fields and the eEDM. Fig. 5.6 shows these transitions and their zero crossing of electric field sensitivity at a magic electric field value. This electrically insensitive, magnetically sensitive transition may offer an additional set of transitions useful for systematic effect searches. These transitions are used for the Ramsey fringe demonstration in Fig.5.1 (b), operated at different electric and magnetic fields from Fig.5.1 (c), and chosen as an example with good signal-to-noise ratio. It is worth mentioning that the time-reversed pair of this transition exhibits identical electric field sensitivity but opposite signs of the eEDM sensitivity. This property is advantageous for systematic error rejection in a small magnetic field (like the case here), which is detailed in our previous publication [65].

We conduct two-photon spectroscopy to locate the line position of the EDM-clock

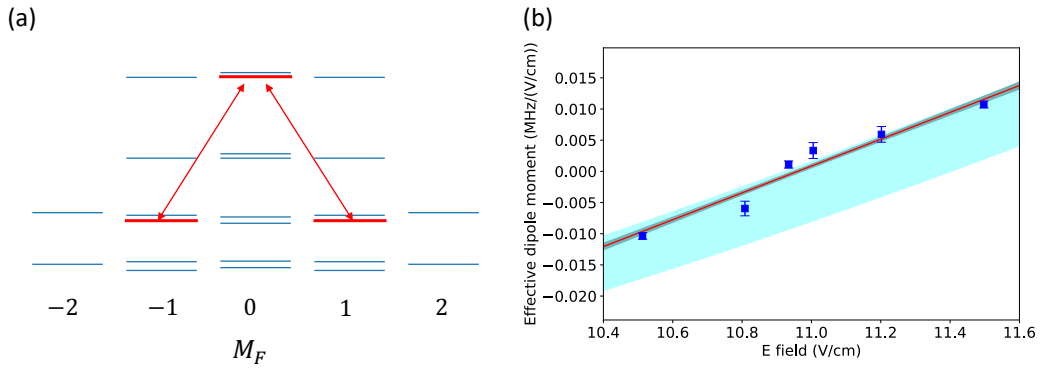

Figure 5.6: (a) Level diagrams of the $N'' = 1$, $\tilde{X}(010)$ state in ^{174}YbOH at $\mathcal{E} = 10.93$ V/cm and $\mathcal{B} = 0$ G, showing an electrically insensitive, magnetically sensitive transition. (b) The electric field sensitivity as functions of the applied electric fields. We applied a ~0.3 G magnetic field to lift the degeneracy between time-reversed pair for demonstration purposes. The electric field sensitivities are expressed in terms of the effective electric dipole moment. Blue square points represent measurements with their 1σ errors, the red line is a linear fit, and the shaded gray region indicates the fit uncertainty. The linear fit yields $(\partial \Delta d_{\text{eff}}/\partial \mathcal{E}) = (21.5 \pm 0.8) \times 10^{-3}$ MHz/(V/cm)^2. The cyan shaded regions indicate the theory uncertainties, which are obtained from the measurement uncertainties of the previous work [66] on the spectroscopic parameters.

transitions at various electric and magnetic fields, and perform Ramsey measurements to measure their Stark and Zeeman shift to extract the field sensitivities. A detailed description of the extraction procedure, together with the associated uncertainty propagation, is provided in section 5.2.

To quantify the sensitivity of a particular transition between two states $|0\rangle$ and $|1\rangle$ to $\boldsymbol{\mathcal{B}}, \boldsymbol{\mathcal{E}}$, and d_e we define the following differential quantities: the differential effective magnetic moment $\Delta\mu_{\text{eff}} \equiv \mu_{\text{eff},0} - \mu_{\text{eff},1}$ in MHz/G, the differential effective dipole moment $\Delta d_{\text{eff}} \equiv d_{\text{eff},0} - d_{\text{eff},1}$ in MHz/(V/cm), and the differential eEDM sensitivities $\Delta P \equiv (P_0 - P_1)$. For the $\tilde{X}(010)$ state in YbOH, the maximum differential eEDM sensitivity obtainable in the limit of full mixing of the parity doublets (i.e., at electric fields that are large enough to fully mix parity doublets) is given by $\Delta P_{\text{max}} = |P_{N''=1,M_F=2,M_N\ell=1} - P_{N''=1,M_F=2,M_N\ell=-1}| = 1$, where $M_N\ell$ indicates molecular orientation in the lab-frame axis. This is the EDM sensitivity

conventionally considered, as many EDM experiments operate at sufficiently high electric fields, and is therefore used as a reference in this thesis. Note, however, that at the "intermediate" electric field regime, there are also local sensitivity maxima, which can result in ΔP exceeding 1, as observed elsewhere [92, 78]. Note also that the angular momentum coupling in $|\tilde{X}(010), N'' = 1\rangle$ results in the molecular polarization on the lab-frame $\hat{\boldsymbol{Z}}$ axis of $\langle \hat{\boldsymbol{n}} \cdot \hat{\boldsymbol{Z}} \rangle = \frac{M_N \ell}{N''(N''+1)}$, where $\Delta P_{\max}$ is smaller by a factor of two than in a $^3\Delta_1$ state. Without employing engineered EDM-clock transitions, typical transitions have electromagnetic sensitivities given by the molecular dipole moment $D = 2.16$ Debye and Bohr magneton μ_B [66]. These parameters yield sensitivities of $\Delta d_{\text{typ}} \sim 1$ MHz/(V/cm) and $\Delta \mu_{\text{typ}} \sim 1.4$ MHz/G.

The observed field sensitivities of the EDM-clock transition exhibit zero crossings and are consistent with the predictions using the molecular parameters from previous optical spectroscopy to within the expected uncertainties [66]. These zero-crossings are summarized in Fig. 5.7. This indicates that EDM-clock transitions can be located with only moderate uncertainty on spectroscopic parameters. The observed field sensitivities are $\Delta d_{\text{eff}} = (-0.0009 \pm 0.0006)$ MHz/(V/cm) and $\Delta \mu_{\text{eff}} = (-0.0004 \pm 0.0055)$ MHz/G, or $|\Delta d_{\text{eff}}| < 0.0015$ MHz/(V/cm) and $|\Delta \mu_{\text{eff}}| < 0.006$ MHz/G. This corresponds to a suppression in electric and magnetic field sensitivities by at least a factor of 710 and 230 compared to Δd_{typ} and $\Delta \mu_{\text{typ}}$ respectively. Note that the sensitivities are predicted to be even lower, so these limits correspond to our ability to measure them directly.

Figure 5.7 details. In (a,b), field sensitivities are expressed as effective electric and magnetic dipole moments. Blue square points are measurements with 1σ errors, blue lines are linear fits, dark shaded regions indicate fit uncertainties, and light shaded regions indicate the original theory uncertainty from earlier spectroscopy [65]. The applied magnetic field in (a) is 12.15 G and the applied electric field in (b) is 39.60 V/cm. Linear fits yield $(\partial \Delta \mu_{\text{eff}} / \partial \mathcal{B}) = (1.6 \pm 0.1) \times 10^{-1}$

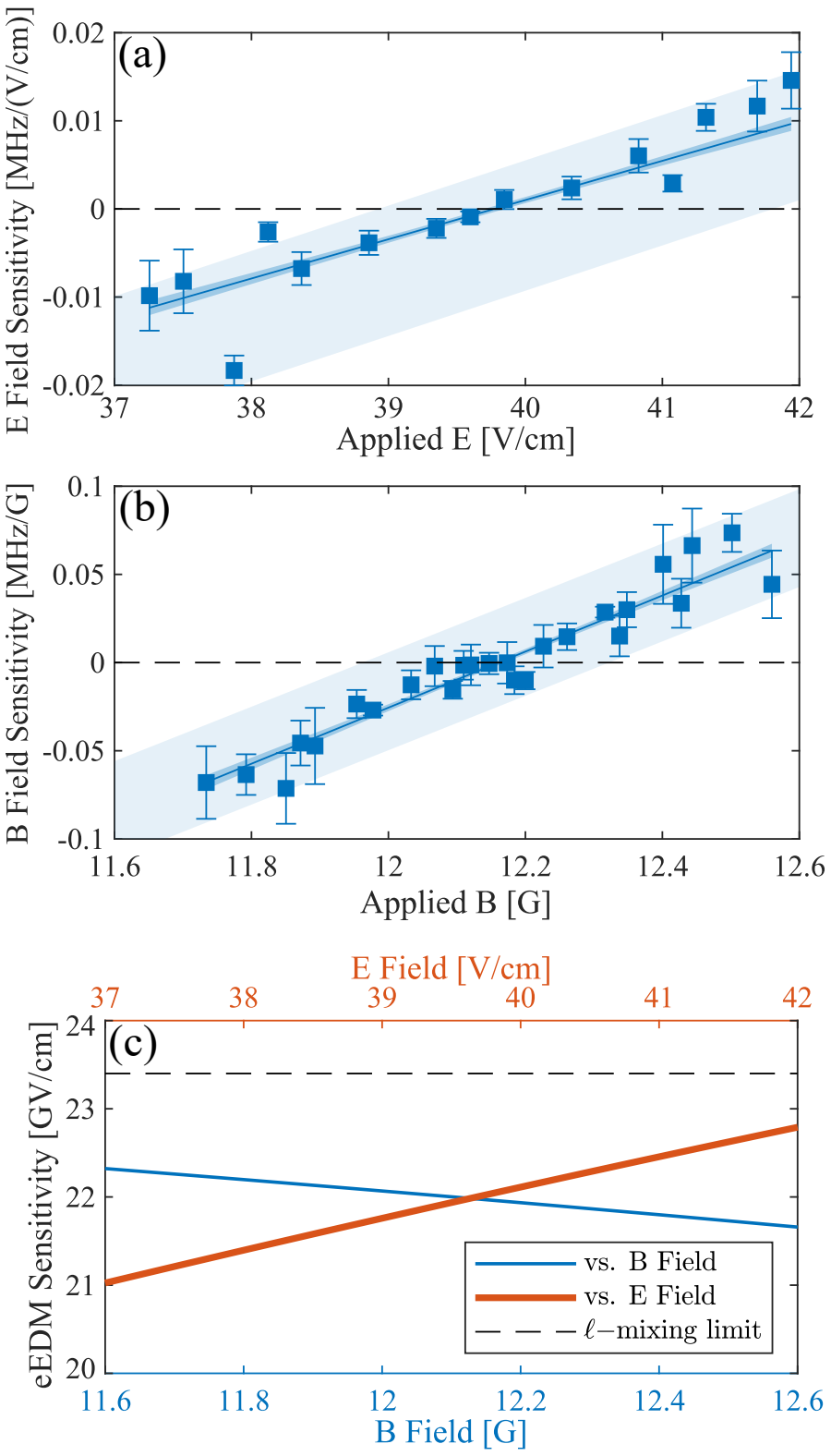

Figure 5.7: Measured electric-field sensitivity (a), measured magnetic-field sensitivity (b), and calculated eEDM sensitivity (c) of the EDM-clock transition versus applied electric and magnetic fields.

MHz/G^2 and $(\partial\Delta d_{\text{eff}}/\partial\mathcal{E}) = (4.4 \pm 0.3) \times 10^{-3}$ MHz/(V/cm)^2, demonstrating that suppression of Δd_{eff} and $\Delta\mu_{\text{eff}}$ is maintained over a range of a few V/cm and ~1 G, respectively. In (c), the predicted eEDM sensitivity is shown as $\mathcal{E}_{eff}\Delta P$ (GV/cm), with the solid blue and red lines corresponding to 39.6 V/cm and 12.15 G, and dashed black lines indicating the full-mixing limit of the ℓ parity doublets.

At the same time, the EDM-clock transition maintains a large internal effective electric field of $\mathcal{E}_{eff}\Delta P \approx$22 GV/cm, or $\Delta P/\Delta P_{max} \gtrsim 93\%$. This indicates that one can suppress the electromagnetic field sensitivities by orders-of-magnitude while maintaining high eEDM sensitivity. It is worth mentioning that our upper limit of magnetic sensitivity in the magic condition is on the same order of the $^3\Delta_1$ state in ThO [124] and HfF^+ [133].

We previously performed high-resolution spectroscopy on the $\tilde{A}^2\Pi_{1/2}(000)-\tilde{X}^2\Sigma^+(010)$ band in YbOH [66, 65] to extract the molecular parameters of the $\tilde{X}^2\Sigma^+(010)$ state (See chap. 3). The uncertainties of the measured molecular parameters were $\lesssim$MHz, which is relatively high compared to the energy scale of Ramsey fringes in this work ($\lesssim$10 kHz). Nevertheless, the theory prediction with the molecular parameters agrees with the properties of EDM-clock transitions explored in this work within the uncertainties, as can be seen from Fig. 5.7. We can then manually adjust the molecular parameters within their spectroscopic uncertainties to better reproduce the observed field sensitivities. The adjusted molecular parameters used in this work are given in Table 5.1. These parameters were not obtained from a least-squares fit to the present data since the amount of new data points in the present work is not sufficient to fit all the molecular constants. No formal statistical uncertainties are therefore assigned. Note that in the previous work, the hyperfine structure from the distant hydrogen nuclear spin was optically unresolved. Thus, we take the values from the previous two-photon spectroscopy work for the hydrogen hyperfine parameters (Fermi contact term b_F(H) and spin dipolar term c(H)) [126].

Table 5.1: Spectroscopic parameters for the $\tilde{X}^2\Sigma^+(010)$ state of YbOH.

Parameter		^{174}YbOH (previous work [66])	^{174}YbOH (adjusted in this work)
T_0/cm^{-1}	Origin energy	319.90901(6)	319.90901
B/MHz	Rotation	7,328.6(2)	7,328.43[b]
γ/MHz	Spin-rotation	–88.7(9)	–87.7[b]
γ_G/MHz	Axial spin-rotation	16(2)	15.6[b]
q_G/MHz	ℓ-doubling	–12.0(2)	–12.2[b]
p_G/MHz	P-odd ℓ-doubling	–11(1)	–10.3[b]
b_F(H)/MHz	Fermi contact	4.07(18)[a]	4.07[a]
c(H)/MHz	Spin dipolar	3.49(38)[a]	3.49[a]
D_{mol}/Debye	Molecular dipole moment	2.16(1)	2.17[b]
g_S	Effective electron g-factor	2.07(2)	2.07[b]

[a] These parameters are taken from the previous spectroscopy work [126].
[b] These parameters are manually adjusted in this work to better reproduce the observed field sensitivities.

5.4 Demonstration of suppression of field-induced noise

A key component of the Ramsey measurement is coherence. Suppressing decoherence enables longer coherence times and thus enhances the statistical sensitivity to the eEDM. To demonstrate robustness against decoherence from electric and magnetic fields, we measure the contrast of a Ramsey fringe with applied field noise and compare the EDM-clock transition to a field-sensing transition with large field sensitivities. Note that the field-sensing transition discussed here is different from the field-sensing transition shown in Fig. 5.1 (c) and is chosen for its higher field sensitivities. Applied field amplitudes are varied shot-to-shot with a uniform distribution. Ramsey contrast C is extracted through the measurement of asymmetry difference $\mathcal{A}(\delta = 0) - \mathcal{A}(\delta = \frac{\pi}{\tau}) \propto C$. The contrast of field-sensing transitions decays rapidly with field noise amplitudes of $\lesssim$0.1 V/cm and $\lesssim$0.02 G, whereas the EDM-clock transitions tolerate noise amplitudes of $\lesssim$10 V/cm and $\lesssim$1 G as shown in Fig. 5.8 and consistent with predictions.

Figure 5.9 shows the reduction of Ramsey fringe contrast as a function of electric and magnetic field noise amplitude in linear scale. The noise has uniform distribution with amplitude defined as the difference between the minimum and maximum values. The applied field noise distribution is discretized due to the finite resolution of the

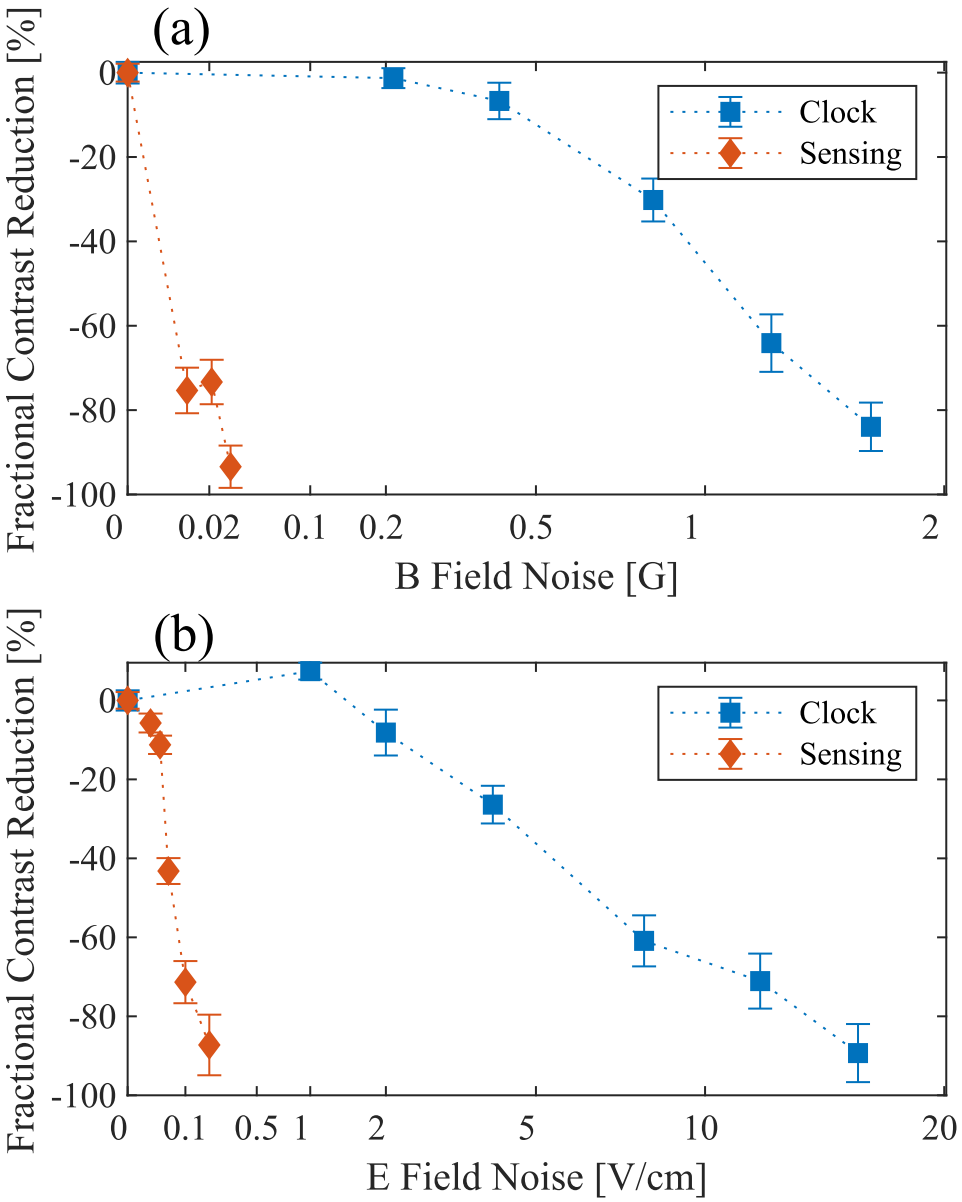

Figure 5.8: Reduction in Ramsey fringe contrast as a function of electric and magnetic field noise amplitude. The noise has uniform distribution with amplitude defined as the difference between the minimum and maximum values. The $x-$axis scale is non-linear to more clearly show the behavior at low noise values. Data with 1σ error bars in (a) were taken with zero applied electric field noise, and in (b) with zero applied magnetic field noise. The applied field noise distributions are centered at $\mathcal{E} = 39.60$ V/cm and $\mathcal{B} = 12.15$ G for the EDM-clock ("Clock") transition, and $\mathcal{E} = 20.00$ V/cm and $\mathcal{B} = 0.30$ G for the field-sensing ("Sensing") transition. The field sensitivities of the field-sensing transition around these fields are $\Delta d_{\text{eff}} = (0.120 \pm 0.001)$ MHz/(V/cm) $\sim 0.1\Delta d_{\text{typ}}$ and $\Delta\mu_{\text{eff}} = (0.952 \pm 0.008)$ MHz/G $\sim \Delta\mu_{\text{typ}}$.

current and voltage supply for the magnetic coil and electric field plate, respectively. For the EDM-clock transition, the applied fields sample 20-1300 discrete values, whereas for the field-sensing transition, the small applied fields sample 2–25 discrete values. For the field-sensing transition, the data are plotted on an expanded scale for clarity. For the field-sensing transition, the calculation explicitly includes the discretization of the applied field noise distribution. (For the EDM-clock transition, since the number of the field samples is large, the calculation assumes a continuous noise distribution.) Note that they exhibit a reduced rate of decline at large noise amplitude (e.g., $\gtrsim$1.25 G and $\gtrsim$7 V/cm for the EDM-clock transition) because strong fluctuations distort the original shape of the Ramsey fringe. Note that the contrast decay observed here reflects how far the suppression remains robust as one moves away from the magic point. This measurement does not directly determine the local first-order Stark or Zeeman sensitivity at the magic point itself, which remains limited by our ability to resolve small frequency shifts.

We can model the contrast decay under applied field noise by mapping field fluctuations to an effective distribution of two-photon detunings using the measured first derivative of the field sensitivities of the EDM-clock transitions. The measured contrast corresponds to an ensemble average of the Ramsey fringe over this detuning distribution. To provide a simple quantitative interpretation of the contrast roll-off in Fig. 5.8, we model the clock-transition frequency shift (δf) near the magic point in terms of electric and magnetic field shifts from the magic point ($\delta E, \delta B$),

$$\delta f \simeq \frac{1}{2}\left(\frac{\partial \Delta\mu_{\text{eff}}}{\partial B}\right)\delta B^2 + \frac{1}{2}\left(\frac{\partial \Delta d_{\text{eff}}}{\partial E}\right)\delta E^2, \tag{5.14}$$

using the experimentally measured curvatures ($\partial\Delta\mu_{\text{eff}}/\partial B$) and ($\partial\Delta d_{\text{eff}}/\partial E$). The accumulated phase is $\delta\phi \sim 2\pi\,\delta f\,T$. Assuming uniform noise distributions $\delta B \sim$ Uniform$[-B_n, B_n]$ and $\delta E \sim$ Uniform$[-E_n, E_n]$, one finds Var$(\delta B^2) = (4/45)B_n^4$

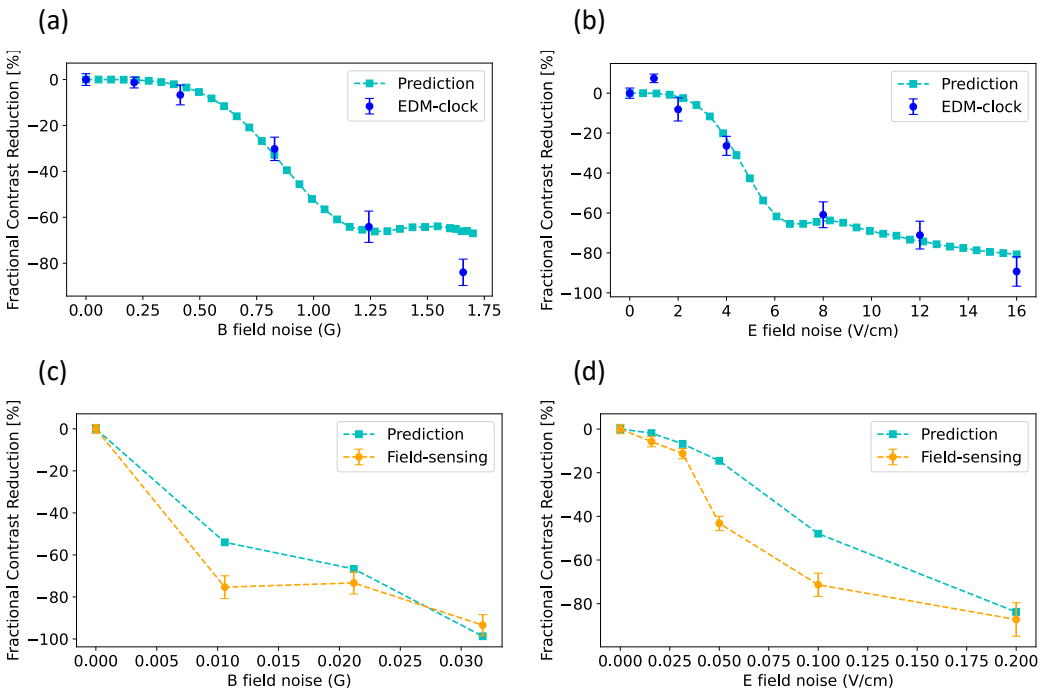

Figure 5.9: Reduction in Ramsey fringe contrast as a function of electric and magnetic field noise amplitude. Data with 1σ error bars in (a) and (c) were taken with zero applied electric field noise, and in (b) and (d) with zero applied magnetic field noise. The dashed cyan lines indicate the theory predictions.

and $\mathrm{Var}(\delta E^2) = (4/45)E_n^4$. This yields frequency fluctuations

$$\sigma_{f,B} \simeq \frac{1}{\sqrt{45}} \left| \frac{\partial \Delta\mu_{\mathrm{eff}}}{\partial B} \right| B_n^2, \qquad \sigma_{f,E} \simeq \frac{1}{\sqrt{45}} \left| \frac{\partial \Delta d_{\mathrm{eff}}}{\partial E} \right| E_n^2. \tag{5.15}$$

A noticeable contrast reduction begins when $\sigma_f \sim (2\pi T)^{-1}$, consistent with the qualitative roll-off observed in Fig. 5.8. For example, taking $T \simeq 25\ \mu$s gives $(2\pi T)^{-1} \simeq 6.4$ kHz, which corresponds (using $(\partial\Delta\mu_{\mathrm{eff}}/\partial B) = 1.6\times10^{-1}$ MHz/G^2 and $(\partial\Delta d_{\mathrm{eff}}/\partial E) = 4.4\times10^{-3}$ MHz/(V/cm)^2) to the onset of contrast roll-off at $B_n \simeq 0.52$ G or $E_n \simeq 3.1$ V/cm.

For the field-sensing transition, the dominant frequency shift is linear in the applied fields,

$$\delta f \simeq \Delta\mu_{\mathrm{eff}}\delta B + \Delta d_{\mathrm{eff}}\delta E. \tag{5.16}$$

Since $\mathrm{Var}(\delta B) = B_n^2/3$ and $\mathrm{Var}(\delta E) = E_n^2/3$, the frequency fluctuation is

$$\sigma_{f,B} \simeq \Delta\mu_{\mathrm{eff}} \frac{B_n}{\sqrt{3}}, \qquad \sigma_{f,E} \simeq \Delta d_{\mathrm{eff}} \frac{E_n}{\sqrt{3}}. \tag{5.17}$$

Using experimentally measured field sensitivities $\Delta d_{\mathrm{eff}} = (0.120 \pm 0.001)$ MHz/(V/cm) and $\Delta\mu_{\mathrm{eff}} = (0.952 \pm 0.008)$ MHz/G for field-sensing transitions here gives $B_n \simeq$ 12 mG or $E_n \simeq 92$ mV/cm. Using the measured sensitivities and the applied noise amplitudes, this simple model reproduces the observed qualitative trends and provides an order-of-magnitude estimate for the noise level at which contrast begins to roll off.

5.5 Sensing the field-induced systematic shifts

Our approach also provides the tools to sense and correct field imperfections which could give rise to eEDM-mimicking systematic errors – a primary obstacle in experiments. In particular, background "non-reversing" electric and magnetic fields ($\mathcal{E}_{nr}$, $\mathcal{B}_{nr}$) which do not change when the applied fields are purposefully reversed are a common concern. Here, we show that alternating between EDM-clock transition and field-sensing transition measurements can sense the electric and magnetic environment directly. Since the approach here uses the same rotational state in the molecule and the same lasers are used for the measurement, this approach can also be used to directly sense higher order effects which rely on the combination of multiple errors, such as those observed with ThO [93]. Since many nearby field-sensing transitions exist within the same electronic and vibrational state, alternating between EDM-clock transition and field-sensing transition is straightforward – we simply adjust the two-photon frequency detuning. In our case we change the frequency of the acousto-optic modulator which generates the two-photon detuning by ~400 kHz. Note that under our experimental conditions, the two-photon linewidth is approximately ~200 kHz. The ~400 kHz frequency shift used to address the field-sensing transition is therefore sufficient to avoid significant spectral overlap with the EDM-clock transition at the level relevant for the present demonstration;

alternative field-sensing transitions with larger spectral separations are also available if needed to avoid any potential complications from proximity in frequency. Furthermore, because the transition can be connected via linearly polarized light in the presence of a magnetic field, one can reverse the eEDM shift by reversing only the electric or magnetic field, without changing the laser polarization. Since the laser is polarized along the electric field direction, the laser does not need to be sent through the electric field plates, offering further technical advantages [93].

To isolate the eEDM shift from other shifts, we measure the transition frequency f under all combinations of three binary "switches": the electric field up/down switch ($\hat{\mathcal{E}}$), the magnetic field up/down switch ($\hat{\mathcal{B}}$), and the EDM-clock/field-sensing (magic/non-magic) switch ($\hat{\mathcal{M}}$). The EDM-clock transition and field-sensing transition employed here are shown in Fig. 5.1 (c). We then take linear combinations of these eight frequencies to form "switch channels," denoted by f^s, so that each channel singles out effects correlated with the listed switches s [93]. For instance, $f^{\mathcal{EB}}$ singles out the effects correlated with both $\hat{\mathcal{E}}$ and $\hat{\mathcal{B}}$ switches but not the $\hat{\mathcal{M}}$ switch, and contains both the genuine eEDM signal and potential eEDM-mimicking systematic effects. On the other hand, the switch channels $f^{\mathcal{ME}}$ and $f^{\mathcal{MB}}$ serve as sensitive probes of $\mathcal{E}_{nr}$ and $\mathcal{B}_{nr}$ with measured slopes $f^{\mathcal{ME}}/\mathcal{E}_{nr} = (17.2 \pm 1.5)$ kHz/(V/cm) and $f^{\mathcal{MB}}/\mathcal{B}_{nr} = (-65.6 \pm 6.4)$ kHz/G, respectively (Fig. 5.10). The uncertainties are computed from a statistical ensemble of 120 molecular pulses per data point. This enables highly sensitive measurements of the electromagnetic fields directly, using the same science state, same lasers, same preparation and readout scheme, etc., thereby providing a very robust and easy-to-implement approach to field-sensing and co-magnetometry – a feature challenging to realize with other approaches. Note that these field-sensing transitions are measured independently and used exclusively for systematic studies; to monitor electric and magnetic fields, to search for correlations that could generate EDM-mimicking effects, and to correct these effects if

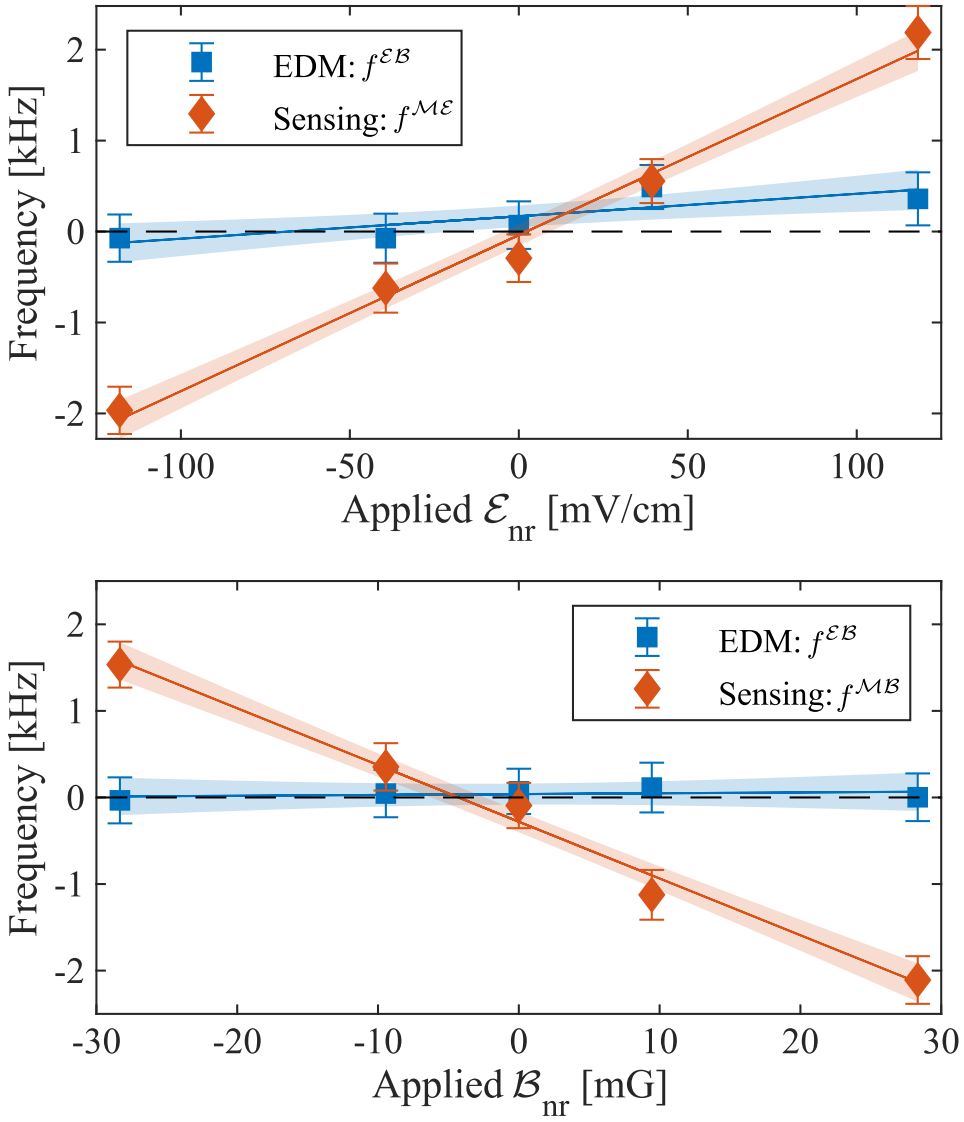

Figure 5.10: $f^{\mathcal{ME}}$, $f^{\mathcal{MB}}$, and $f^{\mathcal{EB}}$ measured at various applied $\mathcal{E}_{nr}$ and $\mathcal{B}_{nr}$. Data in (a) were taken at applied $\mathcal{B}_{nr} = 0$ G and in (b) at applied $\mathcal{E}_{nr} = 0$ V/cm. Blue (square) and orange (diamond) points represent measurements with their 1σ errors, while the corresponding blue and orange solid lines are linear fits to the data. The shaded regions indicate the uncertainty of the fit. The fit results for $f^{\mathcal{EB}}/\mathcal{E}_{nr}$ and $f^{\mathcal{EB}}/\mathcal{B}_{nr}$ are (2.5 ± 1.5) kHz/(V/cm) and (1.0 ± 6.4) kHz/G, which are smaller than that of $f^{\mathcal{ME}}/\mathcal{E}_{nr}$ and $f^{\mathcal{MB}}/\mathcal{B}_{nr}$, respectively. All the data in this figure are taken at $\mathcal{E} = 10.93$ V/cm and $\mathcal{B} = 0.30$ G. "EDM" and "Sensing" refer to the EDM-clock and field-sensing transitions, respectively.

necessary. The cadence with which measurements on the field-sensing transitions are interleaved with the EDM measurements is determined by the characteristic time scale over which relevant systematic effects are expected to vary. Slowly drifting field imperfections may require only occasional field-sensing measurements, while more rapidly varying effects need to be probed more frequently as needed, without compromising the intrinsic field insensitivity of the EDM channel.

These measured fields can then be used to shim out field imperfections, or calculate and subtract systematic errors arising from them, analogous to the approach utilized in HfF^+ [134]. Additionally, our scheme works for higher-order effects like field imperfections coupled to laser effects [93], since the same lasers are used in the $\hat{\mathcal{M}}$ switch. There are also added benefits of high sensitivity to both electric *and* magnetic fields, and the ability to directly measure them without relying on auxiliary measurements, in contrast to the scheme in ThO [93, 135]. For example, offset fields can be deliberately applied to shim out non-reversing fields by minimizing shifts in $f^{\mathcal{ME}}$ and $f^{\mathcal{MB}}$. Additionally, the false eEDM arising from a simultaneous non-reversing electric and magnetic field [93] $d_e^{\text{false}} \propto \mathcal{E}_{nr}\mathcal{B}_{nr}$ can be determined from the $f^{\mathcal{MB}}$ and $f^{\mathcal{ME}}$ channels since $\mathcal{E}_{nr}\mathcal{B}_{nr} \propto f^{\mathcal{MB}} f^{\mathcal{ME}}$. This shows that the switching between EDM-clock transitions and field-sensing transitions serve as a robust protocol against systematic effects induced by uncontrolled electromagnetic fields. Other channels such as $f^{\mathcal{E}}$, $f^{\mathcal{B}}$, $f^{\mathcal{MEB}}$ also provide additional cross-checks of the eEDM signal and stray fields. Note that while $\mathcal{E}_{nr}$ and $\mathcal{B}_{nr}$ are important cases of systematic errors that we examine in detail in this work, other systematic errors can be introduced by additional imperfections, such as field gradients and transverse fields arising from misalignment between electric field, magnetic field, and laser polarization axis, all of which require careful consideration and measurement. Importantly, a range of EDM-clock transitions and field-sensing transitions with different sensitivities to different imperfections can be selected to diagnose

and mitigate these systematic errors [65], in addition to auxiliary measurements and other standard approaches [93].

5.6 Details of the switch channels

In this section, we present a systematic analysis of switch channels to identify, characterize, and constrain potential systematic effects in the EDM measurement. We first define the switch channels employed in this work and establish the associated notation. We then discuss the expected signatures of both genuine EDM signals and dominant systematic effects in these channels based on symmetry considerations. Using these expectations, we provide order-of-magnitude estimates of relevant systematic effects and describe how corresponding corrections or bounds on them are obtained from the data. Finally, we briefly discuss additional switch channels that are not central to the present analysis but may be useful for future measurements or extended systematic studies.

Definitions of the switch channels

The transition frequency $f\left(\hat{\mathcal{M}}, \hat{\mathcal{E}}|\mathcal{E}|, \hat{\mathcal{B}}|\mathcal{B}|\right)$ is measured under each experimental configuration defined by three binary switches: transition ($\hat{\mathcal{M}}$), electric field ($\hat{\mathcal{E}}$), and magnetic field ($\hat{\mathcal{B}}$). The values of these switches are taken to be ± 1 and correspond to the two states of each parameter in which the experiment is operated: two directions of the electric field, two directions of the magnetic field, and two transitions. Here $\hat{\mathcal{E}} = \text{sign}(\boldsymbol{\mathcal{E}} \cdot \hat{\boldsymbol{Z}})$, $\hat{\mathcal{B}} = \text{sign}(\boldsymbol{\mathcal{B}} \cdot \hat{\boldsymbol{Z}})$, and $\hat{\mathcal{M}} = +1$ (-1) for the non-magic field-sensing (magic EDM-clock) transition.

We form "switch channels," denoted by f^s, where the superscript s indicates the set of switches for which the quantity is odd under reversal. This is a standard practice for eEDM experiments, and the details can be found in the literature [53], but we summarize the important points and distinctions here. These switch channels are defined as satisfying

$$
\begin{aligned}
f(\hat{\mathcal{M}},\hat{\mathcal{E}}|\mathcal{E}|,\hat{\mathcal{B}}|\mathcal{B}|) = f^{(0)}(|\mathcal{E}|,|\mathcal{B}|) &+ \hat{\mathcal{B}}\,\hat{f}^{\mathcal{B}}(|\mathcal{E}|,|\mathcal{B}|) + \hat{\mathcal{E}}\,\hat{f}^{\mathcal{E}}(|\mathcal{E}|,|\mathcal{B}|) \\
&+ \hat{\mathcal{M}}\,\hat{f}^{\mathcal{M}}(|\mathcal{E}|,|\mathcal{B}|) + \hat{\mathcal{M}}\hat{\mathcal{B}}\,\hat{f}^{\mathcal{M}\mathcal{B}}(|\mathcal{E}|,|\mathcal{B}|) \\
&+ \hat{\mathcal{M}}\hat{\mathcal{E}}\,\hat{f}^{\mathcal{M}\mathcal{E}}(|\mathcal{E}|,|\mathcal{B}|) + \hat{\mathcal{E}}\hat{\mathcal{B}}\,\hat{f}^{\mathcal{E}\mathcal{B}}(|\mathcal{E}|,|\mathcal{B}|) \\
&+ \hat{\mathcal{M}}\hat{\mathcal{E}}\hat{\mathcal{B}}\,\hat{f}^{\mathcal{M}\mathcal{E}\mathcal{B}}(|\mathcal{E}|,|\mathcal{B}|).
\end{aligned}
\tag{5.18}
$$

This is a convenient parameterization since different phases can be categorized and distinguished by their switch channels. The switch channels depend on $|\mathcal{E}|$ and $|\mathcal{B}|$, but not the switch states $(\hat{\mathcal{M}},\hat{\mathcal{E}},\hat{\mathcal{B}})$, and are calculated from the measurements by sums with either addition or subtraction depending on the switch channel, for example

$$f^{(0)} = \frac{1}{8}\sum_{\hat{\mathcal{M}},\hat{\mathcal{E}},\hat{\mathcal{B}}} f\big(\hat{\mathcal{M}},\hat{\mathcal{E}}|\mathcal{E}|,\hat{\mathcal{B}}|\mathcal{B}|\big) \tag{5.19}$$

$$f^{\mathcal{M}} = \frac{1}{8}\sum_{\hat{\mathcal{M}},\hat{\mathcal{E}},\hat{\mathcal{B}}} \hat{\mathcal{M}}\, f\big(\hat{\mathcal{M}},\hat{\mathcal{E}}|\mathcal{E}|,\hat{\mathcal{B}}|\mathcal{B}|\big) \tag{5.20}$$

$$f^{\mathcal{E}\mathcal{B}} = \frac{1}{8}\sum_{\hat{\mathcal{M}},\hat{\mathcal{E}},\hat{\mathcal{B}}} \hat{\mathcal{E}}\,\hat{\mathcal{B}}\, f\big(\hat{\mathcal{M}},\hat{\mathcal{E}}|\mathcal{E}|,\hat{\mathcal{B}}|\mathcal{B}|\big) \tag{5.21}$$

$$f^{\mathcal{M}\mathcal{E}\mathcal{B}} = \frac{1}{8}\sum_{\hat{\mathcal{M}},\hat{\mathcal{E}},\hat{\mathcal{B}}} \hat{\mathcal{M}}\,\hat{\mathcal{E}}\,\hat{\mathcal{B}}\, f\big(\hat{\mathcal{M}},\hat{\mathcal{E}}|\mathcal{E}|,\hat{\mathcal{B}}|\mathcal{B}|\big) \tag{5.22}$$

with the rest defined similarly [93]. Note that here we choose to drop the explicit dependence of switch channels on $|\mathcal{E}|$ and $|\mathcal{B}|$. Standard error propagation of f^s yields

$$\sigma_{f^s} = \frac{1}{8}\sqrt{\sum_{\hat{\mathcal{M}},\hat{\mathcal{E}},\hat{\mathcal{B}}} \sigma^2_{f(\hat{\mathcal{M}},\hat{\mathcal{E}}|\mathcal{E}|,\hat{\mathcal{B}}|\mathcal{B}|)}} := \sigma_f. \tag{5.23}$$

Here, σ_f is the same for all switch configurations s. Thus, the error of f^s is the same for all switch channels.

Expected signatures of systematic effects and EDM signals in switch channels

The transition frequency of any transition depends on electric and magnetic fields due to Stark and Zeeman effects. Since we shall examine the transition frequency of

EDM-clock transitions where the first order linear Stark and Zeeman shifts vanish or become very small, we have to include the dependence of the transition frequency on electric and magnetic fields up to second order terms. It is worth noting that when we reverse the magnetic field we drive the transition with the different sign of the M_F quantum number if we apply approximately the same frequency, such that the energies derived from the molecular, Stark, and Zeeman Hamiltonian are unchanged. We therefore express

$$f(\mathcal{E},\mathcal{B}) = C_0 + C_{\mathcal{E}}|\mathcal{E}| + C_{\mathcal{B}}|\mathcal{B}| + C_{\mathcal{E}\mathcal{B}}|\mathcal{E}\mathcal{B}| + C_{\mathcal{E}\mathcal{E}}\mathcal{E}^2 + C_{\mathcal{B}\mathcal{B}}\mathcal{B}^2 \quad (5.24)$$

$$= C_0 + C_{\mathcal{E}}\mathcal{E}\hat{\mathcal{E}} + C_{\mathcal{B}}\mathcal{B}\hat{\mathcal{B}} + C_{\mathcal{E}\mathcal{B}}\mathcal{E}\mathcal{B}\hat{\mathcal{E}}\hat{\mathcal{B}} + C_{\mathcal{E}\mathcal{E}}\mathcal{E}^2 + C_{\mathcal{B}\mathcal{B}}\mathcal{B}^2. \quad (5.25)$$

Here the transition frequency is expanded around some electric and magnetic fields ($\mathcal{E}_0$ and $\mathcal{B}_0$) that are in the vicinity of the electric and magnetic field magic points of the EDM-clock transition. C_0 correspond to the transition frequency at $\mathcal{E}_0$ and $\mathcal{B}_0$ and all other coefficients are also given at $\mathcal{E}_0$ and $\mathcal{B}_0$. (Note that here we do not assume the existence of simultaneous zero-crossings of both the electric and magnetic field sensitivities at a particular electromagnetic field point.) The absolute values are required to enforce the symmetry that in the absence of imperfections (or CP-violation) the transition energy shifts must be even under field reversals. Notice again that when we change the sign of the magnetic field we are changing the sign of the M_F quantum number if we address a transition with approximately the same frequency, so this symmetry with $\mathcal{B}$-reversal is enforced here unlike in most other eEDM experiments [93]. The symmetry under $\mathcal{E}$-reversal arises from the usual T and P symmetry of the Hamiltonian. These coefficients are determined by fitting to the calculated $\mathcal{E}$ and $\mathcal{B}$ dependence of the transitions around the predicted magic points of the EDM-clock transition, and are shown in Tab. 5.2.

To include the effects of the state switch $\hat{\mathcal{M}}$, we can define $\bar{C}_{\{\}}$ and $\delta\bar{C}_{\{\}}$ for all of the coefficients as the average and the half of the difference of the parameter $C_{\{\}}$

Table 5.2: Predicted coefficients in the electromagnetic sensitivities of the EDM-clock transition and field-sensing transition. Note that for these predictions we use spectroscopic parameters given in Tab. 5.1, which have larger uncertainties from optical spectroscopy than the experimental energy scale of ~few kHz in this work as explained above. Furthermore, the nuclear spin and rotational Zeeman terms are neglected.

Coefficient	Units	Magic	Non-magic
$C_{\mathcal{E}}$	kHz/(V/cm)	0	+45.04
$C_{\mathcal{B}}$	kHz/G	0	−197.20
$C_{\mathcal{E}\mathcal{E}}$	kHz/(V/cm)^2	+2.59	+2.61
$C_{\mathcal{B}\mathcal{B}}$	kHz/G^2	+76.91	+73.89
$C_{\mathcal{E}\mathcal{B}}$	kHz/(G×V/cm)	−30.73	−31.19

between the two transitions, respectively. For instance,

$$\bar{C}_{\mathcal{E}} = (C_{\mathcal{E}}^{\mathrm{FST}} + C_{\mathcal{E}}^{\mathrm{ECT}})/2, \qquad \delta\bar{C}_{\mathcal{E}} = (C_{\mathcal{E}}^{\mathrm{FST}} - C_{\mathcal{E}}^{\mathrm{ECT}})/2, \tag{5.26}$$

and similarly for all other parameters. Here, ECT denotes the EDM-clock transition, and FST denotes the field-sensing transition. Then, the transition frequency can be expressed as

$$\begin{aligned} f(\hat{\mathcal{M}}, \mathcal{E}, \mathcal{B}) = {} & (\bar{C}_0 + \hat{\mathcal{M}}\delta\bar{C}_0) + (\bar{C}_{\mathcal{E}} + \hat{\mathcal{M}}\delta\bar{C}_{\mathcal{E}})\mathcal{E}\hat{\mathcal{E}} \\ & + (\bar{C}_{\mathcal{B}} + \hat{\mathcal{M}}\delta\bar{C}_{\mathcal{B}})\mathcal{B}\hat{\mathcal{B}} + (\bar{C}_{\mathcal{E}\mathcal{B}} + \hat{\mathcal{M}}\delta\bar{C}_{\mathcal{E}\mathcal{B}})\mathcal{E}\mathcal{B}\hat{\mathcal{E}}\hat{\mathcal{B}} \\ & + (\bar{C}_{\mathcal{E}\mathcal{E}} + \hat{\mathcal{M}}\delta\bar{C}_{\mathcal{E}\mathcal{E}})\mathcal{E}^2 + (\bar{C}_{\mathcal{B}\mathcal{B}} + \hat{\mathcal{M}}\delta\bar{C}_{\mathcal{B}\mathcal{B}})\mathcal{B}^2. \end{aligned} \tag{5.27}$$

Notice that the field sensitivities defined in Sec. 5.6 are the first derivative of the transition frequency with respect to $\mathcal{E}$ and $\mathcal{B}$,

$$\begin{aligned} \Delta d_{\mathrm{eff}} &= \frac{\partial}{\partial\mathcal{E}} f(\hat{\mathcal{M}}, \mathcal{E}, \mathcal{B}) \\ &= (\bar{C}_{\mathcal{E}} + \hat{\mathcal{M}}\delta\bar{C}_{\mathcal{E}}) + (\bar{C}_{\mathcal{E}\mathcal{B}} + \hat{\mathcal{M}}\delta\bar{C}_{\mathcal{E}\mathcal{B}})\mathcal{B} \\ &\quad + 2(\bar{C}_{\mathcal{E}\mathcal{E}} + \hat{\mathcal{M}}\delta\bar{C}_{\mathcal{E}\mathcal{E}})\mathcal{E}, \end{aligned} \tag{5.28}$$

$$\begin{aligned} \Delta\mu_{\mathrm{eff}} &= \frac{\partial}{\partial\mathcal{B}} f(\hat{\mathcal{M}}, \mathcal{E}, \mathcal{B}) \\ &= (\bar{C}_{\mathcal{B}} + \hat{\mathcal{M}}\delta\bar{C}_{\mathcal{B}}) + (\bar{C}_{\mathcal{E}\mathcal{B}} + \hat{\mathcal{M}}\delta\bar{C}_{\mathcal{E}\mathcal{B}})\mathcal{E} \\ &\quad + 2(\bar{C}_{\mathcal{B}\mathcal{B}} + \hat{\mathcal{M}}\delta\bar{C}_{\mathcal{B}\mathcal{B}})\mathcal{B}, \end{aligned} \tag{5.29}$$

and thus their slopes (the second derivative of the transition frequency) are

$$\frac{\partial}{\partial \mathcal{E}}\Delta d_{\text{eff}} = \frac{\partial^2}{\partial^2 \mathcal{E}} f(\hat{\mathcal{M}}, \mathcal{E}, \mathcal{B}) = 2(\bar{C}_{\mathcal{E}\mathcal{E}} + \hat{\mathcal{M}}\delta\bar{C}_{\mathcal{E}\mathcal{E}}), \tag{5.30}$$

$$\frac{\partial}{\partial \mathcal{B}}\Delta \mu_{\text{eff}} = \frac{\partial^2}{\partial^2 \mathcal{B}} f(\hat{\mathcal{M}}, \mathcal{E}, \mathcal{B}) = 2(\bar{C}_{\mathcal{B}\mathcal{B}} + \hat{\mathcal{M}}\delta\bar{C}_{\mathcal{B}\mathcal{B}}). \tag{5.31}$$

The electric and magnetic fields we apply in our experiment can be expressed as $(\mathcal{E}_0 + \Delta\mathcal{E})\hat{\mathcal{E}}$ and $(\mathcal{B}_0 + \Delta\mathcal{B})\hat{\mathcal{B}}$. Here $\Delta\mathcal{E}$ and $\Delta\mathcal{B}$ are the displacements of the fields from $\mathcal{E}_0$ and $\mathcal{B}_0$. There are also non-reversing fields, which result in field magnitudes that change upon nominal reversal. Thus, the actual total fields we apply ($\mathcal{E}$ and $\mathcal{B}$) are the sum of ($\mathcal{E}_0\hat{\mathcal{E}}$ and $\mathcal{B}_0\hat{\mathcal{B}}$), displacements ($\Delta\mathcal{E}\hat{\mathcal{E}}$ and $\Delta\mathcal{B}\hat{\mathcal{B}}$) and non-reversing fields ($\mathcal{E}_{nr}$ and $\mathcal{B}_{nr}$), and we can therefore express the fields as

$$\mathcal{E} = \mathcal{E}_0\hat{\mathcal{E}} + \Delta\mathcal{E}\hat{\mathcal{E}} + \mathcal{E}_{nr}, \tag{5.32}$$

$$\mathcal{B} = \mathcal{B}_0\hat{\mathcal{B}} + \Delta\mathcal{B}\hat{\mathcal{B}} + \mathcal{B}_{nr}. \tag{5.33}$$

For clarity, we now focus only on systematic errors arising from non-reversing electric and magnetic fields, $\mathcal{E}_{nr}$ and $\mathcal{B}_{nr}$, which are some of the most common and important cases. Other imperfections, such as field gradients or transverse components introduced by misalignment of the electric field, magnetic field, and laser-polarization axes, can also produce systematic errors. The significance of these additional imperfections depends on specific details of each experiment, and any future precision measurement must examine and suppress them carefully and thoroughly. In some cases, our protocol offers sensitive electric and magnetic field probes to assist these investigations [134]. Importantly, a range of EDM-clock transitions and field-sensing transitions with different sensitivities to different imperfections can be selected to diagnose and mitigate these systematic errors.

Finally, we can include the eEDM shift $d_e\mathcal{E}_{eff}\hat{\mathcal{E}}\hat{\mathcal{B}}$. Similar to the considerations needed for the Stark and Zeeman shifts, the eEDM shift here is manifestly $\mathcal{E}$- and $\mathcal{B}$- odd since reversal of $\mathcal{B}$ also effectively means reversal of M_F and therefore the

eEDM shift. We can understand this in the following way. First, the state-dependent molecular orientation $\hat{\boldsymbol{n}}$ follows the applied electric-field direction like $\hat{\boldsymbol{n}} = \hat{\mathcal{E}}\,\hat{\boldsymbol{Z}}$. Second, we also have $\hat{\boldsymbol{S}} = \text{sign}(M_F)$ and M_F is the projection of the total angular momentum along $\hat{\boldsymbol{Z}}$ axis. Again, the magnetic field reversal means M_F reversal and therefore we have $\hat{\boldsymbol{S}} = \hat{\mathcal{B}}\,\hat{\boldsymbol{Z}}$. Finally, the Hamiltonian for the eEDM term is $d_e\mathcal{E}_{eff}\hat{\boldsymbol{S}}\cdot\hat{\boldsymbol{n}} = d_e\mathcal{E}_{eff}\hat{\mathcal{E}}\hat{\mathcal{B}}$.

Using these parameterizations, and including the eEDM shift, we can build a table of the switch channels.

Channel	Terms
$f^{(0)}$	$\Delta\mathcal{B}\bar{C}_{\mathcal{B}} + \mathcal{B}_{nr}^2\bar{C}_{\mathcal{B}\mathcal{B}} + \Delta\mathcal{B}^2\bar{C}_{\mathcal{B}\mathcal{B}} + \Delta\mathcal{E}\bar{C}_{\mathcal{E}} + \Delta\mathcal{B}\Delta\mathcal{E}\bar{C}_{\mathcal{E}\mathcal{B}} + \Delta\mathcal{E}^2\bar{C}_{\mathcal{E}\mathcal{E}} + \mathcal{E}_{nr}^2\bar{C}_{\mathcal{E}\mathcal{E}}$
$f^{\mathcal{B}}$	$\mathcal{B}_{nr}\bar{C}_{\mathcal{B}} + 2\mathcal{B}_{nr}\Delta\mathcal{B}\bar{C}_{\mathcal{B}\mathcal{B}} + \mathcal{B}_{nr}\Delta\mathcal{E}\bar{C}_{\mathcal{E}\mathcal{B}}$
$f^{\mathcal{E}}$	$\mathcal{E}_{nr}\bar{C}_{\mathcal{E}} + \Delta\mathcal{B}\mathcal{E}_{nr}\bar{C}_{\mathcal{E}\mathcal{B}} + 2\Delta\mathcal{E}\mathcal{E}_{nr}\bar{C}_{\mathcal{E}\mathcal{E}}$
$f^{\mathcal{E}\mathcal{B}}$	$\mathcal{B}_{nr}\mathcal{E}_{nr}\bar{C}_{\mathcal{E}\mathcal{B}} + d_e\mathcal{E}_{eff}$
$f^{\mathcal{M}}$	$\Delta\mathcal{B}\delta C_{\mathcal{B}} + \mathcal{B}_{nr}^2\delta C_{\mathcal{B}\mathcal{B}} + \Delta\mathcal{B}^2\delta C_{\mathcal{B}\mathcal{B}} + \Delta\mathcal{E}\delta C_{\mathcal{E}} + \Delta\mathcal{B}\Delta\mathcal{E}\delta C_{\mathcal{E}\mathcal{B}} + \Delta\mathcal{E}^2\delta C_{\mathcal{E}\mathcal{E}} + \mathcal{E}_{nr}^2\delta C_{\mathcal{E}\mathcal{E}}$
$f^{\mathcal{M}\mathcal{B}}$	$\mathcal{B}_{nr}\delta C_{\mathcal{B}} + 2\mathcal{B}_{nr}\Delta\mathcal{B}\delta C_{\mathcal{B}\mathcal{B}} + \mathcal{B}_{nr}\Delta\mathcal{E}\delta C_{\mathcal{E}\mathcal{B}}$
$f^{\mathcal{M}\mathcal{E}}$	$\mathcal{E}_{nr}\delta C_{\mathcal{E}} + \Delta\mathcal{B}\mathcal{E}_{nr}\delta C_{\mathcal{E}\mathcal{B}} + 2\Delta\mathcal{E}\mathcal{E}_{nr}\delta C_{\mathcal{E}\mathcal{E}}$
$f^{\mathcal{M}\mathcal{E}\mathcal{B}}$	$\mathcal{B}_{nr}\mathcal{E}_{nr}\delta C_{\mathcal{E}\mathcal{B}} + d_e\delta\mathcal{E}_{eff}$

Table 5.3: A table of switch channels in the general case.

For convenience we can simplify these expressions with new notation. Notice that $f^{\mathcal{B}}$ and $f^{\mathcal{M}\mathcal{B}}$ are proportional to $\mathcal{B}_{nr}$. Since the EDM-clock field sensitivities are much smaller than that of the field sensing transition, we have that $\bar{C}_{\{\}} \approx \delta C_{\{\}}$ (see eq. 5.6) for the various field sensitivity coefficients. These sensitivity to $\mathcal{B}_{nr}$ is therefore similar for these two channels, so we define $f^{\mathcal{B}} = \mathcal{B}_{nr}\mu_{\text{eff}}$ and $f^{\mathcal{M}\mathcal{B}} = \mathcal{B}_{nr}\mu_{\text{eff}}$ where $\mu_{\text{eff}} = (\bar{C}_{\mathcal{B}} + \Delta\mathcal{E}\bar{C}_{\mathcal{E}\mathcal{B}} + 2\Delta\mathcal{B}\bar{C}_{\mathcal{B}\mathcal{B}}) \approx (\delta C_{\mathcal{B}} + \Delta\mathcal{E}\delta C_{\mathcal{E}\mathcal{B}} + 2\Delta\mathcal{B}\delta C_{\mathcal{B}\mathcal{B}})$. Very similarly, we can define $f^{\mathcal{E}} = \mathcal{E}_{nr}d_{\text{eff}}$ and $f^{\mathcal{M}\mathcal{E}} = \mathcal{E}_{nr}d_{\text{eff}}$ where $d_{\text{eff}} = (\bar{C}_{\mathcal{E}} + \Delta\mathcal{B}\bar{C}_{\mathcal{E}\mathcal{B}} + 2\Delta\mathcal{E}\bar{C}_{\mathcal{E}\mathcal{E}}) \approx (\delta C_{\mathcal{E}} + \Delta\mathcal{B}\delta C_{\mathcal{E}\mathcal{B}} + 2\Delta\mathcal{E}\delta C_{\mathcal{E}\mathcal{E}})$. We can thus further simplify the table:

Channel	Terms
$f^{(0)}$	$\Delta\mathcal{B}\bar{C}_{\mathcal{B}} + \mathcal{B}_{nr}^2\bar{C}_{\mathcal{B}\mathcal{B}} + \Delta\mathcal{B}^2\bar{C}_{\mathcal{B}\mathcal{B}} + \Delta\mathcal{E}\bar{C}_{\mathcal{E}} + \Delta\mathcal{B}\Delta\mathcal{E}\bar{C}_{\mathcal{E}\mathcal{B}} + \Delta\mathcal{E}^2\bar{C}_{\mathcal{E}\mathcal{E}} + \mathcal{E}_{nr}^2\bar{C}_{\mathcal{E}\mathcal{E}}$
$f^{\mathcal{B}}$	$\mathcal{B}_{nr}\mu_{\text{eff}}$
$f^{\mathcal{E}}$	$\mathcal{E}_{nr}d_{\text{eff}}$
$f^{\mathcal{E}\mathcal{B}}$	$\mathcal{B}_{nr}\mathcal{E}_{nr}\bar{C}_{\mathcal{E}\mathcal{B}} + d_e\bar{\mathcal{E}}_{eff}$
$f^{\mathcal{M}}$	$\Delta\mathcal{B}\delta C_{\mathcal{B}} + \mathcal{B}_{nr}^2\delta C_{\mathcal{B}\mathcal{B}} + \Delta\mathcal{B}^2\delta C_{\mathcal{B}\mathcal{B}} + \Delta\mathcal{E}\delta C_{\mathcal{E}} + \Delta\mathcal{B}\Delta\mathcal{E}\delta C_{\mathcal{E}\mathcal{B}} + \Delta\mathcal{E}^2\delta C_{\mathcal{E}\mathcal{E}} + \mathcal{E}_{nr}^2\delta C_{\mathcal{E}\mathcal{E}}$
$f^{\mathcal{M}\mathcal{B}}$	$\mathcal{B}_{nr}\mu_{\text{eff}}$
$f^{\mathcal{M}\mathcal{E}}$	$\mathcal{E}_{nr}d_{\text{eff}}$
$f^{\mathcal{M}\mathcal{E}\mathcal{B}}$	$\mathcal{B}_{nr}\mathcal{E}_{nr}\delta\bar{C}_{\mathcal{E}\mathcal{B}} + d_e\delta\bar{\mathcal{E}}_{eff}$

Table 5.4: A simplified table of switch channels.

For the specific pair of transitions considered in this chapter, the two transitions have the same $\mathcal{E}_{eff}$ to within 4%, so $\delta\bar{\mathcal{E}}_{eff} \approx 0$. Therefore we regard $f^{\mathcal{E}\mathcal{B}}$ as the "eEDM channel." Other transitions could be chosen with different relative eEDM sensitivity, providing further systematic checks of the eEDM channels.

Estimates and corrections of systematic effects

As can be seen from Table 5.4, $\mathcal{E}_{nr}$ and $\mathcal{B}_{nr}$ contribute to eEDM channel $f^{\mathcal{E}\mathcal{B}} = \bar{C}_{\mathcal{E}\mathcal{B}}\mathcal{E}_{nr}\mathcal{B}_{nr}$ and also to $f^{\mathcal{M}\mathcal{E}} = d_{\text{eff}}\mathcal{E}_{nr}$ and $f^{\mathcal{M}\mathcal{B}} = \mu_{\text{eff}}\mathcal{B}_{nr}$. Thus, $f^{\mathcal{M}\mathcal{E}}$ and $f^{\mathcal{M}\mathcal{B}}$ serve as sensitive probes of $\mathcal{E}_{nr}$ and $\mathcal{B}_{nr}$, respectively, with much larger sensitivities than the eEDM channel $f^{\mathcal{E}\mathcal{B}}$. The direct non-reversing field systematic error can be expressed in more experimentally relevant units as $\bar{C}_{\mathcal{E}\mathcal{B}} \approx 30\ \mu\text{Hz}/(\mu\text{G}\times\text{mV/cm})$, or $d_{e,false} \approx 6\times10^{-30}$ e cm/(μG×mV/cm). It is worth noting that $\bar{C}_{\mathcal{E}\mathcal{B}}$ is a parameter that depends only on molecular transition properties (but not experimental properties), and can be determined straightforwardly and independently from the slope measurements of switch channels such as $f^{\mathcal{E}\mathcal{B}}/\mathcal{E}_{nr}$ and $f^{\mathcal{E}\mathcal{B}}/\mathcal{B}_{nr}$, for example, by direct Stark and Zeeman measurements. This allows us to distinguish between the direct non-reversing field systematic error and the systematic errors arising from the complicated higher-order effects like non-reversing fields coupling to laser effects if present.

Importantly, one can correct the false eEDM contribution by using the other channels, $Q = \bar{C}_{\mathcal{E}\mathcal{B}}\mathcal{E}_{nr}\mathcal{B}_{nr} = \bar{C}_{\mathcal{E}\mathcal{B}}/(d_{\text{eff}}\mu_{\text{eff}})f^{\mathcal{M}\mathcal{E}}f^{\mathcal{M}\mathcal{B}}$. Here $d_e\bar{\mathcal{E}}_{eff} = f^{\mathcal{E}\mathcal{B}} - Q$. When

the field sensitivities and coefficients are determined with relative uncertainties of $\sigma_{d_{\rm eff}}/d_{\rm eff}, \sigma_{\mu_{\rm eff}}/\mu_{\rm eff}, \sigma_{\bar{C}_{\mathcal{EB}}}/\bar{C}_{\mathcal{EB}} < \sigma_f/f^{\mathcal{ME}}, \sigma_f/f^{\mathcal{MB}}$, error propagation yields

$$\begin{aligned}
\sigma_Q &= Q\sqrt{\left(\frac{\sigma_f}{f^{\mathcal{ME}}}\right)^2 + \left(\frac{\sigma_f}{f^{\mathcal{MB}}}\right)^2 + \left(\frac{\sigma_{\bar{C}_{\mathcal{EB}}}}{\bar{C}_{\mathcal{EB}}}\right)^2 + \left(\frac{\sigma_{d_{\rm eff}}}{d_{\rm eff}}\right)^2 + \left(\frac{\sigma_{\mu_{\rm eff}}}{\mu_{\rm eff}}\right)^2 + \frac{2\sigma_{\mathcal{EB}}}{f^{\mathcal{ME}} f^{\mathcal{MB}}}} \\
&< Q\sqrt{\left(\frac{\sigma_f}{f^{\mathcal{ME}}}\right)^2 + \left(\frac{\sigma_f}{f^{\mathcal{MB}}}\right)^2 + \left(\frac{\sigma_{\bar{C}_{\mathcal{EB}}}}{\bar{C}_{\mathcal{EB}}}\right)^2 + \left(\frac{\sigma_{d_{\rm eff}}}{d_{\rm eff}}\right)^2 + \left(\frac{\sigma_{\mu_{\rm eff}}}{\mu_{\rm eff}}\right)^2 + \frac{2\sigma_f^2}{f^{\mathcal{ME}} f^{\mathcal{MB}}}} \\
&\sim Q\sqrt{\left(\frac{\sigma_f}{f^{\mathcal{ME}}}\right)^2 + \left(\frac{\sigma_f}{f^{\mathcal{MB}}}\right)^2 + \frac{2\sigma_f^2}{f^{\mathcal{ME}} f^{\mathcal{MB}}}} \\
&= \frac{\bar{C}_{\mathcal{EB}}}{d_{\rm eff}\mu_{\rm eff}}\sqrt{(f^{\mathcal{ME}} f^{\mathcal{MB}}\sigma_f)^2\left\{\left(\frac{1}{f^{\mathcal{ME}}}\right)^2 + \left(\frac{1}{f^{\mathcal{MB}}}\right)^2 + \frac{2}{f^{\mathcal{ME}} f^{\mathcal{MB}}}\right\}} \\
&= \frac{\bar{C}_{\mathcal{EB}}}{d_{\rm eff}\mu_{\rm eff}}\sqrt{\left(f^{\mathcal{ME}}\right)^2 + \left(f^{\mathcal{MB}}\right)^2 + 2f^{\mathcal{ME}} f^{\mathcal{MB}}}\,\sigma_f \\
&\sim 8\times 10^{-6}[\frac{1}{\rm Hz}]\sqrt{\left(f^{\mathcal{ME}}\right)^2 + \left(f^{\mathcal{MB}}\right)^2 + 2f^{\mathcal{ME}} f^{\mathcal{MB}}}\,\sigma_f \\
&\ll \sigma_f .
\end{aligned} \tag{5.34}$$

Thus, σ_Q is suppressed compared to σ_f. Here, in eq. (22), we use $f^{\mathcal{MB}}, f^{\mathcal{ME}} \ll 100$ kHz. In eq. (17), $\sigma_{\mathcal{EB}}$ is the covariance of $f^{\mathcal{ME}}$ and $f^{\mathcal{MB}}$, and follows

$$\begin{aligned}
\sigma_{\mathcal{EB}} &= \frac{1}{64}\Big(\sigma^2_{f(+1,+|\mathcal{E}|,+|\mathcal{B}|)} - \sigma^2_{f(+1,+|\mathcal{E}|,-|\mathcal{B}|)} - \sigma^2_{f(+1,-|\mathcal{E}|,+|\mathcal{B}|)} + \sigma^2_{f(+1,-|\mathcal{E}|,-|\mathcal{B}|)} \\
&\quad + \sigma^2_{f(-1,+|\mathcal{E}|,+|\mathcal{B}|)} - \sigma^2_{f(-1,+|\mathcal{E}|,-|\mathcal{B}|)} - \sigma^2_{f(-1,-|\mathcal{E}|,+|\mathcal{B}|)} + \sigma^2_{f(-1,-|\mathcal{E}|,-|\mathcal{B}|)}\Big) \\
&< \frac{1}{64}\sum_{\hat{\mathcal{M}},\hat{\mathcal{E}},\hat{\mathcal{B}}} \sigma^2_{f(\hat{\mathcal{M}},\hat{\mathcal{E}}|\mathcal{E}|,\hat{\mathcal{B}}|\mathcal{B}|)} = \sigma_f^2
\end{aligned} \tag{5.35}$$

or simply,

$$\sigma_{\mathcal{EB}} = \rho_{\mathcal{EB}}\sigma_{f^{\mathcal{ME}}}\sigma_{f^{\mathcal{MB}}} = \rho_{\mathcal{EB}}\sigma_f^2 \ll \sigma_f^2, \tag{5.36}$$

where $\rho_{\mathcal{EB}}$ is the correlation between $f^{\mathcal{ME}}$ and $f^{\mathcal{MB}}$ and satisfies $-1 \le \rho \le 1$. We define covariance between $f^{\mathcal{EB}}$ and Q as $\sigma_{\mathcal{EB}Q}$ and its magnitude satisfies the following,

$$\sigma_{\mathcal{EB}Q} = \rho\sigma_{f^{\mathcal{EB}}}\sigma_Q = \rho\sigma_f\sigma_Q \leq \sigma_f\sigma_Q \ll \sigma_f^2, \tag{5.37}$$

where ρ is, again, the correlation between $f^{\mathcal{EB}}$ and Q and satisfies $-1 \leq \rho \leq 1$. Thus, the uncertainty of the term $d_e\bar{\mathcal{E}}_{eff}$ is dominated by the uncertainty of $f^{\mathcal{EB}}$, σ_f.

The high suppression of $\bar{C}_{\mathcal{EB}}/(d_{\text{eff}}\mu_{\text{eff}})$ relies on the high field sensitivities of the field-sensing transition on the order of Δd_{typ} and $\Delta\mu_{\text{typ}}$, and therefore is a general feature of field-sensing transitions. The result shows that switching between EDM-clock transitions and field-sensing transitions serves as a robust protocol against systematic effects induced by non-reversing fields. This systematic error correction protocol is very similar to that of the HfF^+ experiment [134], which has effectively suppressed systematic errors arising from these effects. Note again that all the possible additional systematic shifts in $f^{\mathcal{MB}}$, $f^{\mathcal{ME}}$, and $f^{\mathcal{EB}}$ must be thoroughly explored to measure and place limits on them, which can be assisted by our "sensing channels" such as $f^{\mathcal{ME}}$ and $f^{\mathcal{MB}}$, similarly to the HfF^+ experiment [134]. Again, a range of EDM-clock transitions and field-sensing transitions with different sensitivities to different imperfections could further assist in investigation of the systematic errors. The field-sensing transition here is chosen purely for its experimental accessibility; however, other field-sensing transitions with different eEDM and field sensitivities can be used if desired.

Other switch channels

Other channels such as $f^{\mathcal{E}}$, $f^{\mathcal{B}}$, $f^{\mathcal{MEB}}$ also provide information on $\mathcal{E}_{nr}$, $\mathcal{B}_{nr}$, and the eEDM, offering an extra cross-check of the eEDM signal and its associated systematics, which can be seen from the Fig. 5.11. Here, $f^{\mathcal{E}}$ and $f^{\mathcal{B}}$ also show sharp linear responses to $\mathcal{E}_{nr}$ and $\mathcal{B}_{nr}$ with fitted slopes of $\Delta\bar{d}_{\text{eff}} = 14.1 \pm 1.5$ kHz/(V/cm) $\sim \delta\Delta d_{\text{eff}}$ and $\Delta\bar{\mu}_{\text{eff}} = -66.3 \pm 6.4$ kHz/G $\sim \delta\Delta\mu_{\text{eff}}$, respectively, thereby serving as

Table 5.5: A table of measured (Meas.) slopes with errors (Err.) and predictions (Pred.) for the different switch parity channels versus both $\mathcal{E}_{nr}$ and $\mathcal{B}_{nr}$. The numbers in parentheses indicate prediction uncertainties from the spectroscopic parameter uncertainties.

Channel	Slope vs. $\mathcal{E}_{nr}$			Slope vs. $\mathcal{B}_{nr}$		
	Pred	Meas.	Err.	Pred	Meas.	Err.
$f^{(0)}$	0	+2.6	1.5	0	−0.61	6.4
$f^{\mathcal{B}}$	0	+1.3	1.5	−99(39)	−66	6.4
$f^{\mathcal{E}}$	+22(11)	+14	1.5	0	+6.0	6.4
$f^{\mathcal{EB}}$	0	+2.5	1.5	0	+0.96	6.4
$f^{\mathcal{M}}$	0	+0.72	1.5	0	−2.1	6.4
$f^{\mathcal{MB}}$	0	+1.1	1.5	−99(39)	−66	6.4
$f^{\mathcal{ME}}$	+22(11)	+17	1.5	0	−6.1	6.4
$f^{\mathcal{MEB}}$	0	−0.83	1.5	0	+1.3	6.4
Units:	Hz/(mV/cm)			Hz/mG		

another independent probe of $\mathcal{E}_{nr}$ and $\mathcal{B}_{nr}$.

5.7 Discussion and Conclusions

In summary, we present the first experimental demonstration of engineered clock transitions that simultaneously suppress the sensitivities to electric and magnetic fields by orders-of-magnitude, enable sensing of the electromagnetic environment, and offer high sensitivity to a wide range of new physics, including fundamental symmetry violations and dark matter. The protocol is versatile and well-suited for a wide range of species, including those with large angular momentum commonly encountered in nuclear CP-violation searches, such as a nuclear MQM search [75, 67, 65] and many more [136, 137, 111].

Employing our protocol in YbOH offers two key advantages. First, laser cooling and slowing can potentially increase both the usable interaction time and the detected molecule number. Direct laser cooling of YbOH has been demonstrated [138], and related work in YbF has realized ultracold, substantially brighter molecular beams and outlines pathways for beam-based precision measurements [139, 140, 141] which could reach $< 10^{-31}$ e cm sensitivity. Such methods are applicable

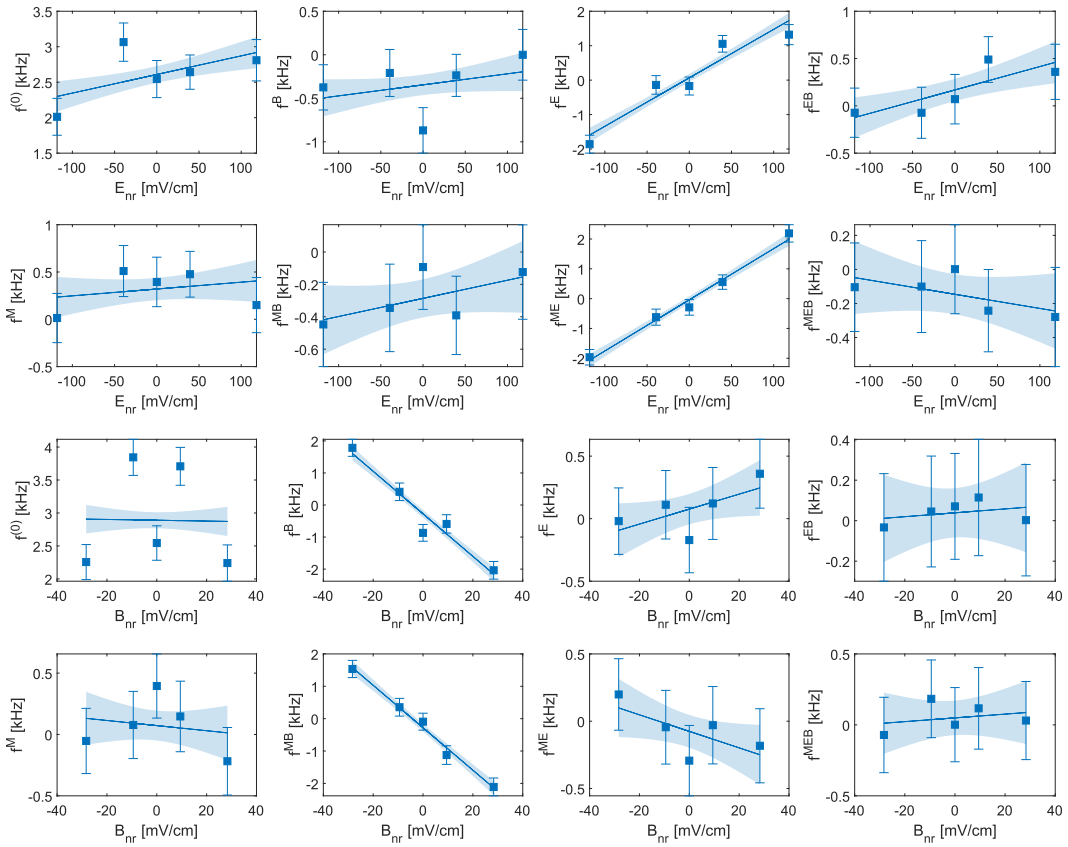

Figure 5.11: A plot of all switch parity channels vs. non-reversing fields. Note that the (0) channel is susceptible to overall drifts and is therefore expected to be noisy [89].

to YbOH, offering potential eEDM constraint comparable to YbF assuming the same experimental conditions, but with the added benefits of field-insensitive measurements schemes and tunable electromagnetic moments available at much lower electric fields by roughly three orders of magnitude, like those demonstrated here, thanks to the parity doublets. This reduction of required electric fields for field insensitivity and robustness against systematic errors is important as statistical sensitivity improves, and will be useful when implementing new approaches such as optical dipole trapping for even further sensitivity improvements. Second, YbOH is a compelling platform for the study of nuclear symmetry violation, where these EDM-clock transitions provide relatively straightforward measurement protocols even in species with very complex hyperfine structure [65]. Our current efforts

with this apparatus are focused on searching for the MQM in ^{173}YbOH using this EDM-clock approach, as discussed in chapter 6.

Similar magnetically insensitive transitions have been demonstrated in rare-earth–ion-doped crystals [142] and our scheme could be adopted for solid state dark matter and CP-violation searches [121]. The tunability of field sensitivities via application of external fields, combined with ultracold assembly or electromagnetic control techniques (electric and magnetic guiding, opto-electrical and ion trapping), could extend the protocol to non-laser-coolable species in symmetry-violation searches [143, 144, 145]. Looking forward, these EDM-clock transitions could be also combined with quantum-enhanced protocols to further boost sensitivity to CP-violating signals while retaining suppression of field sensitivities, and the present work establishes the transition-engineering and control tools needed for such future extensions [146]. Beyond these applications in fundamental nuclear and particle physics, engineered clock transitions in polarized molecules naturally offer long interaction times with long-range dipole–dipole interactions, and thus could benefit molecular quantum simulation and computation [85, 82, 145, 147] and ultracold chemistry [148]. Our demonstration, together with these prospects, suggests that engineered clock transitions can suppress decoherence and systematic errors across diverse platforms, holding promise for molecular quantum science and fundamental physics.

Chapter 6

Coherent Control of ^{173}YbOH for Magnetic Quadrupole Moment Searches

6.1 Introduction

While the eEDM is primarily sensitive to new physics in the lepton sector, the NSM and MQM provide especially strong probes of hadronic and nuclear sources of CP violation as explained in chap. 1.5. In particular, deformed nuclei are predicted to exhibit substantially enhanced NSM and MQM, making heavy polar molecules with parity doublets and deformed nuclei especially attractive platforms for probing nuclear symmetry violation.

Among such species, ^{173}YbOH is a particularly compelling candidate. The ^{173}Yb nucleus is heavy, has nuclear spin $I = 5/2$, and exhibits quadrupole deformation, leading to more enhanced sensitivity of the MQM to underlying CP-violating parameters such as $\bar{\theta}_{\mathrm{QCD}}$, the quark EDM, and the quark chromo-EDM by roughly an order of magnitude than the spherical nuclei. The OH ligand makes YbOH strongly polar, providing the internal molecular electromagnetic environment needed to convert an MQM into a measurable energy shift. In addition, the polyatomic nature

of YbOH offers mechanical vibrational bending mode that supports closely spaced opposite-parity states, enabling polarization in laboratory electric fields of only $\sim$ 10–100 V/cm. YbOH is also compatible with advanced control techniques developed for precision measurements: direct laser cooling has already been demonstrated in YbOH [138], and related work in YbF has realized substantially brighter and colder molecular beams while establishing routes to beam-based spin-precession measurements [139, 140, 141]. These advances suggest a path toward YbOH-based measurements with competitive sensitivity available at 2-3 orders-of-magnitude lower electric-fields than laser-coolable diatomics and with robust methods to sense and reject systematic errors.

Despite this promise, MQM searches pose a distinct experimental challenge. Sensitivity to the MQM requires nuclei with $I \geq 1$ and molecular states with nonzero electronic spin, which naturally leads to complicated hyperfine structure. In molecules, this complexity makes state preparation, coherent control, and readout substantially more difficult than in atomic searches. Indeed, the only experimental constraint on a nuclear MQM to date comes from Cs. Realizing a molecular MQM search therefore requires establishing precise quantum state control within a dense hyperfine manifold and identifying practical optical pathways for state preparation and detection.

In this chapter, we discuss the demonstration of state preparation, coherent control, and readout on MQM-sensitive states in the $\tilde{X}^2\Sigma^+(01^10)$ manifold of ^{173}YbOH, which supports parity doublets. We perform Ramsey interferometry on MQM-sensitive transitions whose magnetic-field sensitivity is suppressed by more than an order of magnitude at electric fields of a few tens of V/cm. We also identify magnetic-field-sensitive transitions and use them to implement the switching protocols needed to distinguish a genuine MQM signal from systematic backgrounds that can mimic it. Because the dense level structure of ^{173}YbOH leads to substan-

tial spectral congestion and distributes population over many hyperfine states, these capabilities rely on extensive spectroscopy. We therefore investigate two optical bands, $\tilde{X}^2\Sigma^+(000) \rightarrow \tilde{A}^2\Pi_{1/2}(01^10)$ and $\tilde{X}^2\Sigma^+(01^10) \rightarrow \tilde{A}^2\Pi_{1/2}(01^10)$ to map the relevant internal structure and identify strong transitions and favorable states for efficient preparation and readout. The identified state structure will also be useful for establishing measurement protocols for searches for nuclear-spin-dependent parity violation. Together, these results establish the quantum-control toolkit needed for nuclear symmetry violation searches in polyatomic molecules with deformed nuclei and intricate hyperfine structure.

6.2 Optical pumping transition spectroscopy

The vibrationally excited bending manifold $\tilde{X}^2\Sigma^+(01^10)$ of ^{173}YbOH contains closely spaced opposite-parity doublets (Fig. 3.1) and is therefore the science state for MQM-sensitive measurements. In a cryogenic buffer-gas beam, however, the population in $\tilde{X}^2\Sigma^+(01^10)$ is typically about an order of magnitude smaller than in $\tilde{X}^2\Sigma^+(000)$. In addition, the large hyperfine manifold arising from the ^{173}Yb nuclear spin ($I = 5/2$) and the unpaired electron distributes this population over many Zeeman sublevels. Efficient optical pumping from $\tilde{X}^2\Sigma^+(000)$ into selected states of $\tilde{X}^2\Sigma^+(01^10)$ is therefore essential.

To realize this transfer, we use the $\tilde{A}^2\Pi_{1/2}(01^10)$ manifold as an intermediate state. Because YbOH has highly diagonal Franck–Condon factors, excitation to $\tilde{A}^2\Pi_{1/2}(01^10)$ decays predominantly back to the same vibrational manifold; approximately 90% of the population returns to $\tilde{X}^2\Sigma^+(01^10)$. The branching to $\tilde{X}^2\Sigma^+(000)$ is correspondingly weak, so the $\tilde{X}^2\Sigma^+(000) \rightarrow \tilde{A}^2\Pi_{1/2}(01^10)$ transition is weak but nonetheless useful for state-selective optical pumping.

The spectroscopy apparatus follows earlier YbOH beam measurements [66, 65] and was adapted for pump–probe depletion spectroscopy (Fig. 6.2). Molecules first inter-

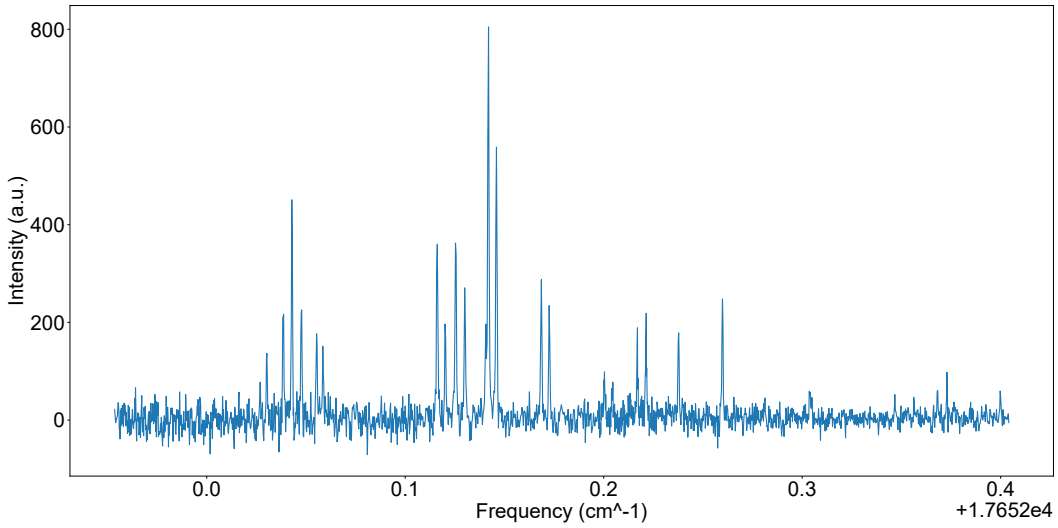

Figure 6.1: Representative upstream laser-induced-fluorescence spectrum of the $\tilde{X}^2\Sigma^+(000) \rightarrow \tilde{A}^2\Pi_{1/2}(01^10)$ optical pumping band in ^{173}YbOH. The figure shows the portion of the all recoded spectral regions.

act with an upstream pump beam that drives candidate $\tilde{X}^2\Sigma^+(000) \rightarrow \tilde{A}^2\Pi_{1/2}(01^10)$ transitions. They are then interrogated in a downstream probe region, where fluorescence on a known transition is monitored to detect pump-induced depletion. Fluorescence from both regions is collected with photomultiplier detection.

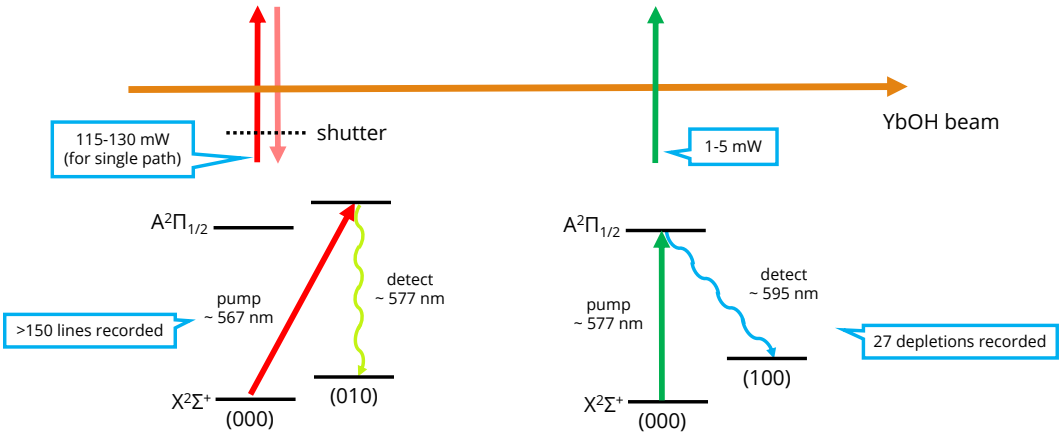

Figure 6.2: Measurement configuration used for survey and pump–probe depletion spectroscopy of the $\tilde{X}^2\Sigma^+(000) \rightarrow \tilde{A}^2\Pi_{1/2}(01^10)$ band in ^{173}YbOH. Molecules in the cryogenic buffer-gas beam propagate from left to right. In the upstream region (left), a relatively high-power laser is scanned across candidate transitions near 567 nm and fluorescence near 577 nm is collected to record the spectrum of the band. In the downstream region (right), a weaker probe laser is fixed to the known $\tilde{X}^2\Sigma^+(000) \rightarrow \tilde{A}^2\Pi_{1/2}(000)$ transition near 577 nm, and off-diagonal fluorescence to $\tilde{X}^2\Sigma^+(100)$ near 595 nm is monitored. When the scanned upstream pump and the fixed downstream probe address a common ground state, depletion of the downstream signal identifies connected transitions and enables assignment of the $\tilde{A}^2\Pi_{1/2}(01^10)$ manifold.

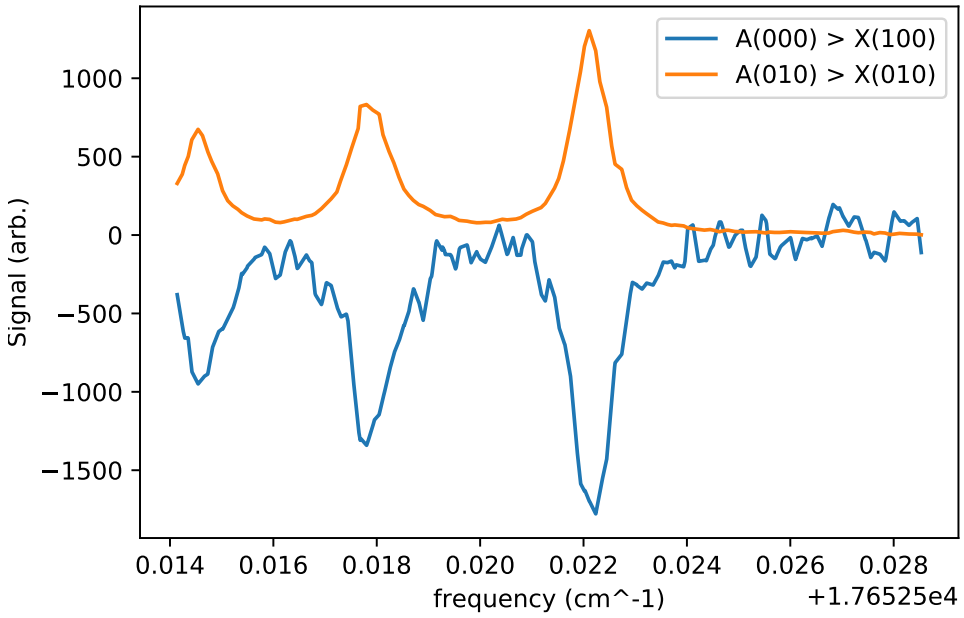

Figure 6.3: Example pump–probe depletion spectrum used to connect transitions in the $\tilde{X}^2\Sigma^+(000) \rightarrow \tilde{A}^2\Pi_{1/2}(01^10)$ band of ^{173}YbOH. The orange trace shows the upstream fluorescence signal recorded while the pump laser is scanned across candidate transitions. The blue trace shows the corresponding change in the downstream probe fluorescence, measured as the difference between the probe signal with the upstream pump shutter open and closed. Resonances that appear as increased fluorescence in the upstream region produce correlated depletion in the downstream region, demonstrating that the pump and probe address a common ground state and enabling robust line assignments.

We first recorded more than 150 lines in the $\tilde{X}^2\Sigma^+(000) \rightarrow \tilde{A}^2\Pi_{1/2}(01^10)$ band in the upstream, as shown in Fig. 6.3. To identify the underlying structure, we used combination differences referenced to the previously established $\tilde{X}^2\Sigma^+(000)$ level structure, which revealed clear recurring patterns in the spectrum. We then used pump–probe depletion spectroscopy (Fig. 6.2) to assign quantum numbers in the $\tilde{A}^2\Pi_{1/2}(01^10)$ manifold.

In the depletion measurements, the upstream pump laser was scanned across candidate transitions, while the downstream probe was fixed to the $\tilde{X}^2\Sigma^+(000) \rightarrow \tilde{A}^2\Pi_{1/2}(000)$ transition at 577 nm, with detection of off-diagonal fluorescence to $\tilde{X}^2\Sigma^+(100)$ at 595 nm. When the pump and probe addressed a common ground state, increased fluorescence in the pump region was accompanied by reduced fluorescence in the probe region (Fig. 6.3). This correlated signal provided a robust way to connect transitions and establish assignments. The observed line positions and their ground assignments are presented in Tab. 6.1.

Motivated by previous work showing that the corresponding $\tilde{A}^2\Pi_{1/2}(01^10)$ manifold in ^{174}YbOH is well described by an effective Hund's case (b) picture, we analyzed the ^{173}YbOH data within the same framework. This provided a useful organizing principle for the observed spectra and enabled assignment of the $\tilde{A}^2\Pi_{1/2}(01^10)$ structure shown in Fig. 6.4.

Table 6.1: Observed transitions on $\tilde{X}^2\Sigma^+(000) \rightarrow \tilde{A}^2\Pi_{1/2}(01^10)$ band with ground state quantum numbers (N'', G'', F_1'', p'') assigned via correlated depletion signals. The rightmost column gives the measured transition frequency.

N''	G''	F_1''	p''	Frequency (cm^{-1})
0	2	2	+	17651.7508
0	2	2	+	17651.7595
0	2	2	+	17651.7647
0	2	2	+	17652.5145
0	2	2	+	17652.5180
0	2	2	+	17652.5220
0	3	3	+	17651.9299
0	3	3	+	17651.9398
0	3	3	+	17652.7070
0	3	3	+	17652.7110
0	3	3	+	17652.7155
1	2	1	−	17650.8458
1	2	1	−	17651.2715
1	2	1	−	17651.2765
1	2	2	−	17651.2914
1	2	2	−	17651.3050
1	3	3	−	17651.0659
1	3	3	−	17651.0745
1	3	3	−	17651.4729
1	3	3	−	17652.2599
1	3	4	−	17651.0525
1	3	4	−	17651.4505
1	3	4	−	17652.2377
2	2	2	+	17649.8998
2	2	3	+	17649.9063
2	2	3	+	17649.9158

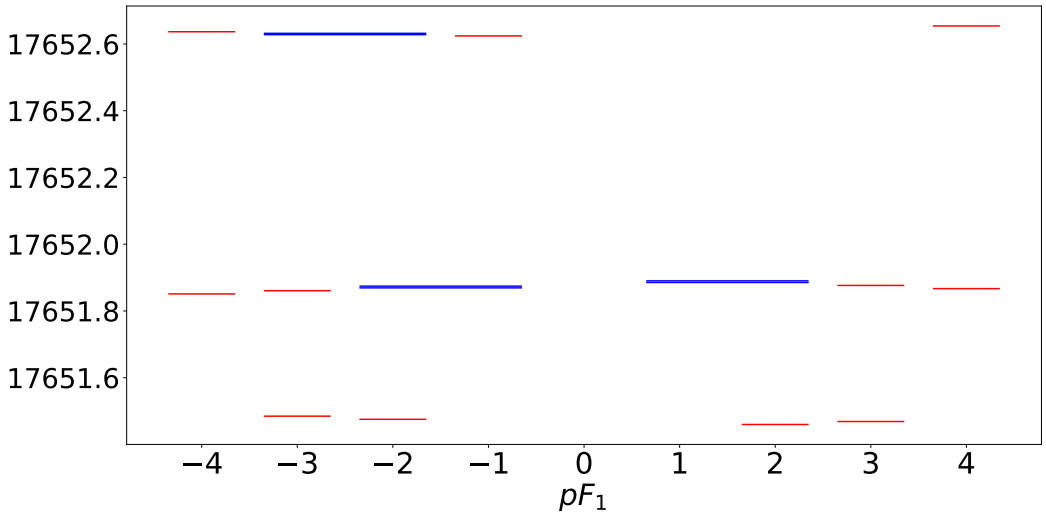

Figure 6.4: Assigned level positions of the $\tilde{A}^2\Pi_{1/2}(01^10)$ manifold in ^{173}YbOH. The horizontal position of each level is labeled by pF_1, i.e. the product of the state parity $p = \pm$ and the hyperfine quantum number F_1, rather than by F_1 alone. Red levels correspond to assignments finalized using the correlated pump–probe depletion measurements. Blue levels indicate states for which two assignments remain possible within the present analysis.

6.3 Detection transition spectroscopy

Having assigned the structure of the $\tilde{A}^2\Pi_{1/2}(01^10)$ manifold, we next identified a practical readout pathway. Previous spectroscopy of the $\tilde{X}^2\Sigma^+(01^10) \rightarrow \tilde{A}^2\Pi_{1/2}(000)$ band in ^{171,173,174}YbOH established the molecular constants of the $\tilde{X}^2\Sigma^+(01^10)$ state [66, 65], and in principle this band could also be used for state readout. In practice, however, this transition is vibrationally forbidden and therefore weak [66]. Efficient excitation requires relatively high laser power of $\sim$ 50 mW, which leads to substantial scattered light at the detector. This is particularly problematic because the excitation wavelength ($\sim$ 588 nm) lies close to the main fluorescence wavelength ($\sim$ 577 nm), making it difficult to suppress scattered pump light with optical filters without also attenuating the signal. As a result, readout on this band suffers from a relatively poor signal-to-noise ratio.

We therefore turned to the $\tilde{X}^2\Sigma^+(01^10) \rightarrow \tilde{A}^2\Pi_{1/2}(01^10)$ band as the detection pathway. Because this is a diagonal vibrational transition, it is expected to have a substantially larger transition dipole moment and to provide correspondingly improved readout efficiency.

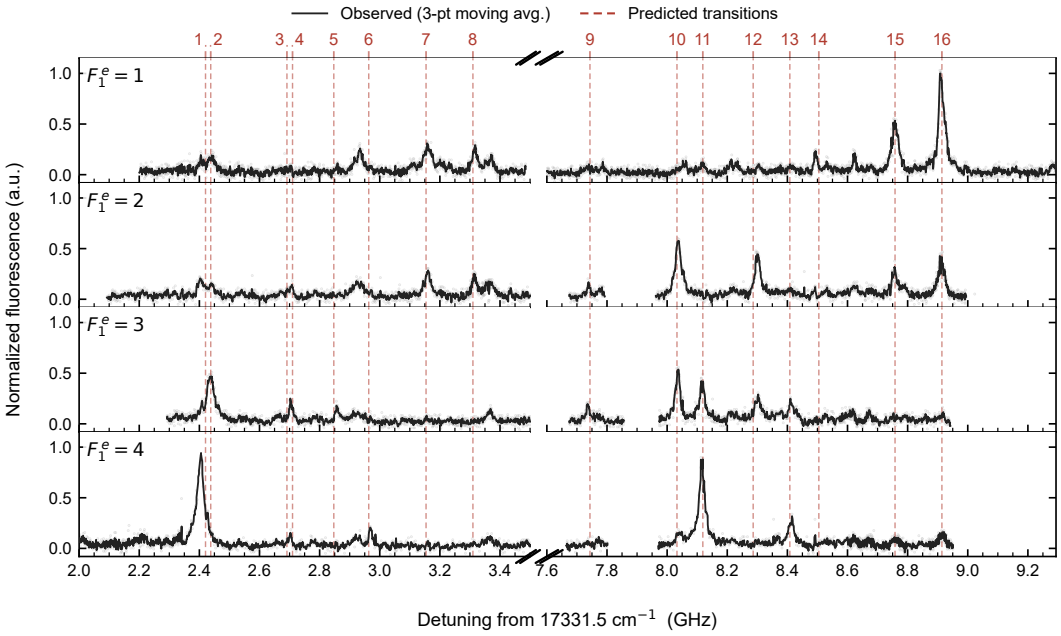

Figure 6.5: Observed and predicted spectra of the $\tilde{X}^2\Sigma^+(01^10) \rightarrow \tilde{A}^2\Pi_{1/2}(01^10)$ detection band in ^{173}YbOH. Black traces show the observed fluorescence spectra after a 3-point moving average, and gray points show the underlying data. The spectra are grouped by the excited-state quantum number F_1^e accessed in the optical-pumping step from the $\tilde{X}^2\Sigma^+(01^10), F_3^g$ state, as indicated on the left of each panel. Red dashed lines mark predicted transition positions. The red numbers above the dashed lines identify the transitions listed in Table 6.4. Several peaks remain unassigned. Because their heights do not change with the optical-pumping configuration, we expect that they arise from overtone transitions in other bands or possibly from other species. The observed peak intensities are normalized to the largest peak height, and the same vertical scaling is used for all four optical-pumping-configuration plots.

To evaluate both the optical pumping efficiency into specific states of the $\tilde{X}^2\Sigma^+(01^10)$ manifold and the strength of candidate detection transitions, we implemented a two-step pump–probe measurement. Molecules were first optically pumped upstream via the weak $\tilde{X}^2\Sigma^+(000) \rightarrow \tilde{A}^2\Pi_{1/2}(01^10)$ transition and were then interrogated downstream on the $\tilde{X}^2\Sigma^+(01^10) \rightarrow \tilde{A}^2\Pi_{1/2}(01^10)$ band while the resulting fluorescence was monitored. Since the molecular beam emerging from the cryogenic buffer-gas source has a temperature of only a few kelvin, most molecules initially occupy the lowest rotational level, $N'' = 0$, of $\tilde{X}^2\Sigma^+(000)$, with positive parity. In the upstream pumping region no electric field is applied, so parity remains a

good quantum number. We therefore drive transitions from $\tilde{X}^2\Sigma^+(000)$, $N'' = 0$, $G'' = 2, 3$, $F_1'' = 2, 3$, $p = +$, to $\tilde{A}^2\Pi_{1/2}(01^10)$, $N' = 1$, $J' = 3/2$, $F_1' = 1, 2, 3, 4$, $p = -$, which subsequently populate positive-parity states in $\tilde{X}^2\Sigma^+(01^10)$. For each upstream pumping transition, we recorded the downstream spectrum and identified the lines with the largest fluorescence signal, corresponding to the most efficient population transfer and the strongest candidate readout transitions. The resulting spectrum is shown in Fig. 6.5, and the predictions from the molecular constants provided in Tab. 6.3 are given in Tab. 6.4.

Because the $\tilde{X}^2\Sigma^+(000) \rightarrow \tilde{A}^2\Pi_{1/2}(01^10)$ pumping transition is weak, we enhanced the optical pumping efficiency by multipassing the ~ 0.8 W pump beam through the interaction region, for a total of 36 passes.

As shown in Fig. 6.5, the strongest readout signals originate from transitions from the $\tilde{X}^2\Sigma^+(01^10)$, $N'' = 0$, $G'' = 3$, $F_1'' = 3^+, 4^+$ states to $\tilde{A}^2\Pi_{1/2}(01^10)$, $N' = 1$, $J' = 3/2$, $F_1' = 3^-, 4^-$, following optical pumping on the $\tilde{X}^2\Sigma^+(000)$, $N'' = 0$, $G'' = 3, 4$, $F_1'' = 3, 4$, $p = + \rightarrow \tilde{A}^2\Pi_{1/2}(01^10)$, $N' = 1$, $J' = 3/2$, $F_1' = 3, 4$, $p = -$ transitions. We therefore choose the $\tilde{X}^2\Sigma^+(000)$, $N'' = 0$, $G'' = 4$, $F_1'' = 4$, $p = + \rightarrow \tilde{A}^2\Pi_{1/2}(01^10)$, $N' = 1$, $J' = 3/2$, $F_1' = 4$, $p = -$ line as the optical pumping pathway and use the two $\tilde{X}^2\Sigma^+(01^10) \rightarrow \tilde{A}^2\Pi_{1/2}(01^10)$ transitions above as the primary detection channels.

6.4 Two-photon spectroscopy and Ramsey interferometry

Having identified suitable readout transitions, we next drive two-photon Raman transitions between the $\tilde{X}^2\Sigma^+(01^10)$, $N'' = 1$, $G'' = 3$, $F_1'' = 4$, $p = +$ and $\tilde{X}^2\Sigma^+(01^10)$, $N'' = 1$, $G'' = 3$, $F_1'' = 3$, $p = +$ manifolds at various electric and magnetic fields to identify transitions with large MQM sensitivity.

The two-photon Raman transitions are driven by laser light containing two frequencies whose beat note addresses the transition of interest. The light is detuned

by approximately 1 GHz from the $|\tilde{X}(010)\rangle \rightarrow |\tilde{A}(010)\rangle$ optical resonance, as shown in Fig. 6.6. We recorded two-photon spectra over electric and magnetic fields ranging from 0 to 40 V/cm and from 0 to 3.6 G, respectively. Some expected two-photon transitions are not observed, particularly those originating from states with small total angular-momentum projection $|M_F| < F$. This is expected: the Raman transition amplitude is given by the sum over all pathways through the excited-state manifold, and as the number of contributing pathways increases, destructive interference can suppress the net transition dipole moment. Because fewer intermediate states contribute at larger $|M_F|$, transitions involving smaller $|M_F|$ are more susceptible to such suppression. Nevertheless, as shown in Fig. 6.7, the observed spectra for transitions involving relatively large $|M_F|$ exhibit good overall structural agreement with predictions based on the molecular constants listed in Table 6.3. These transitions with relatively large $|M_F|$ typically exhibit large Stark shifts in applied electric fields and are therefore also expected to have large MQM sensitivity. The molecular constants B, γ, γ_G, q_G, p_G, b_F^{Yb}, c^{Yb}, and e^2Qq_0 were found to have little effect on the structure of the two-photon spectrum, that is, on the relative frequency separations between two-photon transitions, and instead mainly shift the overall spectrum uniformly. This is expected because these constants govern the molecular structures on energy scales much larger than the hydrogen hyperfine structure, which sets the relevant scale for the two-photon spectroscopy. We did not perform a fit on these molecular constants since the two-photon spectrum within the single band involving $\tilde{X}^2\Sigma^+(01^10)$, $N'' = 1$, $G'' = 3$, $F_1'' = 4$, $p = +$ and $\tilde{X}^2\Sigma^+(01^10)$, $N'' = 1$, $G'' = 3$, $F_1'' = 3$, $p = +$ does not provide enough data points to determine these molecular constants reliably from a fit. The constants we used in this work are broadly consistent with the values reported previously for the $\tilde{X}^2\Sigma^+(01^10)$ state in spectroscopy of the $\tilde{X}^2\Sigma^+(01^10) \rightarrow \tilde{A}^2\Pi_{1/2}(000)$ band, at the level of roughly twice the reported fit uncertainties [65]. Note that the quoted uncertainties in the previous work do not account for the relatively large

uncertainties in the $\tilde{A}^2\Pi_{1/2}(01^10)$ state inherited from earlier spectroscopy of the $\tilde{X}^2\Sigma^+(000) \rightarrow \tilde{A}^2\Pi_{1/2}(000)$ band [67]. To determine these constants uniquely, future spectroscopy on additional F_1 manifolds will be necessary.

We fitted the observed two-photon spectrum using a hydrogen hyperfine Hamiltonian containing the four hydrogen hyperfine parameters a^{H}, b_F^{H}, c^{H}, and d^{H}, together with the electric dipole moment μ_E. For the electronic $\tilde{X}^2\Sigma^+$ state, only the b_F^{H} and c^{H} terms are typically used to describe the effective Hamiltonian governing the hyperfine structure, whereas for the electronic $\tilde{A}^2\Pi_{1/2}$ state, the description usually uses only the $h_{1/2}^{\mathrm{H}}$ and d^{H} terms, where $h_{1/2}^{\mathrm{H}} = a^{\mathrm{H}} - b_F^{\mathrm{H}}/2 - c^{\mathrm{H}}/3$. In the present case, however, the relevant science state is the electronic $\tilde{X}^2\Sigma^+(01^10)$ state, but is vibronic $\tilde{A}^2\Pi_{1/2}(01^10)$ state due to the vibrational angular momentum, which is an unusual case. We therefore included all four constants in the fit. Indeed, we found that fits using only b_F^{H} and c^{H}, or only $h_{1/2}^{\mathrm{H}}$ and d^{H}, do not fully reproduce the observed two-photon spectrum. The matrix elements of the a^{H} and d^{H} terms are given by

$$
\begin{aligned}
&\langle K_0; N_0, S, I, G_0, F_{1,0}, I_H, F_0, M_0 | H_d^{(H)} | K_1; N_1, S, I, G_1, F_{1,1}, I_H, F_1, M_1 \rangle \\
&= \delta_{F_0,F_1}\, \delta_{M_0,M_1}\, (-1)^{F_{1,1}+F_0+I_H+G_0+I+1+S} \sqrt{5 I_H (I_H+1)(2I_H+1)} \\
&\quad \times \sqrt{(2F_{1,0}+1)(2F_{1,1}+1)\,(2G_0+1)(2G_1+1)\, S(S+1)(2S+1)} \\
&\quad \times \begin{Bmatrix} I_H & F_{1,1} & F_0 \\ F_{1,0} & I_H & 1 \end{Bmatrix} \begin{Bmatrix} N_0 & N_1 & 2 \\ G_0 & G_1 & 1 \\ F_{1,0} & F_{1,1} & 1 \end{Bmatrix} \begin{Bmatrix} S & G_1 & I \\ G_0 & S & 1 \end{Bmatrix} \\
&\quad \times (-1)^{N_0-K_0} \sqrt{(2N_0+1)(2N_1+1)} \sum_{q=\pm 2} \begin{pmatrix} N_0 & 2 & N_1 \\ -K_0 & q & K_1 \end{pmatrix}. \qquad (6.1)
\end{aligned}
$$

$$
\begin{aligned}
&\langle K_0; N_0, S, I, G_0, F_{1,0}, I_H, F_0, M_0 | H_a^{(H)} | K_1; N_1, S, I, G_1, F_{1,1}, I_H, F_1, M_1 \rangle \\
&= \delta_{F_0,F_1}\, \delta_{M_0,M_1}\, \delta_{G_0,G_1}\, \delta_{K_0,K_1}\, K_0\, (-1)^{N_0-K_0+2F_{1,1}+F_0+I_H+N_0+G_0+1} \\
&\quad \times \sqrt{(2N_0+1)(2N_1+1)\,(2F_{1,0}+1)(2F_{1,1}+1)\, I_H(I_H+1)(2I_H+1)} \\
&\quad \times \begin{pmatrix} N_0 & 1 & N_1 \\ -K_0 & 0 & K_1 \end{pmatrix} \begin{Bmatrix} I_H & F_{1,1} & F_0 \\ F_{1,0} & I_H & 1 \end{Bmatrix} \begin{Bmatrix} N_1 & F_{1,1} & G_0 \\ F_{1,0} & N_0 & 1 \end{Bmatrix}. \qquad (6.2)
\end{aligned}
$$

The fit results are listed in Table 6.3. At present, we do not have a complete microscopic physical interpretation of the fitted hydrogen hyperfine constants. The small fit uncertainties may indicate some degree of overfitting, but they may also reflect the fact that the present error analysis does not yet include uncertainties in the observed peak positions; incorporating those uncertainties is planned for future work. More extensive two-photon spectroscopy will also likely be needed to provide a larger data set for a more robust determination. We therefore regard the fitted parameters as tentative. Nevertheless, even substantial variations in these parameters do not significantly alter the MQM or field sensitivities of the transition with large $|M_F|$ shown in Fig. 6.10, and therefore do not affect the main conclusion of this work.

A complete list of assigned two-photon line positions, together with the corresponding predictions and residuals, is provided in Table 6.2.

Table 6.2: Summary of observed and predicted two-photon transition frequencies. The predicted frequencies and residuals are rounded to the same decimal place as the observed frequencies. Here $\Delta\nu \equiv \nu_{\text{obs}} - \nu_{\text{pred}}$. The quantum numbers F_1 and F are assigned according to the dominant component of the states participating in the transition, since these quantum numbers are no longer good in the presence of external fields.

E_z (V/cm)	ν_{obs} (MHz)	ν_{pred} (MHz)	$\Delta\nu$ (MHz)	$F_{1,0}$	F_0	M_0	$F_{1,1}$	F_1	M_1
0.0	375.678	375.779	-0.101	4.0	3.5	3.5	3.0	2.5	2.5
0.0	375.163	375.135	0.028	4.0	4.5	4.5	3.0	3.5	3.5
10.0	374.855	374.903	-0.048	4.0	3.5	3.5	3.0	2.5	2.5
10.0	374.269	374.248	0.021	4.0	4.5	4.5	3.0	3.5	3.5
10.0	374.623	374.604	0.019	4.0	4.5	3.5	3.0	3.5	2.5
20.0	371.261	371.326	-0.065	4.0	4.5	3.5	3.0	2.5	2.5
20.0	372.969	373.011	-0.042	4.0	4.5	3.5	3.0	3.5	2.5
20.0	371.942	371.909	0.033	4.0	4.5	4.5	3.0	3.5	3.5
20.0	372.766	372.761	0.005	4.0	3.5	3.5	3.0	2.5	2.5
22.0	372.328	372.282	0.046	4.0	3.5	3.5	3.0	2.5	2.5
22.0	372.522	372.555	-0.033	4.0	4.5	3.5	3.0	3.5	2.5
22.0	371.336	371.325	0.011	4.0	4.5	4.5	3.0	3.5	3.5
24.0	371.900	371.805	0.095	4.0	3.5	3.5	3.0	2.5	2.5
24.0	371.967	372.040	-0.073	4.0	4.5	3.5	3.0	3.5	2.5
24.0	370.300	370.365	-0.065	4.0	4.5	3.5	3.0	2.5	2.5
24.0	370.722	370.711	0.011	4.0	4.5	4.5	3.0	3.5	3.5
30.0	370.126	370.382	-0.256	4.0	3.5	3.5	3.0	2.5	2.5
30.0	370.563	370.382	0.181	4.0	3.5	3.5	3.0	2.5	2.5

E_z (V/cm)	ν_{obs} (MHz)	ν_{pred} (MHz)	$\Delta\nu$ (MHz)	$F_{1,0}$	F_0	M_0	$F_{1,1}$	F_1	M_1
30.0	368.758	368.722	0.036	4.0	4.5	4.5	3.0	3.5	3.5
30.0	368.558	368.563	-0.005	4.0	3.5	3.5	3.0	2.5	2.5
40.0	366.576	366.697	-0.121	4.0	3.5	3.5	3.0	3.5	2.5
40.0	365.230	365.113	0.117	4.0	4.5	4.5	3.0	3.5	3.5
40.0	365.107	365.017	0.090	4.0	3.5	3.5	3.0	2.5	2.5

We further test several of these assignments by applying small magnetic fields of a few gauss in addition to the electric field and measuring the resulting Zeeman splittings. This provides an additional discriminant, because each peak observed at nonzero electric field and zero magnetic field corresponds to two degenerate transitions with $\pm M_F$, which often have distinct magnetic-field sensitivities and therefore characteristic Zeeman splittings. An example is the two-photon spectrum measured at 24 V/cm with an additional 1.1 G magnetic field, shown in Fig. 6.8. The observed Zeeman shifts imply a magnetic-field sensitivity of $\sim \pm 0.1$ MHz/G, in good agreement with the prediction.

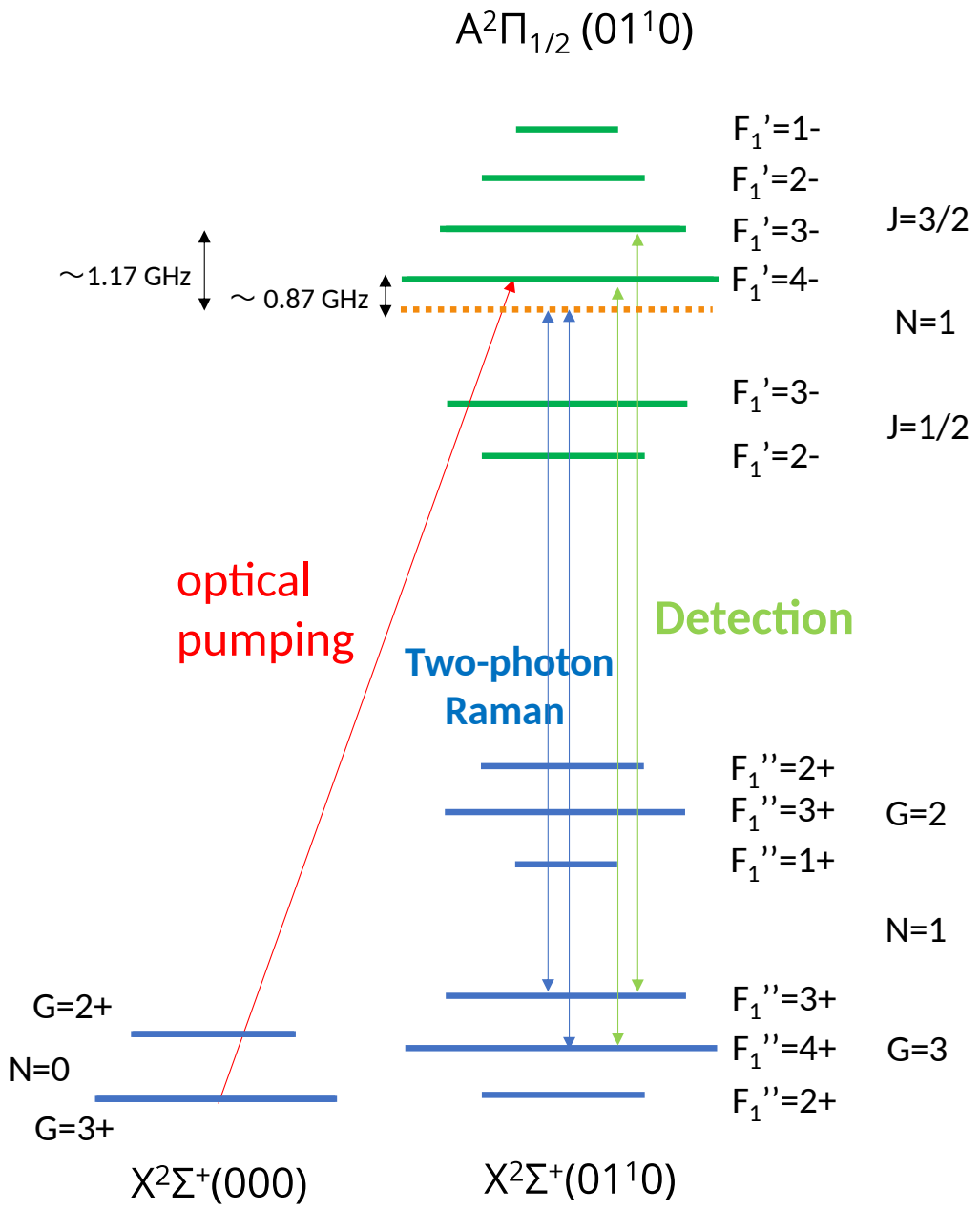

Figure 6.6: Simplified level diagram showing the optical-pumping, two-photon Raman, and detection transitions used in this work. Population is first transferred from the $\tilde{X}^2\Sigma^+(000)$ state into the $\tilde{X}^2\Sigma^+(01^10)$ manifold through the $\tilde{A}^2\Pi_{1/2}(01^10)$ state (red arrow). Population transfer between hyperfine levels in $\tilde{X}^2\Sigma^+(01^10)$ is then driven by a pair of optical frequencies whose beat note is resonant with the Raman transition, while the light is detuned by about 1 GHz from the intermediate $\tilde{A}^2\Pi_{1/2}(01^10)$ resonance (blue arrows). State-selective readout is performed on the $\tilde{X}^2\Sigma^+(01^10) \rightarrow \tilde{A}^2\Pi_{1/2}(01^10)$ detection transitions (green arrow). Note that the assignments of the quantum number F_1 for the $F_1' = 1$ and $F_1' = 2$ levels in the $J' = 1/2$ manifold of the $\tilde{A}^2\Pi_{1/2}(01^10)$ state are currently tentative; however, because these states are not involved in the present measurement scheme, this uncertainty does not affect the results reported here.

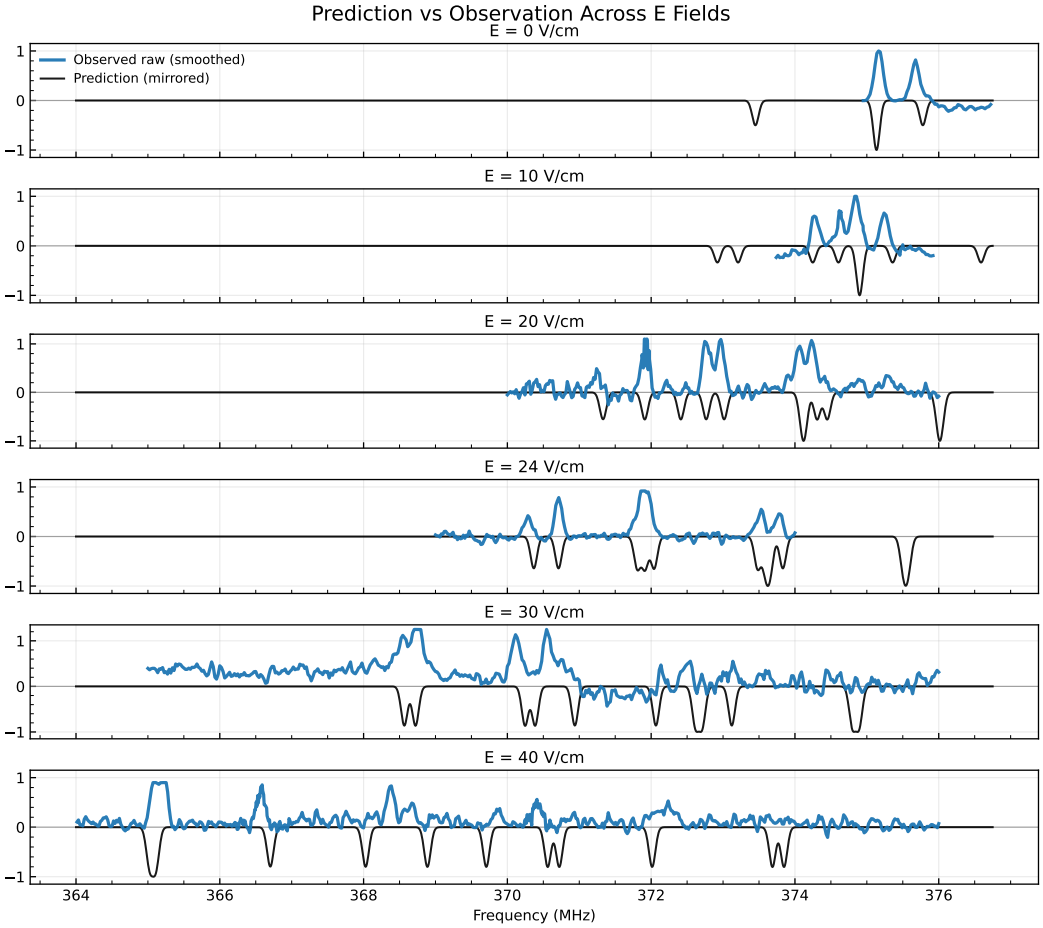

Figure 6.7: Comparison of observed and predicted two-photon Raman spectra in ^{173}YbOH at several applied electric fields. Blue traces show the measured spectra after two-point moving average, and black traces show the predicted transition pattern using the molecular constants listed in Table 6.3, mirrored about zero for clarity. The horizontal axis shows the two-photon frequency (MHz), and the vertical axis shows the normalized intensity. The data are normalized separately for the spectrum at each electric field. As the electric field is increased from 0 to 40 V/cm, transitions with relatively large $|M_F|$ exhibit sizable Stark shifts while remaining in overall structural agreement with the predictions, although some predicted lines are not observed, likely because of complications arising from the complex excited-state structure as mentioned above. The magnetic field is set to 0 G throughout this plot. As can be seen in the figure, the discrepancy between prediction and observation at 40 V/cm is larger than at lower electric fields. The origin of this difference is still under investigation, but it may indicate that the model used to describe the hydrogen hyperfine structure in the $\tilde{X}^2\Sigma^+(000)$ state requires refinement, possibly through the addition or removal of terms.

To understand the MQM and field sensitivity of this transition, we define the sensitivities to magnetic and electric fields, as well as to the eEDM, NSM, and MQM. The Hamiltonian governing the eEDM, NSM, and MQM energy shifts in a molecule interacting with external fields is [20]

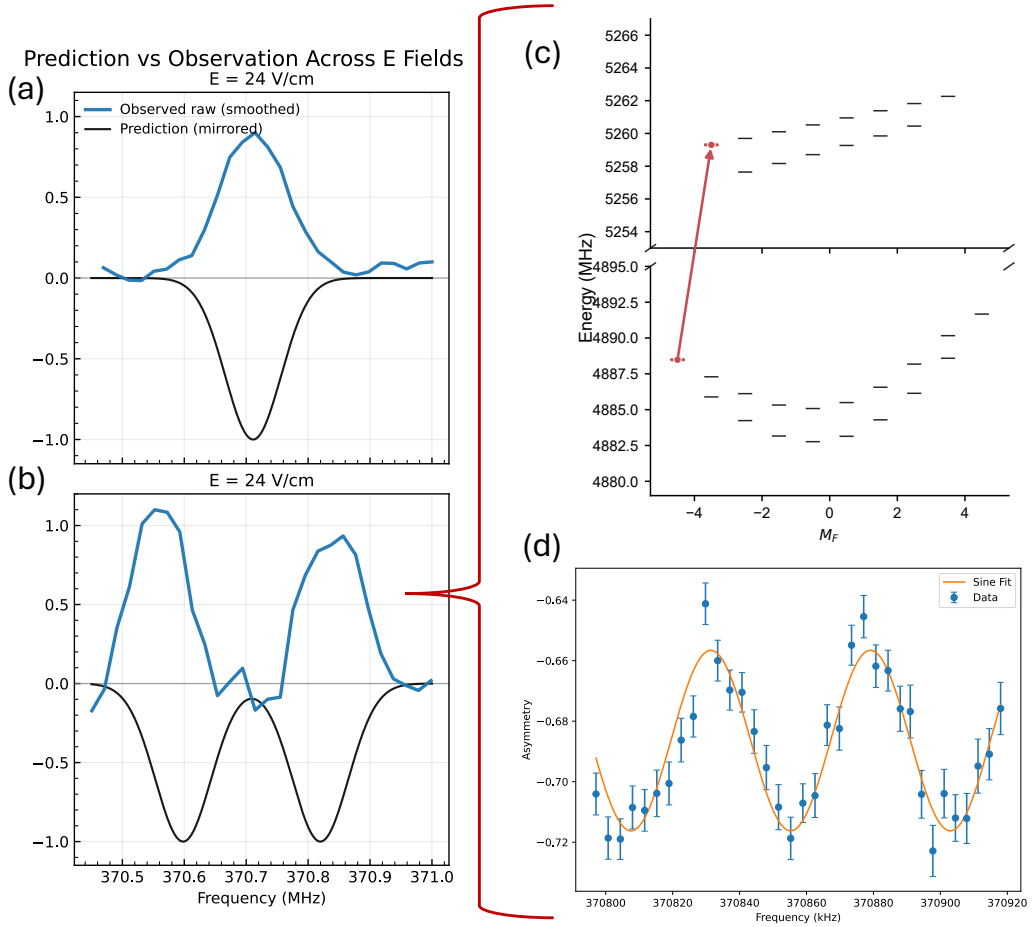

Figure 6.8: Comparison of observed and predicted two-photon spectra for a representative stretched-state transition at $E = 24$ V/cm. Panel (a) shows the measured spectrum (blue, smoothed) together with the predicted spectrum (black), mirrored for visual comparison, at $B = 0$. Panel (b) shows the corresponding comparison at $B = 1.1$ G. The applied magnetic field lifts the degeneracy between the $\pm M_F$ components and produces the characteristic Zeeman splitting used to test the assignment. Panel (c) shows the calculated Stark–Zeeman level structure in the relevant manifold; the red arrow marks the transition here. Panel (d) shows a representative Ramsey fringe recorded on this transition. The observed Zeeman splitting implies a magnetic-field sensitivity of approximately ± 0.1 MHz/G, in good agreement with the prediction.

Table 6.3: Spectroscopic parameters for the $\tilde{X}^2\Sigma^+(01^10)$ state of ^{173}YbOH. Previously obtained values are shown alongside the molecular constants used in this work.

Parameter		Ref. [65]	This work
B/MHz	Rotation	7334.1(4)	7334.1[a]
γ/MHz	Spin-rotation	−87(3)	−84[a]
γ_G/MHz	Axial spin-rotation	14(4)	23[a]
q_G/MHz	ℓ-doubling	−12.5(5)	12.5[a]
p_G/MHz	P-odd ℓ-doubling	−13(5)	0[a]
b_F^{Yb}/MHz	Yb Fermi contact	−1881.0(8)	−1882.0[a]
c^{Yb}/MHz	Yb Spin dipolar	−92(10)	−75[a]
e^2Qq_0/MHz	Quadrupole	−3322(27)	−3293[a]
b_F^{H}/MHz	H Fermi contact	–	2.204(3)
c^{H}/MHz	H spin dipolar	–	17.822(4)
a^{H}/MHz	H spin-orbital	–	2.278(2)
d^{H}/MHz	H spin dipolar (rank 2)	–	9.7368(2)
μ_E/Debye	Dipole moment	–	1.96513(3)
g_S^{eff}	Effective g-factor	–	2.07 [66]

[a] These values were not fit because the observed hydrogen hyperfine structure in the two-photon spectrum of the $\tilde{X}^2\Sigma^+(01^10)$, $N''=1$, $G''=3$, $F_1''=4$, $p=+\rightarrow$ $\tilde{X}^2\Sigma^+(01^10)$, $N''=1$, $G''=3$, $F_1''=3$, $p=+$ band is not sufficiently sensitive to them.

$$H = -D\boldsymbol{n}\cdot\boldsymbol{\mathcal{E}} - g\mu_B\boldsymbol{S}\cdot\boldsymbol{\mathcal{B}} + W_d d_e \boldsymbol{S}\cdot\boldsymbol{n} + W_Q\frac{Q}{I}\boldsymbol{I}\cdot\boldsymbol{n} - W_M\frac{M}{2I(2I-1)}\boldsymbol{S}\hat{\boldsymbol{T}}\boldsymbol{n}. \quad (6.3)$$

The first line describes the interaction with the applied electric and magnetic fields, where D is the molecular dipole moment, $\boldsymbol{n}$ is the unit vector along the molecular axis, g is the magnetic g-factor, and $\boldsymbol{S}$ is the effective electron spin. Here we define the molecular axis as the symmetry axis along which the dipole moment lies. The second line describes the CP-violating interactions: d_e is the eEDM, Q is the NSM, $\boldsymbol{I}$ is the nuclear spin, M is the MQM, and $\boldsymbol{T}$ is the rank-2 tensor operator

$T_{ij} = I_i I_j + I_j I_i - \frac{2}{3}\delta_{ij} I(I+1)$. The coefficients W_d, W_Q, and W_M characterize the electronic-structure sensitivities to the eEDM, NSM, and MQM, and are, to good approximation, the same for all states within a given electronic manifold. By contrast, $P_d \equiv \langle \boldsymbol{S} \cdot \boldsymbol{n} \rangle$, $P_Q \equiv \frac{1}{I}\langle \boldsymbol{I} \cdot \boldsymbol{n} \rangle$, and $P_M \equiv \frac{1}{2I(2I-1)}\langle \boldsymbol{S}\hat{\boldsymbol{T}}\boldsymbol{n} \rangle$ quantify the corresponding state-dependent sensitivities, since they depend on the relative orientations of $\boldsymbol{S}$, $\boldsymbol{I}$, and $\boldsymbol{n}$ in each quantum state. In this chapter, we refer to these state-dependent quantities P_d, P_Q, and P_M collectively as the "CPV sensitivities," as our discussion is restricted to transitions within a single electronic state.

With these definitions, the predicted MQM sensitivity for this transition is $P_Q = 0.061$. Having identified this MQM-sensitive transition, we perform Ramsey interferometry on it. The apparatus closely follows Ref. [115] and is detailed in the previous chapter, so we summarize only the essential features here again. As the YbOH molecules propagate through the beamline, they encounter two spatially separated Raman pulses. The first pulse prepares a superposition $|\psi\rangle \propto |0\rangle + |1\rangle$, which then evolves in the applied fields for $\tau \approx 25$ μs over a distance of ≈ 5 mm into $|\psi\rangle \propto |0\rangle + e^{i\varphi}|1\rangle$. The accumulated phase φ contains all physical contributions to the spin precession, including Stark and Zeeman shifts and possible CP-violating effects [93]. A second pulse converts this phase into population in $|0\rangle$ and $|1\rangle$, yielding $|\psi\rangle \propto \cos(\varphi/2)|0\rangle + i\sin(\varphi/2)|1\rangle$.

The phase φ is read out via laser-induced fluorescence, from which we form the asymmetry signal $\mathcal{A} = (N_0 - N_1)/(N_0 + N_1)$ and both state populations are measured using fast frequency switching [124]. This suppresses unwanted effects from beam-yield fluctuations both within a single pulse and between successive pulses. Ramsey fringes of transitions of interest are shown in Fig. 6.10. Imperfect optical pumping leaves residual population in nearby states, whose fluorescence contributes a background asymmetry $\mathcal{A}_0$ and reduces the Ramsey contrast C.

The Ramsey fringe period is approximately 46 kHz based on the fitting, corre-

sponding to an effective Ramsey precession time of about 22 μs. In principle, the precession time could be increased by increasing the separation between the two Ramsey pulses. In practice, however, we observe electric-field-dependent decoherence: for instance, when operating at $\sim$ 80 μs of precession time, as the applied electric field increases, the Ramsey fringe contrast decreases significantly around $\gtrsim$40 V/cm electric field. This effect limits the usable precession time, since extending the free-precession interval further reduces the contrast. Although Ramsey fringes remain observable for precession times up to at least $\sim$ 80 μs at $E \sim 24$ V/cm, we operate at 20 μs since it is sufficient for the proof-of-principle demonstration. In fact, in the absence of an applied electric field we have observed Ramsey fringes of $\sim$ 1 ms in ^{174}YbOH (see Fig. 6.9). We suspect that the decoherence in nonzero electric field arises from electric-field gradients associated with imperfections in the field plates, for example distortions of the thin ITO-coated glass plates or residual non-parallelism between the upper and lower plates. Because the transitions used here retain appreciable electric-field sensitivity, they are correspondingly susceptible to such gradients. This limitation could be mitigated through improved electric field plate design and alignment. More fundamentally, we can engineer field-insensitive transitions at "magic" conditions, where the transitions are insensitive to not only magnetic fields but also electric fields while remaining sensitive to MQM as demonstrated in ^{174}YbOH [115]. Such an approach can be applied to ^{173}YbOH and could directly address this issue. However, identifying suitable "magic" transitions requires more spectroscopy and is left for the future work. With these improvements, we expect that the Ramsey precession time could be extended toward the $\sim$ 1 ms scale observed in zero electric field, comparable to the spin-precession times achieved in the ACME I and II experiments.

Using the Ramsey fringe, we can determine the field sensitivities of this transition more precisely than with two-photon spectroscopy alone. The procedure for

extracting the field sensitivities from the Ramsey data is described in Ref. [115] and in the previous chapter. We measure electric- and magnetic-field sensitivities of -0.34 ± 0.07 MHz/(V/cm) and 0.13 ± 0.03 MHz/G, respectively, in good agreement with the predicted values of -0.314 MHz/(V/cm) and 0.102 MHz/G. For comparison, typical transitions have electric- and magnetic-field sensitivities set by the molecular dipole moment $D = 2.16$ Debye and the Bohr magneton μ_B [66], corresponding to ~ 1 MHz$/$(V$/$cm) and ~ 1.4 MHz$/$G, respectively. Thus, the MQM-sensitive transitions selected here exhibit about an order-of-magnitude suppression of magnetic-field sensitivity. This suppression is critical for achieving the measurement precision and accuracy as discussed in the previous section.

We finally note that in this work, AI coding assistants, including GitHub Copilot, Cursor, and Claude Code, were used to optimize the code employed for molecular-structure predictions, improving its execution speed. This speedup is critical because the calculations require diagonalization of large matrices, especially for complicated systems such as ^{173}YbOH, and we additionally took advantage of GPU acceleration for the matrix diagonalization. Because such tools can sometimes introduce hallucinations or other subtle errors that are difficult to detect, we benchmarked the predictions from the AI-assisted code against those from legacy code that we had developed before the advent of LLM-based tools, without any AI assistance. The two implementations produced identical results, giving us confidence that the predicted results reported here are correct.

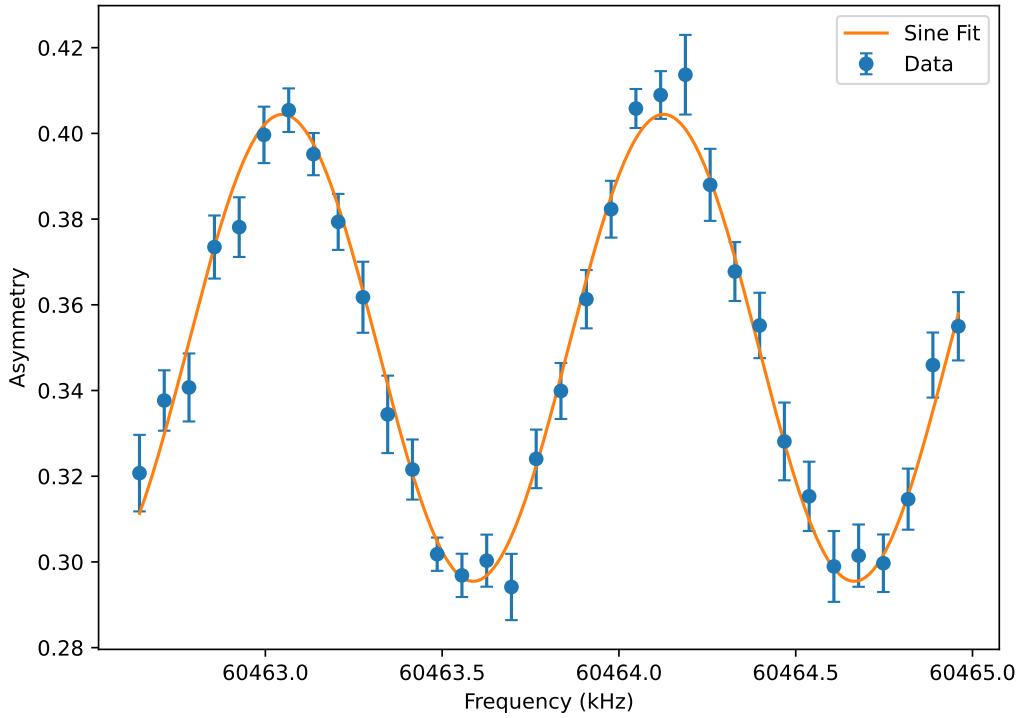

Figure 6.9: Representative Ramsey fringe observed in ^{174}YbOH in the absence of an applied electric field, demonstrating nearly millisecond-scale coherence. Blue points show the measured asymmetry as the Raman beat frequency is scanned, and the orange curve is a sinusoidal fit to the data. The fitted fringe period in frequency space is 1.078 ± 0.008 kHz, corresponding to an effective Ramsey precession time of ~ 0.928 ms.

6.5 Switching for "co-sensing" of unwanted magnetic field components

A primary challenge in any type of precision measurements is the presence of systematic errors that can mimic the true signal. In symmetry-violation searches, including MQM searches, background "non-reversing" fields that do not change when the applied fields are intentionally reversed are a common concern. In previous work with ^{174}YbOH, we demonstrated a switching protocol that alternates between a field-insensitive transition and a field-sensitive transition, enabling us to detect field imperfections that can generate systematic errors and to distinguish a genuine new-physics signal from energy shifts induced by non-reversing fields [115].

To demonstrate this protocol, we select two transitions at $E = 24$ V/cm and $B =$

3 G, shown in Fig. 6.10, as representative "field-insensitive" and "field-sensitive" transitions. Their measured electric-field sensitivities are -0.17 ± 0.03 kHz/(V/cm) and -0.16 ± 0.04 kHz/(V/cm), respectively, while their measured magnetic-field sensitivities are -0.066 ± 0.010 kHz/G and 0.14 ± 0.03 kHz/G, respectively. Note that all transitions at $E = 24$ V/cm and $B = 3$ G shown in Fig. 6.10 are predicted to have MQM sensitivities of $|P_Q| \gtrsim 0.04$.

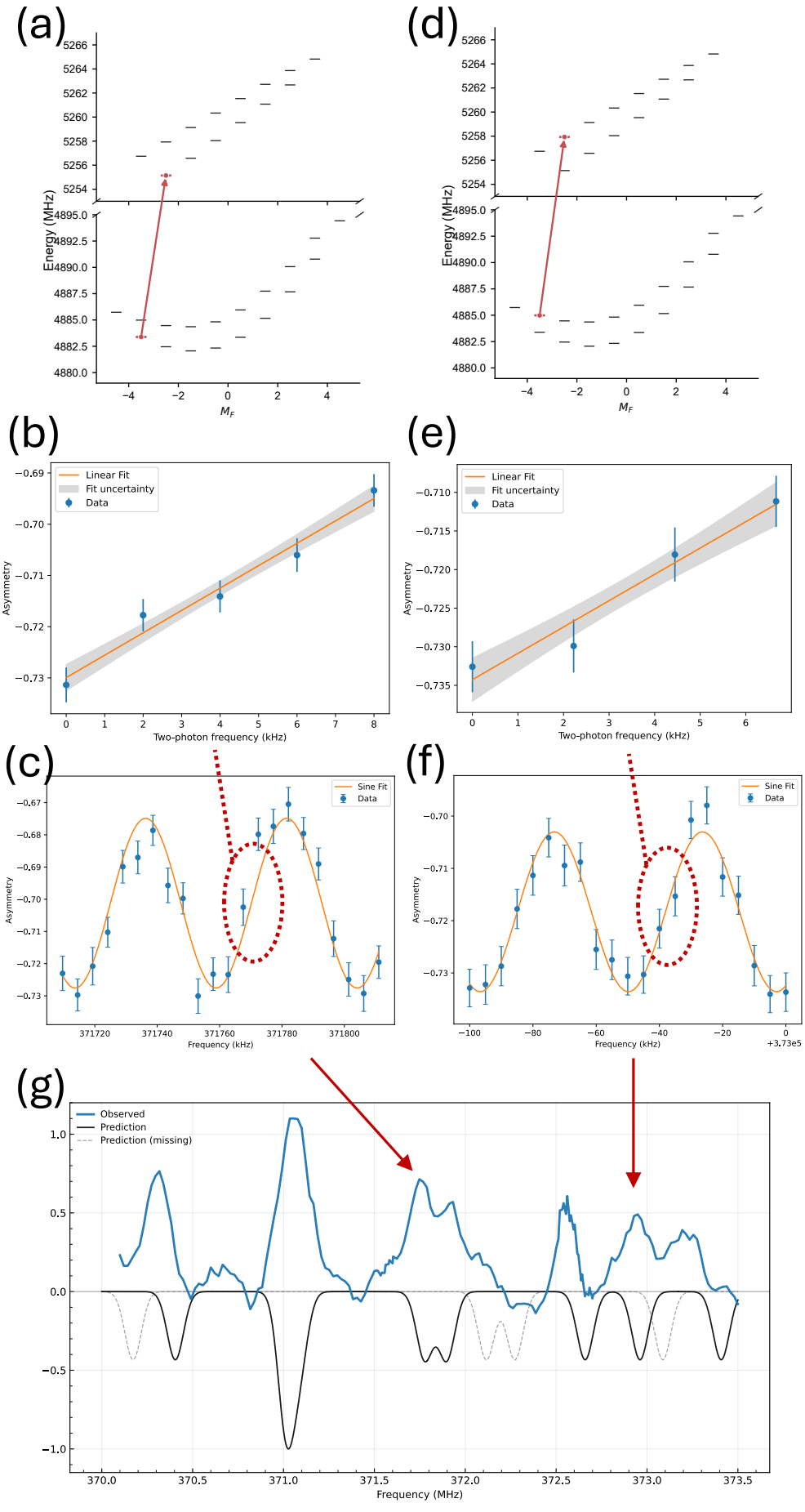
(a)
(d)
Energy (MHz)
M_F
(b)
(e)
Linear Fit
Fit uncertainty
Data
Asymmetry
Two-photon frequency (kHz)
(c)
(f)
Sine Fit
Data
Frequency (kHz)
(g)
Observed
Prediction
Prediction (missing)
Frequency (MHz)

Figure 6.10: Selection of representative "field-insensitive" and "field-sensitive" transitions used for the co-sensing protocol at $E = 24$ V/cm and $B = 3$ G. Panels (a)–(c) correspond to the field-insensitive transition and panels (d)–(f) to the field-sensitive transition. In panels (a) and (d), the red arrows indicate the selected transitions within the calculated Stark–Zeeman level structure. Note that these correspond to the current tentative assignments. Panels (b) and (e) show local linear fits used to convert the measured Ramsey asymmetry into a frequency shift near the operating point, while panels (c) and (f) show representative Ramsey-fringe data for the two selected transitions. Panel (g) compares the observed and predicted two-photon spectrum in the relevant frequency range; the red arrows mark the selected transitions used in the switching measurement.

With these two transitions, we implement the same protocol to measure the unwanted non-reversing magnetic field, as shown in Fig. 6.11. The details of the extraction procedure of the frequency shift from the observed Ramsey fringe and the switching protocol (including parity switches) are given in Ref. [115] and in the previous chapter. We also placed bounds on the possible AC Stark shift for these two transitions under the two-photon laser power used with the intensity servo and found it to be negligible. This demonstration establishes the ability to sense magnetic fields directly using the same science state, lasers, state-preparation scheme, and readout method as in the MQM measurement itself, thereby providing a robust and experimentally simple approach to field sensing and co-magnetometry—a feature that is critical for accurate MQM measurements.

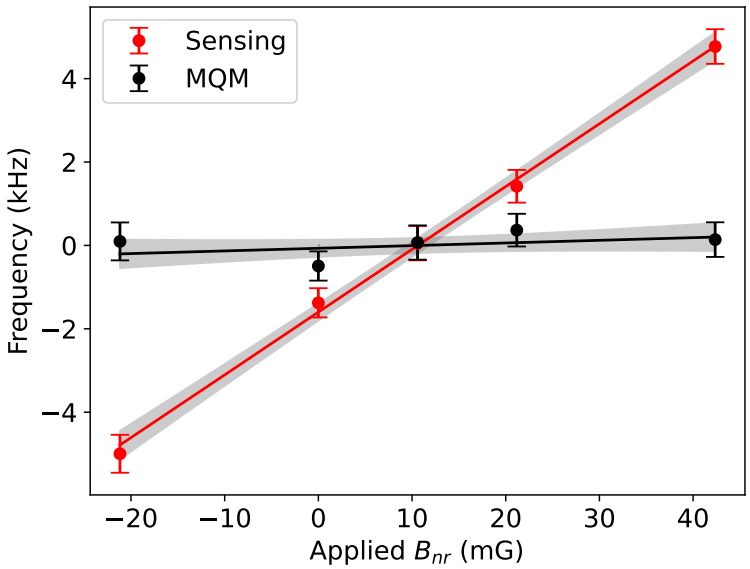

Figure 6.11: Measurements illustrating the use of switch channels to sense unwanted non-reversing magnetic fields. The extracted frequencies f^{MB} (red) and f^{MEB} (black), labeled "Sensing" and "MQM," respectively, are shown as functions of the applied non-reversing magnetic field B_{nr}. Solid lines show linear fits and the shaded bands indicate their uncertainties. The fit results for $f^{\mathcal{MEB}}/\mathcal{B}_{nr}$ and $f^{\mathcal{MB}}/\mathcal{B}_{nr}$ are (6 ± 9) and (151 ± 9) kHz/G, respectively. These measured slopes of $f^{\mathcal{MB}}/\mathcal{B}_{nr}$ are consistent with expectations from the measured magnetic field sensitivities of these transitions. The channels f^{MB} exhibit clear linear dependence on B_{nr}, whereas f^{MEB} remain comparatively insensitive, demonstrating the switching protocol used to co-sense magnetic-field systematics in the MQM measurement.

6.6 Conclusion

In this chapter, we demonstrated the key ingredients needed for an MQM search in ^{173}YbOH. We carried out extensive spectroscopy on both the optical-pumping and detection bands, together with two-photon Raman spectroscopy in the $\tilde{X}^2\Sigma^+(01^10)$ manifold, to identify practical pathways for state preparation, coherent control, and readout in this dense hyperfine system. Building on this spectroscopic outcome, we demonstrated Ramsey interferometry on the transition that remains MQM-sensitive while exhibiting substantially suppressed magnetic-field sensitivity in applied electric fields. We also demonstrated a switching protocol utilizing a magnetic-field-sensitive sensing transition, showing that unwanted non-reversing magnetic fields

can be monitored to mitigate the MQM-mimicking systematic shifts.

At the same time, the observed two-photon spectrum for transitions with relatively small M_F is not yet fully understood, and additional spectroscopy, particularly on other F_1 bands, will be needed to complete the assignments, refine the molecular constants, and identify the most favorable transitions for future measurements. Nevertheless, this incomplete understanding does not affect the assignments of the transitions with large M_F or the central conclusions of this work: we have demonstrated Ramsey interferometry on MQM-sensitive transitions in ^{173}YbOH with substantially suppressed magnetic-field sensitivity. Taken together, these results establish a robust proof-of-principle for coherent control and precise, accurate measurements in ^{173}YbOH using field-insensitive transitions, while also motivating the broader spectroscopic work needed to fully optimize this molecule for the ongoing MQM measurement.

Table 6.4: Predicted transitions in the $\tilde{X}^2\Sigma^+(01^10) \rightarrow \tilde{A}^2\Pi_{1/2}(01^10)$ detection band of ^{173}YbOH corresponding to the labeled dashed lines in Fig. 6.5. The first column gives the transition number used in the figure. $\Delta\nu$ is the detuning from 17331.5 cm^{-1}, $\tilde{\nu}$ is the absolute transition wavenumber, and the remaining columns list the assigned ground- and excited-state quantum numbers.

No.	$\Delta\nu$ (GHz)	$\tilde{\nu}$ (cm^{-1})	G''	F_1''	P''	N'	J'	F_1'	P'
1	2.4204	17331.580737	2	3	+1	1	1.5	4	−1
2	2.4378	17331.581317	2	2	+1	1	1.5	3	−1
3	2.6913	17331.589771	2	2	+1	1	1.5	2	−1
4	2.7099	17331.590392	2	3	+1	1	1.5	3	−1
5	2.8472	17331.594971	2	2	+1	1	1.5	1	−1
6	2.9634	17331.598847	2	3	+1	1	1.5	2	−1
7	3.1540	17331.605206	2	1	+1	1	1.5	2	−1
8	3.3099	17331.610406	2	1	+1	1	1.5	1	−1
9	7.7433	17331.758289	3	3	+1	1	1.5	4	−1
10	8.0328	17331.767944	3	3	+1	1	1.5	3	−1
11	8.1187	17331.770812	3	4	+1	1	1.5	4	−1
12	8.2862	17331.776398	3	3	+1	1	1.5	2	−1
13	8.4082	17331.780467	3	4	+1	1	1.5	3	−1
14	8.5046	17331.783684	3	2	+1	1	1.5	3	−1
15	8.7581	17331.792139	3	2	+1	1	1.5	2	−1
16	8.9140	17331.797339	3	2	+1	1	1.5	1	−1

Chapter 7

Conclusion and outlook

Heavy polar molecules offer an unusual combination of opportunities and challenges for precision measurements. Their large internal electromagnetic fields make them exceptionally sensitive probes of symmetry-violating physics beyond the Standard Model, but the same molecular structure that provides this sensitivity also creates substantial experimental complexity. Dense level structure, strong Stark and Zeeman responses, and the need for high-fidelity state preparation and readout all make precision measurement difficult. A central theme of this thesis has been that this complexity need not simply be tolerated: it can be engineered and exploited. In particular, the work presented here shows that molecular structure can be used to realize field-insensitive "clock" transitions that strongly suppress sensitivity to field-induced noise and systematic shifts while preserving sensitivity to the symmetry-violating observables of interest.

The first part of this thesis developed tools and physical intuition needed to build the experimental platform. Simulations of cryogenic buffer-gas beams provided a practical framework for understanding molecular extraction, beam properties, and geometric optimization of the source. That work established methods for numerically connecting the hydrodynamic behavior inside the cell to the downstream beam characteristics that matter for spectroscopy and precision measurement. In the

broader context of this thesis, these studies on CBGB form an important foundation: robust new-physics searches require not only sensitive quantum states, but also bright, cold, and reasonably slow molecular beams.

The next major step was spectroscopy of the vibrational bending mode in odd isotopologues of YbOH, especially ^{171}YbOH and ^{173}YbOH. These studies mapped the dense hyperfine structure of the $\tilde{X}^2\Sigma^+(01^10)$ manifold and established how the rotational, hyperfine, Stark, and Zeeman structure evolve in the isotopologues most relevant for symmetry-violation searches. This spectroscopy was essential because it provided the extremely useful starting point for selecting useful science states, optical-pumping pathways, and readout transitions.

A central result of the thesis is the development of a general framework for engineering field-insensitive clock transitions for symmetry-violation searches. In the theoretical work, we showed that molecules can support transitions whose electric- and magnetic-field sensitivities are dramatically reduced while their sensitivity to new physics remains large. This idea is especially important for molecular experiments, where polarization in applied fields is necessary to access symmetry-violating energy shifts, but where the same fields can also introduce decoherence and systematic error. The analysis showed that these engineered transitions are not a special feature of certain molecular structure, but rather a general and versatile resource that should be available in a wide range of species, including systems with large angular momentum and intricate hyperfine structure.

That conceptual framework was then realized experimentally in YbOH. Using Ramsey interferometry on engineered clock transitions, this thesis demonstrated the first field-insensitive clock transitions for symmetry-violation searches in a system with large sensitivity to new physics. In ^{174}YbOH, we observed suppression of electric- and magnetic-field sensitivities by at least factors of 700 and 200, respectively, while maintaining large eEDM sensitivity. Just as importantly, the same level structure

also provides transitions that are deliberately field-sensitive and can therefore be used to sense the electromagnetic environment seen by the molecules. The ability to alternate between field-insensitive science transitions and field-sensitive sensing transitions is a powerful way to reduce systematic uncertainty, and it is one of the main advantages of the approach developed here.

The final major component of this thesis extended these ideas to ^{173}YbOH, a particularly attractive molecule for searches for hadronic sources of CP violation through the nuclear magnetic quadrupole moment. Because ^{173}Yb has a large nuclear spin and a quadrupole-deformed nucleus, it offers enhanced sensitivity to MQM-induced energy shifts. At the same time, its dense hyperfine structure makes state preparation, coherent control, and readout significantly more difficult than in the even isotopologues. In this thesis, we established the essential quantum-control toolkit needed for such a measurement. This included spectroscopy of the optical-pumping and detection bands, identification of useful state-transfer and readout pathways, two-photon Raman control in the $\tilde{X}^2\Sigma^+(01^10)$ manifold, Ramsey interferometry on MQM-sensitive transitions, and switching protocols that use field-sensitive transitions to diagnose unwanted non-reversing magnetic fields. We showed that MQM-sensitive transitions in ^{173}YbOH can exhibit magnetic-field sensitivity suppressed by more than a factor of 10, demonstrating that the core logic of engineered field-insensitive measurements remains viable even in this much more complicated system.

Taken together, these results directly support the main claim emphasized in the thesis throughout: molecular structure can be engineered and controlled to make heavy polar molecules into robust quantum sensors for symmetry-violation searches. The work shows not only that field-insensitive clock transitions can be designed and demonstrated in a realistic molecule, but also that the same strategy extends to more complex nuclei and more intricate hyperfine structure. In that sense, the thesis turns molecular complexity from an obstacle into a resource. Rather than avoiding

complex species, one can use their structure to access suppressed field sensitivities, co-magnetometry, low-field polarization through parity doublets, and sensitivity to a broader class of fundamental symmetry-violating observables.

Finally, the most powerful aspect of this protocol is its versatility. As discussed in Chap. 4, the same general strategy can be applied across a wide range of molecular species, rather than being tied to a small number of unusually simple or favorable molecules. That flexibility is especially important for symmetry-violation searches, because different systems offer access to different observables, different enhancement mechanisms, and different strategies for controlling systematic error. More broadly, the underlying logic of engineering long-coherence transitions that remain sensitive to symmetry-violating observables while suppressing sensitivity to external fields is not limited to molecules. Closely related ideas can also be implemented in other quantum platforms, including optically trapped cold atoms and paramagnetic ions embedded in crystal hosts [111, 149]. If this design principle can be realized across such diverse systems, it could improve experimental sensitivity significantly not only for molecular experiments, but for symmetry-violation searches more generally: it offers a path toward combining strong intrinsic sensitivity with long coherence times, reduced susceptibility to field-induced noise, and more robust rejection of systematic effects. In that sense, engineered field-insensitive transitions should be viewed not as a molecule-specific technique, but as a broadly applicable design principle for precision measurements in complex quantum systems.

7.1 Outlook for an MQM search in ^{173}YbOH

The immediate outlook suggested by this work is a next-generation MQM measurement in ^{173}YbOH based on field-insensitive transitions. The present demonstration already shows the essential ingredients: optical pumping into the relevant bending-mode manifold, coherent state manipulation, Ramsey measurement on MQM-sensitive transitions, and construction of switch channels that can diagnose

magnetic-field-related systematics using the same molecule, state, and the same experimental sequence. The most important remaining step is to identify and implement transitions in ^{173}YbOH that are insensitive not only to magnetic fields but also, as much as possible, to electric field while retaining MQM sensitivity. Achieving that goal would directly address the electric-field-dependent decoherence seen in the current proof-of-principle measurements.

The path forward is motivated by an encouraging experimental fact already established in this thesis work: in zero applied electric field, we can observe the Ramsey precession time of nearly 1 ms in ^{174}YbOH. This suggests that the present coherence limitation is not fundamental to the molecule itself, but instead arises from the applied-field environment. If suitable field-insensitive MQM transitions can be located in ^{173}YbOH, and if the electric-field plates flatness and/or alignment are improved so that residual gradients are reduced, then extending the MQM interrogation time toward $\tau \sim 1$ ms appears realistic.

Reaching that timescale would have an important impact on statistical sensitivity. As a rough estimate, an experiment operating with an effective Ramsey time of $\tau \sim 1$ ms and an effective shot budget of $N_{\mathrm{shot}} \sim 10^6$ would reach a frequency sensitivity on the order of

$$\delta f \sim 100\ \mu\mathrm{Hz}. \tag{7.1}$$

Current bounds on hadronic CP-violating parameters correspond to MQM-induced shifts in ^{173}YbOH of roughly $\delta f \sim 10\ \mu$Hz for $\bar{\theta}_{\mathrm{QCD}} \sim 4\times10^{-11}$ and $\delta f \sim 200\ \mu$Hz for $\bar{g} g_\pi^{(2)} \sim 1.8 \times 10^{-10}$. In other words, a millisecond-scale Ramsey experiment in ^{173}YbOH would begin to probe an especially interesting regime: it would approach or overlap the frequency scale implied by existing hadronic CP-violation constraints, and it would do so in a system with a different systematic-error structure than existing atomic measurements.

This estimate should be viewed as a realistic target rather than a final projection. In practice, the ultimate sensitivity of an MQM experiment will also depend on the state-preparation efficiency, detected molecule number, duty cycle, fringe contrast, and the ability to reject non-reversing electromagnetic fields and other systematics. Several of the improvements required to reach this regime are already clearly indicated by the work in this thesis. First, more complete spectroscopy of additional F_1 manifolds in ^{173}YbOH should identify better science and sensing transitions and clarify the level assignments. Second, identifying and implementing field-insensitive transitions with suppressed sensitivity to not only magnetic field but also electric field should reduce sensitivity to electric-field gradients and thereby enable longer coherent interrogation in applied fields. Third, better optical pumping and readout should increase the usable molecule number. Finally, the broader YbOH program points toward additional future gains from brighter and colder beams, magnetic and electrical focusing and collimating, and laser cooling implementations.

More generally, the challenges encountered in ^{173}YbOH, and the ideas demonstrated here to address them, are likely to be directly useful in a broader class of heavy molecules for symmetry-violation searches. Many of the central issues in this work—dense internal structure, the need for selective state preparation and readout, sensitivity to electric- and magnetic-field inhomogeneity, and the need to distinguish genuine symmetry-violating signals from field-induced systematics—are not unique to YbOH, but are common features of many of the most promising next-generation systems. In that sense, the value of this work is not only that it advances a particular experiment in ^{173}YbOH, but also that it develops a practical set of ideas for working in similarly complex molecules. Those ideas should be relevant not only to other stable polyatomic candidates, but also to recently emerging radioactive species such as RaF and RaOH, which offer exciting opportunities for future symmetry-violation measurements [150, 151].

Appendix A

Matrix elements for $\tilde{X}^2\Sigma^+(01^10)$ state in ^{171,173}YbOH

We have derived the matrix elements for calculating the structure and CPV sensitivities of $\tilde{X}^2\Sigma^+(01^10)$ state in ^{171,173}YbOH. Here I present the matrix elements we have used to calculate the eigenstates of all Hamiltonian terms for $\tilde{X}^2\Sigma^+(01^10)$ state in ^{171,173}YbOH. The matrix elements are evaluated in the following case (b) basis. Note that $K = \Lambda + \ell = N \cdot \hat{n}$. In $\tilde{X}^2\Sigma^+(01^10)$ state, $\Lambda = 0$.

The rotation term:

$$\langle K; N, S, I, G, F_1, I_H, F, M|(N^2 - \ell^2)|K'; N', S, I, G', F_1', I_H, F', M'\rangle = \delta_{F,F'}\delta_{M,M'}\delta_{F_1,F_1'}\delta_{G,G'}\delta_{N,N'}\delta_{K,K'}\{N(N+1) - K^2\} \tag{A.1}$$

The spin-rotation term (without subtraction of axial spin-rotation term):

$$\begin{aligned}
&\langle K; N, S, I, G, F_1, I_H, F, M | T^1(N) \cdot T^1(S) | K'; N', S, I, G', F_1', I_H, F', M' \rangle \\
&\qquad = \delta_{F,F'} \delta_{M,M'} \delta_{F_1,F_1'} \delta_{K,K'} \delta_{N,N'} \\
&\qquad \times (-1)^{N'+F_1+G} \begin{Bmatrix} G' & N' & F_1 \\ N & G & 1 \end{Bmatrix} \\
&\qquad \times \sqrt{N(N+1)(2N+1)} \\
&\qquad \times (-1)^{G'+S+1+I} \sqrt{(2G+1)(2G'+1)} \begin{Bmatrix} S & G' & I \\ G & S & 1 \end{Bmatrix} \\
&\qquad \sqrt{S(S+1)(2S+1)}
\end{aligned} \tag{A.2}$$

The axial spin-rotation term:

$$\begin{aligned}
&\langle K; N, S, I, G, F_1, I_H, F, M | T^1_{q=0}(N) T^1_{q=0}(S) | K'; N', S, I, G', F_1', I_H, F', M' \rangle \\
&\qquad = \delta_{F,F'} \delta_{M,M'} \delta_{F_1,F_1'} \\
&\qquad \times (-1)^{N'+F_1+G} \begin{Bmatrix} G' & N' & F_1 \\ N & G & 1 \end{Bmatrix} \\
&\qquad \times K \times (-1)^{N-K} \begin{pmatrix} N & -K & 1 \\ 0 & N' & K' \end{pmatrix} \sqrt{(2N+1)(2N'+1)} \\
&\qquad \times (-1)^{G'+S+1+I} \sqrt{(2G+1)(2G'+1)} \begin{Bmatrix} S & G' & I \\ G & S & 1 \end{Bmatrix} \\
&\qquad \sqrt{S(S+1)(2S+1)}
\end{aligned} \tag{A.3}$$

This can be derived formally by using eq. (2.3.35) in ref. [91].

The Fermi contact (Yb) term:

$$\begin{aligned}\langle K; N, S, I, G, F_1, I_H, F, M|T^1(I)\cdot T^1(S)|K'; N', S, I, G', F_1', I_H, F', M'\rangle \\ = \delta_{F,F'}\delta_{M,M'}\delta_{F_1,F_1'}\delta_{G,G'}\delta_{N,N'}\delta_{K,K'} \\ \times (-1)^{I+G'+S}\begin{Bmatrix} S & I & G \\ I & S & 1\end{Bmatrix}\sqrt{S(S+1)(2S+1)} \\ \sqrt{I(I+1)(2I+1)}\end{aligned} \tag{A.4}$$

The Dipolar (Yb) term:

$$\begin{aligned}\langle K; N, S, I, G, F_1, I_H, F, M|T^2(I,S)\cdot T^2(n)|K'; N', S, I, G', F_1', I_H, F', M'\rangle \\ = \delta_{F,F'}\delta_{M,M'}\delta_{F_1,F_1'} \\ \times (-1)^{N'+F_1+G}\begin{Bmatrix} G' & N' & F_1 \\ N & G & 2\end{Bmatrix} \\ \times (-1)^{N-K}\sqrt{(2N+1)(2N'+1)}\begin{pmatrix} N & -K & 2 \\ 0 & N' & K'\end{pmatrix} \\ \times \sqrt{(2G+1)5(2G'+1)}\begin{Bmatrix} I & S & G' \\ 1 & 1 & 2 \\ I & S & G\end{Bmatrix} \\ \times \sqrt{S(S+1)(2S+1)}\sqrt{I(I+1)(2I+1)}\end{aligned} \tag{A.5}$$

The Fermi contact (H) term:

$$\langle K; N, S, I, G, F_1, I_H, F, M | T^1(I_H) \cdot T^1(S) | K'; N', S, I, G', F_1', I_H, F', M' \rangle$$

$$= \delta_{F,F'} \delta_{M,M'} \delta_{N,N'} \delta_{K,K'}$$

$$\times (-1)^{F_1'+F+I_H} \begin{Bmatrix} I_H & F_1' & F \\ F_1 & I_H & 1 \end{Bmatrix} \sqrt{I_H(I_H+1)(2I_H+1)}$$

$$\times (-1)^{F_1+N+1+G'} \sqrt{(2F_1+1)(2F_1'+1)} \begin{Bmatrix} G' & F_1' & N \\ F_1 & G & 1 \end{Bmatrix}$$

$$\times (-1)^{G+I+1+S} \sqrt{(2G+1)(2G'+1)} \begin{Bmatrix} S & G' & I \\ G & S & 1 \end{Bmatrix}$$

$$\sqrt{S(S+1)(2S+1)} \tag{A.6}$$

The Dipolar (H) term:

Using eq. (2.3.80) in ref. [91],

$$\langle K; N, S, I, G, F_1, I_H, F, M | T^2_{q=0}(I_H, S) | K'; N', S, I, G', F_1', I_H, F', M' \rangle$$

$$= \delta_{F,F'} \delta_{M,M'}$$

$$\times (-1)^{F_1'+F'+I_H} \begin{Bmatrix} I_H & F_1 & F' \\ F_1' & I_H & 1 \end{Bmatrix} \sqrt{I_H(I_H+1)(2I_H+1)}$$

$$\times \sqrt{(2F_1+1)5(2F_1'+1)} \begin{Bmatrix} N & N' & 2 \\ G & G' & 1 \\ F_1 & F_1' & 1 \end{Bmatrix}$$

$$\times (-1)^{N-K} \sqrt{(2N+1)(2N'+1)} \begin{pmatrix} N & -K & 2 \\ 0 & N' & K' \end{pmatrix}$$

$$\times (-1)^{G+I+1+S} \sqrt{(2G+1)(2G'+1)} \begin{Bmatrix} S & G' & I \\ G & S & 1 \end{Bmatrix}$$

$$\sqrt{S(S+1)(2S+1)} \tag{A.7}$$

The Quadrupole term:

$$\begin{aligned}
&\langle K; N, S, I, G, F_1, I_H, F, M | T^2(I,I) \cdot T^2(n) | K'; N', S, I, G', F_1', I_H, F', M' \rangle \\
&\qquad = \delta_{F,F'} \delta_{M,M'} \delta_{F_1,F_1'} \\
&\qquad \times (-1)^{N'+F_1+G} \begin{Bmatrix} G' & N' & F_1 \\ N & G & 2 \end{Bmatrix} \\
&\qquad \times (-1)^{N-K} \sqrt{(2N+1)(2N'+1)} \begin{pmatrix} N & -K & 2 \\ 0 & N' & K' \end{pmatrix} \\
&\qquad \times (-1)^{G'+I+2+S} \sqrt{(2G+1)(2G'+1)} \begin{Bmatrix} I & G' & S \\ G & I & 2 \end{Bmatrix} \\
&\qquad \times \frac{1}{2\sqrt{6}} \sqrt{(2I-1)(2I)(2I+1)(2I+2)(2I+3)}
\end{aligned} \tag{A.8}$$

The ℓ-doubling q_G term:

$$\begin{aligned}
&\langle K; N, S, I, G, F_1, I_H, F, M | T^2_{2q}(N,N) e^{-2iq\phi} | K'; N', S, I, G', F_1', I_H, F', M' \rangle \\
&\qquad = \delta_{F,F'} \delta_{M,M'} \delta_{F_1,F_1'} \delta_{G,G'} \delta_{N,N'} \\
&\qquad \times (-1)^{N-K} \begin{pmatrix} N & -K & 2 \\ 2q & N' & K' \end{pmatrix} \\
&\qquad \times \frac{1}{2\sqrt{6}} \sqrt{(2N-1)(2N)(2N+1)(2N+2)(2N+3)}
\end{aligned} \tag{A.9}$$

The ℓ-doubling p_G term:

Using eq. (2.3.35) in ref. [91],

$$\langle K; N, S, I, G, F_1, I_H, F, M | T^2_{2q}(N,S) e^{-2iq\phi} | K'; N', S, I, G', F_1', I_H, F', M' \rangle$$

$$= \delta_{F,F'} \delta_{M,M'} \delta_{F_1,F_1'}$$

$$\times (-1)^{N'+F_1'+G} \begin{Bmatrix} G' & N' & F_1' \\ N & G & 1 \end{Bmatrix}$$

$$\times (-1)^{G'+S+1+I} \sqrt{(2G+1)(2G'+1)} \begin{Bmatrix} S & G' & I \\ G & S & 1 \end{Bmatrix}$$

$$\sqrt{S(S+1)(2S+1)}$$

$$\times \sqrt{5} \begin{Bmatrix} 1 & 1 & 2 \\ N & N' & N' \end{Bmatrix} \sqrt{N'(N'+1)(2N'+1)}$$

$$\times (-1)^{N-K} \begin{pmatrix} N & -K & 2 \\ 2q & N' & K' \end{pmatrix} \sqrt{(2N+1)(2N'+1)} \tag{A.10}$$

The Stark term:

$$\langle K; N, S, I, G, F_1, I_H, F, M | T^1_{p=0}(D) | K'; N', S, I, G', F_1', I_H, F', M' \rangle$$

$$= (-1)^{F-M} \begin{pmatrix} F & -M & 1 \\ 0 & F' & M' \end{pmatrix}$$

$$\times (-1)^{F'+F_1+1+I_H} \sqrt{(2F+1)(2F'+1)} \begin{Bmatrix} F_1' & F' & I_H \\ F & F_1 & 1 \end{Bmatrix}$$

$$\times \delta_{G,G'} (-1)^{F_1'+N+1+G} \sqrt{(2F_1+1)(2F_1'+1)} \begin{Bmatrix} N' & F_1' & G \\ F_1 & N & 1 \end{Bmatrix}$$

$$\times (-1)^{N-K} \sqrt{(2N+1)(2N'+1)} \begin{pmatrix} N & -K & 1 \\ 0 & N' & K' \end{pmatrix} \tag{A.11}$$

Note that we only consider the contribution from the dipole component along the molecular z axis.

The Zeeman term:

$$\begin{aligned}
&\langle K; N, S, I, G, F_1, I_H, F, M | T^1_{p=0}(S) | K'; N', S, I, G', F_1', I_H, F', M' \rangle \\
&\qquad = (-1)^{F-M} \begin{pmatrix} F & -M & 1 \\ 0 & F' & M' \end{pmatrix} \\
&\qquad \times (-1)^{F'+F_1+1+I_H} \sqrt{(2F+1)(2F'+1)} \begin{Bmatrix} F_1' & F' & I_H \\ F & F_1 & 1 \end{Bmatrix} \\
&\qquad \times \delta_{N,N'} \delta_{K,K'} (-1)^{F_1+N+1+G'} \sqrt{(2F_1+1)(2F_1'+1)} \\
&\qquad \begin{Bmatrix} G' & F_1' & N \\ F_1 & G & 1 \end{Bmatrix} \times (-1)^{G+I+1+S} \sqrt{(2G+1)(2G'+1)} \\
&\qquad \begin{Bmatrix} S & G' & I \\ G & S & 1 \end{Bmatrix} \sqrt{S(S+1)(2S+1)}
\end{aligned} \tag{A.12}$$

The eEDM term:

$$\begin{aligned}
&\langle K; N, S, I, G, F_1, I_H, F, M | T^1(S) \cdot T^1(n) | K'; N', S, I, G', F_1', I_H, F', M' \rangle \\
&\qquad = \delta_{F,F'} \delta_{M,M'} \delta_{F_1,F_1'} \\
&\qquad \times (-1)^{N'+F_1+G} \begin{Bmatrix} G' & N' & F_1 \\ N & G & 1 \end{Bmatrix} \\
&\qquad \times (-1)^{N-K} \sqrt{(2N+1)(2N'+1)} \begin{pmatrix} N & -K & 1 \\ 0 & N' & K' \end{pmatrix} \\
&\qquad \times (-1)^{G'+S+1+I} \sqrt{(2G+1)(2G'+1)} \begin{Bmatrix} S & G' & I \\ G & S & 1 \end{Bmatrix} \\
&\qquad \sqrt{S(S+1)(2S+1)}
\end{aligned} \tag{A.13}$$

The NSM term:

$$\begin{aligned}
&\langle K; N, S, I, G, F_1, I_H, F, M | T^1(I) \cdot T^1(n) | K'; N', S, I, G', F_1', I_H, F', M' \rangle \\
&\qquad = \delta_{F,F'} \delta_{M,M'} \delta_{F_1,F_1'} \\
&\qquad \times (-1)^{N'+F_1+G} \begin{Bmatrix} G' & N' & F_1 \\ N & G & 1 \end{Bmatrix} \\
&\qquad \times (-1)^{N-K} \sqrt{(2N+1)(2N'+1)} \begin{pmatrix} N & -K & 1 \\ 0 & N' & K' \end{pmatrix} \\
&\qquad \times (-1)^{G+S+1+I} \sqrt{(2G+1)(2G'+1)} \begin{Bmatrix} I & G' & S \\ G & I & 1 \end{Bmatrix} \\
&\qquad \sqrt{I(I+1)(2I+1)}
\end{aligned} \tag{A.14}$$

The NMQM term:

NMQM Hamiltonian in spherical notation is given in ref. [21].

$$\begin{aligned}
&\langle K; N, S, I, G, F_1, I_H, F, M | T^1(S,T) \cdot T^1(n) | K'; N', S, I, G', F_1', I_H, F', M' \rangle \\
&\qquad = \delta_{F,F'} \delta_{M,M'} \delta_{F_1,F_1'} \\
&\qquad \times (-1)^{G'+F_1+N} \begin{Bmatrix} N' & G' & F_1 \\ G & N & 1 \end{Bmatrix} \\
&\qquad \times (-1)^{N-K} \sqrt{(2N+1)(2N'+1)} \begin{pmatrix} N & -K & 1 \\ 0 & N' & K' \end{pmatrix} \\
&\qquad \times \sqrt{(2G+1)3(2G'+1)} \begin{Bmatrix} S & I & G' \\ 1 & 2 & 1 \\ S & I & G \end{Bmatrix} \\
&\qquad \times \frac{1}{\sqrt{6}} \sqrt{(2I-1)(2I)(2I+1)(2I+2)(2I+3)} \\
&\qquad \sqrt{S(S+1)(2S+1)}
\end{aligned} \tag{A.15}$$

Note that this matrix element is derived in eq. (14) in ref. [21]. Although the final form is slightly different, if the analytical form of $\begin{Bmatrix} F_1 & F & I_2 \\ F & F_1 & 0 \end{Bmatrix}$ in eq. (14) is substituted, then it coincides with our result above.

Appendix B

Science Chamber Drawings

This appendix collects the mechanical drawings for the science chamber and beamline apparatus that I have made. The drawings are reproduced on the following pages in alphabetical order by filename. Landscape pages are used to preserve readability.

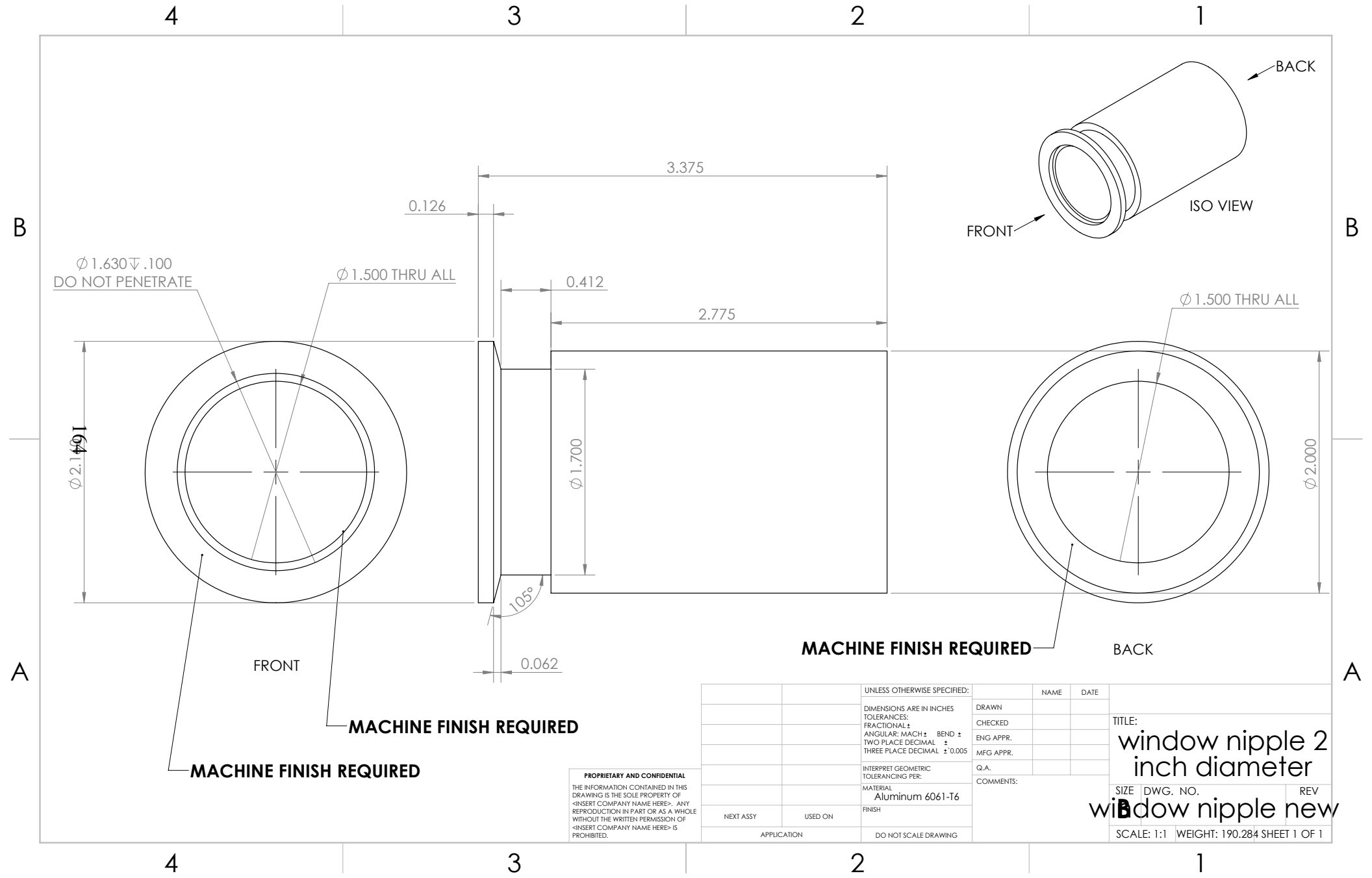

		UNLESS OTHERWISE SPECIFIED:		NAME	DATE
		DIMENSIONS ARE IN INCHES TOLERANCES: FRACTIONAL ± ANGULAR: MACH ± BEND ± TWO PLACE DECIMAL ± THREE PLACE DECIMAL ± 0.005	DRAWN		
			CHECKED		
			ENG APPR.		
			MFG APPR.		
		INTERPRET GEOMETRIC TOLERANCING PER:	Q.A.		
		MATERIAL Aluminum 6061-T6	COMMENTS:		
NEXT ASSY	USED ON	FINISH			
APPLICATION		DO NOT SCALE DRAWING			

TITLE:
window nipple 2 inch diameter

SIZE	DWG. NO.	REV
B	window nipple new	

SCALE: 1:1 | WEIGHT: 190.284 | SHEET 1 OF 1

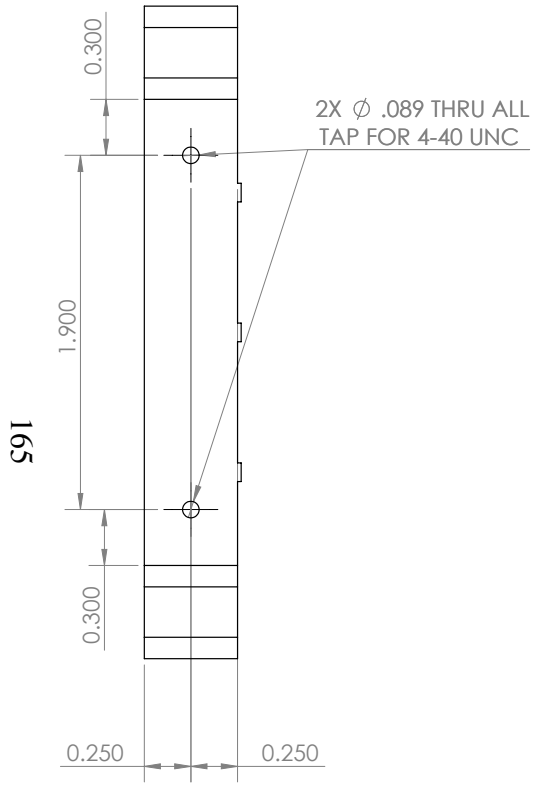

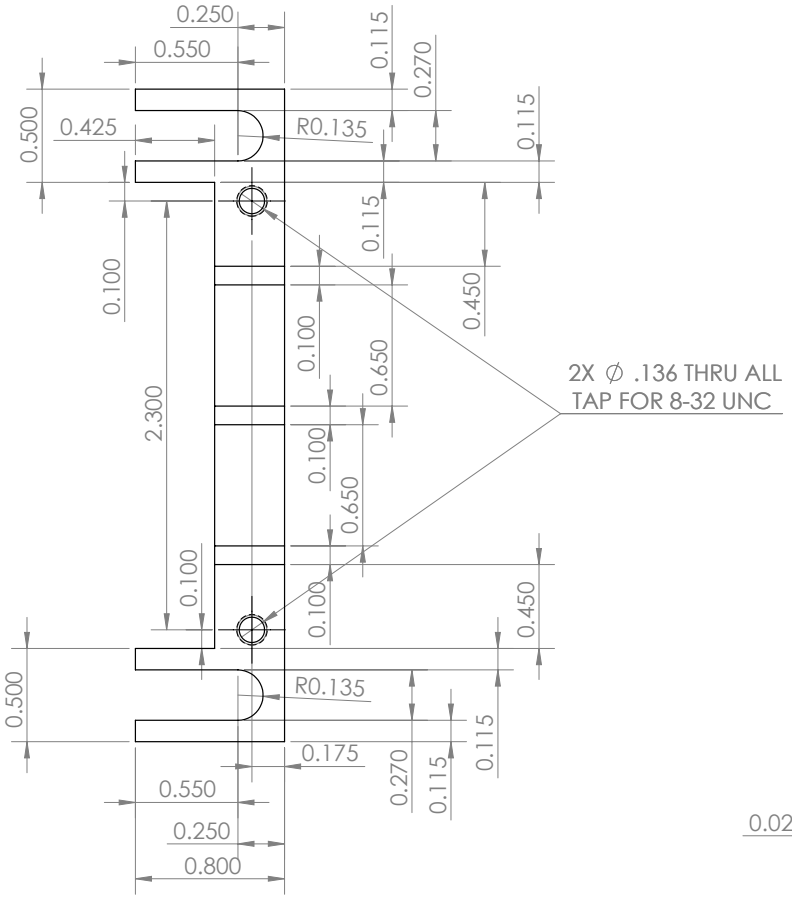

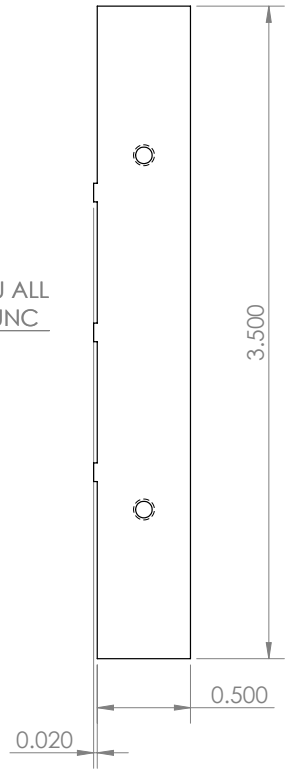

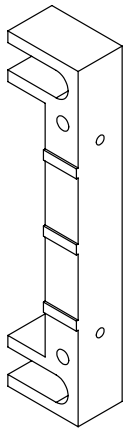

165

All patterns are top/bottom symmetric

		UNLESS OTHERWISE SPECIFIED:		NAME	DATE
		DIMENSIONS ARE IN INCHES TOLERANCES: FRACTIONAL ± ANGULAR: MACH ± BEND ± TWO PLACE DECIMAL ± THREE PLACE DECIMAL ±	DRAWN		
			CHECKED		
			ENG APPR.		
			MFG APPR.		
		INTERPRET GEOMETRIC TOLERANCING PER:	Q.A.		
		MATERIAL	COMMENTS:		
NEXT ASSY	USED ON	FINISH			
APPLICATION		DO NOT SCALE DRAWING			

TITLE:

SIZE	DWG. NO.	REV
B	Adapter_plate_for_new_top_plate_final	
SCALE: 1:1	WEIGHT:	SHEET 1 OF 1

All patterns are top/bottom and left/right symmetric

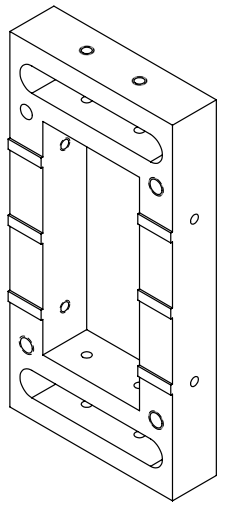

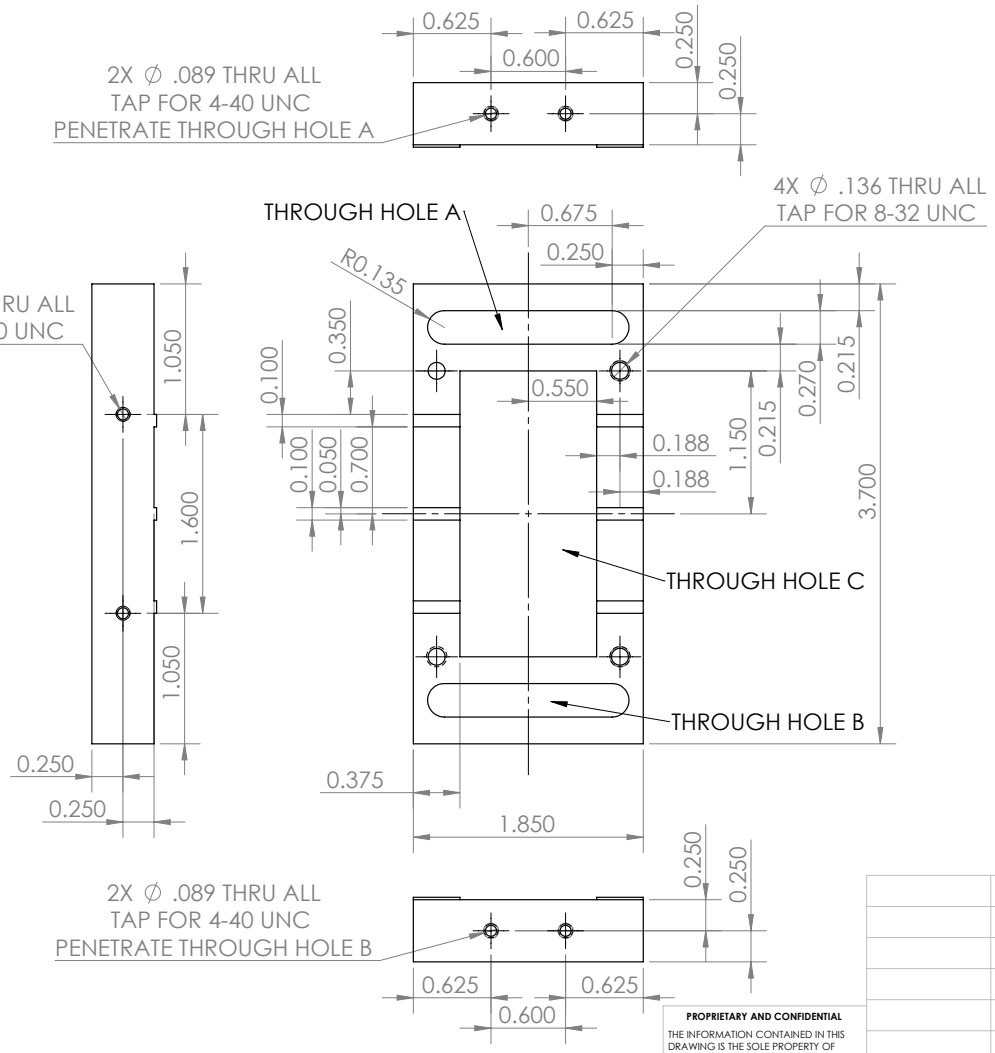

166

		UNLESS OTHERWISE SPECIFIED:		NAME	DATE
		DIMENSIONS ARE IN INCHES TOLERANCES: FRACTIONAL ± ANGULAR: MACH ± BEND ± TWO PLACE DECIMAL ± THREE PLACE DECIMAL ±	DRAWN		
			CHECKED		
			ENG APPR.		
			MFG APPR.		
		INTERPRET GEOMETRIC TOLERANCING PER:	Q.A.		
		MATERIAL	COMMENTS:		
NEXT ASSY	USED ON	FINISH			
APPLICATION		DO NOT SCALE DRAWING			

TITLE:

SIZE	DWG. NO.	REV
B	Adapter_plate_for_new_top_plate_final_recutangular_ring	
SCALE: 1:1	WEIGHT:	SHEET 1 OF 1

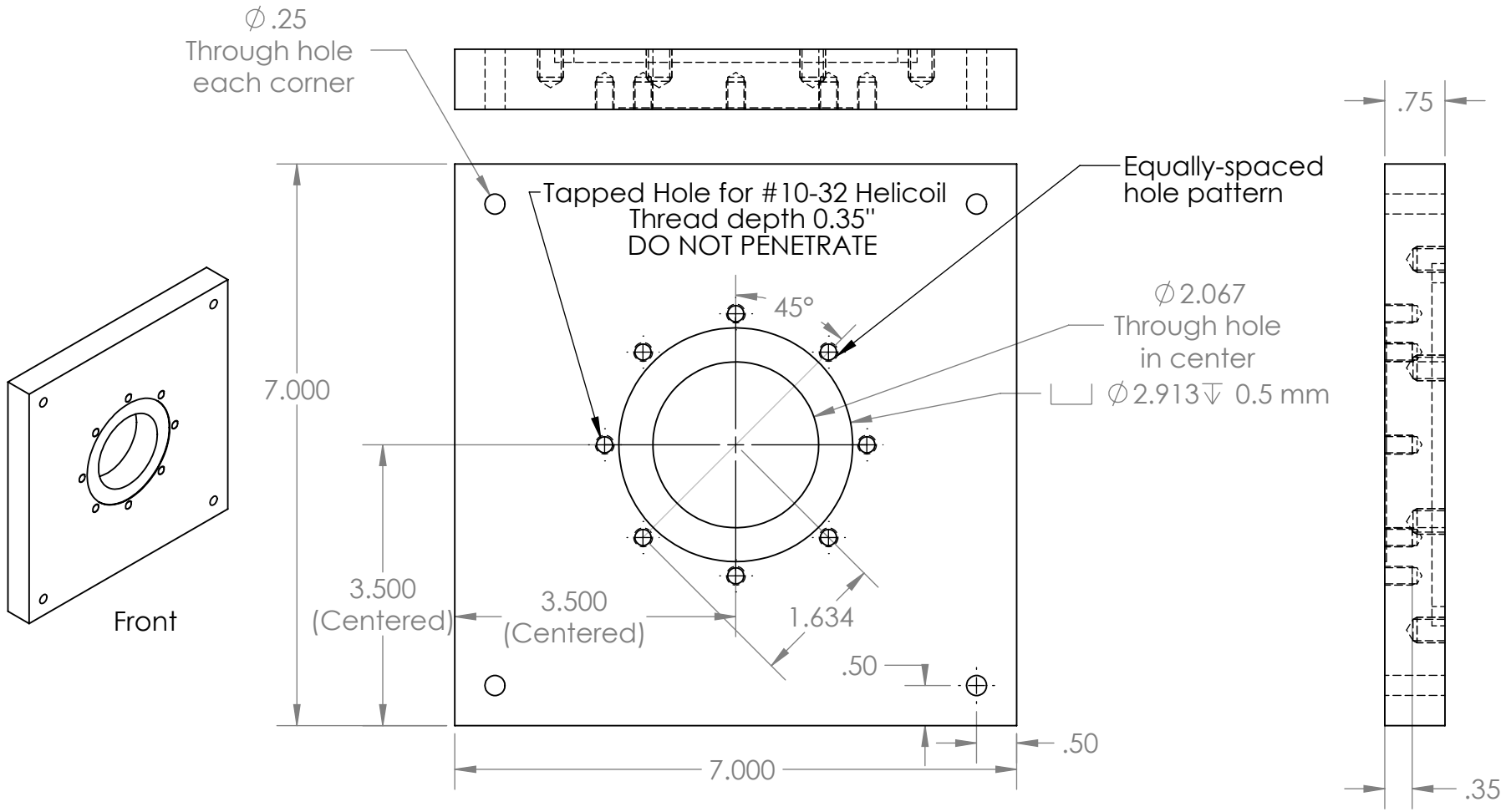

		UNLESS OTHERWISE SPECIFIED:		NAME	DATE
		DIMENSIONS ARE IN INCHES TOLERANCES: FRACTIONAL ± ANGULAR: MACH ± BEND ± TWO PLACE DECIMAL ± THREE PLACE DECIMAL ±	DRAWN		
			CHECKED		
			ENG APPR.		
			MFG APPR.		
		INTERPRET GEOMETRIC TOLERANCING PER:	Q.A.		
		MATERIAL	COMMENTS:		
NEXT ASSY	USED ON	FINISH			
APPLICATION		DO NOT SCALE DRAWING			

TITLE: Front

SIZE	DWG. NO.	REV
A	adaptor plate	
SCALE: 1:4	WEIGHT:	SHEET 1 OF 2

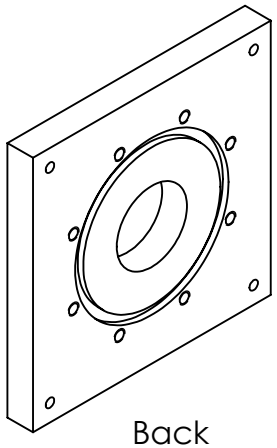

Back

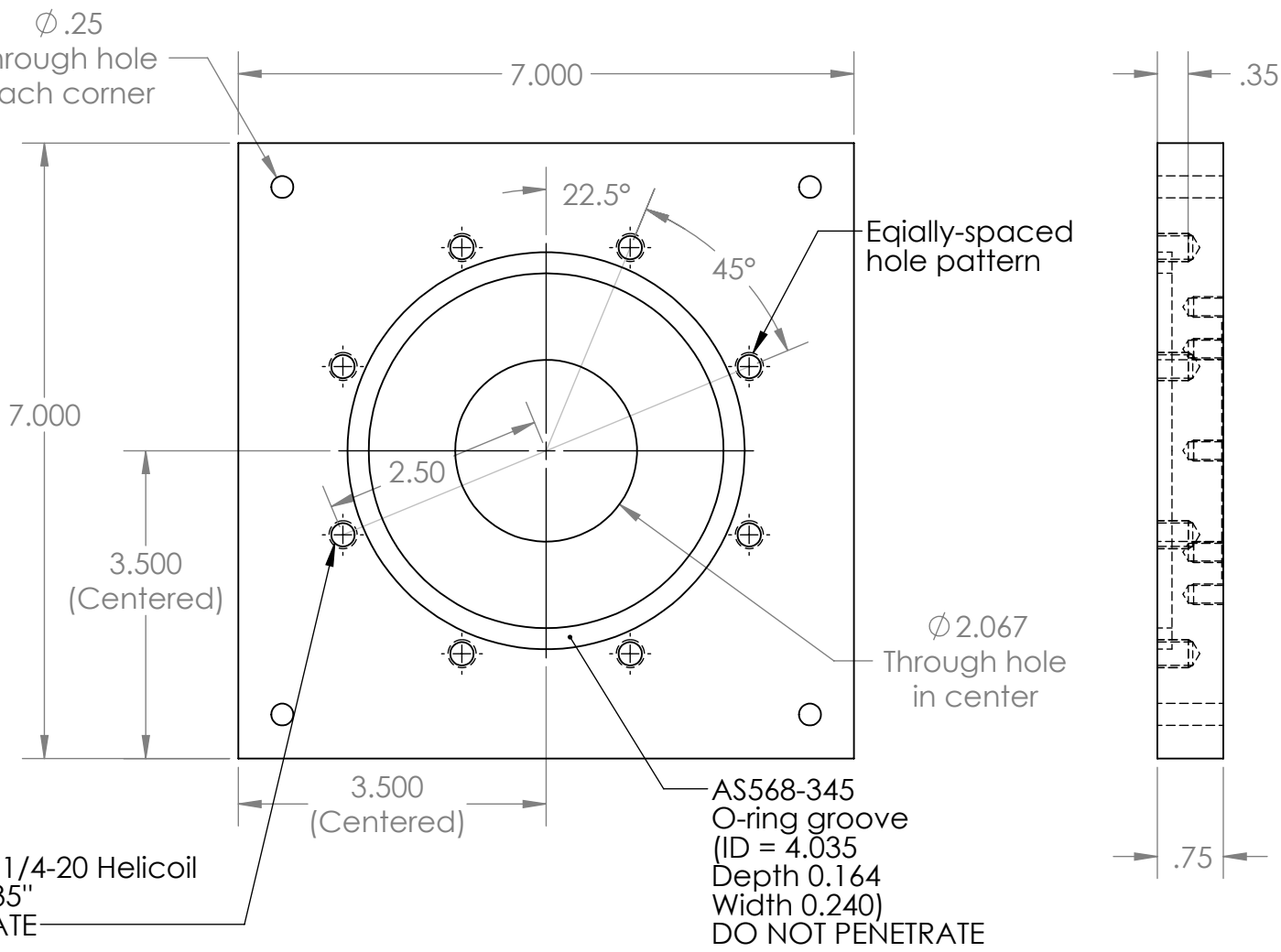

		UNLESS OTHERWISE SPECIFIED:		NAME	DATE
		DIMENSIONS ARE IN INCHES TOLERANCES: FRACTIONAL ± ANGULAR: MACH ± BEND ± TWO PLACE DECIMAL ± THREE PLACE DECIMAL ±	DRAWN		
			CHECKED		
			ENG APPR.		
			MFG APPR.		
		INTERPRET GEOMETRIC TOLERANCING PER:	Q.A.		
		MATERIAL	COMMENTS:		
NEXT ASSY	USED ON	FINISH			
APPLICATION		DO NOT SCALE DRAWING			

TITLE:

Back

SIZE	DWG. NO.	REV
A	adaptor plate	
SCALE: 1:4	WEIGHT:	SHEET 2 OF 2

All patterns are top/bottom symmetric

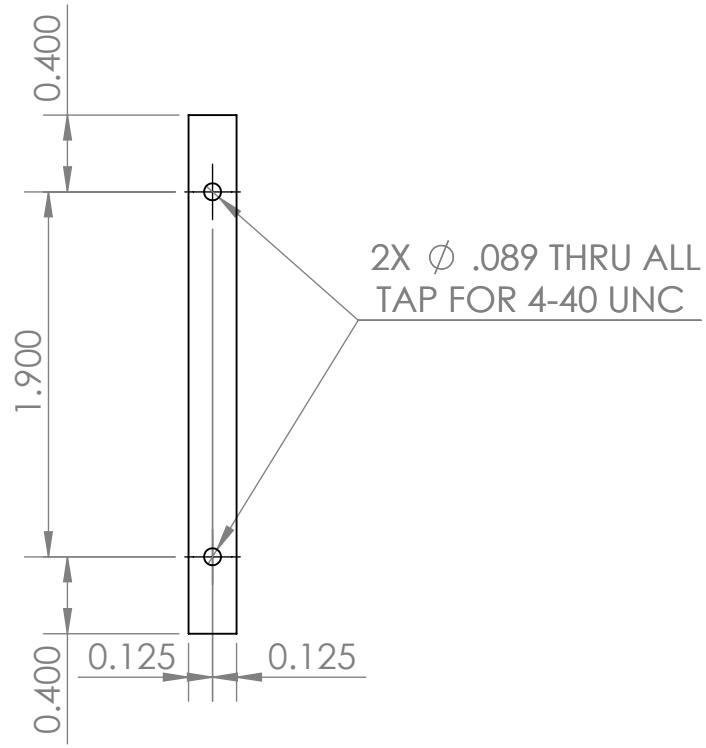

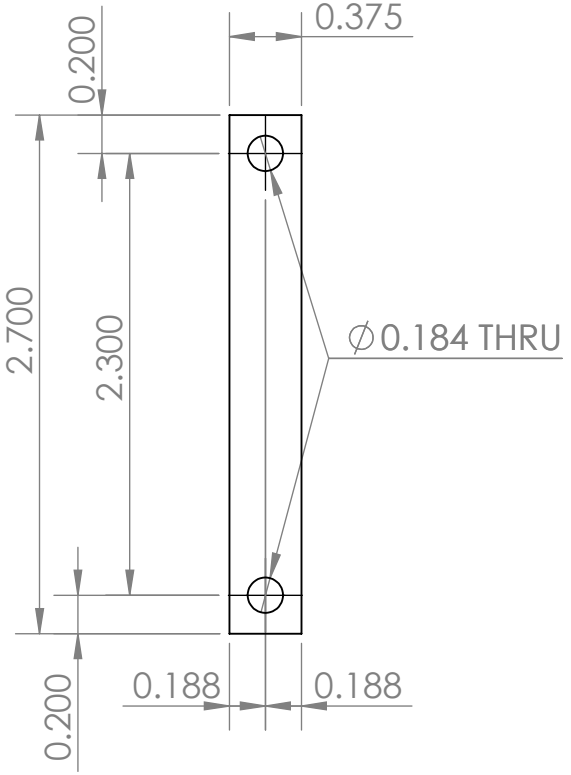

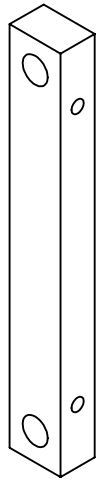

169

		UNLESS OTHERWISE SPECIFIED:		NAME	DATE
		DIMENSIONS ARE IN INCHES TOLERANCES: FRACTIONAL ± ANGULAR: MACH ± BEND ± TWO PLACE DECIMAL ± THREE PLACE DECIMAL ±	DRAWN		
			CHECKED		
			ENG APPR.		
			MFG APPR.		
		INTERPRET GEOMETRIC TOLERANCING PER:	Q.A.		
		MATERIAL	COMMENTS:		
NEXT ASSY	USED ON	FINISH			
APPLICATION		DO NOT SCALE DRAWING			

TITLE:

SIZE	DWG. NO.	REV
A	Aft_for_mount_for_new_top_plate_final	

SCALE: 2:1	WEIGHT:	SHEET 1 OF 1

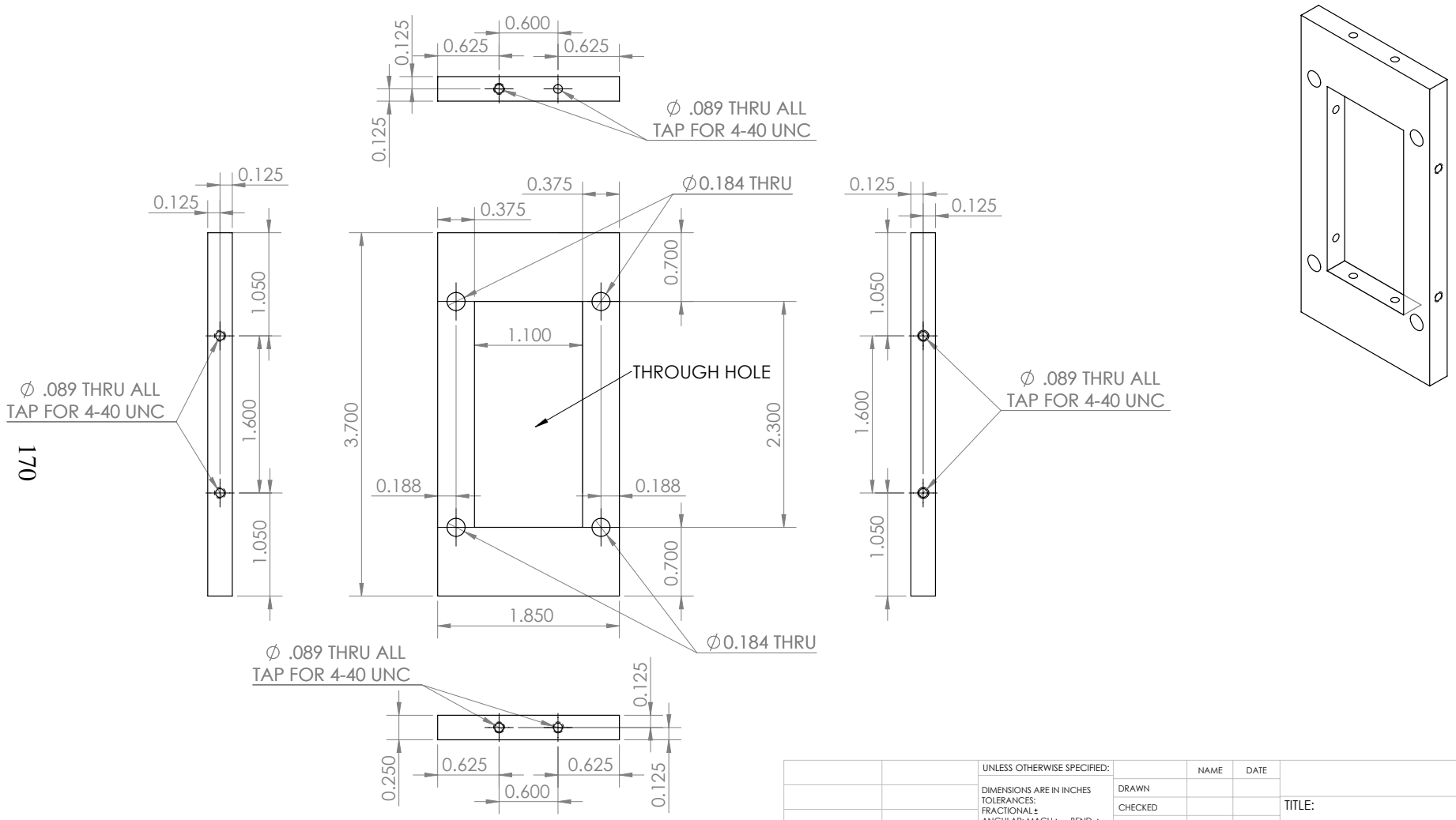

170

		UNLESS OTHERWISE SPECIFIED:		NAME	DATE
		DIMENSIONS ARE IN INCHES TOLERANCES: FRACTIONAL ± ANGULAR: MACH ± BEND ± TWO PLACE DECIMAL ± THREE PLACE DECIMAL ±	DRAWN		
			CHECKED		
			ENG APPR.		
			MFG APPR.		
		INTERPRET GEOMETRIC TOLERANCING PER:	Q.A.		
		MATERIAL	COMMENTS:		
NEXT ASSY	USED ON	FINISH			
APPLICATION		DO NOT SCALE DRAWING			

TITLE:

SIZE	DWG. NO.	REV
B	Aktormount_for_new_top_plate_final_rectangular_ring	

SCALE: 1:1 | WEIGHT: | SHEET 1 OF 1

All patterns are top/bottom and left/right symmetric

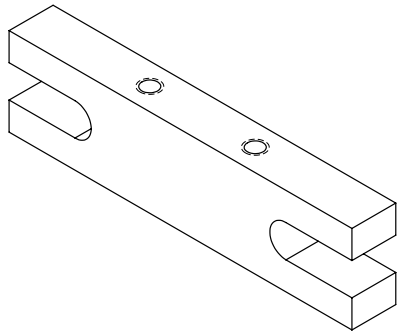

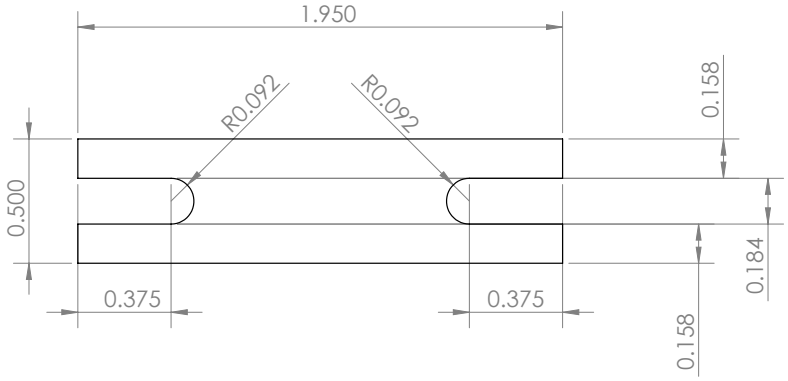

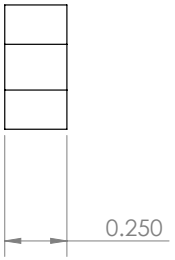

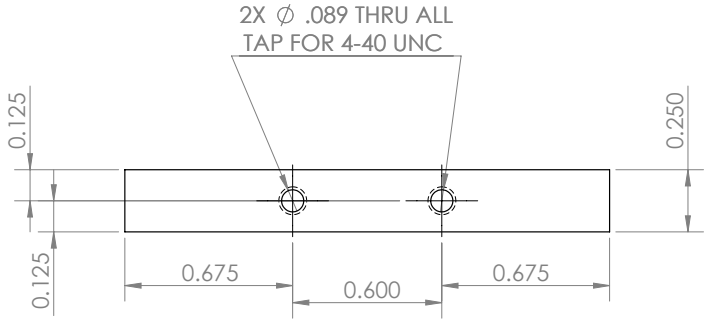

171

		UNLESS OTHERWISE SPECIFIED:		NAME	DATE
		DIMENSIONS ARE IN INCHES TOLERANCES: FRACTIONAL ± ANGULAR: MACH ± BEND ± TWO PLACE DECIMAL ± THREE PLACE DECIMAL ±	DRAWN		
			CHECKED		
			ENG APPR.		
			MFG APPR.		
		INTERPRET GEOMETRIC TOLERANCING PER:	Q.A.		
		MATERIAL	COMMENTS:		
NEXT ASSY	USED ON	FINISH			
APPLICATION		DO NOT SCALE DRAWING			

TITLE:

SIZE	DWG. NO.	REV
B	Akt_mount_for_new_top_plate_final_side	

SCALE: 2:1 | WEIGHT: | SHEET 1 OF 1

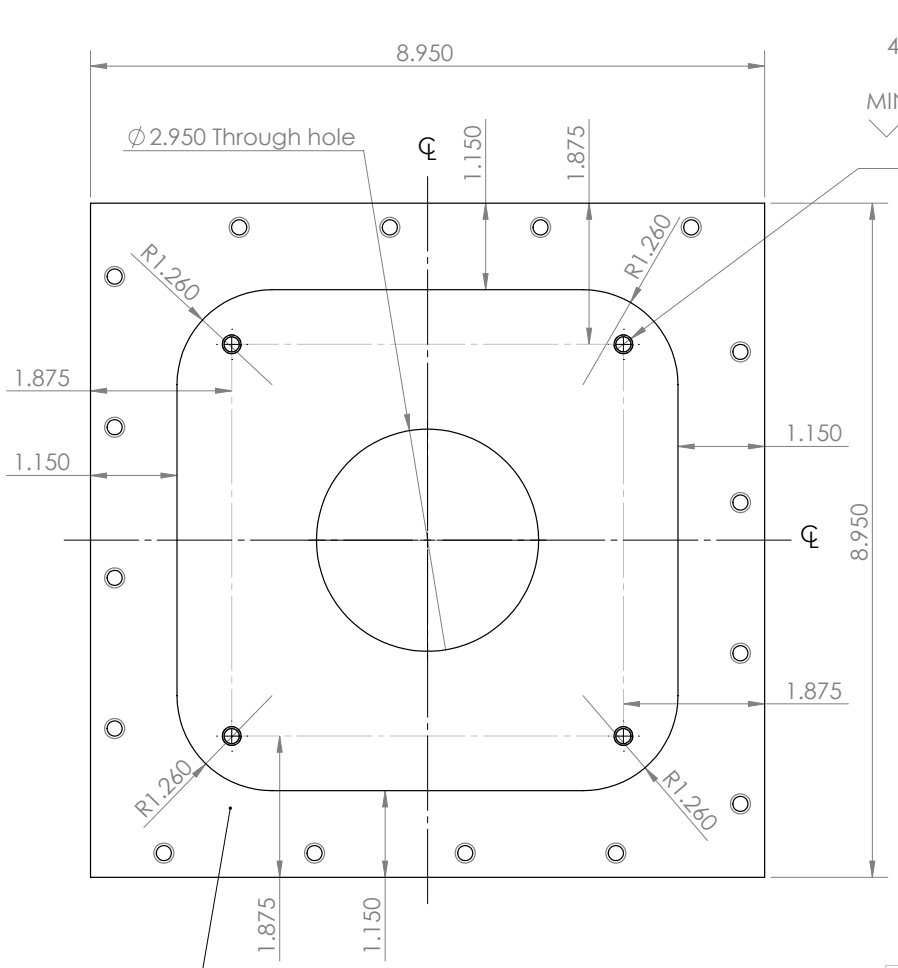

+0.000
4X ∅ .201 ↧ .500 -0.030
TAP FOR 1/4-20 UNC
MINIMUM TAP DEPTH = 0.420
∅ .250 X 90°, NEAR SIDE
DO NOT PENETRATE

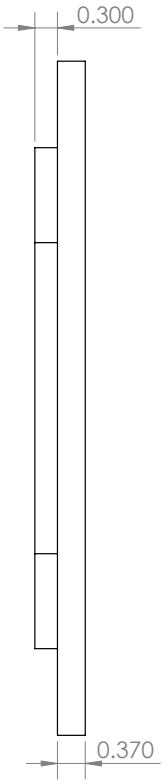

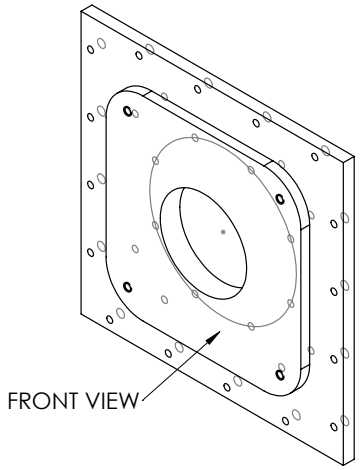

MACHINE FINISH REQUIRED

172

UNLESS OTHERWISE SPECIFIED:		NAME / DATE
DIMENSIONS ARE IN INCHES TOLERANCES: FRACTIONAL ± ANGULAR: MACH ± BEND ± TWO PLACE DECIMAL ± THREE PLACE DECIMAL ±0.002	DRAWN	
	CHECKED	
	ENG APPR.	
	MFG APPR.	
INTERPRET GEOMETRIC TOLERANCING PER:	Q.A.	
MATERIAL	COMMENTS:	
FINISH		
NEXT ASSY / USED ON		
APPLICATION	DO NOT SCALE DRAWING	

TITLE:
FRONT VIEW

SIZE	DWG. NO.	REV
B	back_plate_final	

SCALE: 1:2	WEIGHT:	SHEET 1 OF 2

COUNTERBORE HOLES A

16X ⌀ .201 THRU ALL
⌴ ⌀ .375 ↧ .190

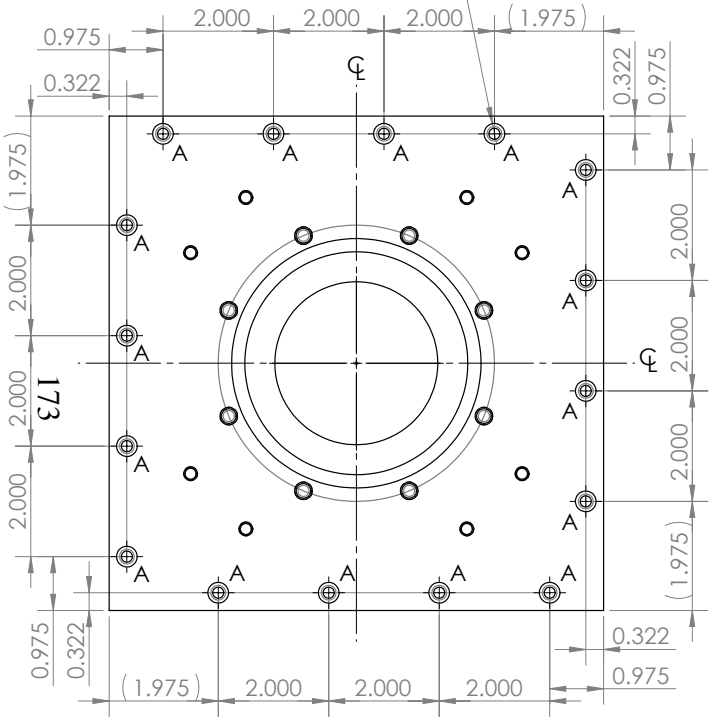

TAPPED HOLES B

8X ⌀ .201 ↧ .500 +0.000 -0.030
TAP FOR 1/4-20 UNC
MINIMUM TAP DEPTH = 0.420
⌵ ⌀ .250 X 90°, NEAR SIDE
DO NOT PENETRATE

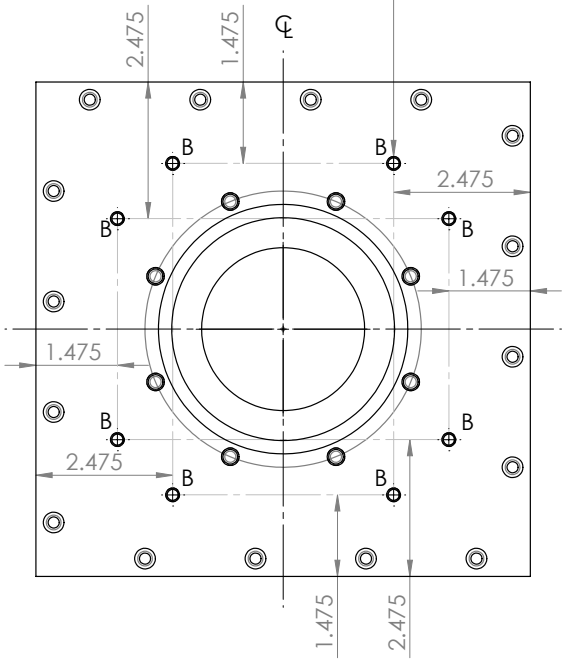

TAPPED HOLES C

8X ⌀ .266 ↧ .500 +0.000 -0.030
TAP FOR 1/4-20 HELICOIL
MINIMUM TAP DEPTH = 0.42
⌵ ⌀ .319 X 90°, NEAR SIDE
equally spaced hole pattern
DO NOT PENETRATE

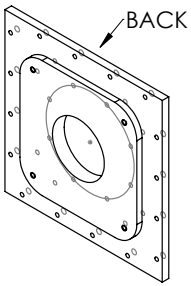

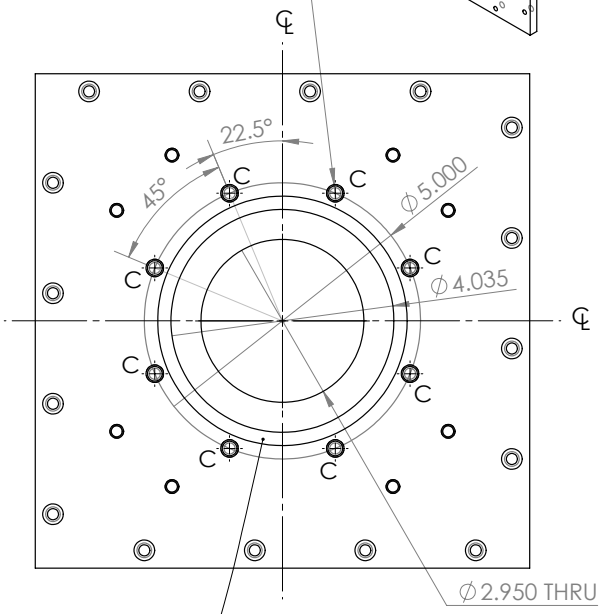

O-ring groove for AS568-345
MACHINE FINISH REQUIRED
ID = 4.035, Depth = 0.164, Width = 0.240
DO NOT PENETRATE

			NAME	DATE
		UNLESS OTHERWISE SPECIFIED:		
		DIMENSIONS ARE IN INCHES TOLERANCES: FRACTIONAL ± ANGULAR: MACH ± BEND ± TWO PLACE DECIMAL ± THREE PLACE DECIMAL ±0.002	DRAWN	
			CHECKED	
			ENG APPR.	
			MFG APPR.	
		INTERPRET GEOMETRIC TOLERANCING PER:	Q.A.	
		MATERIAL	COMMENTS:	
NEXT ASSY	USED ON	FINISH		
APPLICATION		DO NOT SCALE DRAWING		

TITLE:

BACK VIEW

SIZE	DWG. NO.	REV
B	back_plate_final	
SCALE: 1:2	WEIGHT:	SHEET 2 OF 2

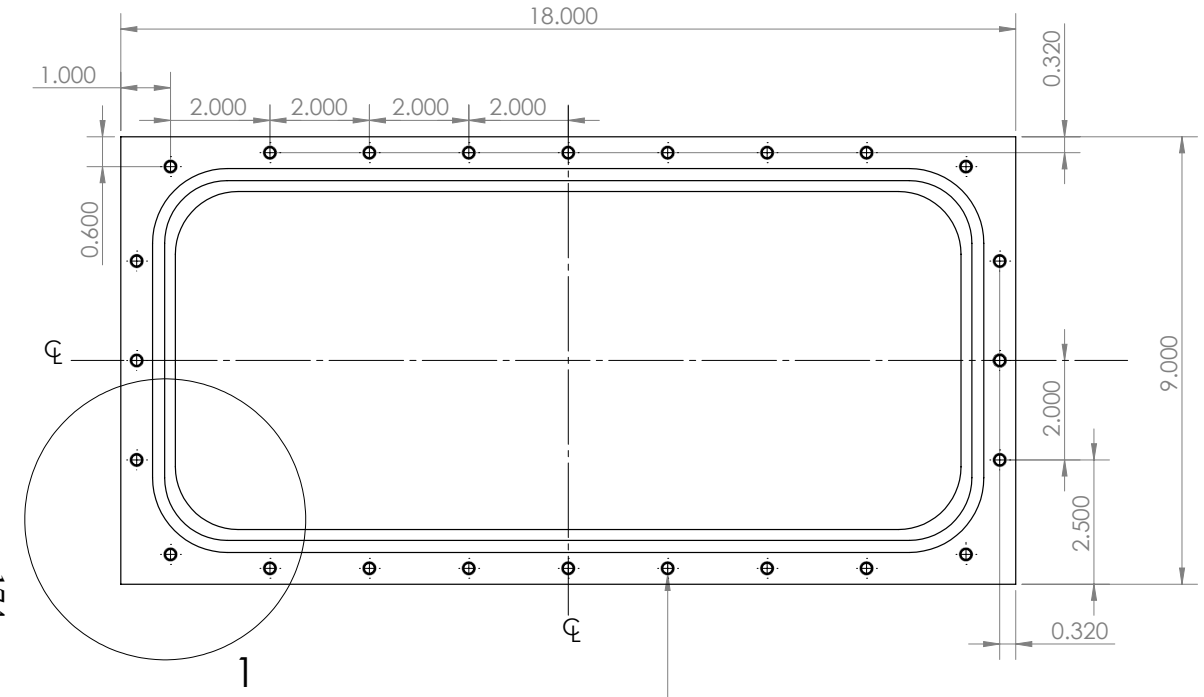

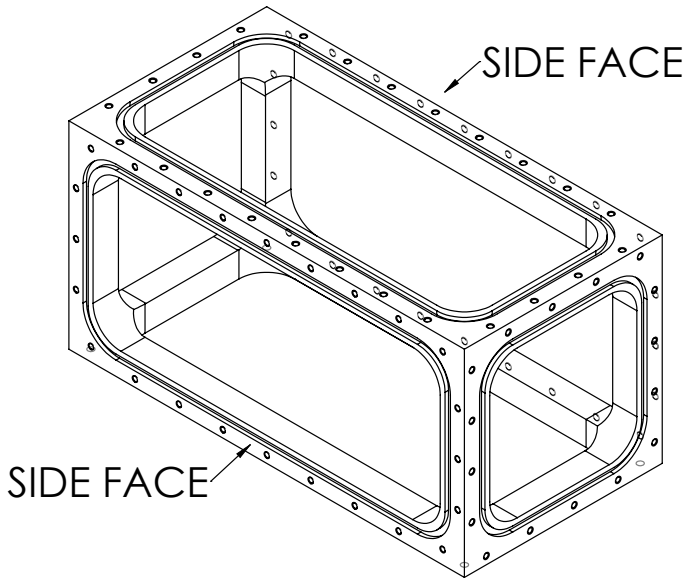

ISO VIEW

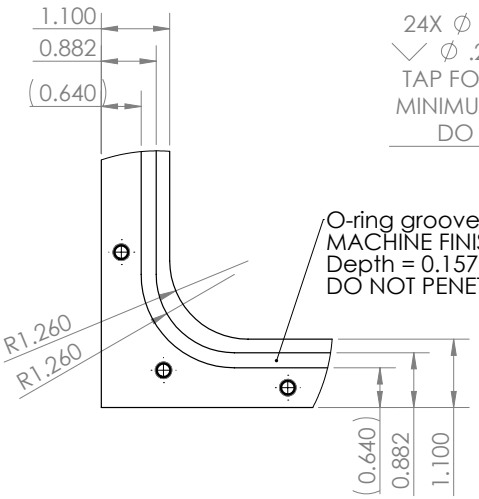

DETAIL 1
SCALE 1 : 2

+0.000
24X ⌀ .201 ↧ .500 -0.030
⌵ ⌀ .240 X 90°, NEAR SIDE
TAP FOR #10-32 HELICOIL
MINIMUM TAP DEPTH = 0.42
DO NOT PENETRATE

OPPOSITE SIDE IS IDENTICAL
face is up/down and left/right symmetric

UNLESS OTHERWISE SPECIFIED:		NAME	DATE
DIMENSIONS ARE IN INCHES TOLERANCES: FRACTIONAL ± ANGULAR: MACH ± BEND ± TWO PLACE DECIMAL ± THREE PLACE DECIMAL ±0.002	DRAWN		
	CHECKED		
	ENG APPR.		
	MFG APPR.		
INTERPRET GEOMETRIC TOLERANCING PER:	Q.A.		
MATERIAL	COMMENTS:		
FINISH			
NEXT ASSY / USED ON			
APPLICATION / DO NOT SCALE DRAWING			

TITLE: SIDE FACES

SIZE	DWG. NO.	REV
B	body_v8_yuiki_v2	

SCALE: 1:4 | WEIGHT: | SHEET 1 OF 5

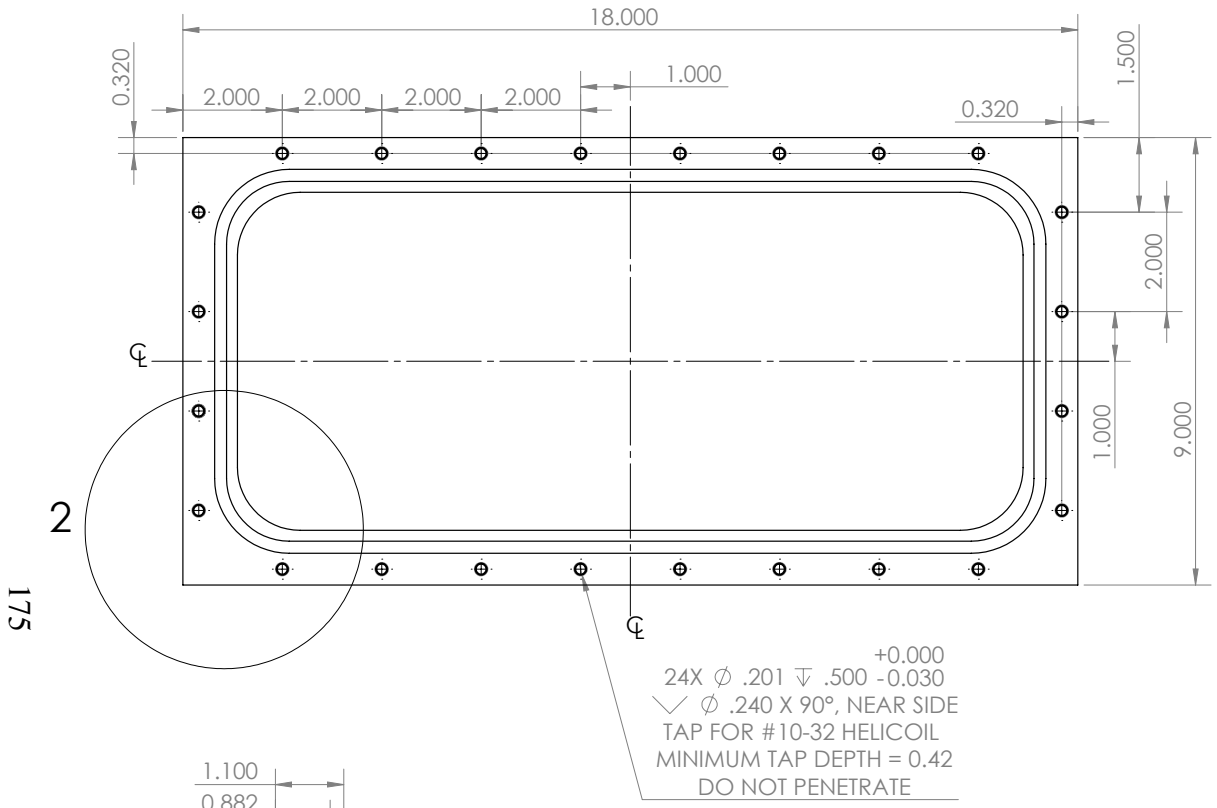

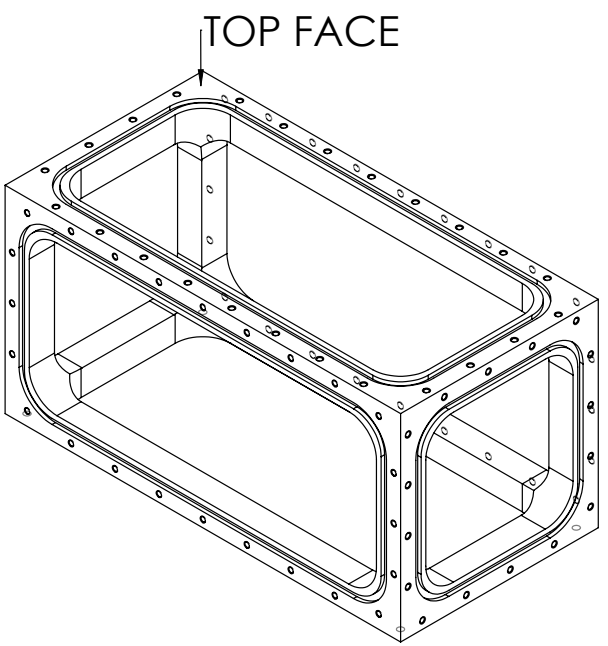

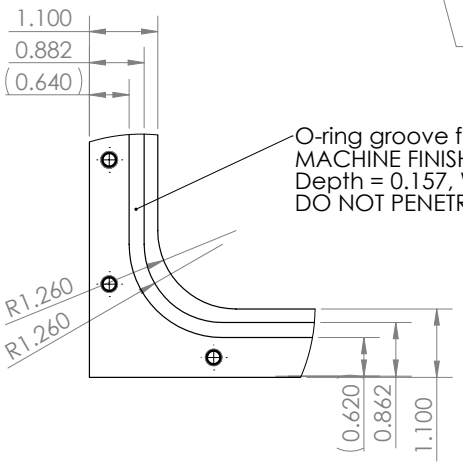

DETAIL 2
SCALE 1 : 2

face is up/down and left/right symmetric

UNLESS OTHERWISE SPECIFIED:		NAME	DATE
DIMENSIONS ARE IN INCHES TOLERANCES: FRACTIONAL ± ANGULAR: MACH ± BEND ± TWO PLACE DECIMAL ± THREE PLACE DECIMAL ±0.002	DRAWN		
	CHECKED		
	ENG APPR.		
	MFG APPR.		
INTERPRET GEOMETRIC TOLERANCING PER:	Q.A.		
MATERIAL	COMMENTS:		
FINISH			
NEXT ASSY / USED ON			
APPLICATION / DO NOT SCALE DRAWING			

TITLE: TOP FACE

SIZE	DWG. NO.	REV
B	body_v8_yuiki_v2	

SCALE: 1:4 | WEIGHT: | SHEET 2 OF 5

Tapped holes A

+0.000
4X ⌀ .266 ↧ .500 -0.030
⌵ ⌀ .319 X 90°, NEAR SIDE
TAP FOR 1/4-20 HELICOIL
MINIMUM TAP DEPTH = 0.42
DO NOT PENETRATE

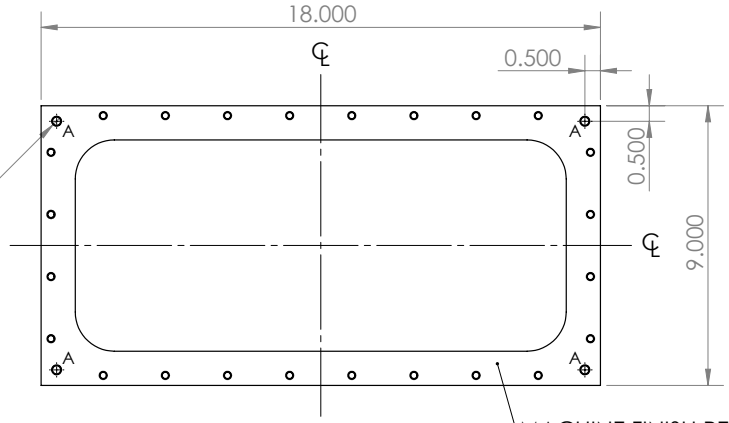

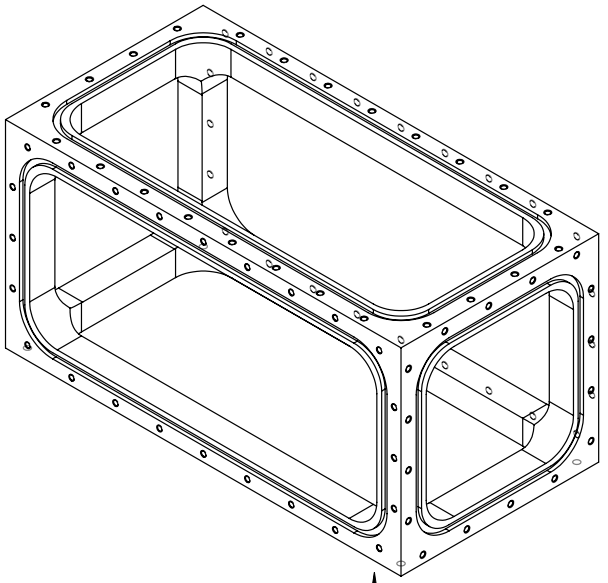

BOTTOM FACE

Tapped holes B

+0.000
24X ⌀ .201 ↧ .500 -0.030
⌵ ⌀ .240 X 90°, NEAR SIDE
TAP FOR #10-32 HELICOIL
MINIMUM TAP DEPTH = 0.42
DO NOT PENETRATE

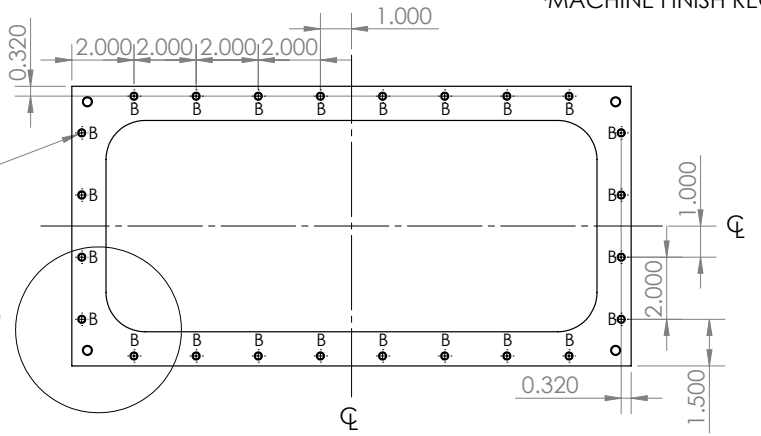

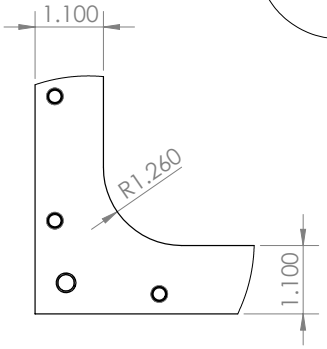

DETAIL 3
SCALE 1 : 2

face is up/down and left/right symmetric

				NAME	DATE
		UNLESS OTHERWISE SPECIFIED:			
		DIMENSIONS ARE IN INCHES TOLERANCES: FRACTIONAL ± ANGULAR: MACH ± BEND ± TWO PLACE DECIMAL ± THREE PLACE DECIMAL ±0.002	DRAWN		
			CHECKED		
			ENG APPR.		
			MFG APPR.		
		INTERPRET GEOMETRIC TOLERANCING PER:	Q.A.		
		MATERIAL	COMMENTS:		
NEXT ASSY	USED ON	FINISH			
APPLICATION		DO NOT SCALE DRAWING			

TITLE:

BOTTOM FACE

SIZE	DWG. NO.	REV
B	body_v8_yuiki_v2	
SCALE: 1:4	WEIGHT:	SHEET 3 OF 5

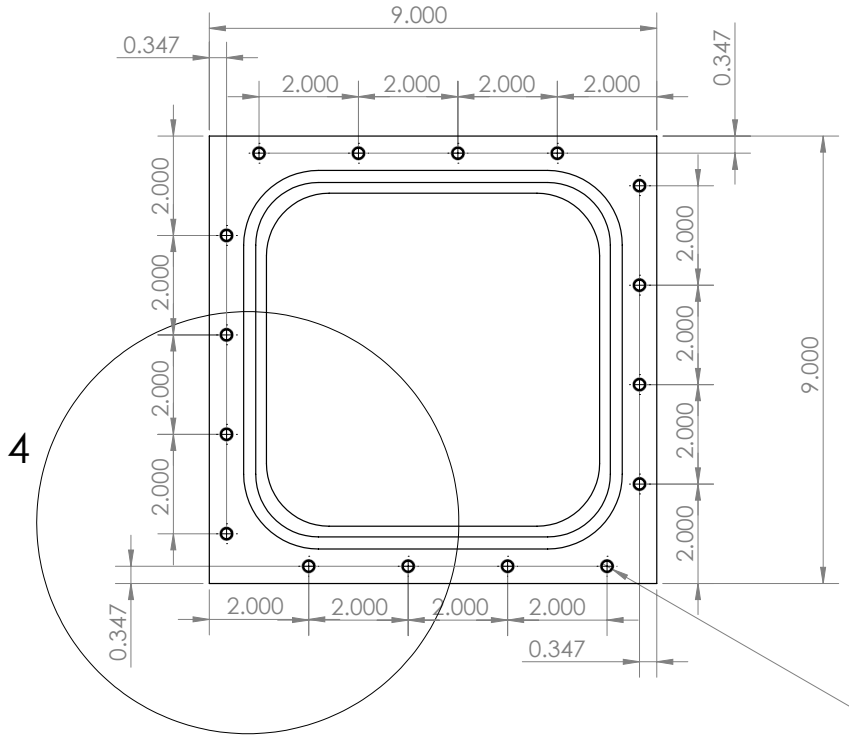

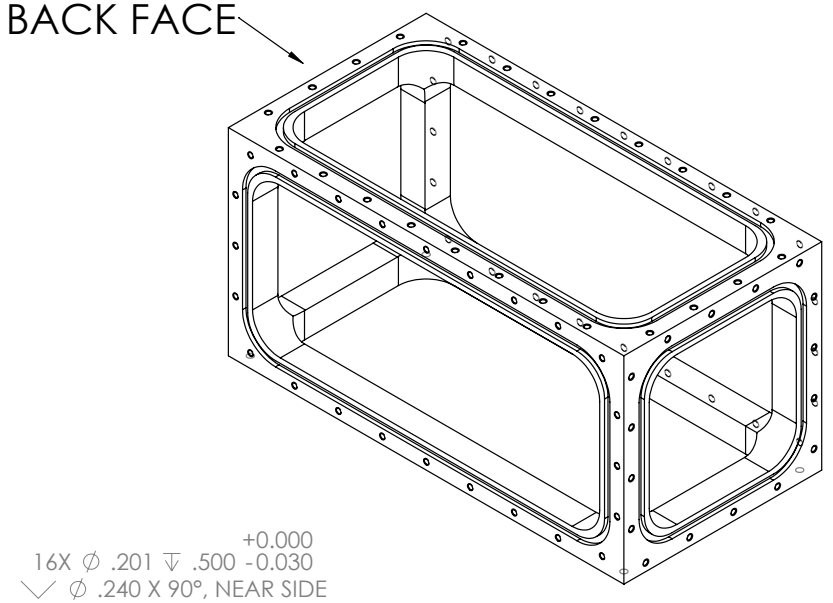

+0.000
16X ∅ .201 ↧ .500 -0.030
⌵ ∅ .240 X 90°, NEAR SIDE
TAP FOR #10-32 HELICOIL
MINIMUM TAP DEPTH = 0.42
DO NOT PENETRATE

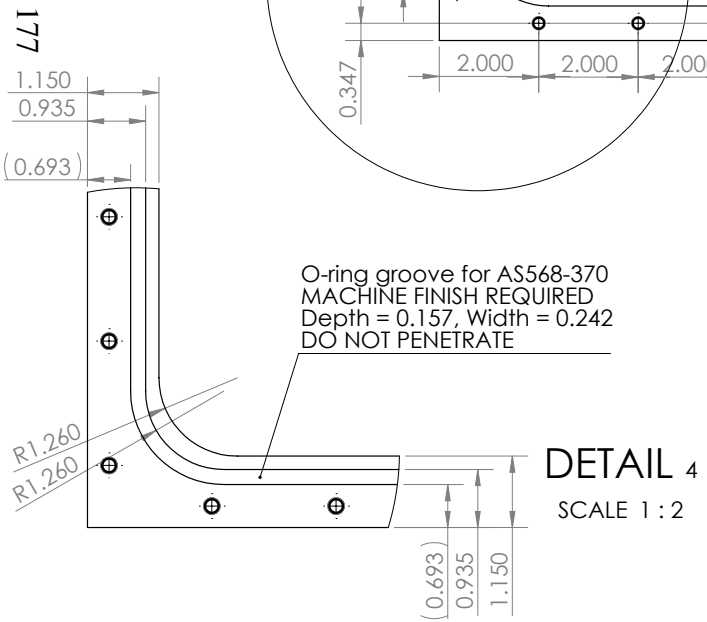

DETAIL 4
SCALE 1 : 2

face is NEITHER up/down NOR left/right symmetric

		UNLESS OTHERWISE SPECIFIED:		NAME	DATE
		DIMENSIONS ARE IN INCHES TOLERANCES: FRACTIONAL ± ANGULAR: MACH ± BEND ± TWO PLACE DECIMAL ± THREE PLACE DECIMAL ±0.002	DRAWN		
			CHECKED		
			ENG APPR.		
			MFG APPR.		
		INTERPRET GEOMETRIC TOLERANCING PER:	Q.A.		
		MATERIAL	COMMENTS:		
NEXT ASSY	USED ON	FINISH			
APPLICATION		DO NOT SCALE DRAWING			

TITLE: BACK FACE

SIZE	DWG. NO.	REV
B	body_v8_yuiki_v2	

SCALE: 1:4 | WEIGHT: | SHEET 4 OF 5

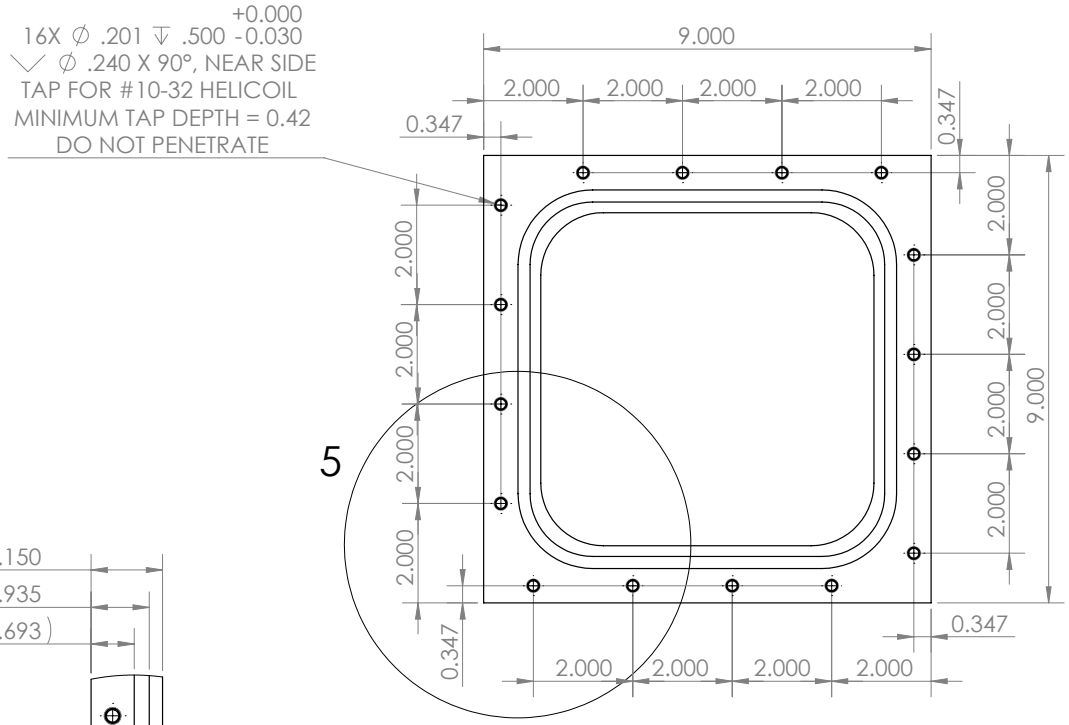

DETAIL 5

SCALE 1 : 2

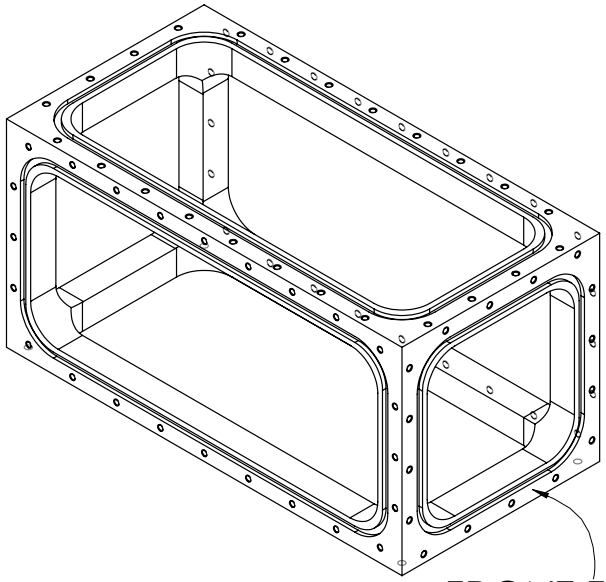

FRONT FACE

face is NEITHER up/down NOR left/right symmetric
FRONT and BACK face are DIFFERENT

		UNLESS OTHERWISE SPECIFIED:		NAME	DATE
		DIMENSIONS ARE IN INCHES TOLERANCES: FRACTIONAL ± ANGULAR: MACH ± BEND ± TWO PLACE DECIMAL ± THREE PLACE DECIMAL ±0.002	DRAWN		
			CHECKED		
			ENG APPR.		
			MFG APPR.		
		INTERPRET GEOMETRIC TOLERANCING PER:	Q.A.		
		MATERIAL	COMMENTS:		
NEXT ASSY	USED ON	FINISH			
APPLICATION		DO NOT SCALE DRAWING			

TITLE: FRONT FACE

SIZE	DWG. NO.	REV
B	body_v8_yuiki_v2	

SCALE: 1:4 | WEIGHT: | SHEET 5 OF 5

All patterns are top/bottom and left/right symmetric

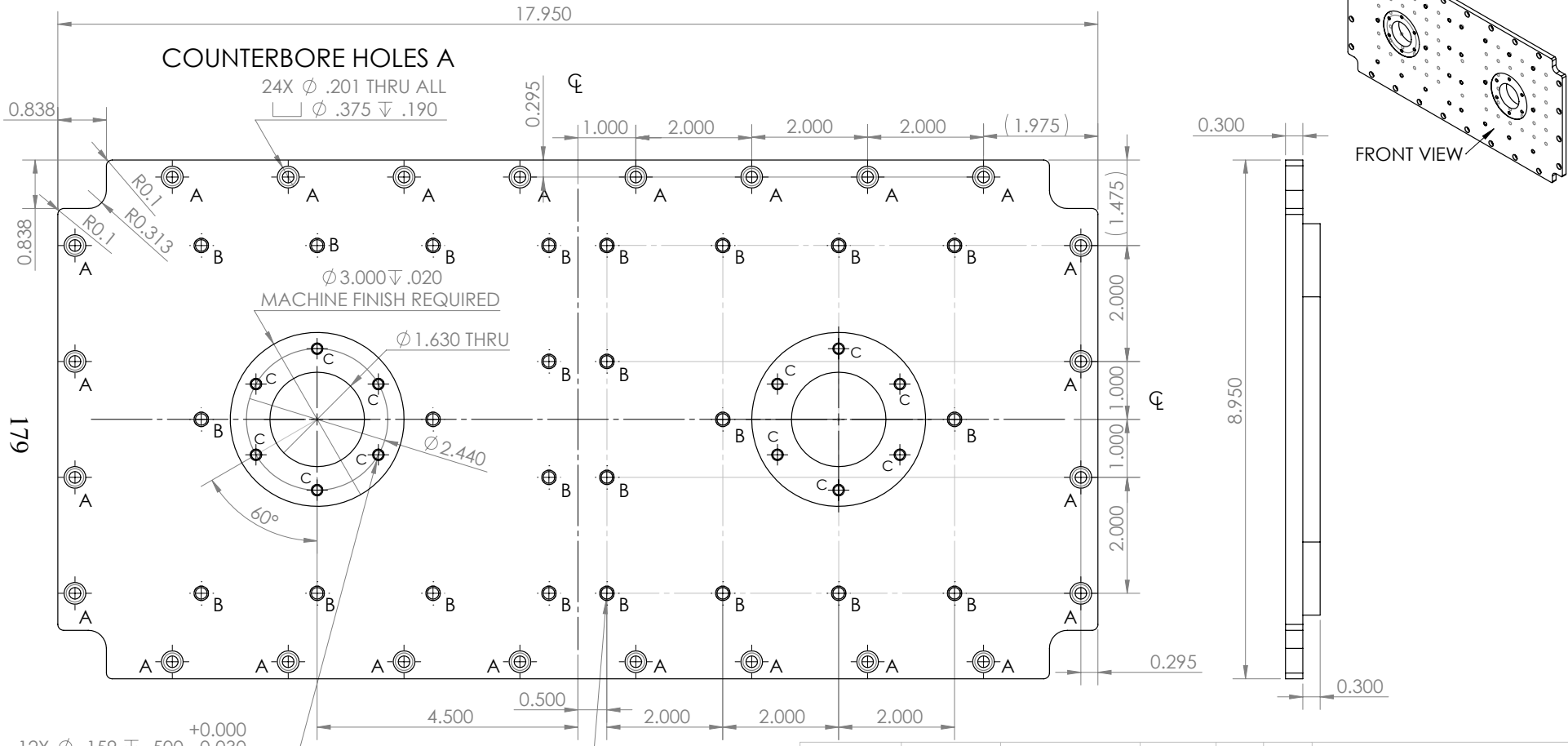

+0.000
12X ⌀ .159 ↧ .500 -0.030
TAP FOR 10-32 UNF
MINIMUM TAP DEPTH = 0.420
⌵ ⌀ .200 X 90°, NEAR SIDE
equally spaced hole pattern
DO NOT PENETRATE

TAPPED HOLES C

+0.000
24X ⌀ .201 ↧ .500 -0.030
TAP FOR 1/4-20 UNC
MINIMUM TAP DEPTH = 0.420
⌵ ⌀ .250 X 90°, NEAR SIDE
DO NOT PENETRATE

TAPPED HOLES B

			NAME	DATE
UNLESS OTHERWISE SPECIFIED:		DRAWN		
DIMENSIONS ARE IN INCHES TOLERANCES: FRACTIONAL ± ANGULAR: MACH ± BEND ± TWO PLACE DECIMAL ± THREE PLACE DECIMAL ±0.002		CHECKED		
		ENG APPR.		
		MFG APPR.		
INTERPRET GEOMETRIC TOLERANCING PER:		Q.A.		
MATERIAL		COMMENTS:		
FINISH				
NEXT ASSY	USED ON			
APPLICATION	DO NOT SCALE DRAWING			

TITLE:
FRONT VIEW

SIZE	DWG. NO.	REV
B	bottom_plate_final	
SCALE: 1:2	WEIGHT:	SHEET 1 OF 2

All patterns are top/bottom and left/right symmetric

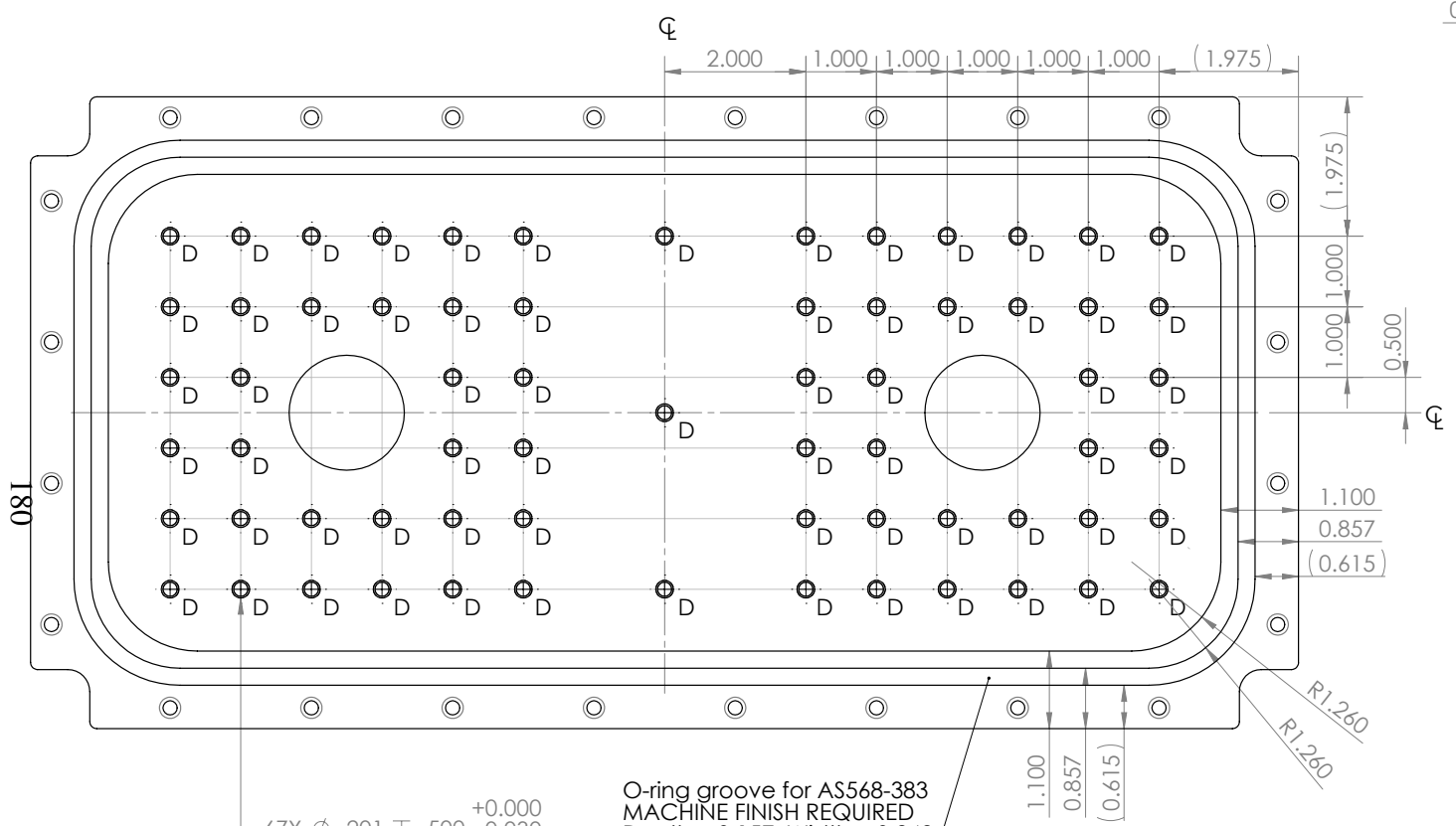

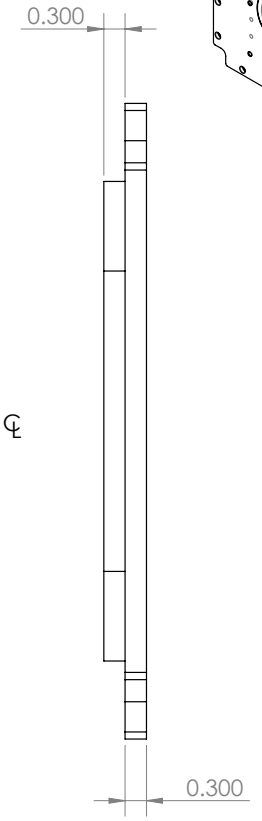

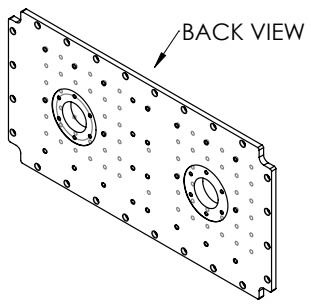

+0.000
67X ⌀ .201 ↧ .500 -0.030
TAP FOR 1/4-20 UNC
MINIMUM TAP DEPTH = 0.420
⌵ ⌀ .250 X 90°, NEAR SIDE
DO NOT PENETRATE

TAPPED HOLES D

O-ring groove for AS568-383
MACHINE FINISH REQUIRED
Depth = 0.157, Width = 0.242
DO NOT PENETRATE

		UNLESS OTHERWISE SPECIFIED:		NAME / DATE
		DIMENSIONS ARE IN INCHES TOLERANCES: FRACTIONAL ± ANGULAR: MACH ± BEND ± TWO PLACE DECIMAL ± THREE PLACE DECIMAL ±0.002	DRAWN CHECKED ENG APPR. MFG APPR. Q.A.	
		INTERPRET GEOMETRIC TOLERANCING PER:	COMMENTS:	
		MATERIAL		
NEXT ASSY	USED ON	FINISH		
APPLICATION		DO NOT SCALE DRAWING		

TITLE:
BACK VIEW

SIZE	DWG. NO.	REV
B	bottom_plate_final	
SCALE: 1:2	WEIGHT:	SHEET 2 OF 2

All patterns are top/bottom and left/right symmetric

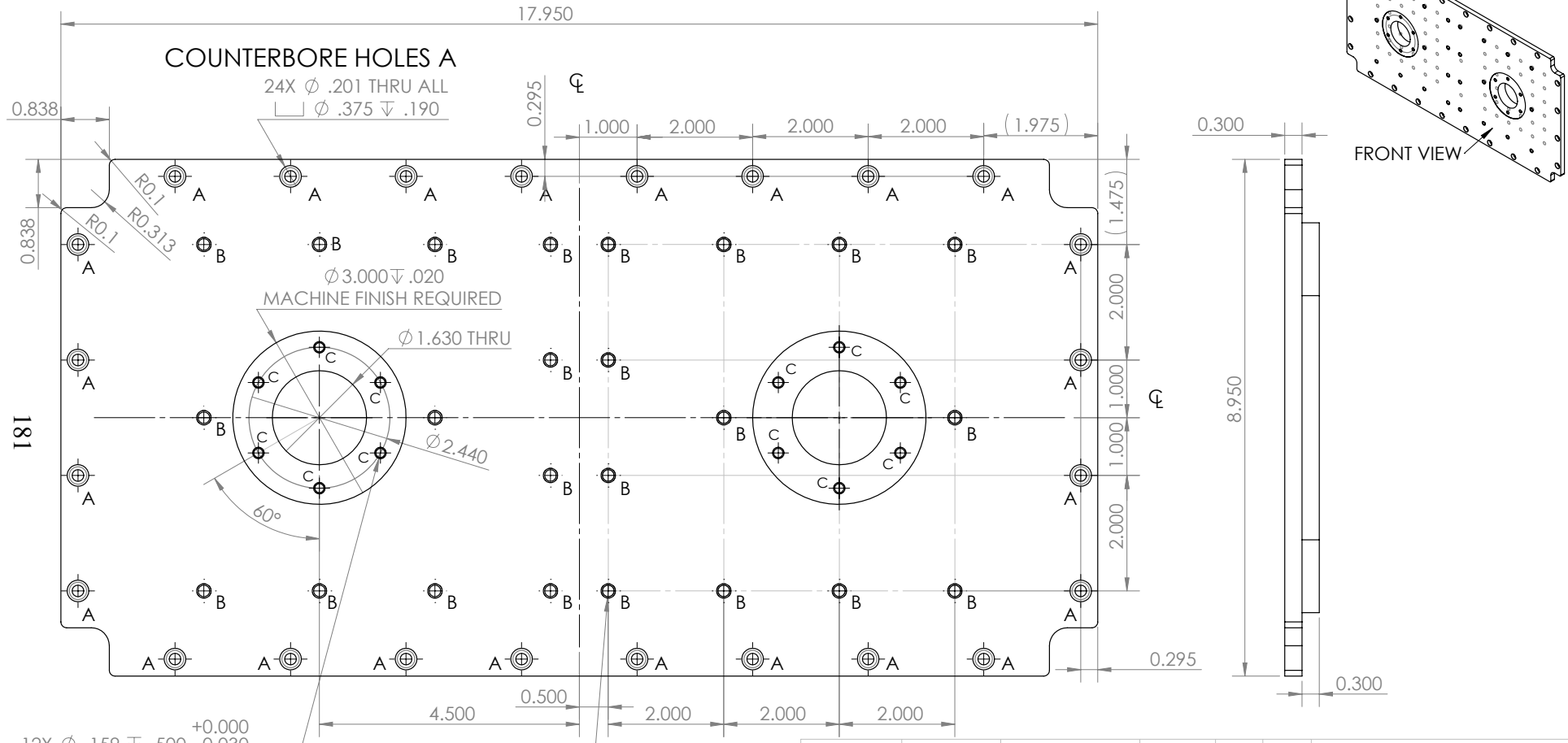

+0.000
12X ⌀ .159 ↧ .500 -0.030
TAP FOR 10-32 UNF
MINIMUM TAP DEPTH = 0.420
⌵ ⌀ .200 X 90°, NEAR SIDE
equally spaced hole pattern
DO NOT PENETRATE

TAPPED HOLES C

+0.000
24X ⌀ .201 ↧ .500 -0.030
TAP FOR 1/4-20 UNC
MINIMUM TAP DEPTH = 0.420
⌵ ⌀ .250 X 90°, NEAR SIDE
DO NOT PENETRATE

TAPPED HOLES B

NEXT ASSY	USED ON	
APPLICATION		DO NOT SCALE DRAWING

UNLESS OTHERWISE SPECIFIED:

DIMENSIONS ARE IN INCHES
TOLERANCES:
FRACTIONAL ±
ANGULAR: MACH ± BEND ±
TWO PLACE DECIMAL ±
THREE PLACE DECIMAL ±0.002

INTERPRET GEOMETRIC TOLERANCING PER:

MATERIAL

FINISH

	NAME	DATE
DRAWN		
CHECKED		
ENG APPR.		
MFG APPR.		
Q.A.		

COMMENTS:

TITLE:
FRONT VIEW

SIZE	DWG. NO.	REV
B	bottom_plate_v2	

SCALE: 1:2 | WEIGHT: | SHEET 1 OF 2

All patterns are top/bottom and left/right symmetric

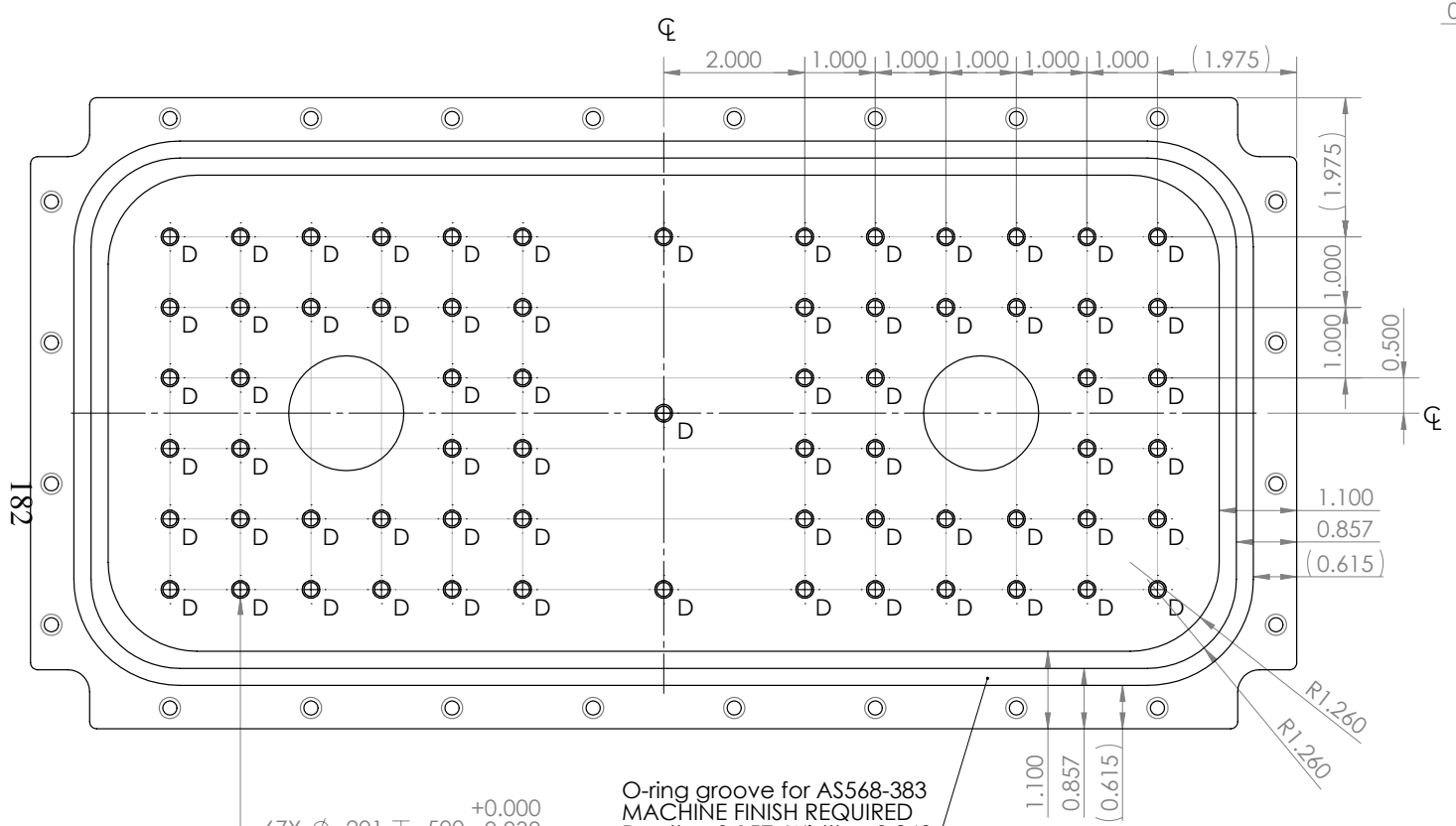

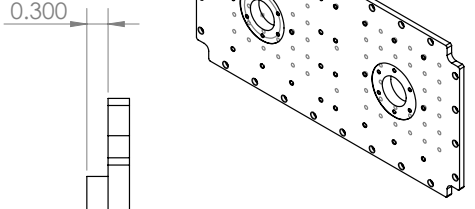

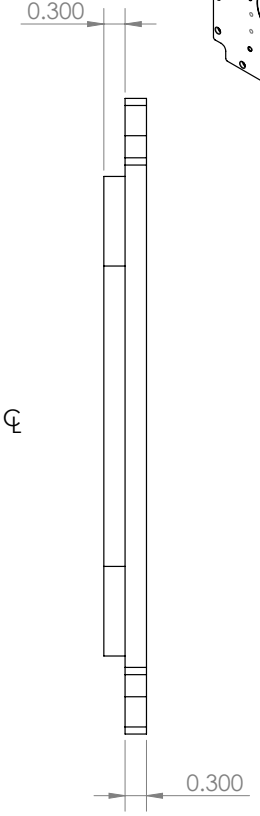

67X ⌀ .201 ↧ .500 +0.000 -0.030
TAP FOR 1/4-20 UNC
MINIMUM TAP DEPTH = 0.420
⌵ ⌀ .250 X 90°, NEAR SIDE
DO NOT PENETRATE

TAPPED HOLES D

O-ring groove for AS568-383
MACHINE FINISH REQUIRED
Depth = 0.157, Width = 0.242
DO NOT PENETRATE

		UNLESS OTHERWISE SPECIFIED:		NAME / DATE
		DIMENSIONS ARE IN INCHES TOLERANCES: FRACTIONAL ± ANGULAR: MACH ± BEND ± TWO PLACE DECIMAL ± THREE PLACE DECIMAL ±0.002	DRAWN CHECKED ENG APPR. MFG APPR. Q.A.	
		INTERPRET GEOMETRIC TOLERANCING PER:	COMMENTS:	
		MATERIAL		
NEXT ASSY	USED ON	FINISH		
APPLICATION		DO NOT SCALE DRAWING		

TITLE: BACK VIEW

SIZE	DWG. NO.	REV
B	bottom_plate_v2	
SCALE: 1:2	WEIGHT:	SHEET 2 OF 2

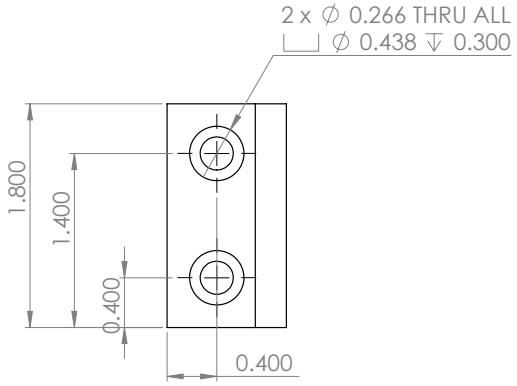

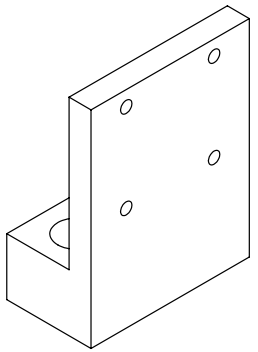

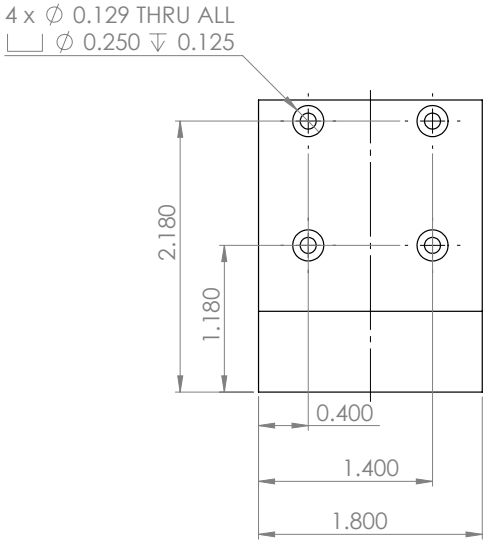

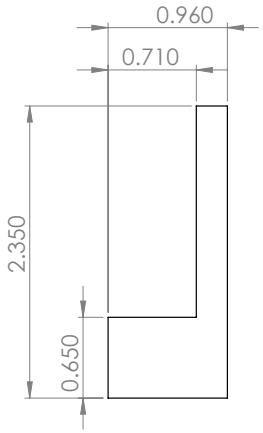

		UNLESS OTHERWISE SPECIFIED:		NAME	DATE
		DIMENSIONS ARE IN INCHES TOLERANCES: FRACTIONAL ± ANGULAR: MACH ± BEND ± TWO PLACE DECIMAL ± THREE PLACE DECIMAL ± 0.005	DRAWN		
			CHECKED		
			ENG APPR.		
			MFG APPR.		
		INTERPRET GEOMETRIC TOLERANCING PER:	Q.A.		
		MATERIAL Aluminum 6061-T6	COMMENTS:		
NEXT ASSY	USED ON	FINISH			
APPLICATION		DO NOT SCALE DRAWING			

TITLE:
Downstream Mirror Adapter Plate

SIZE	DWG. NO.	REV
B		
SCALE: 1:1	WEIGHT:	SHEET 1 OF 1

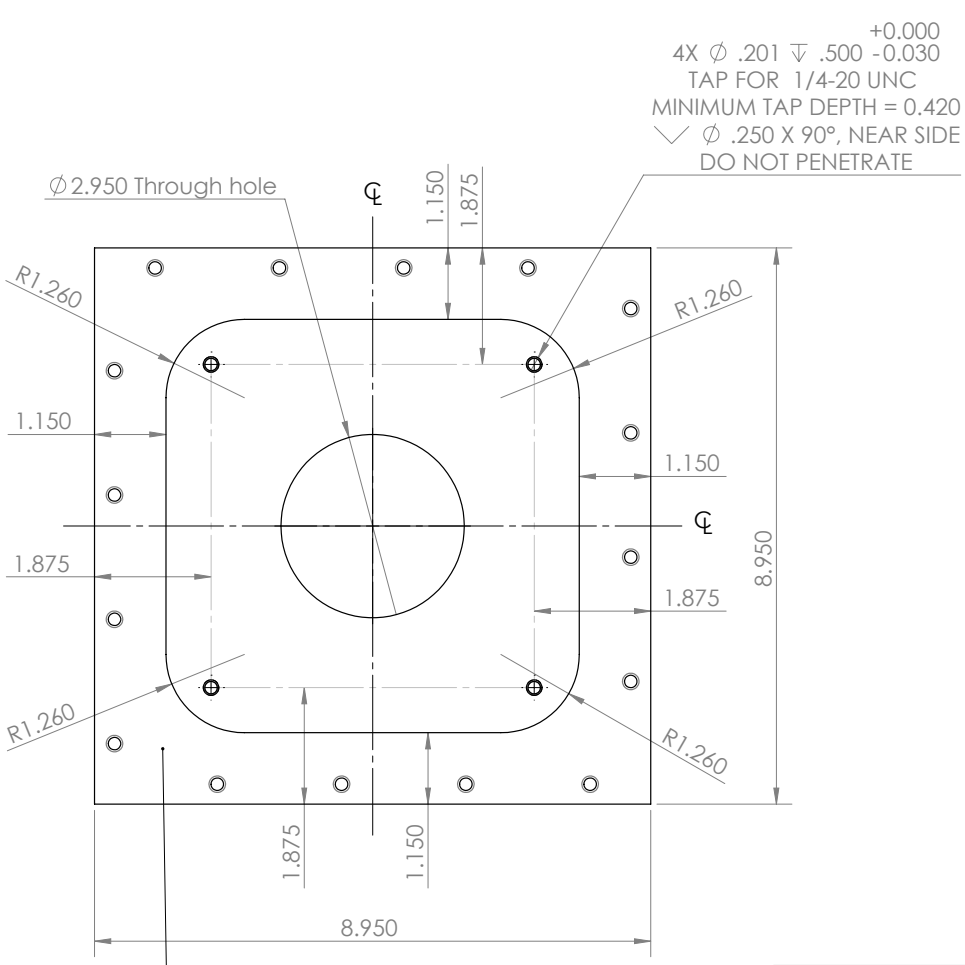

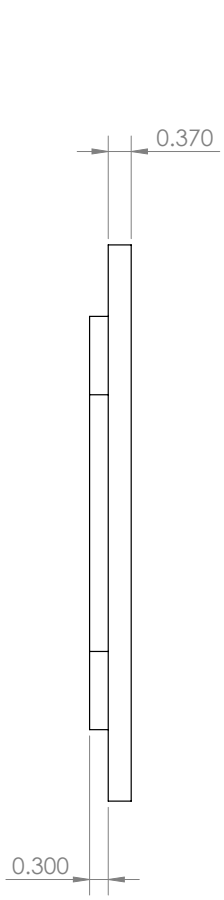

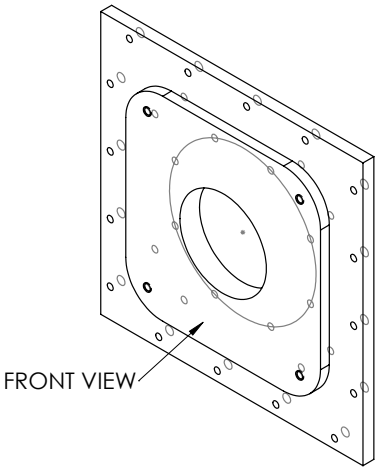

184

		UNLESS OTHERWISE SPECIFIED:		NAME	DATE
		DIMENSIONS ARE IN INCHES TOLERANCES: FRACTIONAL ± ANGULAR: MACH ± BEND ± TWO PLACE DECIMAL ± THREE PLACE DECIMAL ±0.002	DRAWN		
			CHECKED		
			ENG APPR.		
			MFG APPR.		
		INTERPRET GEOMETRIC TOLERANCING PER:	Q.A.		
		MATERIAL	COMMENTS:		
NEXT ASSY	USED ON	FINISH			
APPLICATION		DO NOT SCALE DRAWING			

TITLE:

FRONT VIEW

SIZE	DWG. NO.	REV
B	front_plate_final	
SCALE: 1:2	WEIGHT:	SHEET 1 OF 2

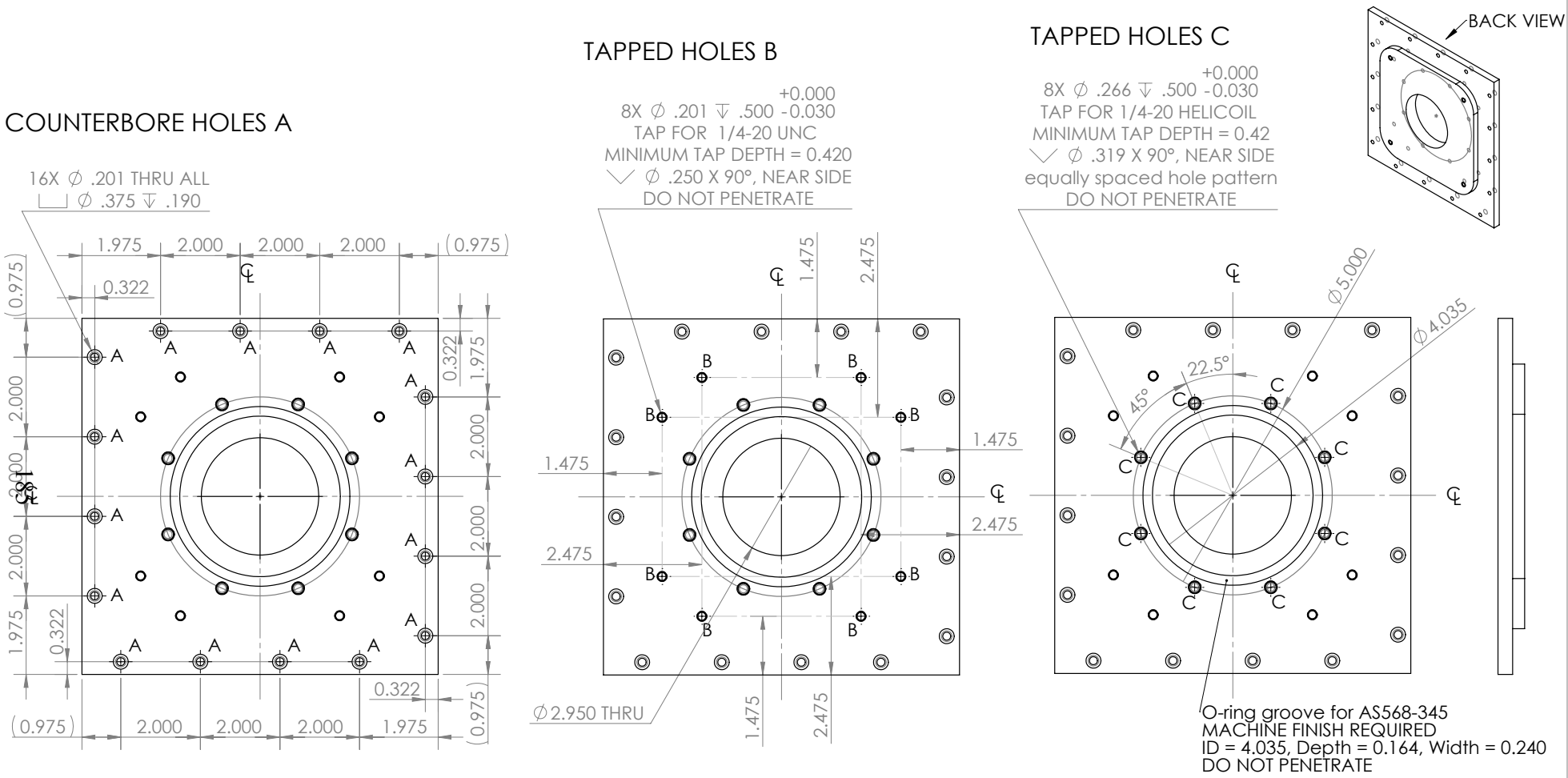

UNLESS OTHERWISE SPECIFIED:		NAME	DATE	
DIMENSIONS ARE IN INCHES TOLERANCES: FRACTIONAL ± ANGULAR: MACH ± BEND ± TWO PLACE DECIMAL ± THREE PLACE DECIMAL ±0.002	DRAWN			TITLE: BACK VIEW
	CHECKED			
	ENG APPR.			
	MFG APPR.			
INTERPRET GEOMETRIC TOLERANCING PER:	Q.A.			
MATERIAL	COMMENTS:			SIZE: B / DWG. NO.: front_plate_final / REV
FINISH				SCALE: 1:2 / WEIGHT: / SHEET 2 OF 2
NEXT ASSY / USED ON				
APPLICATION / DO NOT SCALE DRAWING				

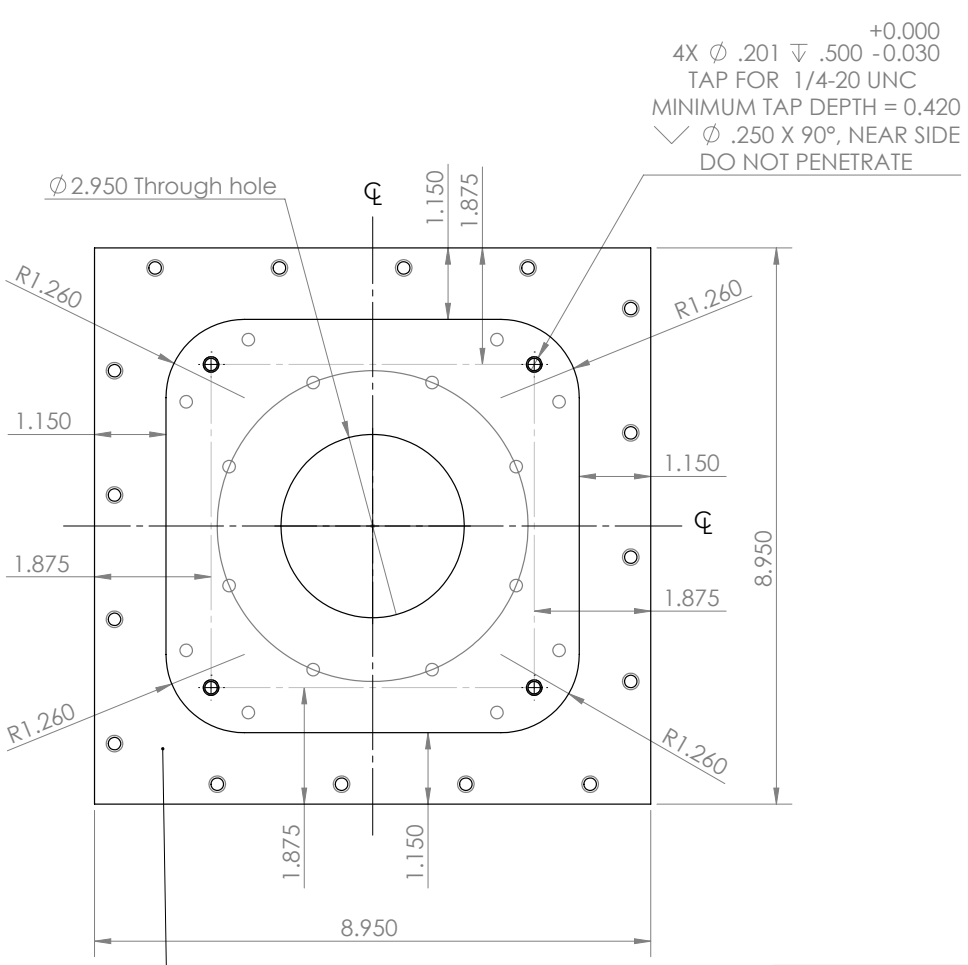

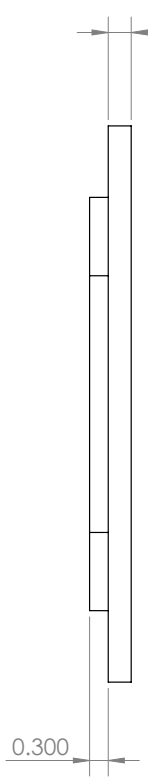

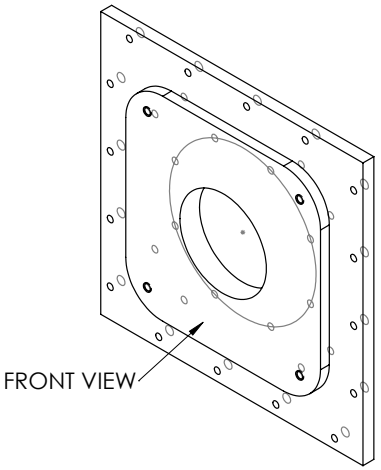

MACHINE FINISH REQUIRED

186

		UNLESS OTHERWISE SPECIFIED:		NAME	DATE
		DIMENSIONS ARE IN INCHES TOLERANCES: FRACTIONAL ± ANGULAR: MACH ± BEND ± TWO PLACE DECIMAL ± THREE PLACE DECIMAL ±0.002	DRAWN		
			CHECKED		
			ENG APPR.		
			MFG APPR.		
		INTERPRET GEOMETRIC TOLERANCING PER:	Q.A.		
		MATERIAL	COMMENTS:		
NEXT ASSY	USED ON	FINISH			
APPLICATION		DO NOT SCALE DRAWING			

TITLE:

FRONT VIEW

SIZE	DWG. NO.	REV
B	front_plate_v2	
SCALE: 1:2	WEIGHT:	SHEET 1 OF 2

COUNTERBORE HOLES A

16X ⌀ .201 THRU ALL
⌴ ⌀ .375 ↧ .190

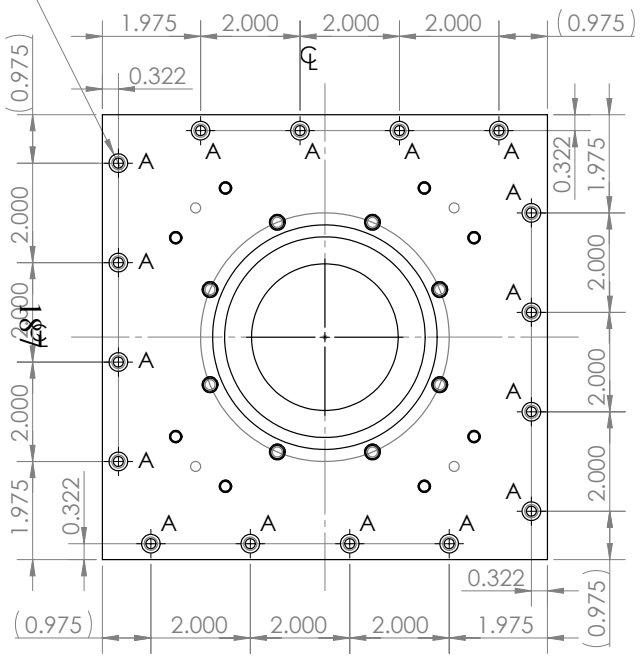

TAPPED HOLES B

+0.000
8X ⌀ .201 ↧ .500 -0.030
TAP FOR 1/4-20 UNC
MINIMUM TAP DEPTH = 0.420
⌵ ⌀ .250 X 90°, NEAR SIDE
DO NOT PENETRATE

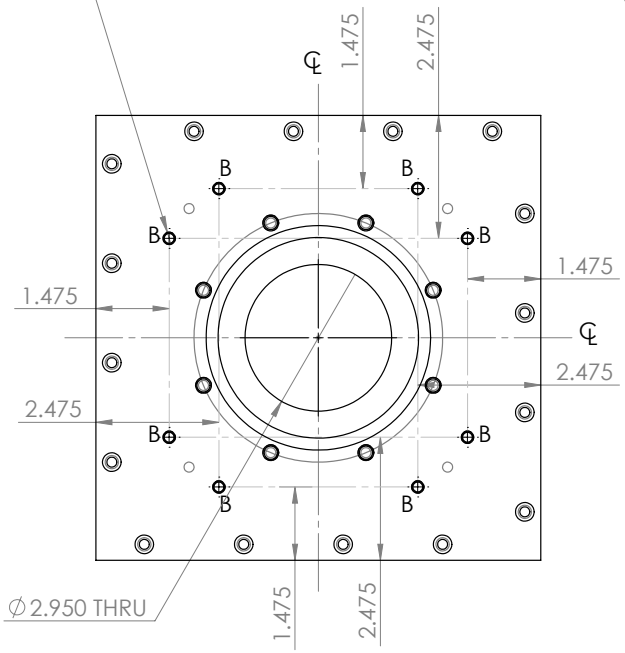

TAPPED HOLES C

+0.000
8X ⌀ .266 ↧ .500 -0.030
TAP FOR 1/4-20 HELICOIL
MINIMUM TAP DEPTH = 0.42
⌵ ⌀ .319 X 90°, NEAR SIDE
equally spaced hole pattern
DO NOT PENETRATE

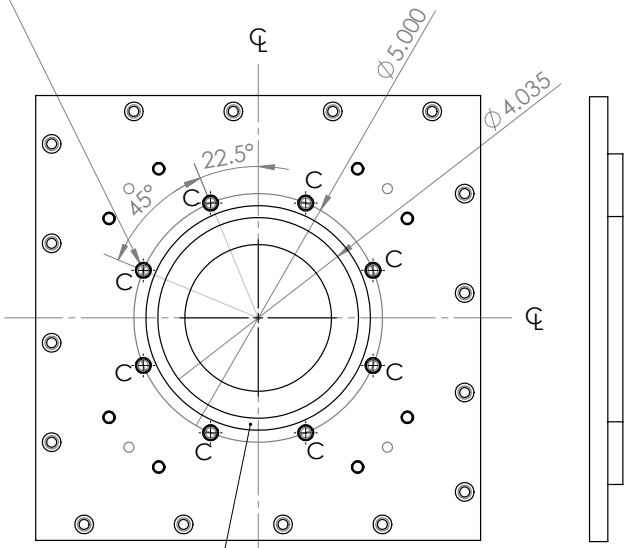

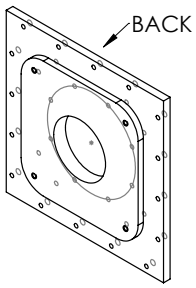

O-ring groove for AS568-345
MACHINE FINISH REQUIRED
ID = 4.035, Depth = 0.164, Width = 0.240
DO NOT PENETRATE

		UNLESS OTHERWISE SPECIFIED:		NAME	DATE
		DIMENSIONS ARE IN INCHES TOLERANCES: FRACTIONAL ± ANGULAR: MACH ± BEND ± TWO PLACE DECIMAL ± THREE PLACE DECIMAL ±0.002	DRAWN		
			CHECKED		
			ENG APPR.		
			MFG APPR.		
		INTERPRET GEOMETRIC TOLERANCING PER:	Q.A.		
		MATERIAL	COMMENTS:		
NEXT ASSY	USED ON	FINISH			
APPLICATION		DO NOT SCALE DRAWING			

TITLE:
BACK VIEW

SIZE	DWG. NO.	REV
B	front_plate_v2	
SCALE: 1:2	WEIGHT:	SHEET 2 OF 2

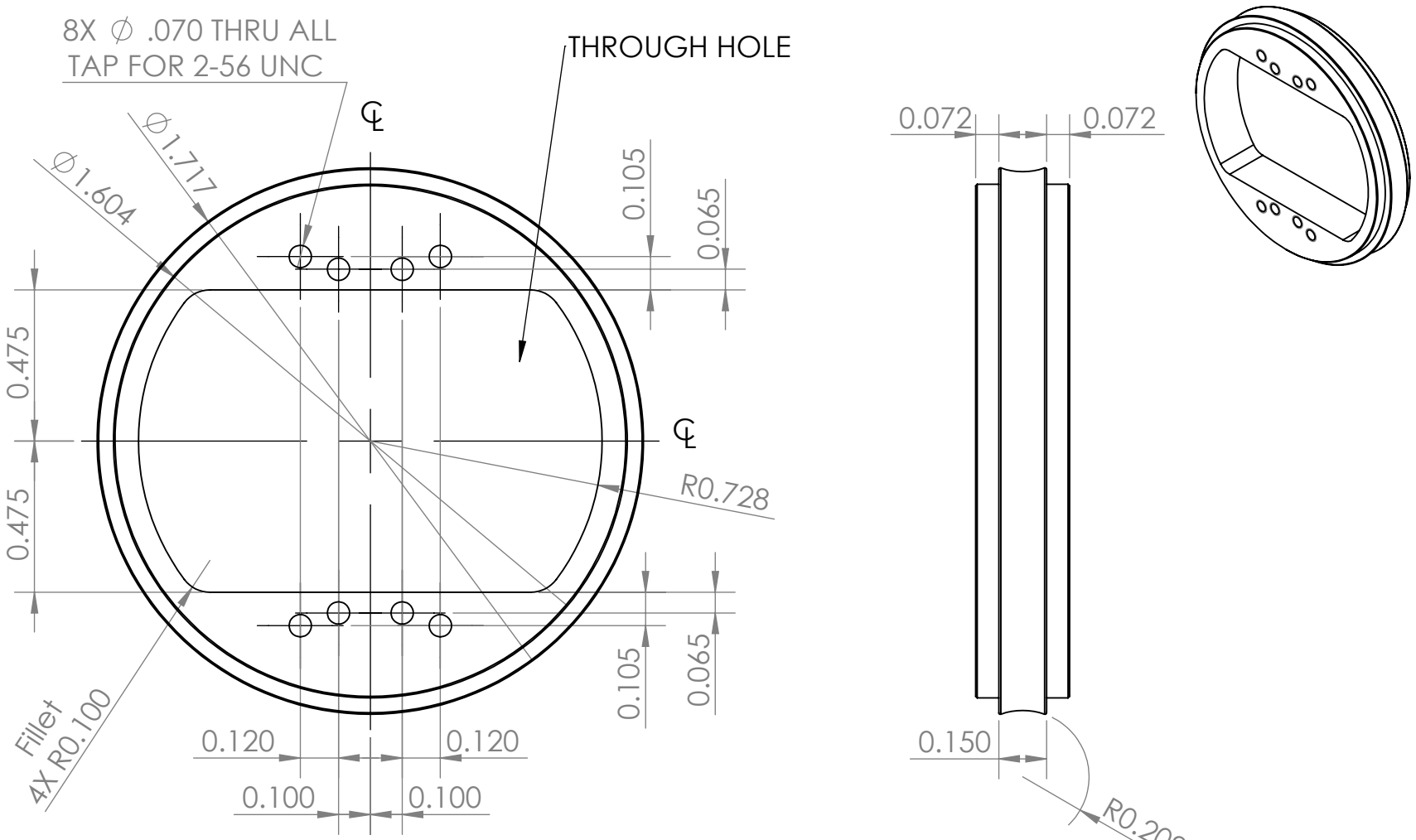

188

		UNLESS OTHERWISE SPECIFIED:		NAME	DATE
		DIMENSIONS ARE IN INCHES TOLERANCES: FRACTIONAL ± ANGULAR: MACH ± BEND ± TWO PLACE DECIMAL ± THREE PLACE DECIMAL ±	DRAWN		
			CHECKED		
			ENG APPR.		
			MFG APPR.		
		INTERPRET GEOMETRIC TOLERANCING PER:	Q.A.		
		MATERIAL	COMMENTS:		
NEXT ASSY	USED ON	FINISH			
APPLICATION		DO NOT SCALE DRAWING			

TITLE:

SIZE	DWG. NO.	REV
A	KF40_in_vacuum_aperture_final	
SCALE: 1:1	WEIGHT:	SHEET 1 OF 1

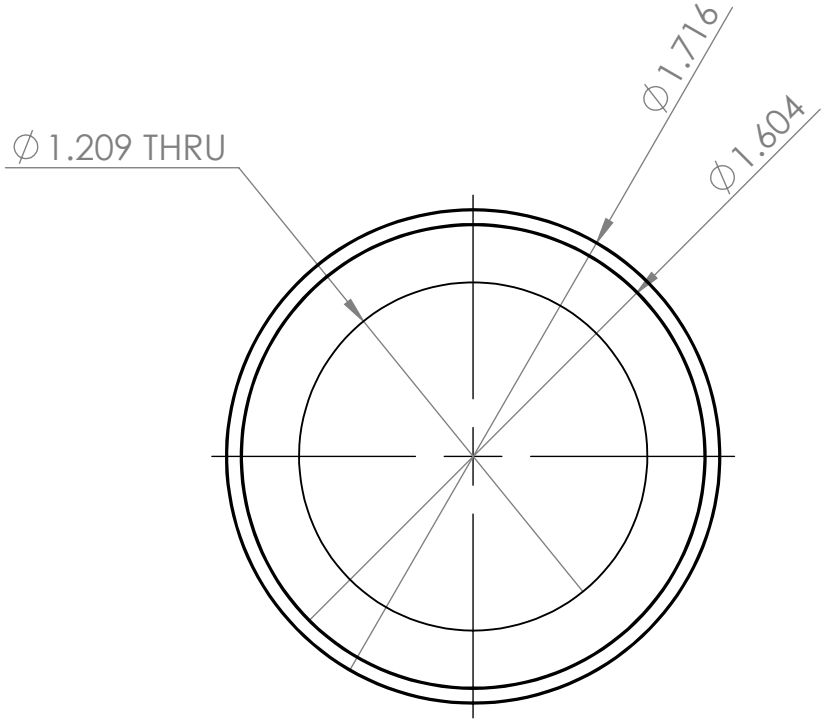

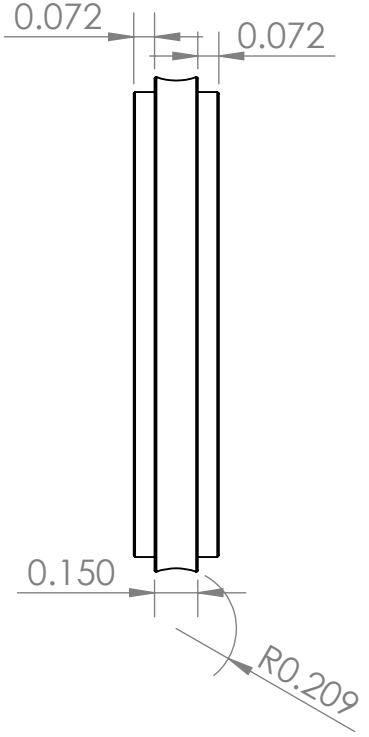

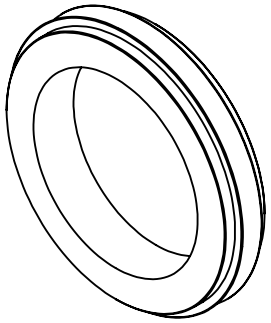

		UNLESS OTHERWISE SPECIFIED:		NAME	DATE
		DIMENSIONS ARE IN INCHES TOLERANCES: FRACTIONAL ± ANGULAR: MACH ± BEND ± TWO PLACE DECIMAL ± THREE PLACE DECIMAL ±	DRAWN		
			CHECKED		
			ENG APPR.		
			MFG APPR.		
		INTERPRET GEOMETRIC TOLERANCING PER:	Q.A.		
		MATERIAL	COMMENTS:		
NEXT ASSY	USED ON	FINISH			
APPLICATION		DO NOT SCALE DRAWING			

TITLE:

SIZE	DWG. NO.	REV
A	KF40_in_vacuum_aperture_for_top_plate_final	
SCALE: 1:1	WEIGHT:	SHEET 1 OF 1

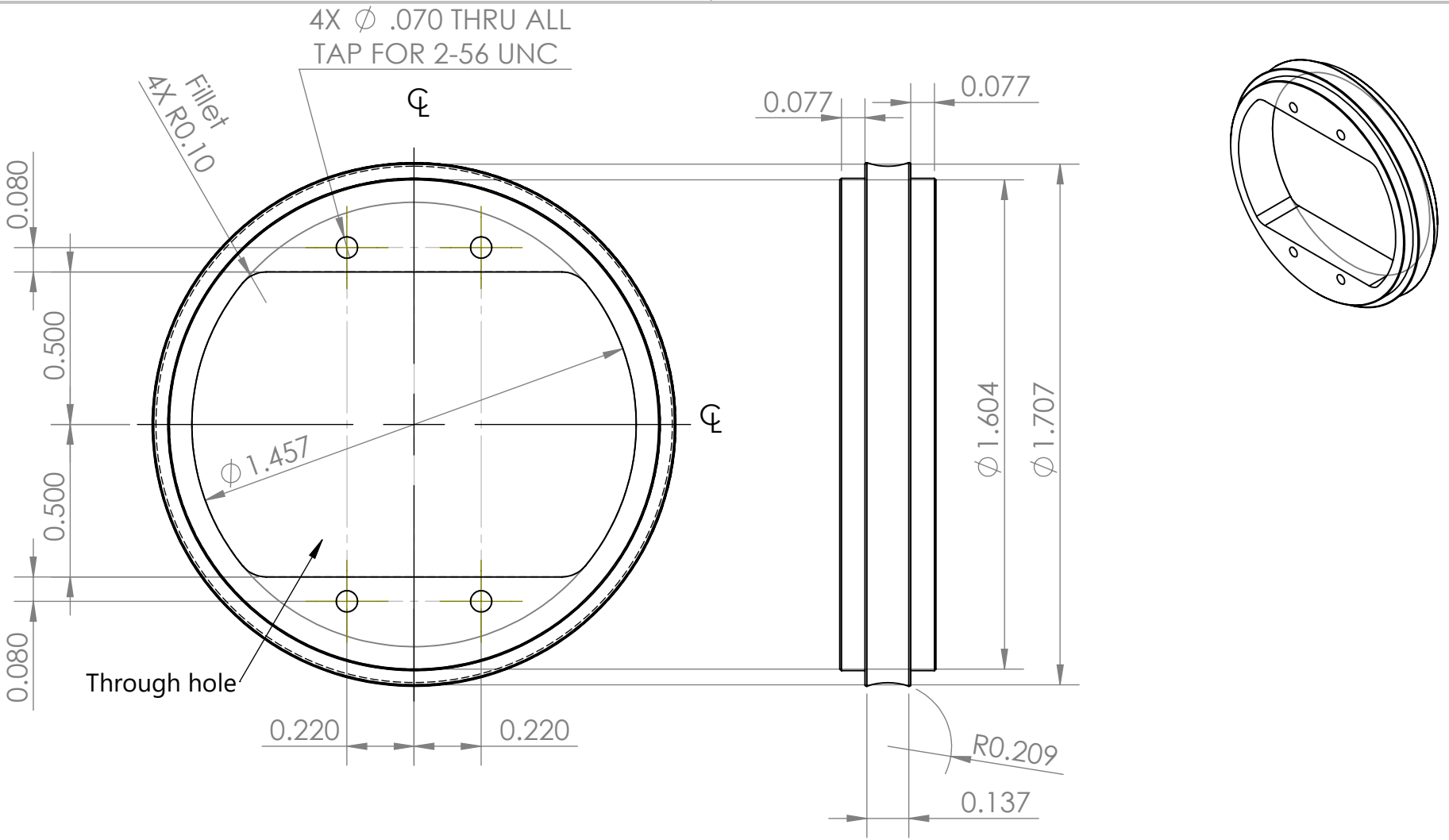

		UNLESS OTHERWISE SPECIFIED:		NAME	DATE
		DIMENSIONS ARE IN INCHES TOLERANCES: FRACTIONAL ± ANGULAR: MACH ± BEND ± TWO PLACE DECIMAL ± THREE PLACE DECIMAL ±	DRAWN		
			CHECKED		
			ENG APPR.		
			MFG APPR.		
		INTERPRET GEOMETRIC TOLERANCING PER:	Q.A.		
		MATERIAL Aluminum 6061-T6	COMMENTS:		
NEXT ASSY	USED ON	FINISH			
APPLICATION		DO NOT SCALE DRAWING			

TITLE:

KF-40 Aktor centering ring

SIZE	DWG. NO.	REV
A		

SCALE: 1:1	WEIGHT:	SHEET 1 OF 1

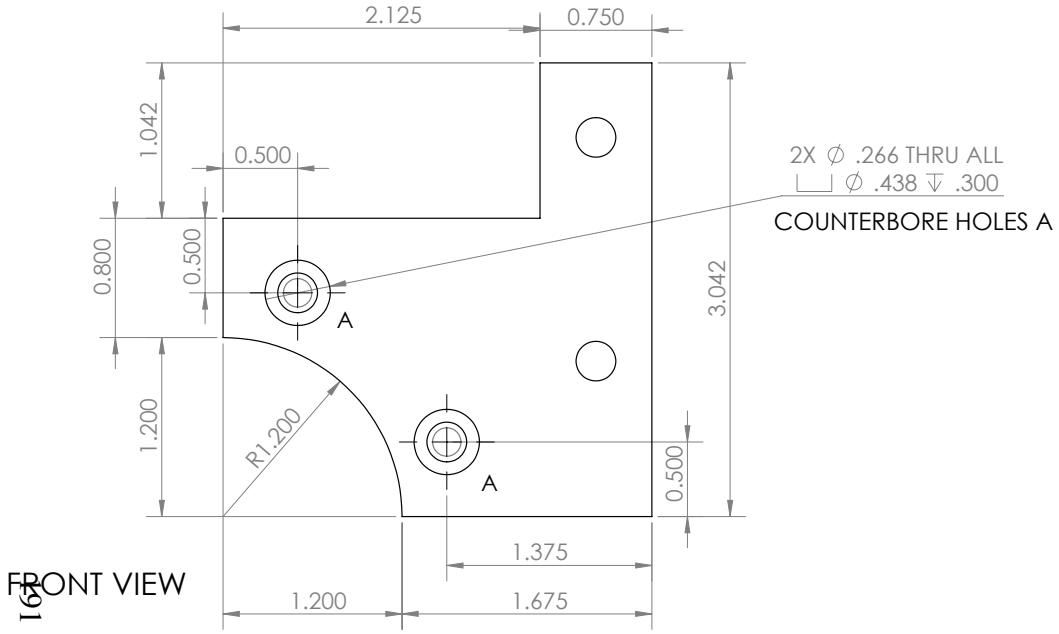

FRONT VIEW

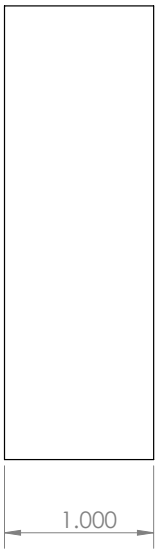

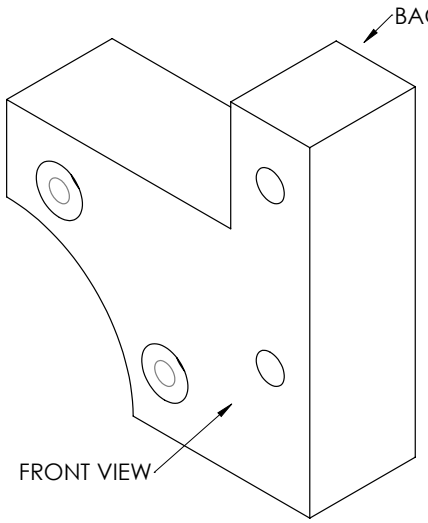

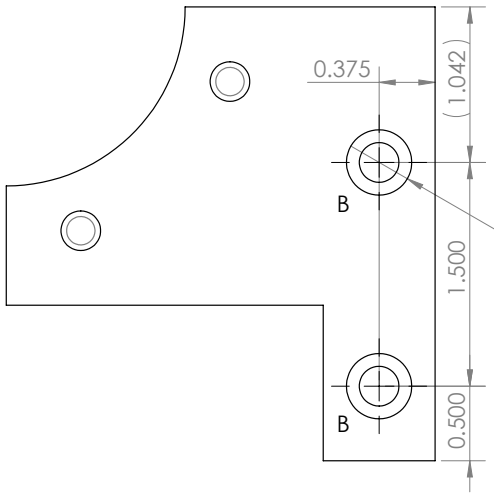

BACK VIEW

		UNLESS OTHERWISE SPECIFIED:		NAME	DATE
		DIMENSIONS ARE IN INCHES TOLERANCES: FRACTIONAL ± ANGULAR: MACH ± BEND ± TWO PLACE DECIMAL ± THREE PLACE DECIMAL ±0.002	DRAWN		
			CHECKED		
			ENG APPR.		
			MFG APPR.		
		INTERPRET GEOMETRIC TOLERANCING PER:	Q.A.		
		MATERIAL	COMMENTS:		
NEXT ASSY	USED ON	FINISH			
APPLICATION		DO NOT SCALE DRAWING			

TITLE:
PCB_mount_left

SIZE	DWG. NO.	REV
B	PCB_mount_left_final	
SCALE: 1:1	WEIGHT:	SHEET 1 OF 1

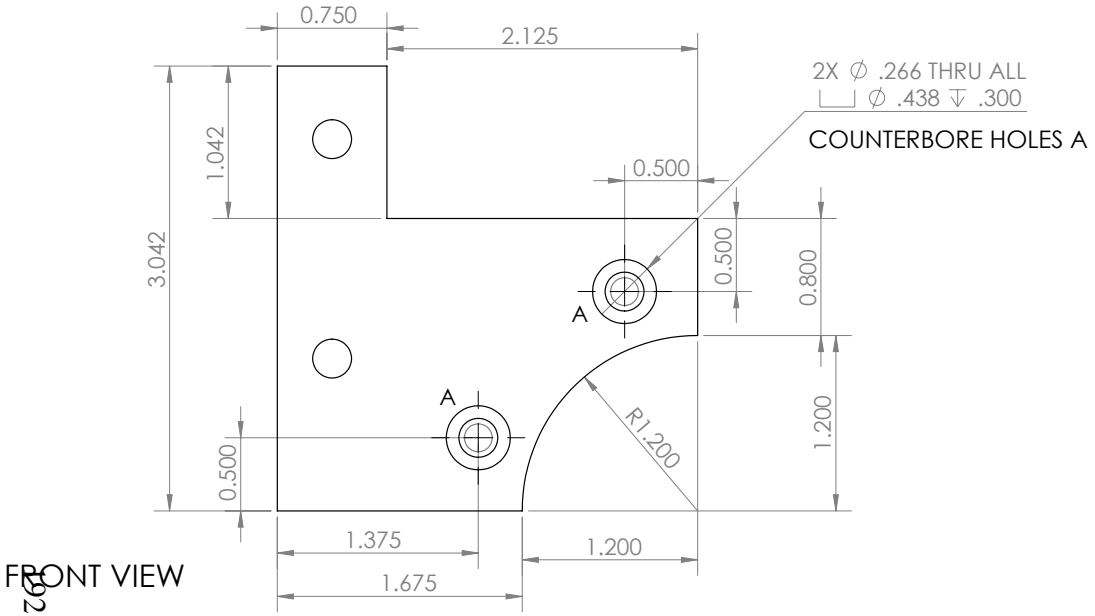

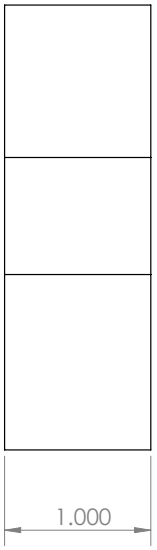

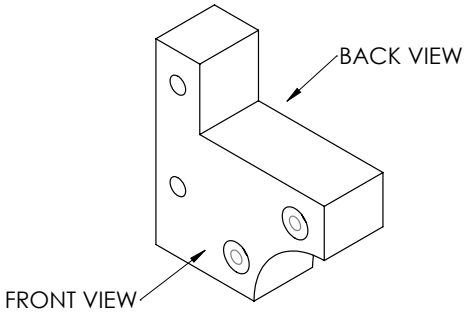

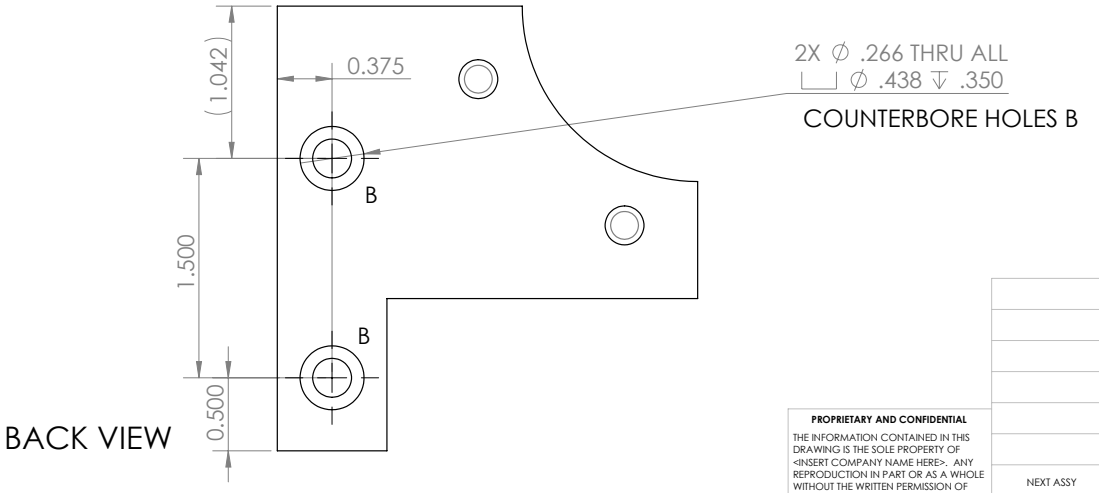

		UNLESS OTHERWISE SPECIFIED:		NAME	DATE
		DIMENSIONS ARE IN INCHES TOLERANCES: FRACTIONAL ± ANGULAR: MACH ± BEND ± TWO PLACE DECIMAL ± THREE PLACE DECIMAL ±0.002	DRAWN		
			CHECKED		
			ENG APPR.		
			MFG APPR.		
		INTERPRET GEOMETRIC TOLERANCING PER:	Q.A.		
		MATERIAL	COMMENTS:		
NEXT ASSY	USED ON	FINISH			
APPLICATION		DO NOT SCALE DRAWING			

TITLE:
PCB_mount_right

SIZE	DWG. NO.	REV
B	PCB_mount_right_final	

SCALE: 1:1 | WEIGHT: | SHEET 1 OF 1

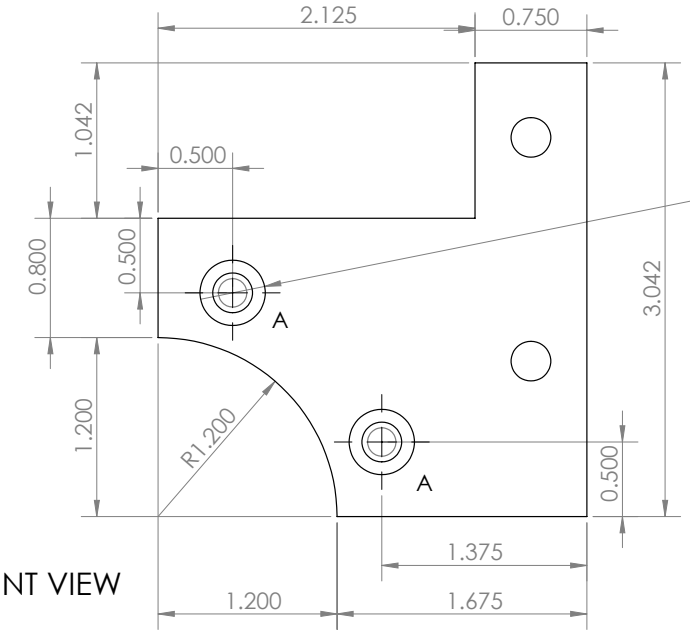

2X ∅ .266 THRU ALL
⌴ ∅ .438 ↧ .300
COUNTERBORE HOLES A

FRONT VIEW

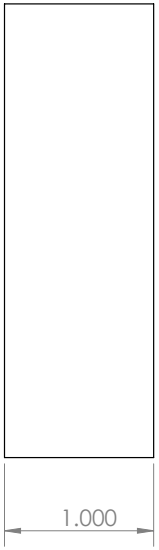

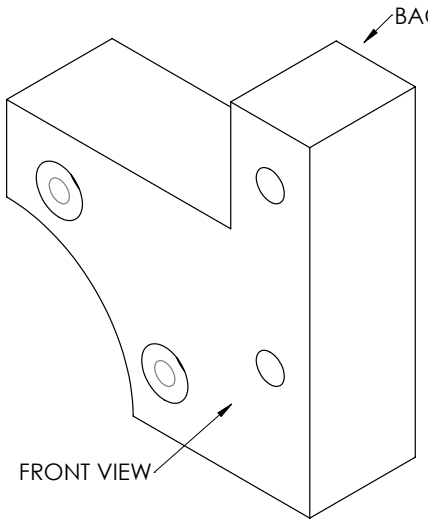

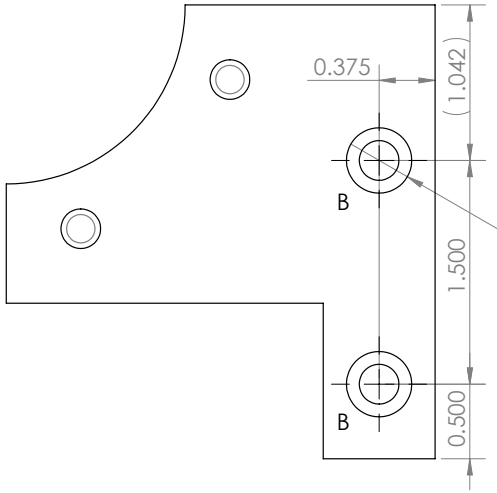

COUNTERBORE HOLES B
2X ∅ .266 THRU ALL
⌴ ∅ .438 ↧ .350

BACK VIEW

		UNLESS OTHERWISE SPECIFIED:		NAME	DATE
		DIMENSIONS ARE IN INCHES TOLERANCES: FRACTIONAL ± ANGULAR: MACH ± BEND ± TWO PLACE DECIMAL ± THREE PLACE DECIMAL ±0.002	DRAWN		
			CHECKED		
			ENG APPR.		
			MFG APPR.		
		INTERPRET GEOMETRIC TOLERANCING PER:	Q.A.		
		MATERIAL	COMMENTS:		
NEXT ASSY	USED ON	FINISH			
APPLICATION		DO NOT SCALE DRAWING			

TITLE:
PCB_mount_left

SIZE	DWG. NO.	REV
B	PCB_mount_yuiki_1_left	
SCALE: 1:1	WEIGHT:	SHEET 1 OF 1

FRONT VIEW

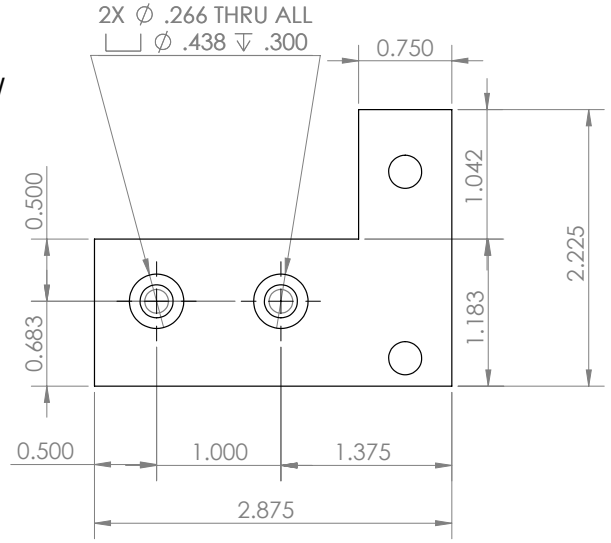

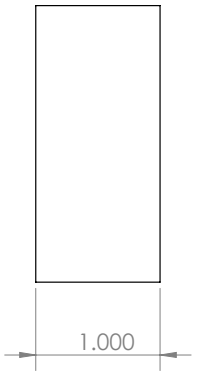

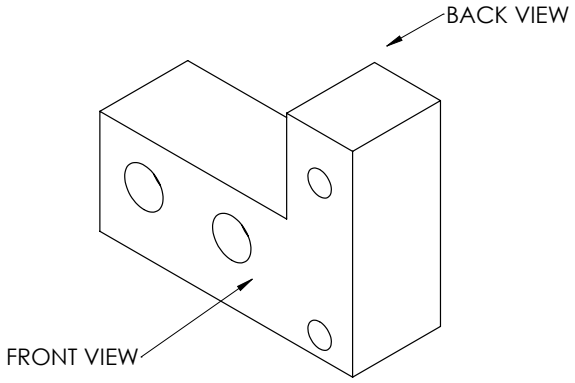

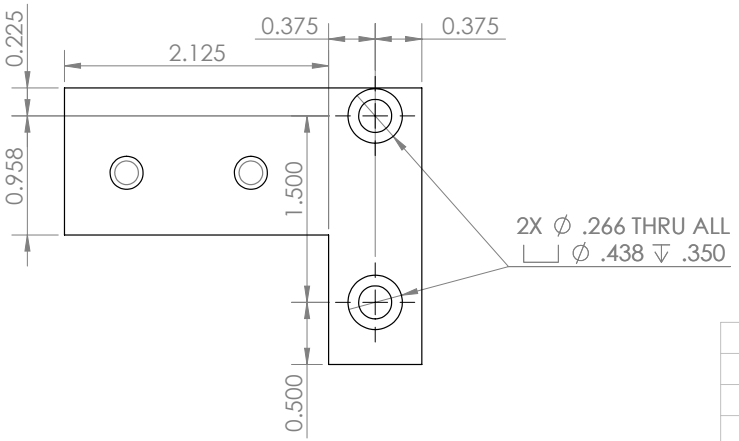

BACK VIEW

194

		UNLESS OTHERWISE SPECIFIED:		NAME	DATE
		DIMENSIONS ARE IN INCHES TOLERANCES: FRACTIONAL ± ANGULAR: MACH ± BEND ± TWO PLACE DECIMAL ± THREE PLACE DECIMAL ±	DRAWN		
			CHECKED		
			ENG APPR.		
			MFG APPR.		
		INTERPRET GEOMETRIC TOLERANCING PER:	Q.A.		
		MATERIAL	COMMENTS:		
		FINISH			
NEXT ASSY	USED ON				
APPLICATION		DO NOT SCALE DRAWING			

TITLE:

SIZE	DWG. NO.	REV
B	PC_mount_yuiki_1_left_for_new_side_plate_midle	

SCALE: 1:1 | WEIGHT: | SHEET 1 OF 1

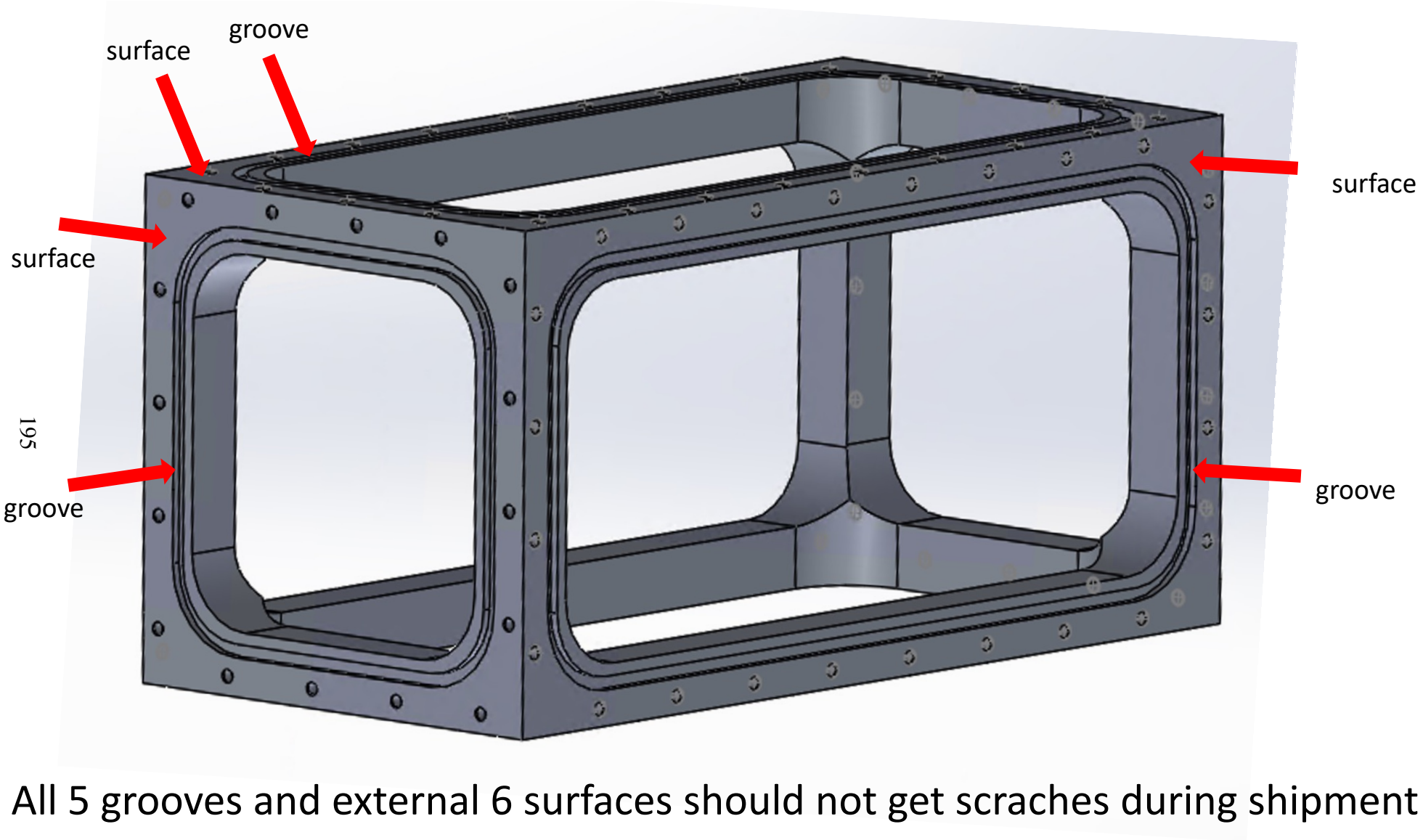

All 5 grooves and external 6 surfaces should not get scraches during shipment

All patterns are top/bottom and left/right symmetric

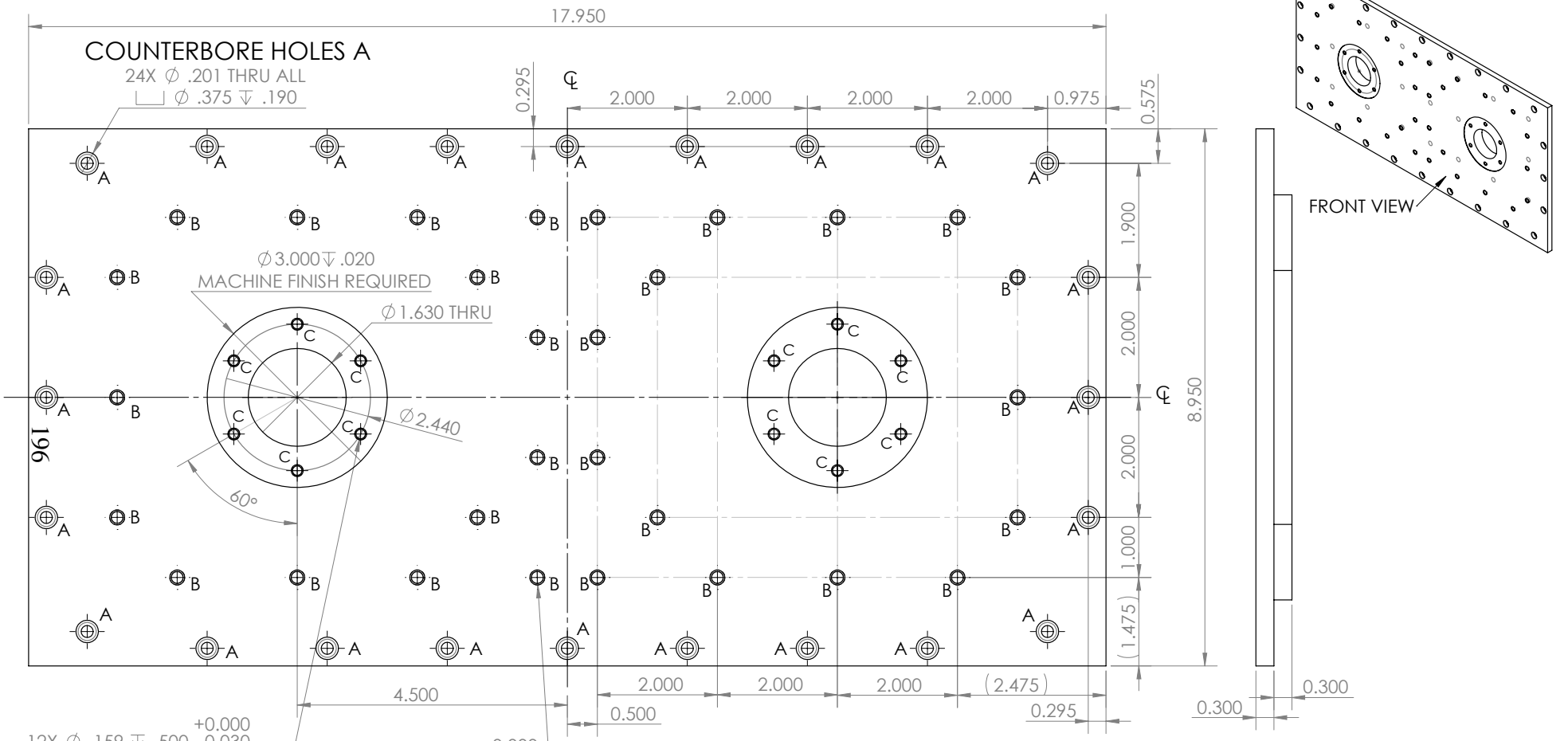

			NAME	DATE
UNLESS OTHERWISE SPECIFIED:		DRAWN		
DIMENSIONS ARE IN INCHES TOLERANCES: FRACTIONAL ± ANGULAR: MACH ± BEND ± TWO PLACE DECIMAL ± THREE PLACE DECIMAL ±0.002		CHECKED		
		ENG APPR.		
		MFG APPR.		
INTERPRET GEOMETRIC TOLERANCING PER:		Q.A.		
MATERIAL		COMMENTS:		
FINISH				
NEXT ASSY	USED ON			
APPLICATION	DO NOT SCALE DRAWING			

TITLE:

FRONT VIEW

SIZE	DWG. NO.	REV
B	side_plate_final	

SCALE: 1:2 | WEIGHT: | SHEET 1 OF 2

All patterns are top/bottom and left/right symmetric

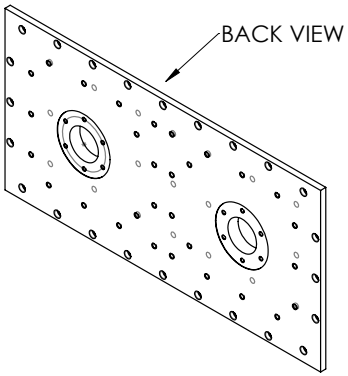

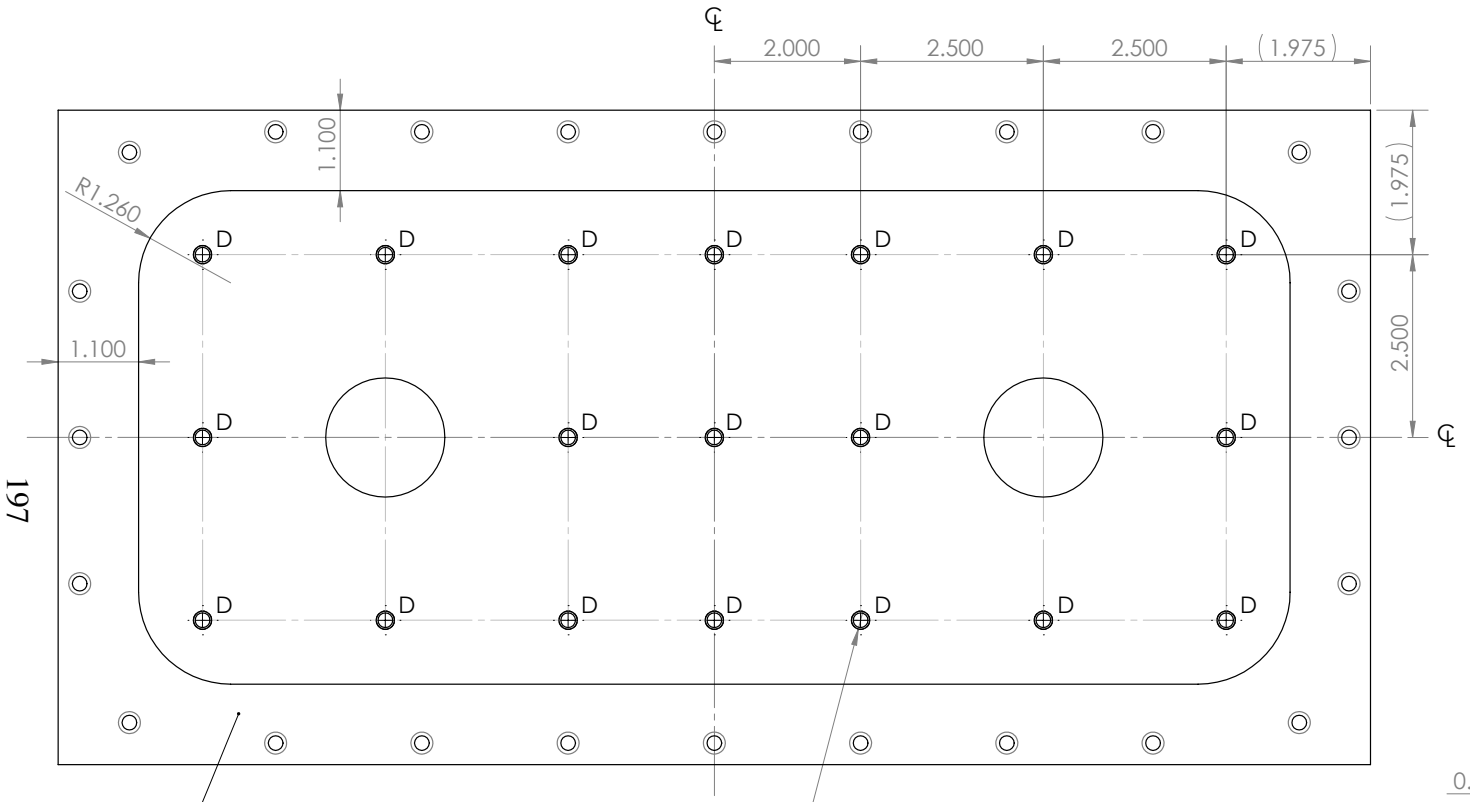

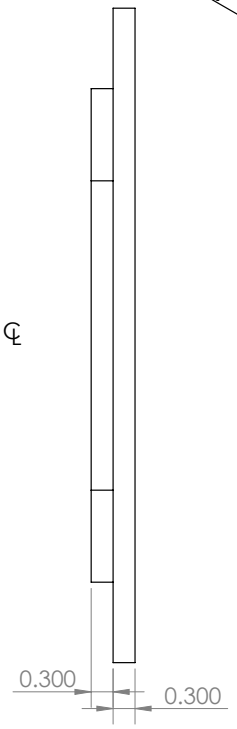

MACHINE FINISH REQUIRED

19X ∅ .201 ↧ .500 +0.000 -0.030
TAP FOR 1/4-20 UNC
MINIMUM TAP DEPTH = 0.420
⌵ ∅ .250 X 90°, NEAR SIDE
DO NOT PENETRATE

TAPPED HOLES D

NEXT ASSY	USED ON
APPLICATION	

UNLESS OTHERWISE SPECIFIED:
DIMENSIONS ARE IN INCHES
TOLERANCES:
FRACTIONAL ±
ANGULAR: MACH ± BEND ±
TWO PLACE DECIMAL ±
THREE PLACE DECIMAL ±0.002
INTERPRET GEOMETRIC TOLERANCING PER:
MATERIAL
FINISH
DO NOT SCALE DRAWING

	NAME	DATE
DRAWN		
CHECKED		
ENG APPR.		
MFG APPR.		
Q.A.		

COMMENTS:

TITLE:
BACK VIEW

SIZE	DWG. NO.	REV
	Bside_plate_final	
SCALE: 1:2	WEIGHT:	SHEET 2 OF 2

All patterns are top/bottom and left/right symmetric

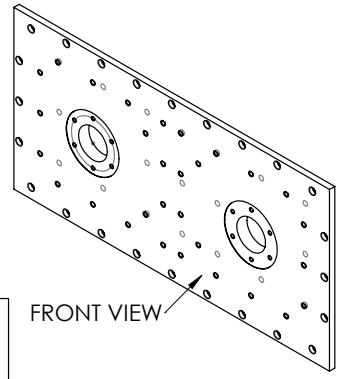

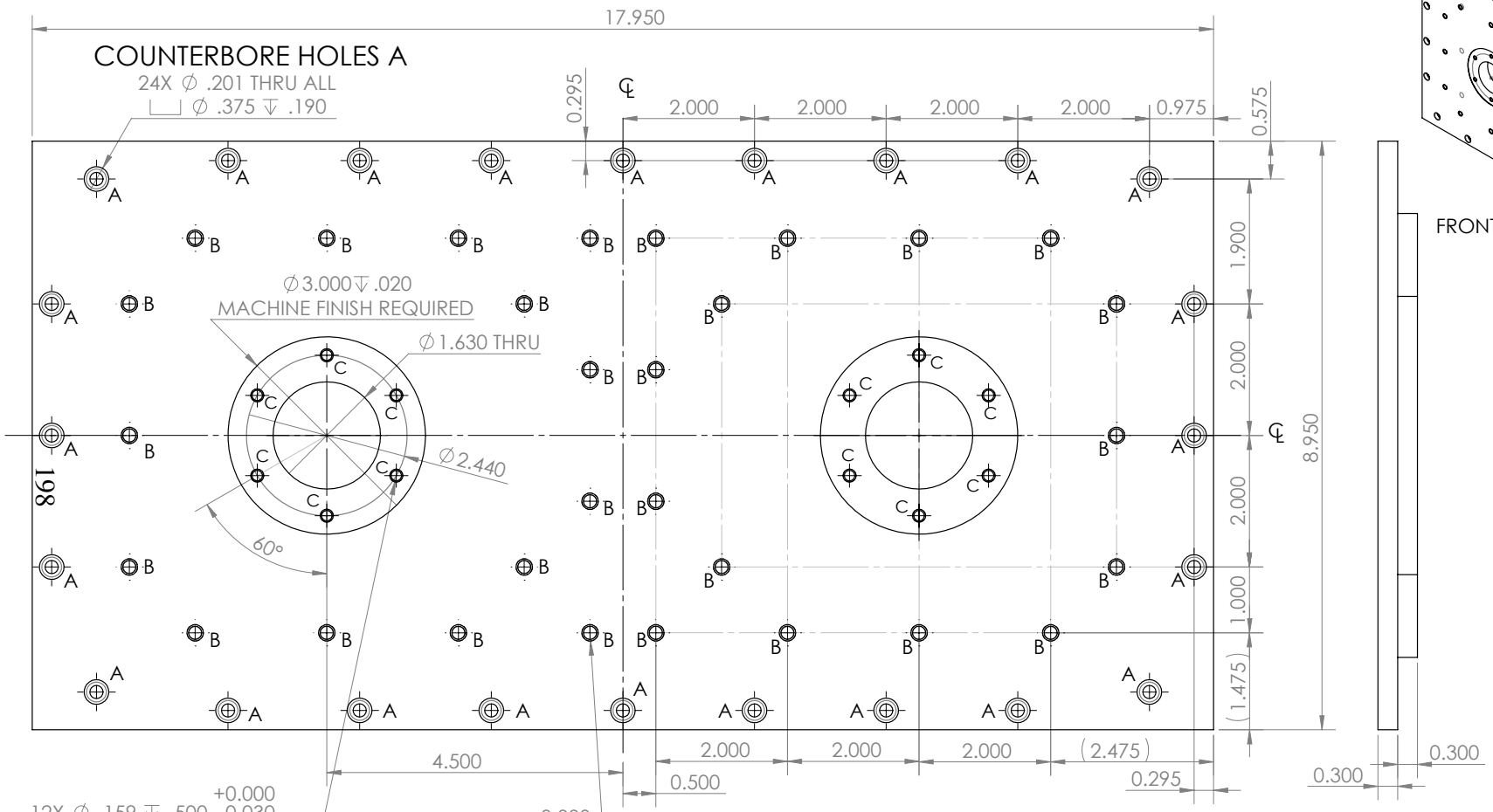

TAPPED HOLES C

TAPPED HOLES B

UNLESS OTHERWISE SPECIFIED:	NAME	DATE
DIMENSIONS ARE IN INCHES TOLERANCES: FRACTIONAL ± ANGULAR: MACH ± BEND ± TWO PLACE DECIMAL ± THREE PLACE DECIMAL ±0.002	DRAWN	
	CHECKED	
	ENG APPR.	
	MFG APPR.	
INTERPRET GEOMETRIC TOLERANCING PER:	Q.A.	
MATERIAL	COMMENTS:	
FINISH		
NEXT ASSY / USED ON		
APPLICATION / DO NOT SCALE DRAWING		

TITLE: FRONT VIEW

SIZE	DWG. NO.	REV
B	side_plate_v2	
SCALE: 1:2	WEIGHT:	SHEET 1 OF 2

All patterns are top/bottom and left/right symmetric

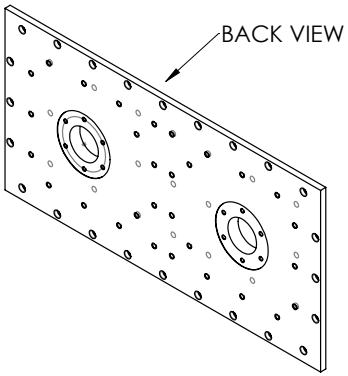

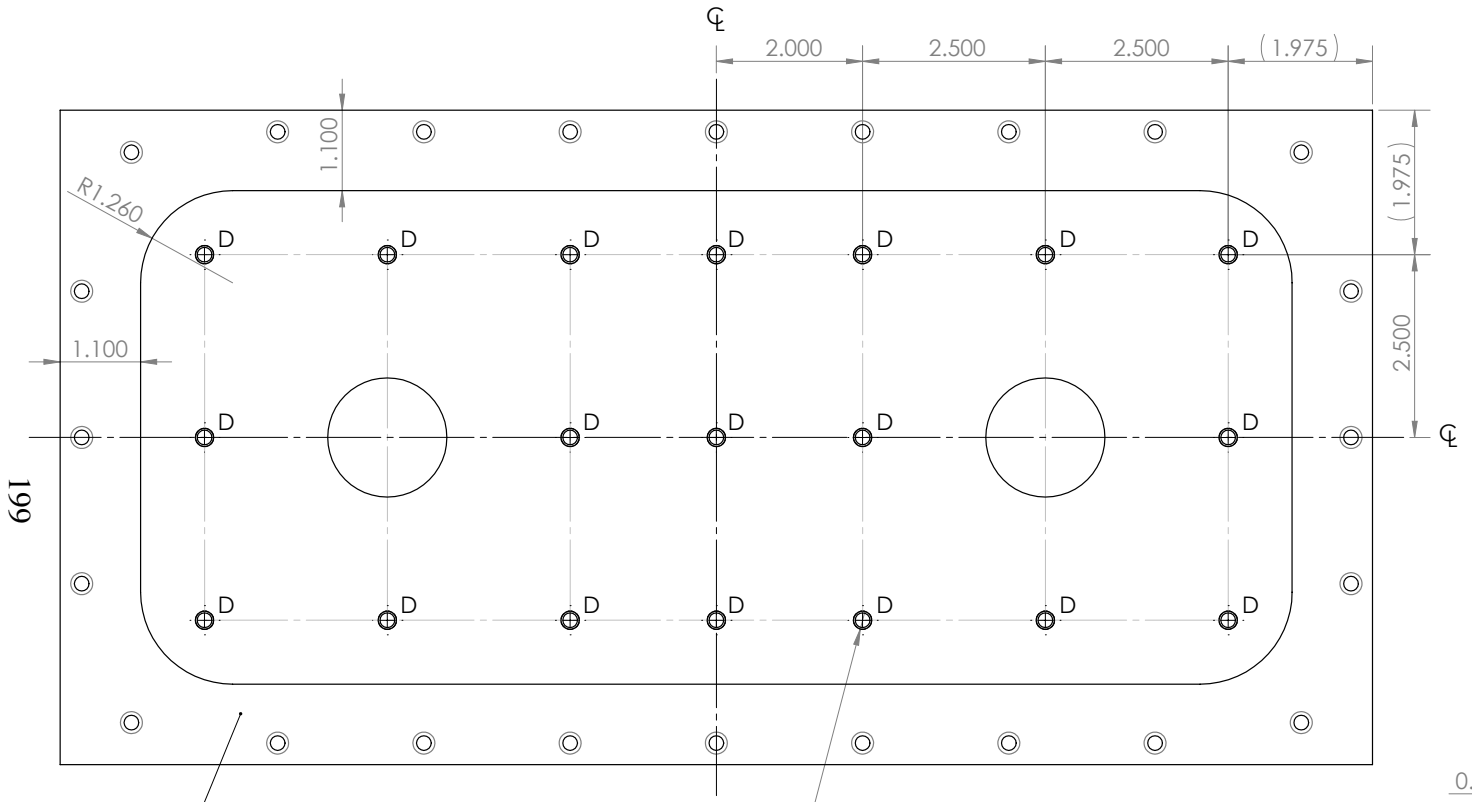

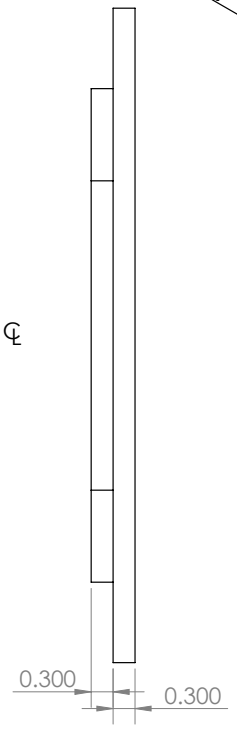

MACHINE FINISH REQUIRED

19X ∅ .201 ↧ .500 +0.000 -0.030
TAP FOR 1/4-20 UNC
MINIMUM TAP DEPTH = 0.420
⌵ ∅ .250 X 90°, NEAR SIDE
DO NOT PENETRATE

TAPPED HOLES D

		UNLESS OTHERWISE SPECIFIED:		NAME / DATE
		DIMENSIONS ARE IN INCHES TOLERANCES: FRACTIONAL ± ANGULAR: MACH ± BEND ± TWO PLACE DECIMAL ± THREE PLACE DECIMAL ±0.002	DRAWN	
			CHECKED	
			ENG APPR.	
			MFG APPR.	
		INTERPRET GEOMETRIC TOLERANCING PER:	Q.A.	
		MATERIAL	COMMENTS:	
NEXT ASSY	USED ON	FINISH		
APPLICATION		DO NOT SCALE DRAWING		

TITLE: BACK VIEW

SIZE	DWG. NO.	REV
B	side_plate_v2	
SCALE: 1:2	WEIGHT:	SHEET 2 OF 2

All patterns are top/bottom and left/right symmetric

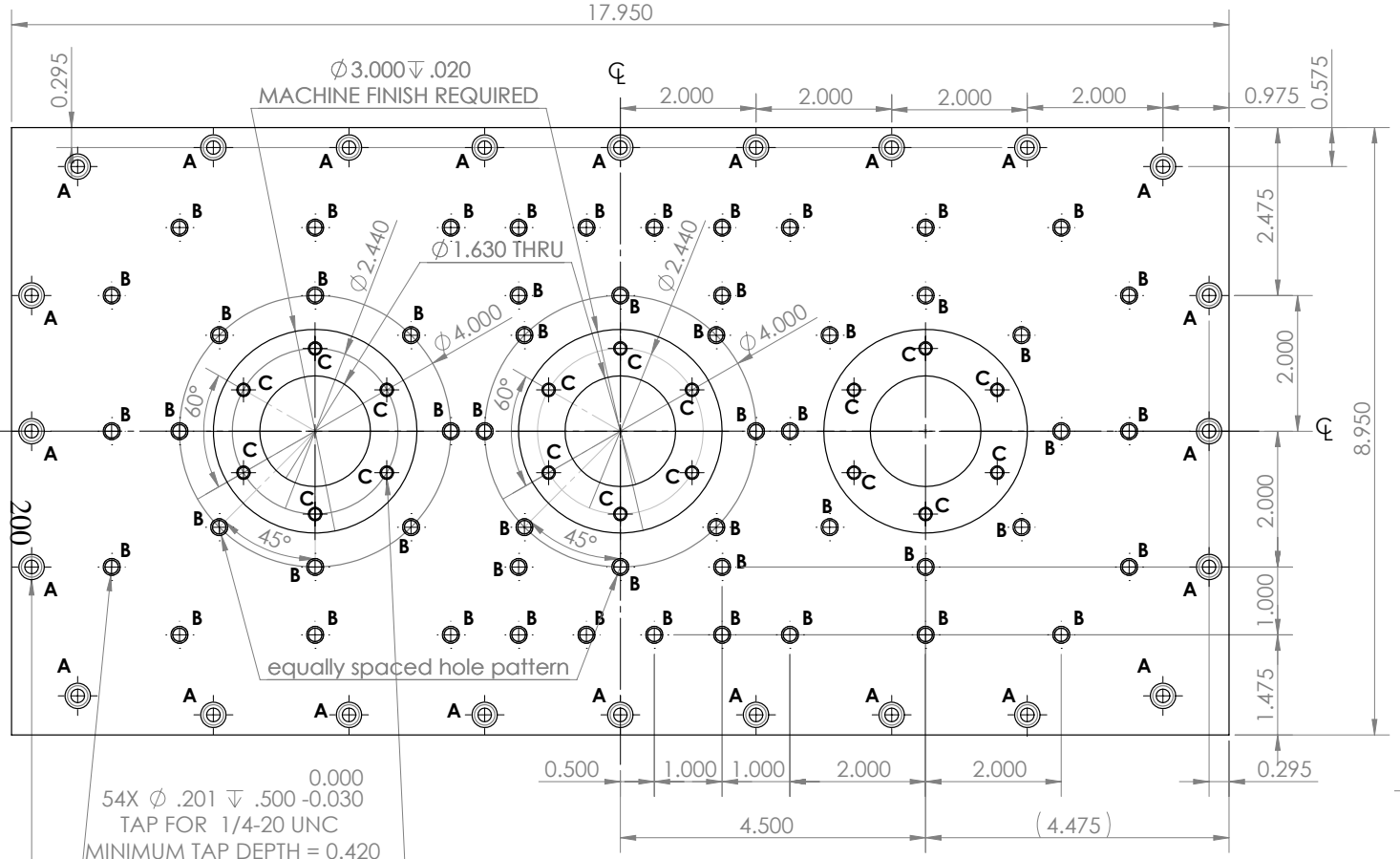

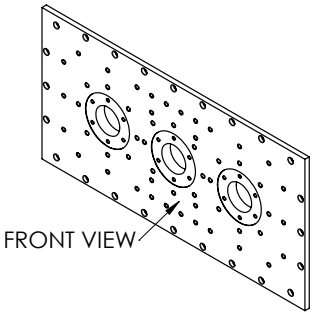

0.000
54X ∅ .201 ↧ .500 -0.030
TAP FOR 1/4-20 UNC
MINIMUM TAP DEPTH = 0.420
⌵ ∅ .250 X 90°, NEAR SIDE
DO NOT PENETRATE
TAPPED HOLES B

24X ∅ .201 THRU ALL
⌴ ∅ .375 ↧ .190
TAPPED HOLES A

+0.000
18X ∅ .159 ↧ .500 -0.030
TAP FOR 10-32 UNF
MINIMUM TAP DEPTH = 0.420
⌵ ∅ .200 X 90°, NEAR SIDE
equally spaced hole pattern
DO NOT PENETRATE
TAPPED HOLES C

UNLESS OTHERWISE SPECIFIED:		NAME / DATE
DIMENSIONS ARE IN INCHES TOLERANCES: FRACTIONAL ± ANGULAR: MACH ± BEND ± TWO PLACE DECIMAL ± THREE PLACE DECIMAL ±0.002	DRAWN	
	CHECKED	
	ENG APPR.	
	MFG APPR.	
INTERPRET GEOMETRIC TOLERANCING PER:	Q.A.	
MATERIAL	COMMENTS:	
FINISH		
NEXT ASSY / USED ON		
APPLICATION / DO NOT SCALE DRAWING		

TITLE:
FRONT VIEW

SIZE	DWG. NO.	REV
B	side_plate_v2_middle_hole_v2	
SCALE: 1:2	WEIGHT:	SHEET 1 OF 2

All patterns are top/bottom and left/right symmetric

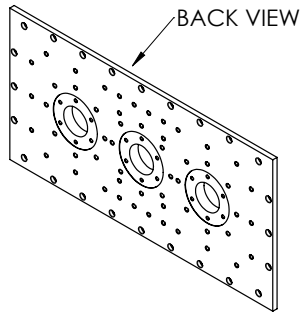

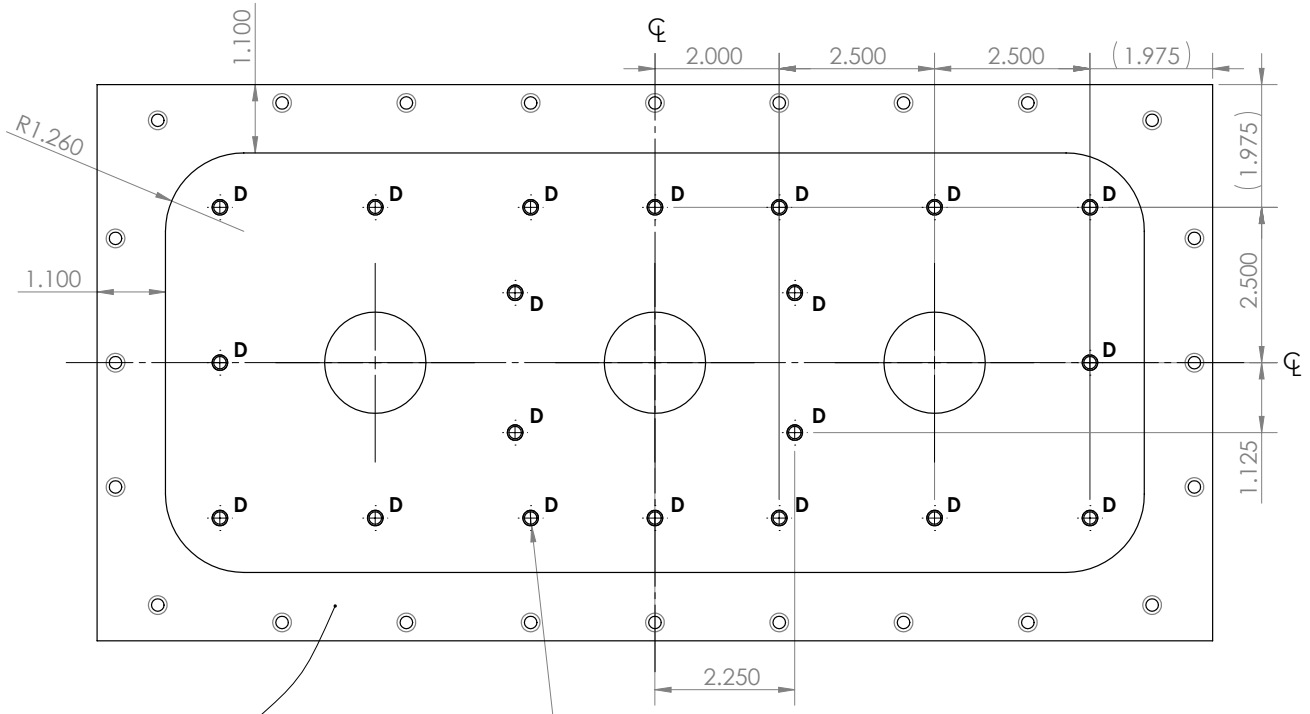

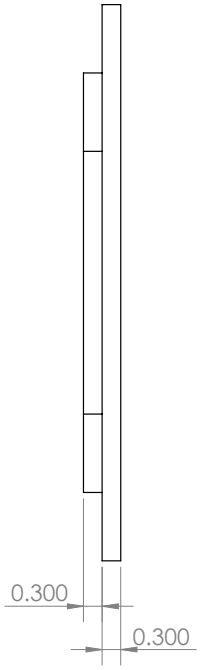

MACHINE FINISH REQUIRED

+0.000
20X ⌀ .201 ↧ .500 -0.030
TAP FOR 1/4-20 UNC
MINIMUM TAP DEPTH = 0.420
⌵ ⌀ .250 X 90°, NEAR SIDE
DO NOT PENETRATE

TAPPED HOLES D

		UNLESS OTHERWISE SPECIFIED:		NAME / DATE
		DIMENSIONS ARE IN INCHES TOLERANCES: FRACTIONAL ± ANGULAR: MACH ± BEND ± TWO PLACE DECIMAL ± THREE PLACE DECIMAL ±0.002	DRAWN CHECKED ENG APPR. MFG APPR. Q.A.	
		INTERPRET GEOMETRIC TOLERANCING PER:	COMMENTS:	
		MATERIAL		
NEXT ASSY	USED ON	FINISH		
APPLICATION		DO NOT SCALE DRAWING		

TITLE: BACK VIEW

SIZE	DWG. NO.	REV
B	side_plate_v2_middle_hole_v2	
SCALE: 1:2	WEIGHT:	SHEET 2 OF 2

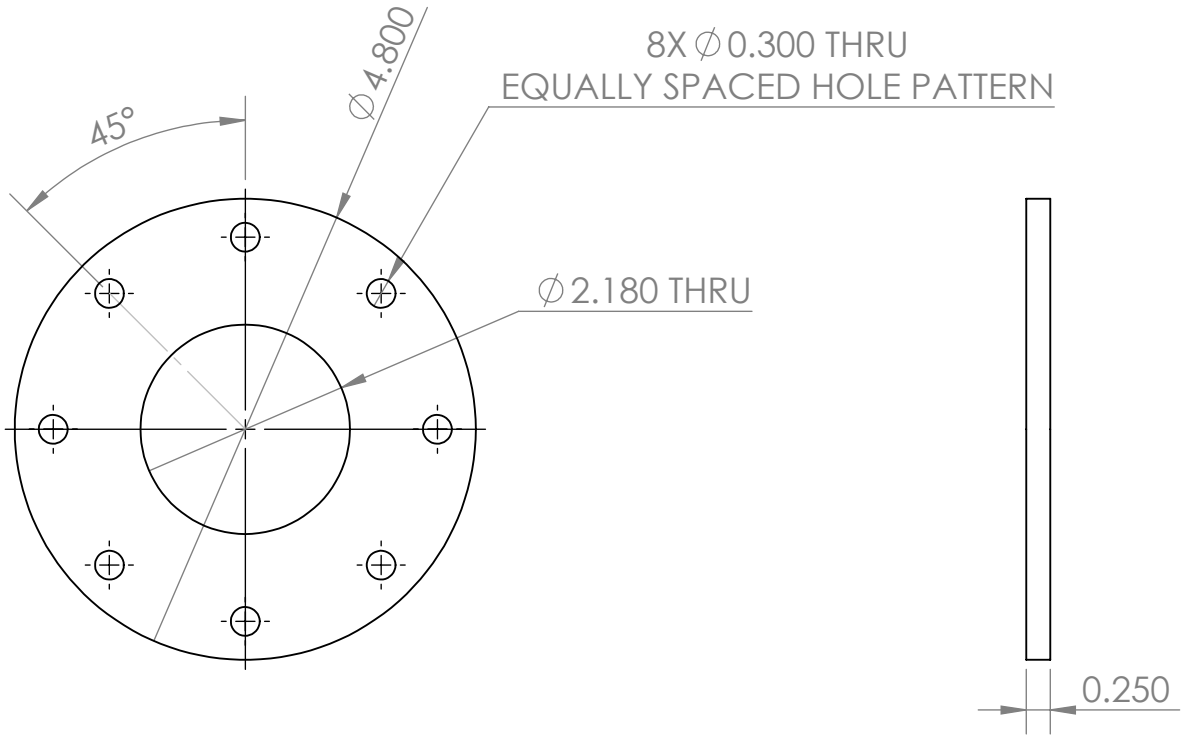

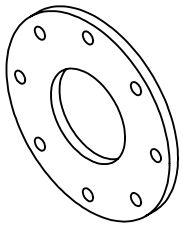

		UNLESS OTHERWISE SPECIFIED:		NAME	DATE
		DIMENSIONS ARE IN INCHES TOLERANCES: FRACTIONAL ± ANGULAR: MACH ± BEND ± TWO PLACE DECIMAL ± THREE PLACE DECIMAL ±	DRAWN		
			CHECKED		
			ENG APPR.		
			MFG APPR.		
		INTERPRET GEOMETRIC TOLERANCING PER:	Q.A.		
		MATERIAL	COMMENTS:		
NEXT ASSY	USED ON	FINISH			
APPLICATION		DO NOT SCALE DRAWING			

TITLE:

SIZE	DWG. NO.	REV
A	smaller_KF40_windows_actuator	
SCALE: 1:2	WEIGHT:	SHEET 1 OF 1

COUNTERBORE HOLES A abd TAPPED HOLES B are top/bottom and left/right symmetric

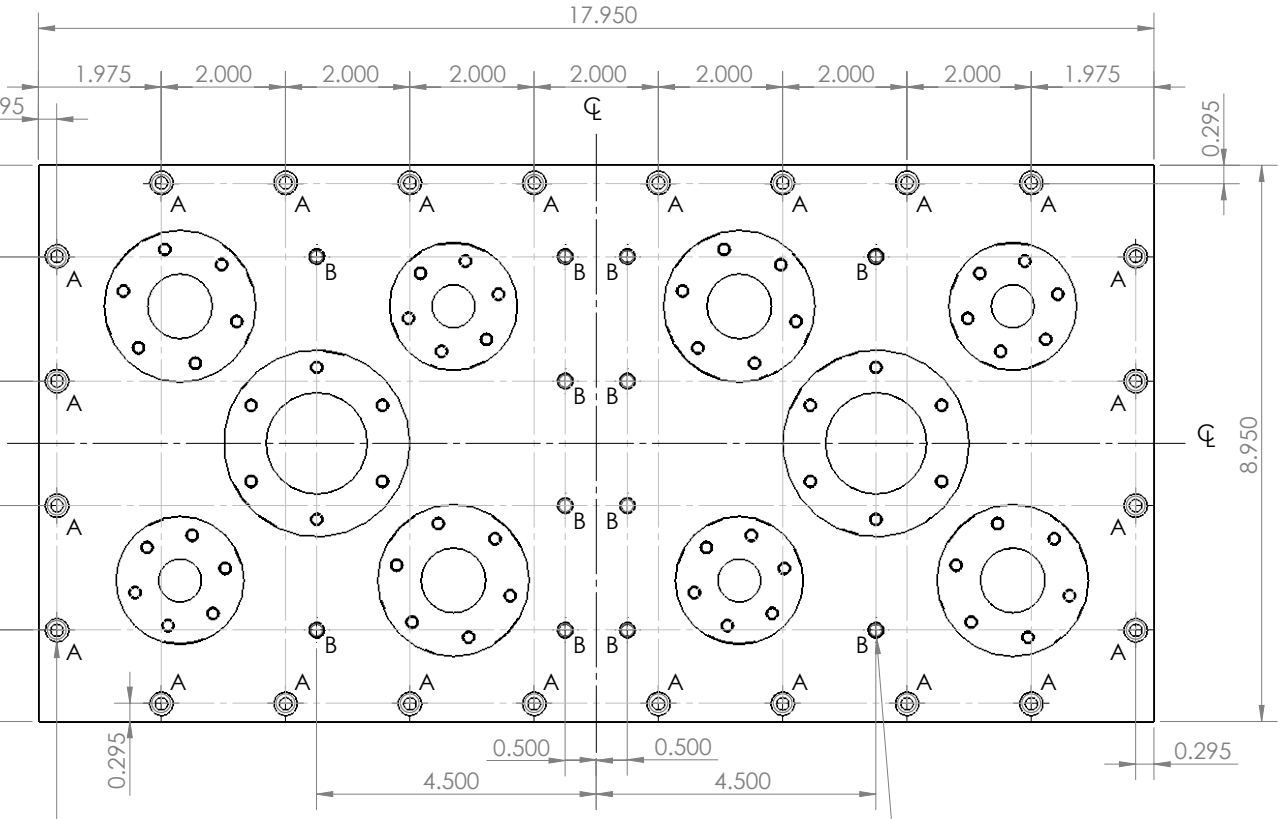

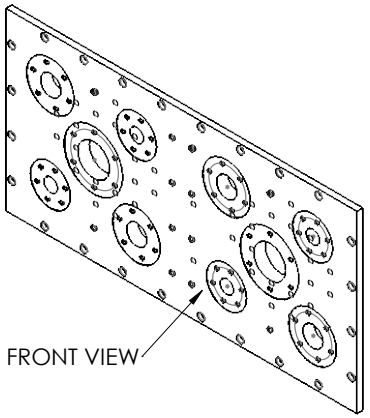

				NAME	DATE
		UNLESS OTHERWISE SPECIFIED:	DRAWN		
		DIMENSIONS ARE IN INCHES TOLERANCES: FRACTIONAL ± ANGULAR: MACH ± BEND ± TWO PLACE DECIMAL ± THREE PLACE DECIMAL ±0.002	CHECKED		
			ENG APPR.		
			MFG APPR.		
		INTERPRET GEOMETRIC TOLERANCING PER:	Q.A.		
		MATERIAL	COMMENTS:		
NEXT ASSY	USED ON	FINISH			
APPLICATION		DO NOT SCALE DRAWING			

TITLE:
FRONT VIEW 1

SIZE	DWG. NO.	REV
B	top_plate_final	
SCALE: 1:2	WEIGHT:	SHEET 1 OF 3

The patterns on this page are called out only for the right side of the plate
Duplicate these patterns to the left side with a 9" horizontal shift (NOT MIRRORED)

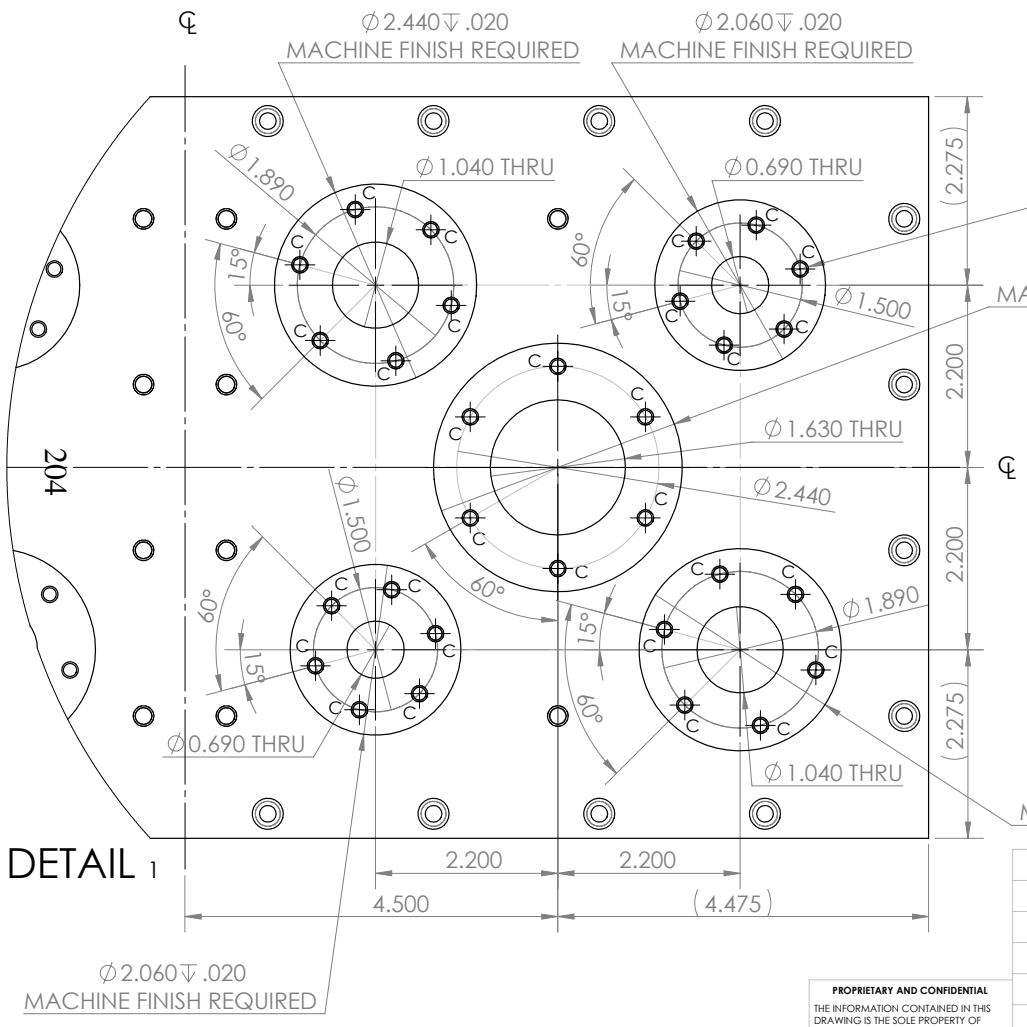

+0.000
30X ∅ .159 ⩛ .500 -0.030
TAP FOR 10-32 UNF
MINIMUM TAP DEPTH = 0.420
◡ ∅ .200 X 90°, NEAR SIDE
equally spaced hole pattern
DO NOT PENETRATE

TAPPED HOLES C

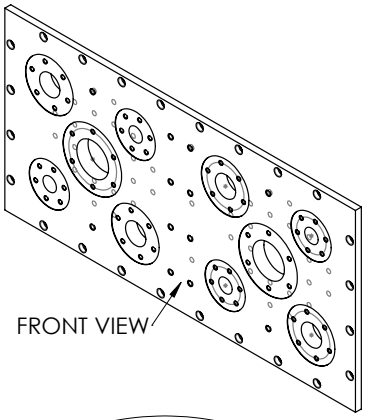

∅3.000⩛.020
MACHINE FINISH REQUIRED

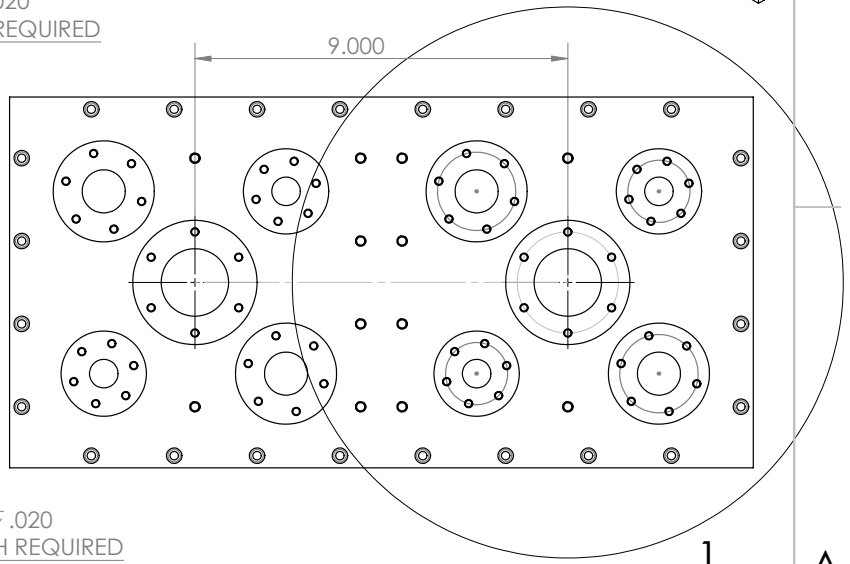

∅2.440⩛.020
MACHINE FINISH REQUIRED

1

DETAIL 1

		UNLESS OTHERWISE SPECIFIED:		NAME	DATE
		DIMENSIONS ARE IN INCHES TOLERANCES: FRACTIONAL ± ANGULAR: MACH ± BEND ± TWO PLACE DECIMAL ± THREE PLACE DECIMAL ±0.002	DRAWN		
			CHECKED		
			ENG APPR.		
			MFG APPR.		
		INTERPRET GEOMETRIC TOLERANCING PER:	Q.A.		
		MATERIAL	COMMENTS:		
NEXT ASSY	USED ON	FINISH			
APPLICATION		DO NOT SCALE DRAWING			

TITLE:
FRONT VIEW 2

SIZE	DWG. NO.	REV
B	top_plate_final	
SCALE: 1:2	WEIGHT:	SHEET 2 OF 3

TAPPED HOLES D are top/bottom and left/right symmetric

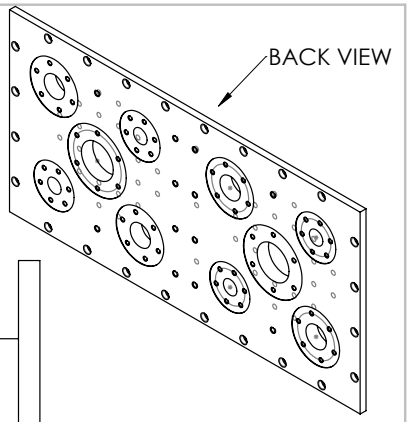

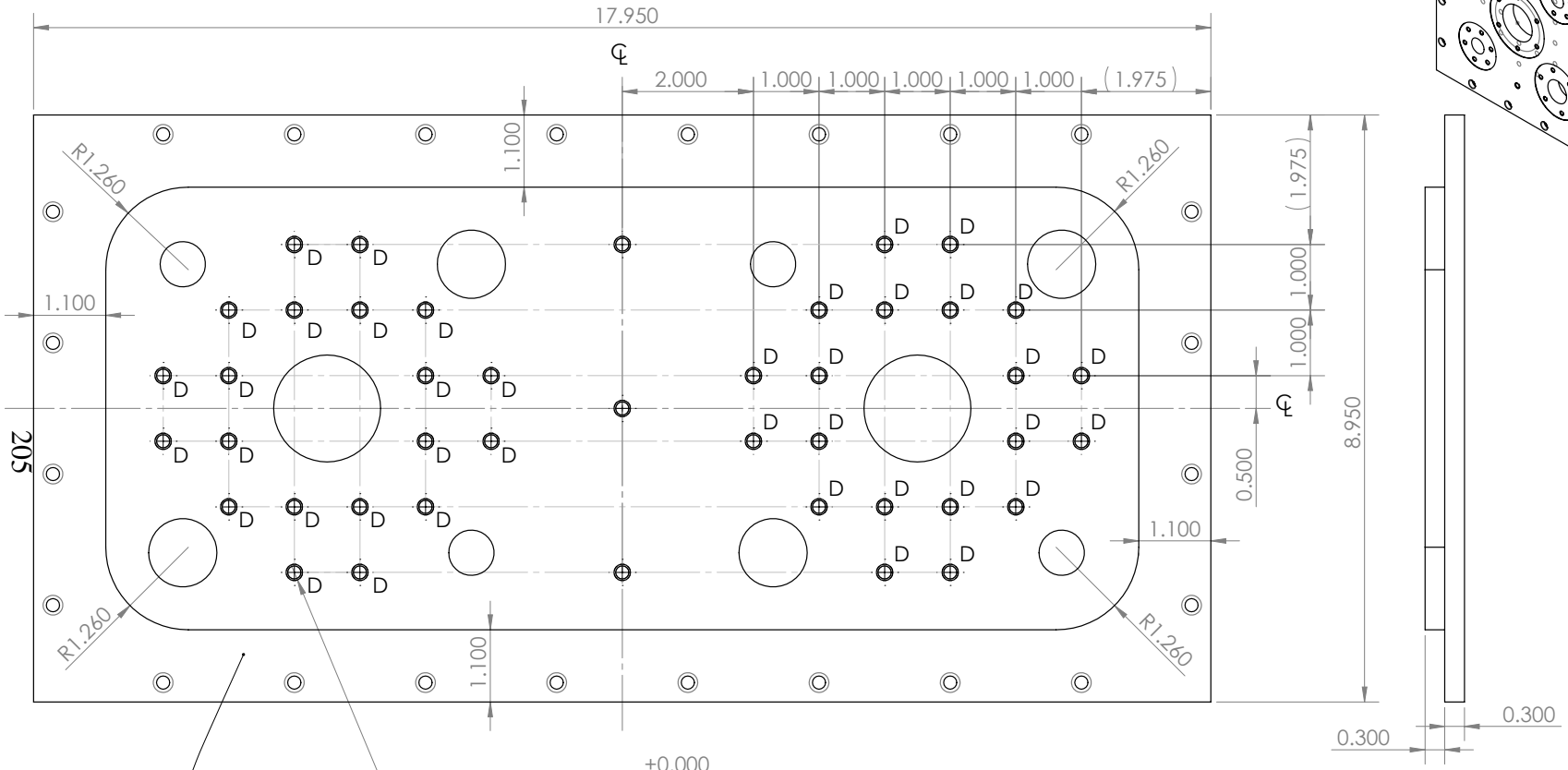

MACHINE FINISH REQUIRED

+0.000
43X ⌀ .201 ↧ .500 -0.030
TAP FOR 1/4-20 UNC
MINIMUM TAP DEPTH = 0.420
⌵ ⌀ .250 X 90°, NEAR SIDE
DO NOT PENETRATE

TAPPED HOLES D

		UNLESS OTHERWISE SPECIFIED:		NAME / DATE
		DIMENSIONS ARE IN INCHES TOLERANCES: FRACTIONAL ± ANGULAR: MACH ± BEND ± TWO PLACE DECIMAL ± THREE PLACE DECIMAL ±0.002	DRAWN	
			CHECKED	
			ENG APPR.	
			MFG APPR.	
		INTERPRET GEOMETRIC TOLERANCING PER:	Q.A.	
		MATERIAL	COMMENTS:	
NEXT ASSY	USED ON	FINISH		
APPLICATION		DO NOT SCALE DRAWING		

TITLE:

BACK VIEW

SIZE	DWG. NO.	REV
B	top_plate_final	
SCALE: 1:2	WEIGHT:	SHEET 3 OF 3

COUNTERBORE HOLES A abd TAPPED HOLES B are top/bottom and left/right symmetric

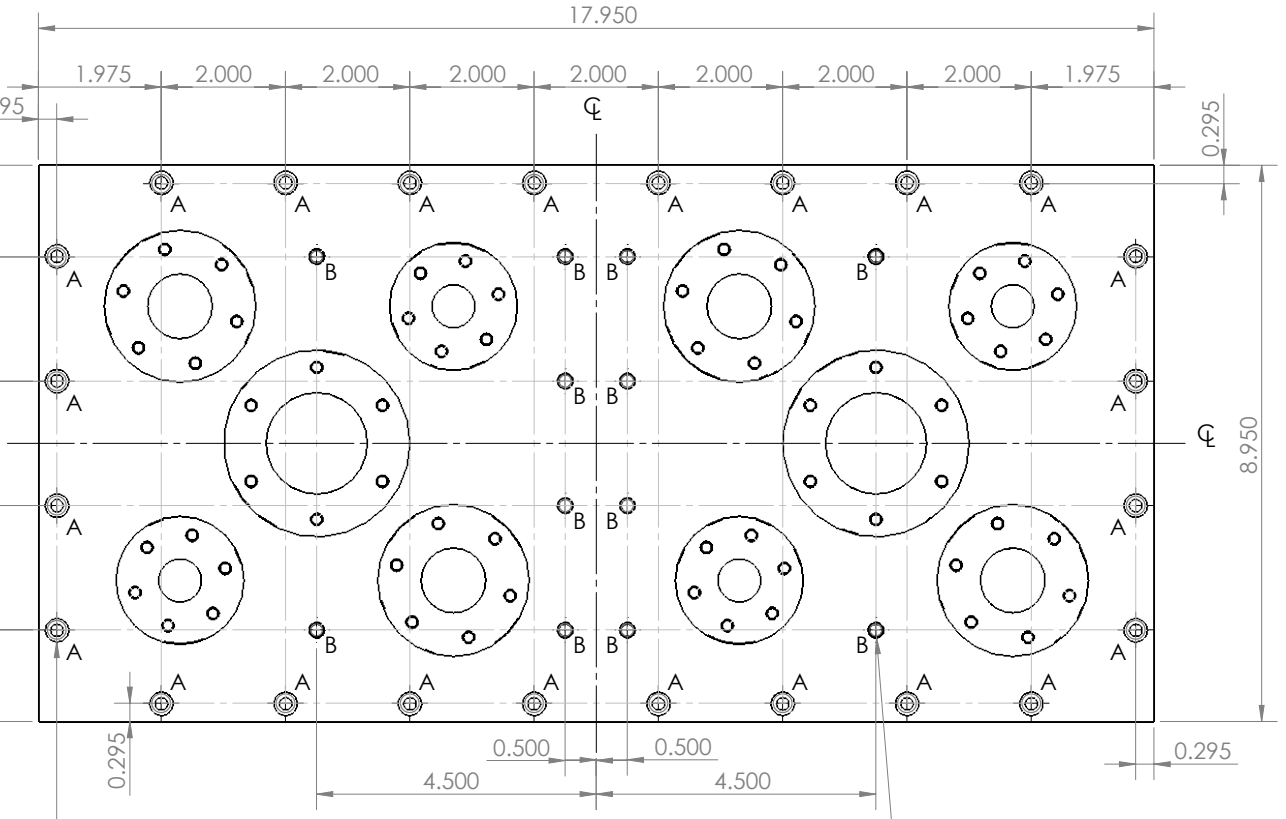

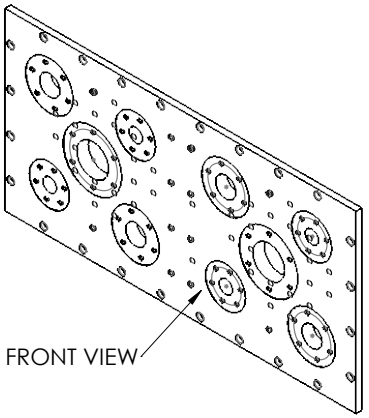

24X ⌀ .201 THRU ALL
⌴ ⌀ .375 ↧ .190
COUNTERBORE HOLES A

+0.000
12X ⌀ .201 ↧ .500 -0.030
TAP FOR 1/4-20 UNC
MINIMUM TAP DEPTH = 0.420
⌵ ⌀ .250 X 90°, NEAR SIDE
DO NOT PENETRATE
TAPPED HOLES B

NEXT ASSY	USED ON	
APPLICATION		DO NOT SCALE DRAWING

UNLESS OTHERWISE SPECIFIED:		NAME	DATE
DIMENSIONS ARE IN INCHES TOLERANCES: FRACTIONAL ± ANGULAR: MACH ± BEND ± TWO PLACE DECIMAL ± THREE PLACE DECIMAL ±0.002	DRAWN		
	CHECKED		
	ENG APPR.		
	MFG APPR.		
INTERPRET GEOMETRIC TOLERANCING PER:	Q.A.		
MATERIAL	COMMENTS:		
FINISH			

TITLE:
FRONT VIEW 1

SIZE	DWG. NO.	REV
B	top_plate_v2	
SCALE: 1:2	WEIGHT:	SHEET 1 OF 4

The patterns on this page are called out only for the right side of the plate
Duplicate these patterns to the left side with a 9" horizontal shift (NOT MIRRORED)

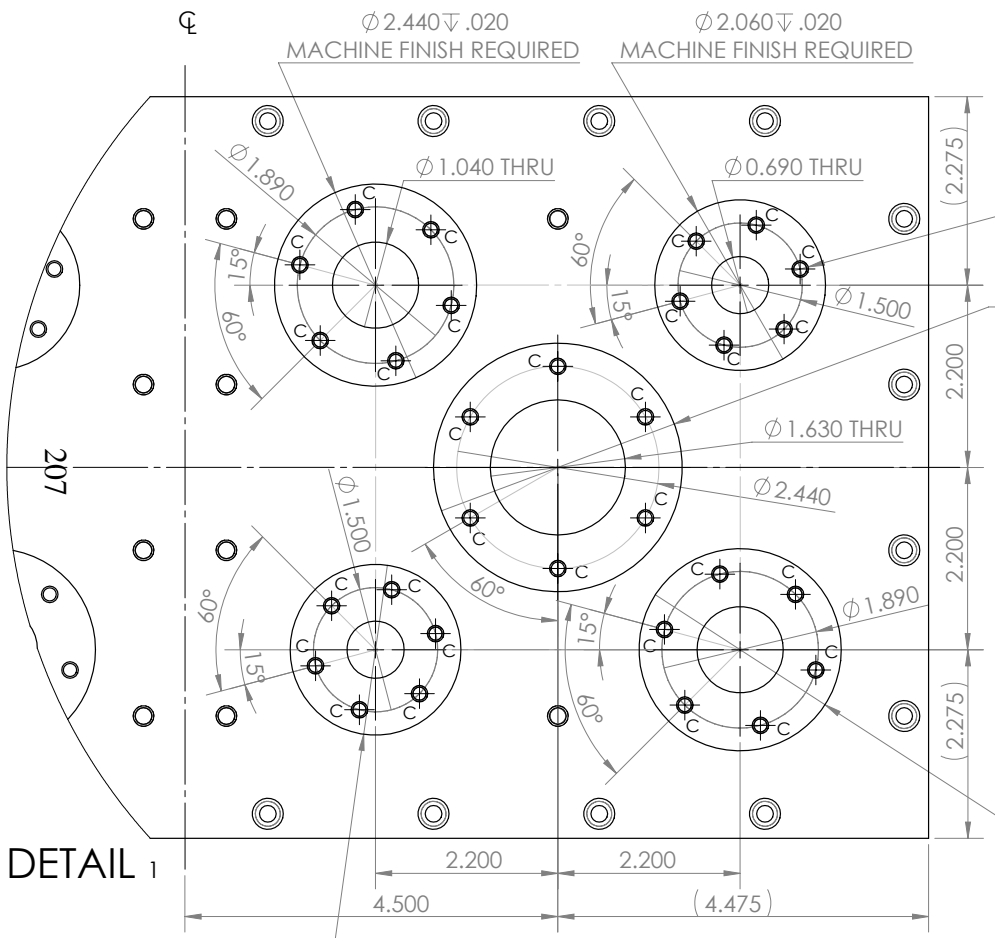

+0.000
30X ∅ .159 ⩛ .500 -0.030
TAP FOR 10-32 UNF
MINIMUM TAP DEPTH = 0.420
◡ ∅ .200 X 90°, NEAR SIDE
equally spaced hole pattern
DO NOT PENETRATE

TAPPED HOLES C

∅3.000⩛.020
MACHINE FINISH REQUIRED

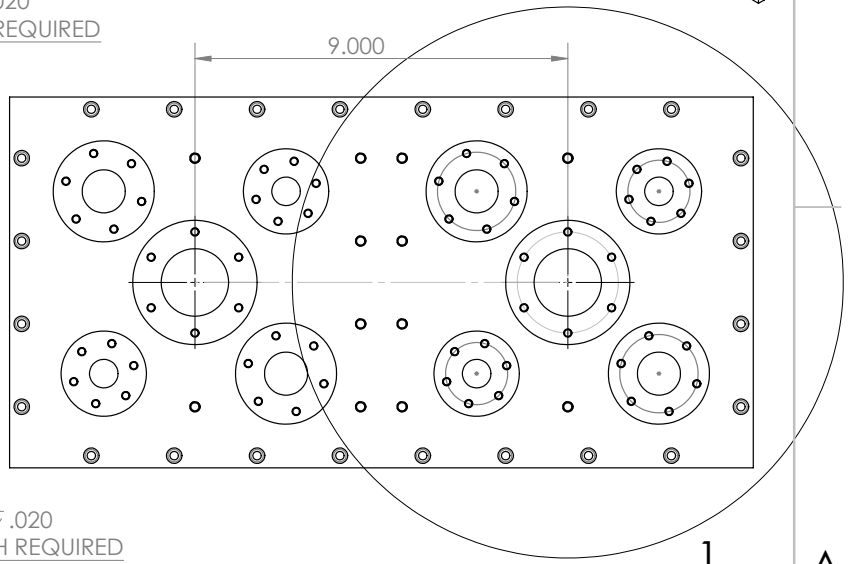

∅2.440⩛.020
MACHINE FINISH REQUIRED

1

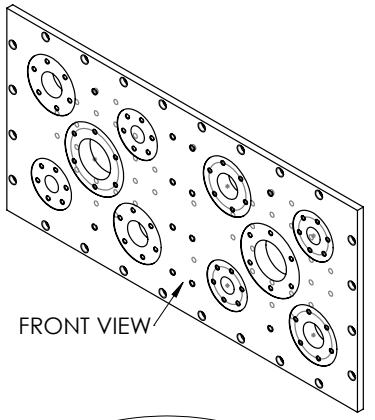

DETAIL 1

		UNLESS OTHERWISE SPECIFIED:		NAME	DATE
		DIMENSIONS ARE IN INCHES TOLERANCES: FRACTIONAL ± ANGULAR: MACH ± BEND ± TWO PLACE DECIMAL ± THREE PLACE DECIMAL ±0.002	DRAWN		
			CHECKED		
			ENG APPR.		
			MFG APPR.		
		INTERPRET GEOMETRIC TOLERANCING PER:	Q.A.		
		MATERIAL	COMMENTS:		
NEXT ASSY	USED ON	FINISH			
APPLICATION		DO NOT SCALE DRAWING			

TITLE:
FRONT VIEW 2

SIZE	DWG. NO.	REV
B	top_plate_v2	
SCALE: 1:2	WEIGHT:	SHEET 2 OF 4

TAPPED HOLES D are top/bottom and left/right symmetric

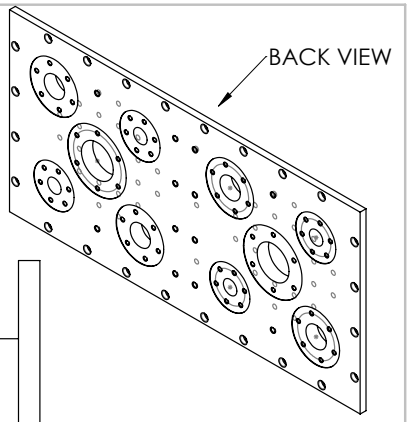

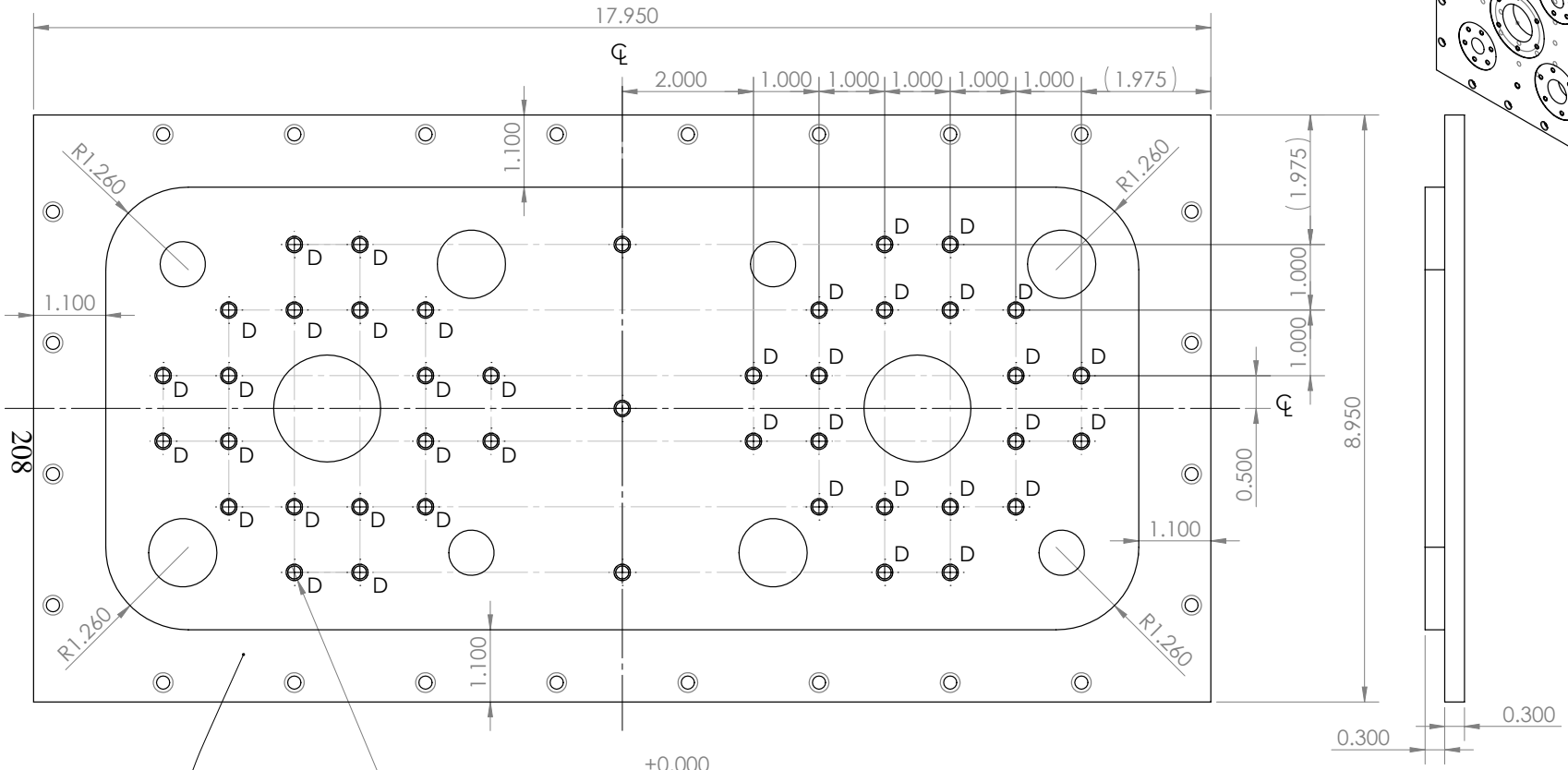

MACHINE FINISH REQUIRED

+0.000
43X ⌀ .201 ↧ .500 -0.030
TAP FOR 1/4-20 UNC
MINIMUM TAP DEPTH = 0.420
⌵ ⌀ .250 X 90°, NEAR SIDE
DO NOT PENETRATE

TAPPED HOLES D

		UNLESS OTHERWISE SPECIFIED:		NAME	DATE
		DIMENSIONS ARE IN INCHES TOLERANCES: FRACTIONAL ± ANGULAR: MACH ± BEND ± TWO PLACE DECIMAL ± THREE PLACE DECIMAL ±0.002	DRAWN		
			CHECKED		
			ENG APPR.		
			MFG APPR.		
		INTERPRET GEOMETRIC TOLERANCING PER:	Q.A.		
		MATERIAL	COMMENTS:		
NEXT ASSY	USED ON	FINISH			
APPLICATION		DO NOT SCALE DRAWING			

TITLE: BACK VIEW

SIZE	DWG. NO.	REV
B	top_plate_v2	

SCALE: 1:2 | WEIGHT: | SHEET 3 OF 4

The patterns on this page are called out only for the right side of the plate
Duplicate these patterns to the left side with a 9" horizontal shift (NOT MIRRORED)

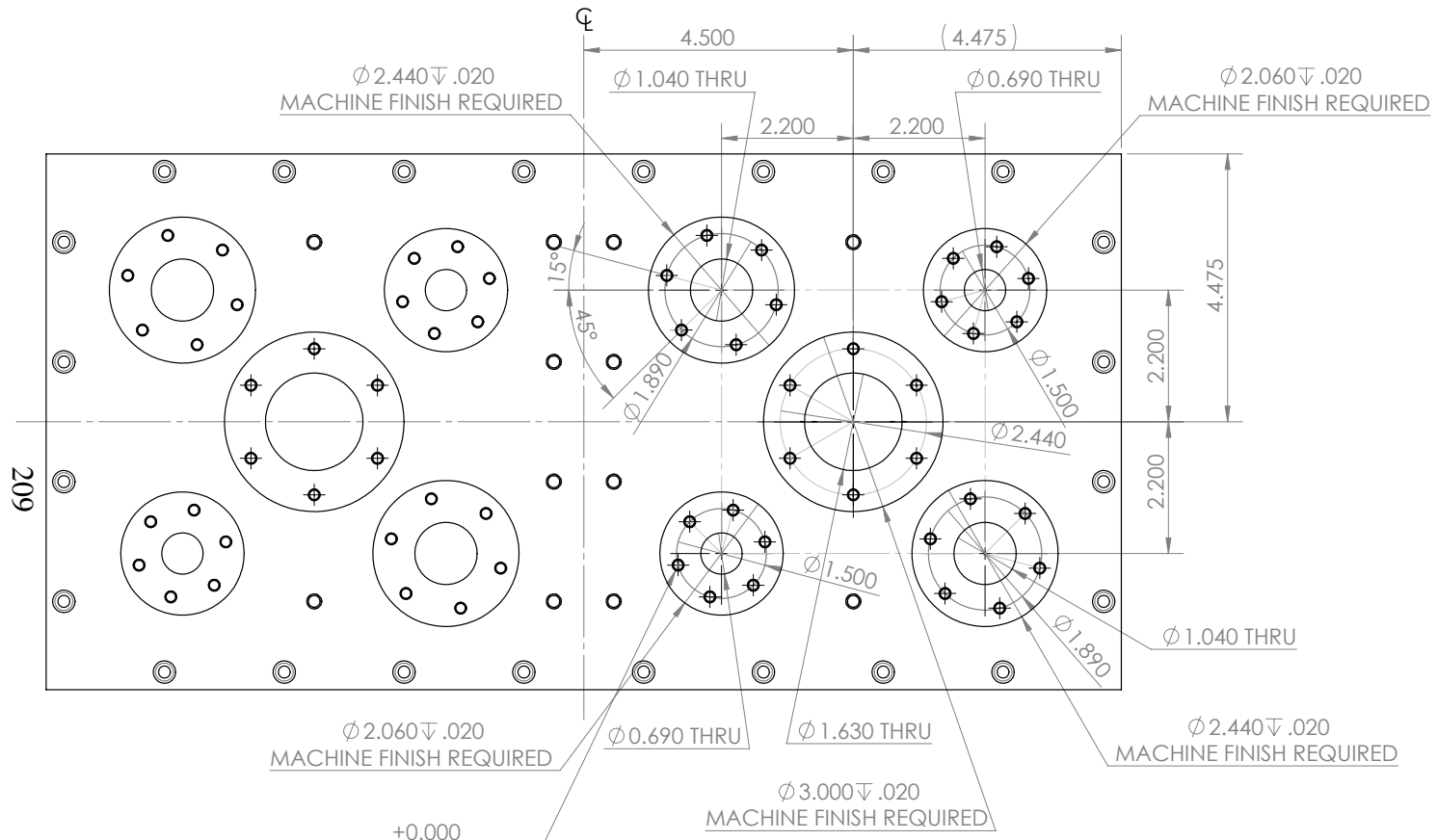

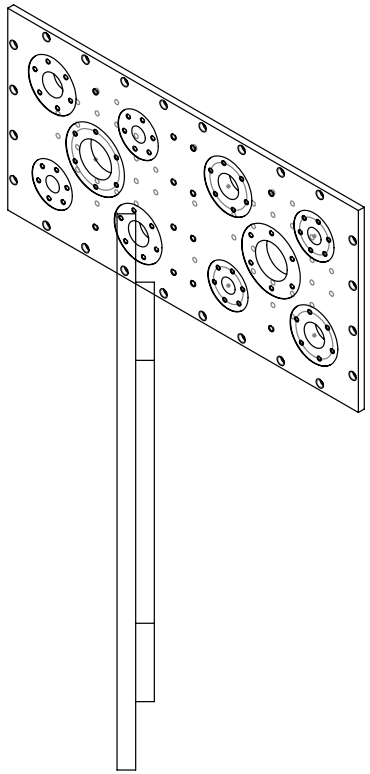

+0.000
30X ∅ .159 ↧ .500 -0.030
⌵ ∅ .200 X 90°, NEAR SIDE
TAP FOR 10-32 UNF
MINIMUM TAP DEPTH = 0.420
DO NOT PENETRATE

TAPPED HOLES C

		UNLESS OTHERWISE SPECIFIED:		NAME	DATE
		DIMENSIONS ARE IN INCHES TOLERANCES: FRACTIONAL ± ANGULAR: MACH ± BEND ± TWO PLACE DECIMAL ± THREE PLACE DECIMAL ±	DRAWN		
			CHECKED		
			ENG APPR.		
			MFG APPR.		
		INTERPRET GEOMETRIC TOLERANCING PER:	Q.A.		
		MATERIAL	COMMENTS:		
NEXT ASSY	USED ON	FINISH			
APPLICATION		DO NOT SCALE DRAWING			

TITLE:

SIZE	DWG. NO.	REV
B	top_plate_v2	
SCALE: 1:2	WEIGHT:	SHEET 4 OF 4

COUNTERBORE HOLES A are top/bottom and left/right symmetric

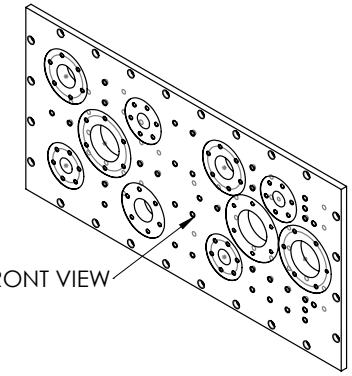

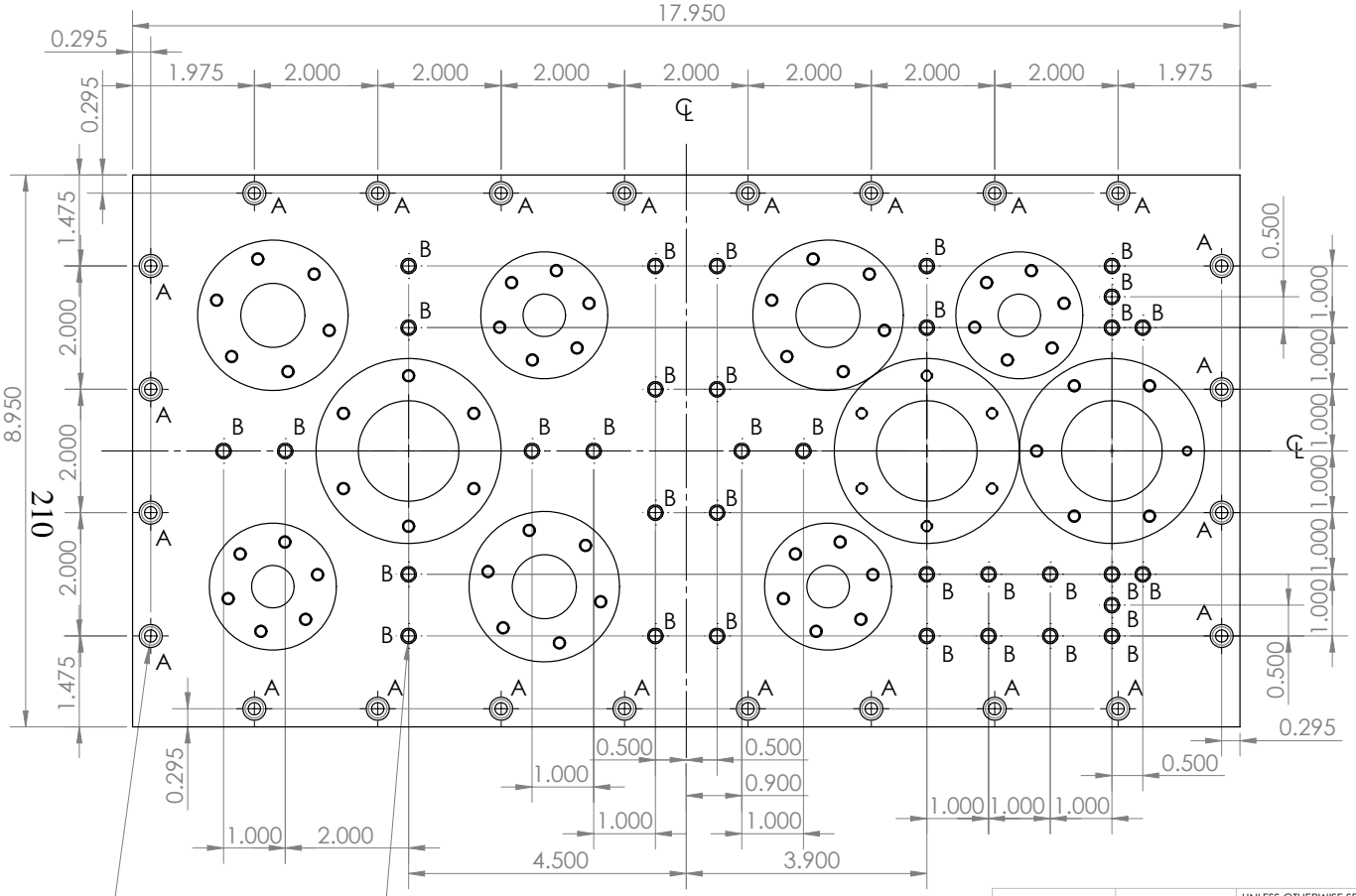

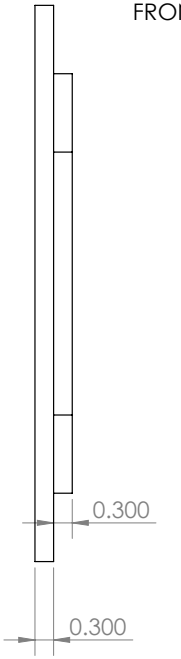

24X ⌀ .201 THRU ALL
⌴ ⌀ .375 ↧ .190
COUNTERBORE HOLES A

34X ⌀ .201 ↧ .500 +0.000 -0.030
TAP FOR 1/4-20 UNC
MINIMUM TAP DEPTH = 0.420
⌵ ⌀ .250 X 90°, NEAR SIDE
DO NOT PENETRATE
TAPPED HOLES B

UNLESS OTHERWISE SPECIFIED:		NAME / DATE
DIMENSIONS ARE IN INCHES TOLERANCES: FRACTIONAL ± ANGULAR: MACH ± BEND ± TWO PLACE DECIMAL ± THREE PLACE DECIMAL ±0.002	DRAWN	
	CHECKED	
	ENG APPR.	
	MFG APPR.	
	Q.A.	
INTERPRET GEOMETRIC TOLERANCING PER:	COMMENTS:	
MATERIAL		
FINISH		
NEXT ASSY / USED ON		
APPLICATION / DO NOT SCALE DRAWING		

TITLE:
FRONT VIEW 1

SIZE	DWG. NO.	REV
B	top_plate_v2_circular_final	

SCALE: 1:2 | WEIGHT: | SHEET 1 OF 4

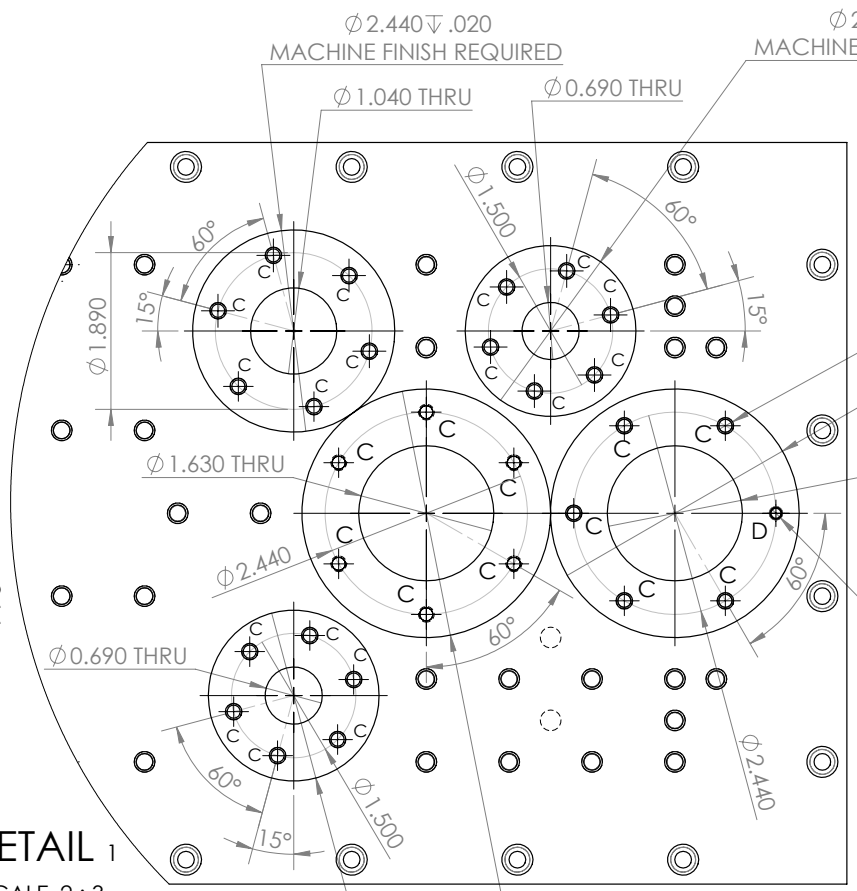

DETAIL 1

SCALE 2 : 3

0.000
29X ⌀ .159 ↧ .500 -0.030
TAP FOR 10-32 UNF
MINIMUM TAP DEPTH = 0.420
⌵ ⌀ .200 X 90°, NEAR SIDE
equally spaced hole pattern
DO NOT PENETRATE

TAPPED HOLES C

⌀3.000↧.020
MACHINE FINISH REQUIRED

⌀1.630 THRU

0.000
1X ⌀ .120 ↧ .200 -0.010
TAP FOR #4-40 HELICOIL
MINIMUM TAP DEPTH = 0.16
⌵ ⌀ .147 X 90°, NEAR SIDE
equally spaced hole pattern
DO NOT PENETRATE

TAPPED HOLES D

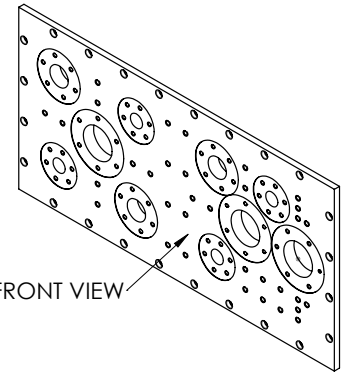

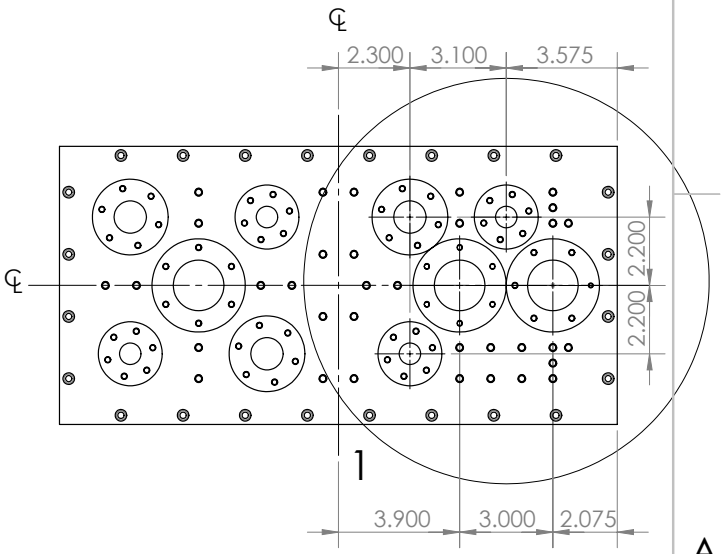

		UNLESS OTHERWISE SPECIFIED:		NAME	DATE
		DIMENSIONS ARE IN INCHES TOLERANCES: FRACTIONAL ± ANGULAR: MACH ± BEND ± TWO PLACE DECIMAL ± THREE PLACE DECIMAL ±0.002	DRAWN		
			CHECKED		
			ENG APPR.		
			MFG APPR.		
		INTERPRET GEOMETRIC TOLERANCING PER:	Q.A.		
		MATERIAL	COMMENTS:		
NEXT ASSY	USED ON	FINISH			
APPLICATION		DO NOT SCALE DRAWING			

TITLE:

FRONT VIEW 2

SIZE	DWG. NO.	REV
B	top_plate_v2_circular_final	

SCALE: 1:2	WEIGHT:	SHEET 2 OF 4

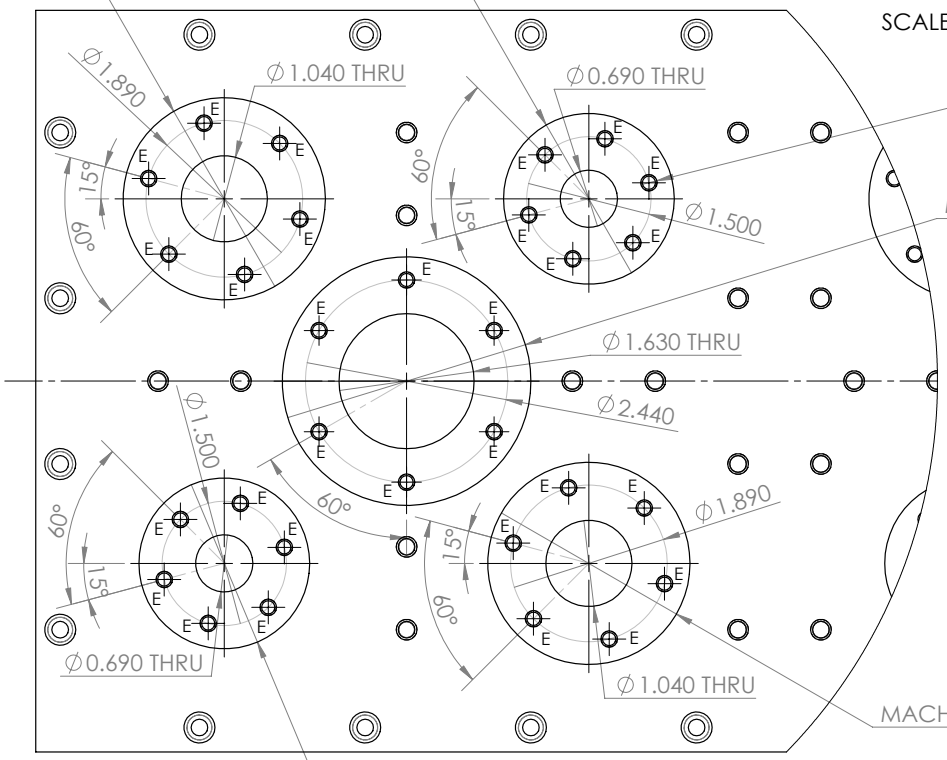

DETAIL 2

SCALE 2 : 3

0.000
30X ⌀ .159 ↧ .500 -0.030
TAP FOR 10-32 UNF
MINIMUM TAP DEPTH = 0.420
⌵ ⌀ .200 X 90°, NEAR SIDE
equally spaced hole pattern
DO NOT PENETRATE

TAPPED HOLES E

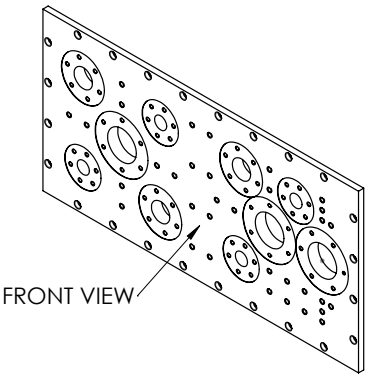

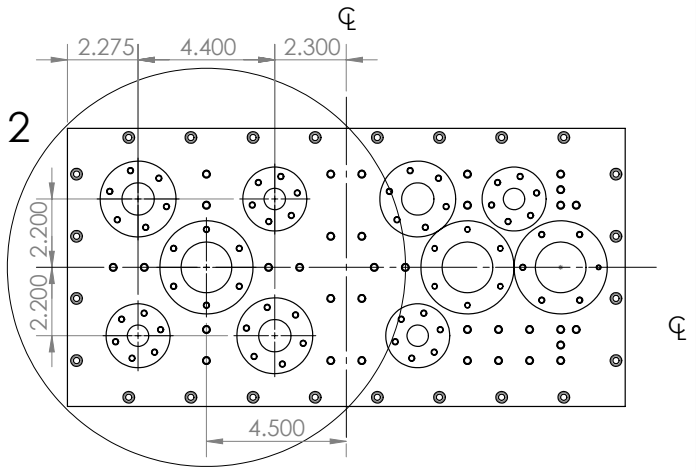

2

		UNLESS OTHERWISE SPECIFIED:		NAME	DATE
		DIMENSIONS ARE IN INCHES TOLERANCES: FRACTIONAL ± ANGULAR: MACH ± BEND ± TWO PLACE DECIMAL ± THREE PLACE DECIMAL ±0.002	DRAWN		
			CHECKED		
			ENG APPR.		
			MFG APPR.		
		INTERPRET GEOMETRIC TOLERANCING PER:	Q.A.		
		MATERIAL	COMMENTS:		
NEXT ASSY	USED ON	FINISH			
APPLICATION		DO NOT SCALE DRAWING			

TITLE:

FRONT VIEW 3

SIZE	DWG. NO.	REV
B	top_plate_v2_circular_final	

SCALE: 1:2 | WEIGHT: | SHEET 3 OF 4

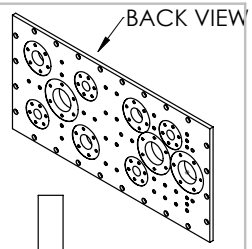

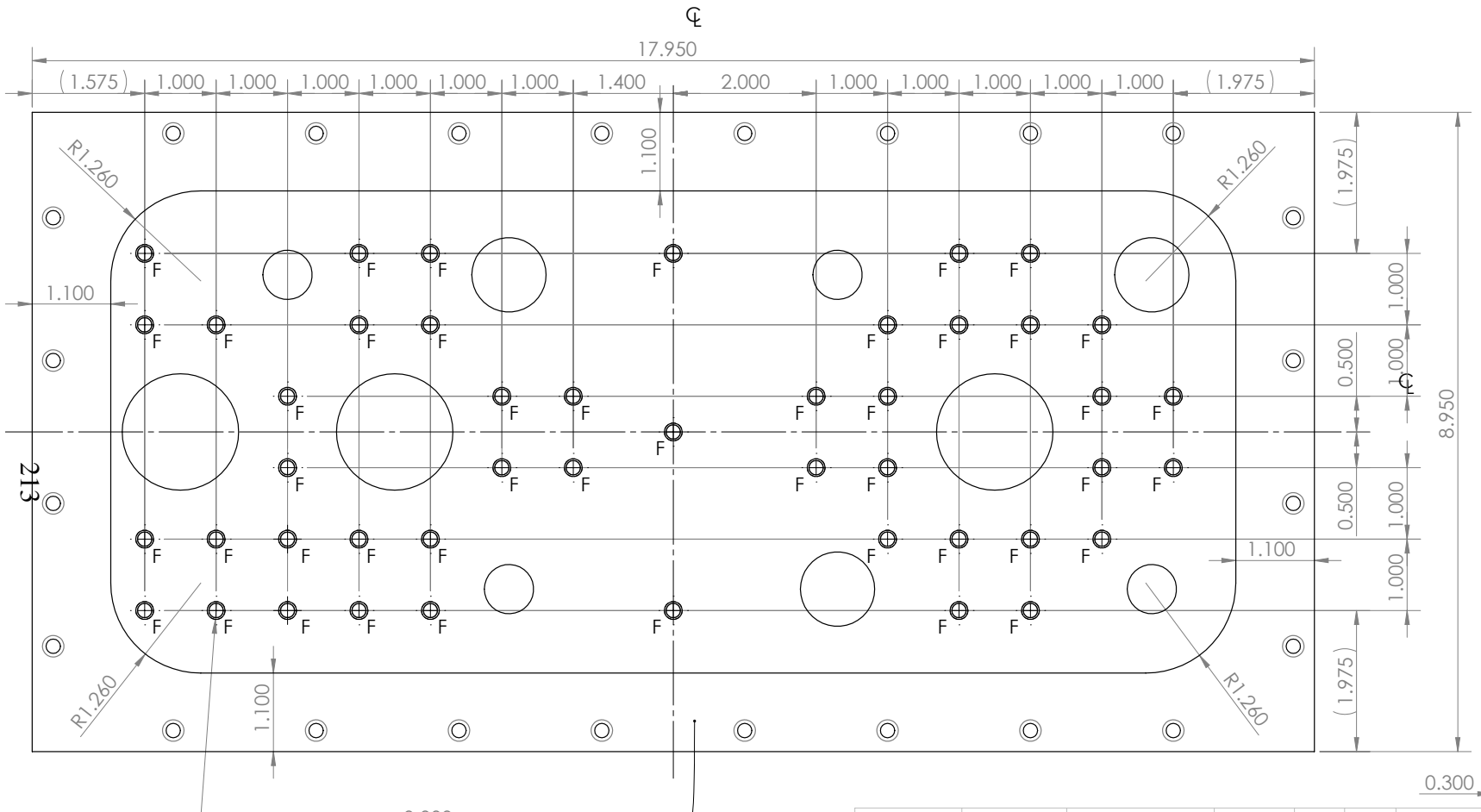

0.300

0.300

+0.000
46X ⌀ .201 ↧ .500 -0.030
TAP FOR 1/4-20 UNC
MINIMUM TAP DEPTH = 0.420
⌵ ⌀ .250 X 90°, NEAR SIDE
DO NOT PENETRATE

TAPPED HOLES F

MACHINE FINISH REQUIRED

UNLESS OTHERWISE SPECIFIED:		NAME / DATE
DIMENSIONS ARE IN INCHES TOLERANCES: FRACTIONAL ± ANGULAR: MACH ± BEND ± TWO PLACE DECIMAL ± THREE PLACE DECIMAL ±0.002	DRAWN	
	CHECKED	
	ENG APPR.	
	MFG APPR.	
INTERPRET GEOMETRIC TOLERANCING PER:	Q.A.	
MATERIAL	COMMENTS:	
FINISH		
NEXT ASSY / USED ON		
APPLICATION / DO NOT SCALE DRAWING		

TITLE:

BACK VIEW

SIZE	DWG. NO.	REV
B	top_plate_v2_circular_final	
SCALE: 1:2	WEIGHT:	SHEET 4 OF 4

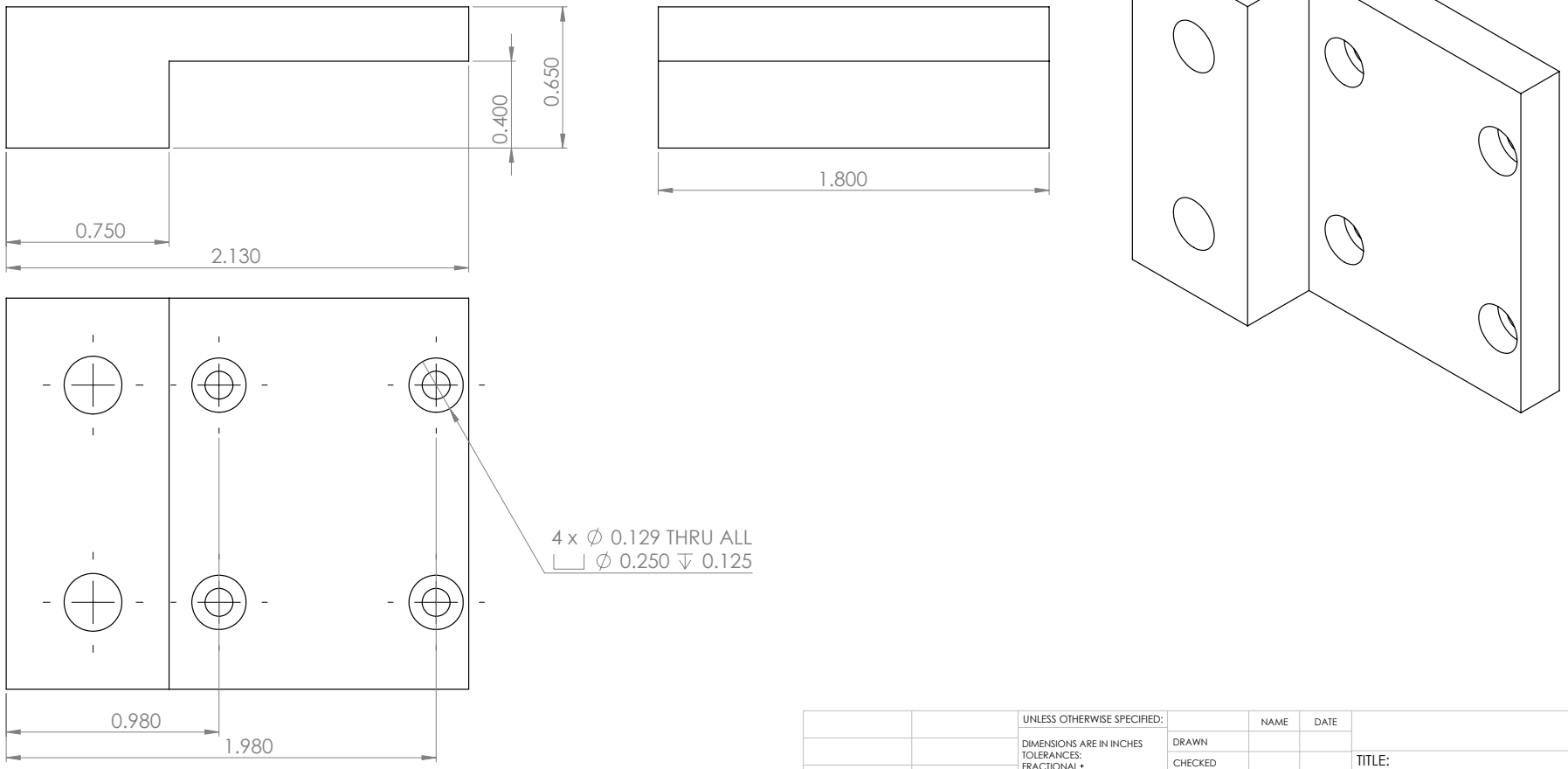

		UNLESS OTHERWISE SPECIFIED:		NAME	DATE
		DIMENSIONS ARE IN INCHES TOLERANCES: FRACTIONAL ± ANGULAR: MACH ± BEND ± TWO PLACE DECIMAL ± THREE PLACE DECIMAL ± 0.005	DRAWN		
			CHECKED		
			ENG APPR.		
			MFG APPR.		
		INTERPRET GEOMETRIC TOLERANCING PER:	Q.A.		
		MATERIAL Aluminum 6061-T6	COMMENTS:		
NEXT ASSY	USED ON	FINISH			
APPLICATION		DO NOT SCALE DRAWING			

TITLE:

Upstream Mirror Adapter Plate

SIZE	DWG. NO.	REV
B		

SCALE: 2:1	WEIGHT:	SHEET 1 OF 2

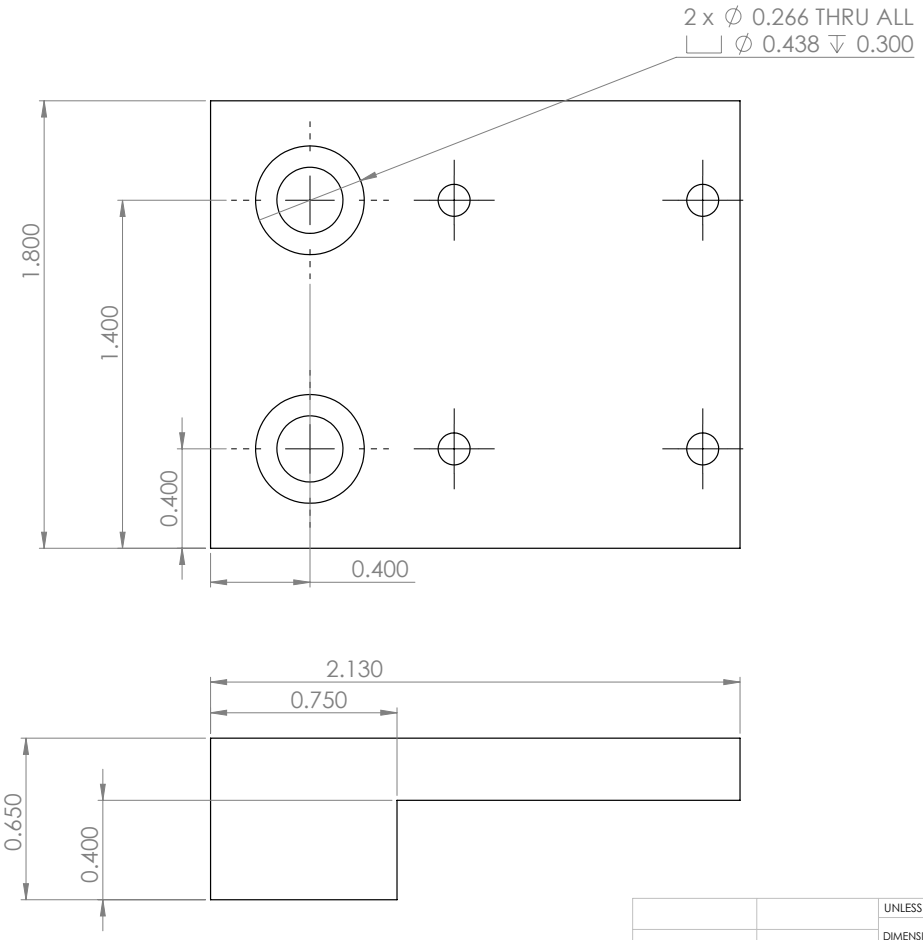

215

		UNLESS OTHERWISE SPECIFIED:		NAME	DATE
		DIMENSIONS ARE IN INCHES TOLERANCES: FRACTIONAL ± ANGULAR: MACH ± BEND ± TWO PLACE DECIMAL ± THREE PLACE DECIMAL ± 0.005	DRAWN		
			CHECKED		
			ENG APPR.		
			MFG APPR.		
		INTERPRET GEOMETRIC TOLERANCING PER:	Q.A.		
		MATERIAL Aluminum 6061-T6	COMMENTS:		
NEXT ASSY	USED ON	FINISH			
APPLICATION		DO NOT SCALE DRAWING			

TITLE:

Upstream Mirror Adapter Plate

SIZE	DWG. NO.	REV
B		
SCALE: 2:1	WEIGHT:	SHEET 2 OF 2

Bibliography

[1] Sacha Davidson, Enrico Nardi, and Yosef Nir. "Leptogenesis". In: *arXiv:0802.2962* (2008). arXiv: 0802.2962.

[2] Laurent Canetti, Marco Drewes, and Mikhail Shaposhnikov. "Matter and antimatter in the universe". In: *New J. Phys.* 14.9 (Sept. 2012), p. 095012. ISSN: 1367-2630. DOI: 10.1088/1367-2630/14/9/095012. arXiv: 1204.4186.

[3] Massimiliano Lattanzi and Mauro Moretti. "Lepton Asymmetries in Cosmology". In: *Symmetry* 16.12 (2024), p. 1657. DOI: 10.3390/sym16121657.

[4] Planck Collaboration. "Planck 2018 results. VI. Cosmological parameters". In: *Astronomy & Astrophysics* 641 (2020), A6. DOI: 10.1051/0004-6361/201833910.

[5] A. D. Sakharov. "Violation of CP Invariance, C Asymmetry, and Baryon Asymmetry of the Universe". In: *JETP Lett.* 5 (1967), pp. 27–30.

[6] ATLAS Collaboration. *Search for higgsinos in compressed mass spectra using low-momentum tracks in pp collisions at* $\sqrt{s}$ = 13 *TeV with the ATLAS detector*. 2025. arXiv: 2511.20042 [hep-ex].

[7] Kaori Fuyuto, Junji Hisano, and Eibun Senaha. "Toward verification of electroweak baryogenesis by electric dipole moments". In: *Phys. Lett. Sect. B Nucl. Elem. Part. High-Energy Phys.* 755 (2016), pp. 491–497. ISSN: 03702693. DOI: 10.1016/j.physletb.2016.02.053.

[8] The T2K Collaboration. "Constraint on the matter–antimatter symmetry-violating phase in neutrino oscillations". In: *Nature* 580 (2020), pp. 339–344. DOI: 10.1038/s41586-020-2177-0.

[9] The NOvA Collaboration and The T2K Collaboration. "Joint neutrino oscillation analysis from the T2K and NOvA experiments". In: *Nature* 646 (2025), pp. 818–824. DOI: 10.1038/s41586-025-09599-3.

[10] Abel, C. *et al*. "Measurement of the Permanent Electric Dipole Moment of the Neutron". In: *Physical Review Letters* 124.8 (Feb. 2020), p. 081803. ISSN: 0031-9007. DOI: 10.1103/PhysRevLett.124.081803.

[11] T. E. Chupp et al. “Electric dipole moments of atoms, molecules, nuclei, and particles”. In: *Reviews of Modern Physics* 91.1 (Jan. 2019), p. 015001. ISSN: 0034-6861. DOI: 10.1103/RevModPhys.91.015001.

[12] M. S. Safronova et al. “Search for new physics with atoms and molecules”. In: *Rev. Mod. Phys.* 90.2 (June 2018), p. 025008. ISSN: 0034-6861. DOI: 10.1103/RevModPhys.90.025008.

[13] Nicholas R. Hutzler. “Polyatomic molecules as quantum sensors for fundamental physics”. In: *Quantum Science and Technology* 5.4 (Oct. 2020), p. 044011. ISSN: 2058-9565. DOI: 10.1088/2058-9565/abb9c5.

[14] David DeMille et al. “Quantum sensing and metrology for fundamental physics with molecules”. In: *Nature Physics* 20.5 (May 2024), pp. 741–749. ISSN: 1745-2481. DOI: 10.1038/s41567-024-02499-9.

[15] V. Andreev et al. “Improved limit on the electric dipole moment of the electron”. In: *Nature* 562.7727 (Oct. 2018), pp. 355–360. ISSN: 0028-0836. DOI: 10.1038/s41586-018-0599-8.

[16] Tanya S. Roussy et al. “An improved bound on the electron’s electric dipole moment”. In: *Science* 381.6653 (2023), pp. 46–50. DOI: 10.1126/science.adg4084. eprint: https://www.science.org/doi/pdf/10.1126/science.adg4084.

[17] Alarcon, R. *et al*. “Electric dipole moments and the search for new physics”. In: *arXiv:2203.08103* (Mar. 2022). arXiv: 2203.08103.

[18] Zack Lasner. “Order-of-magnitude-tighter bound on the electron electric dipole moment”. PhD Thesis. 2019.

[19] O P Sushkov and V V Flambaum. “Parity breaking effects in diatomic molecules”. In: *Sov. Phys. JETP* 48.4 (1978), pp. 608–611.

[20] V. V. Flambaum, D. DeMille, and M. G. Kozlov. “Time-Reversal Symmetry Violation in Molecules Induced by Nuclear Magnetic Quadrupole Moments”. In: *Phys. Rev. Lett.* 113.10 (Sept. 2014), p. 103003. DOI: 10.1103/PhysRevLett.113.103003.

[21] CJ Ho et al. “Measuring the nuclear magnetic quadrupole moment in heavy polar molecules”. In: *Front. Phys. 11:1086980* (2023). DOI: 10.3389/fphy.2023.1086980.

[22] S. A. Murthy et al. “New limits on the electron electric dipole moment from cesium”. In: *Phys. Rev. Lett.* 63.9 (Aug. 1989), pp. 965–968. ISSN: 00319007. DOI: 10.1103/PhysRevLett.63.965.

[23] Yuiki Takahashi et al. “Simulation of cryogenic buffer gas beams”. In: *Phys. Rev. Research* 3 (2 Apr. 2021), p. 023018. DOI: 10.1103/PhysRevResearch.3.023018.

[24] S E Maxwell et al. “High-Flux Beam Source for Cold, Slow Atoms or Molecules”. In: *Phys. Rev. Lett.* 95.17 (Oct. 2005), p. 173201. ISSN: 0031-9007. DOI: 10.1103/PhysRevLett.95.173201.

[25] Nicholas R. Hutzler, Hsin-I Lu, and John M. Doyle. “The buffer gas beam: an intense, cold, and slow source for atoms and molecules.” In: *Chem. Rev.* 112.9 (Sept. 2012), pp. 4803–27. ISSN: 1520-6890. DOI: 10.1021/cr200362u.

[26] J K Messer and Frank C De Lucia. “Measurement of Pressure Broadening Parameters for the CO-He System at 4K”. In: *Phys. Rev. Lett.* 53.27 (Dec. 1984), p. 2555. DOI: 10.1103/PhysRevLett.53.2555.

[27] Ben Spaun et al. “Continuous probing of cold complex molecules with infrared frequency comb spectroscopy”. In: *Nature* 533.7604 (May 2016), pp. 517–520. DOI: 10.1038/nature17440.

[28] Jessica P. Porterfield et al. “High sensitivity microwave spectroscopy in a cryogenic buffer gas cell”. In: *Review of Scientific Instruments* 90.5 (2019), p. 053104. DOI: 10.1063/1.5091773. eprint: https://doi.org/10.1063/1.5091773.

[29] Luigi Santamaria et al. “Comb-assisted cavity ring-down spectroscopy of a buffer-gas-cooled molecular beam”. In: *Phys. Chem. Chem. Phys.* 18 (25 2016), pp. 16715–16720. DOI: 10.1039/C6CP02163H.

[30] M. R. Tarbutt. “Laser cooling of molecules”. In: *Contemp. Phys.* 59.4 (Oct. 2018), pp. 356–376. ISSN: 0010-7514. DOI: 10.1080/00107514.2018.1576338.

[31] Daniel McCarron. “Laser cooling and trapping molecules”. In: *J. Phys. B At. Mol. Opt. Phys.* 51.21 (Nov. 2018), p. 212001. ISSN: 0953-4075. DOI: 10.1088/1361-6455/aadfba.

[32] David Patterson and John M Doyle. “Bright, guided molecular beam with hydrodynamic enhancement.” In: *J. Chem. Phys.* 126.15 (Apr. 2007), p. 154307. ISSN: 0021-9606. DOI: 10.1063/1.2717178.

[33] Nicholas R. Hutzler et al. “A cryogenic beam of refractory, chemically reactive molecules with expansion cooling.” In: *Phys. Chem. Chem. Phys.* 13.42 (Nov. 2011), pp. 18976–85. ISSN: 1463-9084. DOI: 10.1039/c1cp20901a. arXiv: 1101.4217.

[34] Hsin-I Lu et al. “A cold and slow molecular beam.” In: *Phys. Chem. Chem. Phys.* 13.42 (Nov. 2011), pp. 18986–90. DOI: 10.1039/c1cp21206k.

[35] Loïc Anderegg et al. “Radio Frequency Magneto-Optical Trapping of CaF with High Density”. In: *Phys. Rev. Lett.* 119.10 (Sept. 2017), p. 103201. ISSN: 0031-9007. DOI: 10.1103/PhysRevLett.119.103201.

[36] Hsin I. Lu et al. “Magnetic trapping of molecules via optical loading and magnetic slowing”. In: *Phys. Rev. Lett.* 112.March (2014), p. 113006. ISSN: 10797114. DOI: 10.1103/PhysRevLett.112.113006. arXiv: arXiv:1310.2669v1.

[37] G. A. Bird. *Molecular Gas Dynamics and the Direct Simulation of Gas Flows*. Oxford University Press, 1994.

[38] Thomas Gantner et al. “Buffer-gas cooling of molecules in the low-density regime: comparison between simulation and experiment”. In: *Journal of Physics B: Atomic, Molecular and Optical Physics* 53.14 (June 2020), p. 145302. DOI: 10.1088/1361-6455/ab8b42.

[39] Vijay Singh et al. “Optimized cell geometry for buffer-gas-cooled molecular-beam sources”. In: *Phys. Rev. A* 97.3 (Mar. 2018), p. 032704. ISSN: 2469-9926. DOI: 10.1103/PhysRevA.97.032704.

[40] S. Truppe et al. “A buffer gas beam source for short, intense and slow molecular pulses”. In: *J. Mod. Opt.* 65.3 (2018), pp. 246–254. DOI: 10.1080/09500340.2017.1384516.

[41] N. E. Bulleid et al. “Characterization of a cryogenic beam source for atoms and molecules.” In: *Phys. Chem. Chem. Phys.* 15.29 (Aug. 2013), pp. 12299–307. ISSN: 1463-9084. DOI: 10.1039/c3cp51553b. arXiv: 1306.0241.

[42] O. Schullian et al. “Simulating rotationally inelastic collisions using a direct simulation Monte Carlo method”. In: *Molecular Physics* 113.24 (2015), pp. 3972–3978. DOI: 10.1080/00268976.2015.1098740. eprint: https://doi.org/10.1080/00268976.2015.1098740.

[43] Maximilian J. Doppelbauer et al. “Using a direct simulation Monte Carlo approach to model collisions in a buffer gas cell”. In: *The Journal of Chemical Physics* 146.4 (2017), p. 044302. DOI: 10.1063/1.4974253. eprint: https://doi.org/10.1063/1.4974253.

[44] O. Schullian and B. R. Heazlewood. “Beyond direct simulation Monte Carlo (DSMC) modelling of collision environments”. In: *Molecular Physics* 117.21 (2019), pp. 3076–3087. DOI: 10.1080/00268976.2019.1602740.

[45] G. A. Bird. “The DS2V/3V Program Suite for DSMC Calculations”. In: *AIP Conference Proceedings* 762.1 (2005), pp. 541–546. DOI: 10.1063/1.1941592.

[46] J. Kestin et al. “Equilibrium and Transport Properties of the Noble Gases and Their Mixtures at Low Density”. In: *Journal of Physical and Chemical Reference Data* 13.1 (1984), pp. 229–303. DOI: 10.1063/1.555703. eprint: https://doi.org/10.1063/1.555703.

[47] Felix Sharipov and Victor J. Benites. “Transport coefficients of helium-neon mixtures at low density computed from ab initio potentials”. In: *The Journal of Chemical Physics* 147.22 (Dec. 2017), p. 224302. DOI: 10.1063/1.5001711.

[48] J. F. Barry, E. S. Shuman, and D. DeMille. “A bright, slow cryogenic molecular beam source for free radicals.” In: *Phys. Chem. Chem. Phys.* 13.42 (Nov. 2011), pp. 18936–47. ISSN: 1463-9084. DOI: 10.1039/c1cp20335e. arXiv: 1101.4229.

[49] Y Sone. *Molecular gas dynamics*. Boston: Birkhauser, 2007.

[50] H Pauly. *Atom, Molecule, and Cluster Beams I*. Springer, 2000.

[51] S M Skoff et al. “Diffusion, thermalization, and optical pumping of YbF molecules in a cold buffer-gas cell”. In: *Phys. Rev. A* 83.2 (Feb. 2011), p. 23418. ISSN: 1050-2947. DOI: 10.1103/PhysRevA.83.023418.

[52] M. G. Tarallo, G. Z. Iwata, and T. Zelevinsky. “BaH molecular spectroscopy with relevance to laser cooling”. In: *Phys. Rev. A* 93 (3 Mar. 2016), p. 032509. DOI: 10.1103/PhysRevA.93.032509.

[53] Jacob Baron et al. “Order of Magnitude Smaller Limit on the Electric Dipole Moment of the Electron”. In: *Science* 343.6168 (Jan. 2014), pp. 269–272. DOI: 10.1126/science.1248213.

[54] J. F. Barry et al. “Laser Radiation Pressure Slowing of a Molecular Beam”. In: *Phys. Rev. Lett.* 108.10 (Mar. 2012), p. 103002. ISSN: 0031-9007. DOI: 10.1103/PhysRevLett.108.103002.

[55] Hylton R Murphy and David R Miller. “Effects of nozzle geometry on kinetics in free-jet expansions”. In: *J. Phys. Chem.* 88.20 (Sept. 1984), pp. 4474–4478. ISSN: 0022-3654. DOI: 10.1021/j150664a005.

[56] G. P. Sutton and O. Biblarz. *Rocket Propulsion Elements*. Wiley, New York, 2016.

[57] Di Xiao et al. “Shaped nozzles for cryogenic buffer-gas beam sources”. In: *Phys. Rev. A* 99.1 (Jan. 2019), p. 013603. DOI: 10.1103/PhysRevA.99.013603.

[58] M. R. Tarbutt and T. C. Steimle. “Modeling magneto-optical trapping of CaF molecules”. In: *Phys. Rev. A* 92.5 (Nov. 2015), p. 053401. ISSN: 1050-2947. DOI: 10.1103/PhysRevA.92.053401.

[59] Hendrick Bethlem, Giel Berden, and Gerard Meijer. “Decelerating Neutral Dipolar Molecules”. In: *Phys. Rev. Lett.* 83.8 (Aug. 1999), pp. 1558–1561. ISSN: 0031-9007. DOI: 10.1103/PhysRevLett.83.1558.

[60] N. VanHaecke and O. Dulieu. "Precision measurements with polar molecules: the role of the black body radiation". In: *Mol. Phys.* 105.11-12 (June 2007), pp. 1723–1731. ISSN: 0026-8976. DOI: 10.1080/00268970701466261. arXiv: arXiv:0801.3158v1.

[61] Edvardas Narevicius et al. "Stopping Supersonic Beams with a Series of Pulsed Electromagnetic Coils: An Atomic Coilgun". In: *Phys. Rev. Lett.* 100 (9 Mar. 2008), p. 093003. DOI: 10.1103/PhysRevLett.100.093003.

[62] L. D van Buuren et al. "Electrostatic Extraction of Cold Molecules from a Cryogenic Reservoir". In: *Phys. Rev. Lett.* 102.3 (Jan. 2009), p. 033001. ISSN: 0031-9007. DOI: 10.1103/PhysRevLett.102.033001.

[63] Dima Egorov et al. "Buffer-gas cooling of atomic and molecular beams". In: *Physical Review A* 66.4 (Oct. 2002), p. 043401. ISSN: 1050-2947. DOI: 10.1103/PhysRevA.66.043401.

[64] G. D. Sprouse et al. "Laser spectroscopy of light Yb isotopes on-line in a cooled gas cell". In: *Physical Review Letters* 63.14 (Oct. 1989), pp. 1463–1466. DOI: 10.1103/physrevlett.63.1463.

[65] Yuiki Takahashi et al. "Engineering Field-Insensitive Molecular Clock Transitions for Symmetry Violation Searches". In: *Phys. Rev. Lett.* 131 (18 Oct. 2023), p. 183003. DOI: 10.1103/PhysRevLett.131.183003.

[66] Arian Jadbabaie et al. "Characterizing the fundamental bending vibration of a linear polyatomic molecule for symmetry violation searches". In: *New Journal of Physics* 25.7 (July 2023), p. 073014. DOI: 10.1088/1367-2630/ace471.

[67] Nickolas H. Pilgram et al. "Fine and hyperfine interactions in ^{171}YbOH and ^{173}YbOH". In: *J. Chem. Phys.* 154.24 (June 2021), p. 244309. ISSN: 0021-9606. DOI: 10.1063/5.0055293.

[68] Timothy C Steimle et al. "Field-free, Stark, and Zeeman spectroscopy of the $\tilde{A}^2\Pi - \tilde{X}^2\Sigma^+$ transition of ytterbium monohydroxide". In: *Phys. Rev. A* 100.5 (Nov. 2019), p. 052509. ISSN: 2469-9926. DOI: 10.1103/PhysRevA.100.052509.

[69] Hiromitsu Sawaoka et al. "Zeeman-Sisyphus deceleration for heavy molecules with perturbed excited-state structure". In: *Phys. Rev. A* 107 (2 Feb. 2023), p. 022810. DOI: 10.1103/PhysRevA.107.022810.

[70] Sanjay Nakhate et al. "The pure rotational spectrum of YbOH". In: *Chemical Physics Letters* (2019). ISSN: 00092614.

[71] William B. Cairncross et al. "Precision Measurement of the Electron's Electric Dipole Moment Using Trapped Molecular Ions". In: *Phys. Rev. Lett.* 119.15 (Oct. 2017), p. 153001. ISSN: 0031-9007. DOI: 10.1103/PhysRevLett.119.153001.

[72] Tanya S. Roussy et al. *A new bound on the electron's electric dipole moment*. 2022. DOI: 10.48550/ARXIV.2212.11841.

[73] B. Regan et al. "New Limit on the Electron Electric Dipole Moment". In: *Phys. Rev. Lett.* 88.7 (Feb. 2002), p. 071805. ISSN: 0031-9007. DOI: 10.1103/PhysRevLett.88.071805.

[74] C. Abel et al. "Measurement of the Permanent Electric Dipole Moment of the Neutron". In: *Physical Review Letters* 124.8 (Feb. 2020), p. 081803. DOI: 10.1103/PhysRevLett.124.081803.

[75] Ivan Kozyryev and Nicholas R. Hutzler. "Precision Measurement of Time-Reversal Symmetry Violation with Laser-Cooled Polyatomic Molecules". In: *Phys. Rev. Lett.* 119.13 (Sept. 2017), p. 133002. ISSN: 0031-9007. DOI: 10.1103/PhysRevLett.119.133002.

[76] Timur A. Isaev and Robert Berger. "Polyatomic Candidates for Cooling of Molecules with Lasers from Simple Theoretical Concepts". In: *Phys. Rev. Lett.* 116.6 (Feb. 2016), p. 063006. ISSN: 0031-9007. DOI: 10.1103/PhysRevLett.116.063006.

[77] N.J. Fitch and M.R. Tarbutt. "Laser-cooled molecules". In: *Advances in Atomic, Molecular and Optical Physics* 70 (2021), pp. 157–262. DOI: 10.1016/bs.aamop.2021.04.003.

[78] Loïc Anderegg et al. "Quantum control of trapped polyatomic molecules for eEDM searches". In: *Science* 382.6671 (2023), pp. 665–668. DOI: 10.1126/science.adg8155. eprint: https://www.science.org/doi/pdf/10.1126/science.adg8155.

[79] Mohit Verma, Andrew M. Jayich, and Amar C. Vutha. "Electron Electric Dipole Moment Searches Using Clock Transitions in Ultracold Molecules". In: *Physical Review Letters* 125.15 (Oct. 2020), p. 153201. DOI: 10.1103/PhysRevLett.125.153201.

[80] Andrei Derevianko and Hidetoshi Katori. "Colloquium: Physics of optical lattice clocks". In: *Rev. Mod. Phys.* 83 (2 May 2011), pp. 331–347. DOI: 10.1103/RevModPhys.83.331.

[81] Andrew D. Ludlow et al. "Optical atomic clocks". In: *Reviews of Modern Physics* 87.2 (June 2015), pp. 637–701. DOI: 10.1103/revmodphys.87.637.

[82] Alexander Prehn et al. "High-Resolution "Magic"-Field Spectroscopy on Trapped Polyatomic Molecules". In: *Physical Review Letters* 127.17 (Oct. 2021), p. 173602. URL: https://doi.org/10.1103/physrevlett.127.173602.

[83] Chao Li et al. "Non 0–0 states magnetically insensitive transitions in alkali species". In: *Phys. Scr.* 95.4 (Apr. 2020), p. 045402. ISSN: 0031-8949. DOI: 10.1088/1402-4896/ab6ce3.

[84] K. J. Arnold and M. D. Barrett. "Suppression of Clock Shifts at Magnetic-Field-Insensitive Transitions". In: *Phys. Rev. Lett.* 117 (16 Oct. 2016), p. 160802. DOI: 10.1103/PhysRevLett.117.160802.

[85] Kaveh Najafian, Ziv Meir, and Stefan Willitsch. "From megahertz to terahertz qubits encoded in molecular ions: theoretical analysis of dipole-forbidden spectroscopic transitions in N_2^+". In: *Phys. Chem. Chem. Phys.* 22 (40 2020), pp. 23083–23098. DOI: 10.1039/D0CP03906C.

[86] Ivan Kozyryev, Zack Lasner, and John M. Doyle. "Enhanced sensitivity to ultralight bosonic dark matter in the spectra of the linear radical SrOH". In: *Physical Review A* 103.4 (Apr. 2021), p. 043313. URL: https://doi.org/10.1103/physreva.103.043313.

[87] Malika Denis et al. "Enhanced P,T-violating nuclear magnetic quadrupole moment effects in laser-coolable molecules". In: *The Journal of Chemical Physics* 152.8 (Feb. 2020), p. 084303. ISSN: 0021-9606. DOI: 10.1063/1.5141065.

[88] D. E. Maison, L. V. Skripnikov, and V. V. Flambaum. "Theoretical study of ^{173}YbOH to search for the nuclear magnetic quadrupole moment". In: *Phys. Rev. A* 100.3 (Sept. 2019), p. 032514. ISSN: 2469-9926. DOI: 10.1103/PhysRevA.100.032514.

[89] Nicholas Richard Hutzler. "A New Limit on the Electron Electric Dipole Moment". PhD thesis. Harvard University, 2014.

[90] E. J. Campbell and W. G. Read. "Rotational Zeeman effect in ArHCl and ArDF". In: *The Journal of Chemical Physics* 78.11 (1983), pp. 6490–6501. DOI: 10.1063/1.444688. eprint: https://doi.org/10.1063/1.444688.

[91] E Hirota. *High-Resolution Spectroscopy of Transient Molecules*. Vol. 40. Berlin: Springer-Verlag, 1985. ISBN: 978-3-642-82479-1. DOI: 10.1007/978-3-642-82477-7.

[92] Alexander Petrov and Anna Zakharova. "Sensitivity of the YbOH molecule to P,T-odd effects in an external electric field". In: *Physical Review A* 105.5 (May 2022), p. L050801. ISSN: 2469-9926. DOI: 10.1103/PhysRevA.105.L050801. arXiv: 2111.02772.

[93] Jacob Baron et al. "Methods, analysis, and the treatment of systematic errors for the electron electric dipole moment search in thorium monoxide". In: *New J. Phys.* 19.7 (July 2017), p. 073029. ISSN: 1367-2630. DOI: 10.1088/1367-2630/aa708e.

[94] Benjamin L. Augenbraun et al. "Observation and laser spectroscopy of ytterbium monomethoxide, $YbOCH_3$". In: *Physical Review A* 103.2 (Feb. 2021), p. 022814. ISSN: 2469-9926. DOI: 10.1103/PhysRevA.103.022814. eprint: 2012.01212.

[95] Svetlana Kotochigova and David DeMille. "Electric-field-dependent dynamic polarizability and state-insensitive conditions for optical trapping of diatomic polar molecules". In: *Physical Review A* 82 (6 Dec. 2010), p. 063421. ISSN: 1050-2947. DOI: 10.1103/PhysRevA.82.063421.

[96] Sean Burchesky et al. "Rotational Coherence Times of Polar Molecules in Optical Tweezers". In: *Physical Review Letters* 127 (12 Sept. 2021), p. 123202. ISSN: 0031-9007. DOI: 10.1103/PhysRevLett.127.123202.

[97] D. A. Fletcher et al. "Millimeter-wave spectroscopy of vibrationally excited ground state alkaline-earth hydroxide radicals ($X\ ^2\Sigma^+$)". In: *J. Chem. Phys.* 102.11 (1995), p. 4334. ISSN: 00219606. DOI: 10.1063/1.469482.

[98] M.A. Anderson et al. "The millimeter and sub-millimeter spectrum of the BaOH radical". In: *Chemical Physics Letters* 205.4 (1993), pp. 415–422. ISSN: 0009-2614. DOI: 10.1016/0009-2614(93)87144-R.

[99] Hailing Wang et al. "Fine and hyperfine interaction in ^{173}YbF". In: *Phys. Rev. A* 100.2 (Aug. 2019), p. 022516. ISSN: 2469-9926. DOI: 10.1103/PhysRevA.100.022516.

[100] B. E. Sauer, Jun Wang, and E. A. Hinds. "Laser-rf double resonance spectroscopy of ^{174}YbF in the $X^2\Sigma^+$ state: Spin-rotation, hyperfine interactions, and the electric dipole moment". In: *J. Chem. Phys.* 105 (1996), p. 7412. DOI: 10.1063/1.472569.

[101] Zachary Glassman et al. "The hyperfine interaction in the odd isotope of ytterbium fluoride, ^{171}YbF". In: *J. Mol. Spectrosc.* 300 (June 2014), pp. 7–11. ISSN: 00222852. DOI: 10.1016/j.jms.2014.02.003.

[102] T. C. Steimle et al. "A supersonic molecular beam optical Stark study of CaOH and SrOH". In: *The Journal of Chemical Physics* 96.4 (1992), p. 2556. ISSN: 00219606. DOI: 10.1063/1.462007.

[103] Daniel E. Maison et al. "$\mathcal{T},\mathcal{P}$-odd effects in the $LuOH^+$ cation". In: *Phys. Rev. A* 106 (6 Dec. 2022), p. 062827. DOI: 10.1103/PhysRevA.106.062827.

[104] Alexander N. Petrov. private communication.

[105] Ronald Garcia-Ruiz and Silviu-Marian Udrescu. private communication.

[106] A. N. Petrov and L. V. Skripnikov. "Energy levels of radium monofluoride RaF in external electric and magnetic fields to search for P- and T,P-violation effects". In: *Phys. Rev. A* 102 (6 Dec. 2020), p. 062801. DOI: 10.1103/PhysRevA.102.062801.

[107] Daniel N. Gresh et al. "Broadband velocity modulation spectroscopy of ThF^+ for use in a measurement of the electron electric dipole moment". In: *Journal of Molecular Spectroscopy* 319 (2016), pp. 1–9. ISSN: 0022-2852. DOI: 10.1016/j.jms.2015.11.001.

[108] Kia Boon Ng et al. "Spectroscopy on the electron-electric-dipole-moment–sensitive states of ThF^+". In: *Phys. Rev. A* 105 (2 Feb. 2022), p. 022823. DOI: 10.1103/PhysRevA.105.022823.

[109] William B. Cairncross. "Searching for time-reversal symmetry violation with molecular ions: Quantum state control and photofragment imaging". PhD thesis. University of Colorado Boulder, 2016.

[110] T. C. Steimle et al. "A supersonic molecular beam optical Stark study of CaOH and SrOH". In: *The Journal of Chemical Physics* 96.4 (1992), p. 2556. ISSN: 00219606. DOI: 10.1063/1.462007.

[111] Ayaki Sunaga et al. "Measuring the nuclear magnetic quadrupole moment of optically trapped ytterbium atoms in the metastable state". In: *New Journal of Physics* 26.2 (Feb. 2024), p. 023023. DOI: 10.1088/1367-2630/ad2438.

[112] F. M. Gambetta et al. "Engineering NonBinary Rydberg Interactions via Phonons in an Optical Lattice". In: *Phys. Rev. Lett.* 124 (4 Jan. 2020), p. 043402. DOI: 10.1103/PhysRevLett.124.043402.

[113] Filippo M. Gambetta et al. "Long-Range Multibody Interactions and Three-Body Antiblockade in a Trapped Rydberg Ion Chain". In: *Phys. Rev. Lett.* 125 (13 Sept. 2020), p. 133602. DOI: 10.1103/PhysRevLett.125.133602.

[114] Filippo M. Gambetta et al. "Exploring the Many-Body Dynamics Near a Conical Intersection with Trapped Rydberg Ions". In: *Phys. Rev. Lett.* 126 (23 June 2021), p. 233404. DOI: 10.1103/PhysRevLett.126.233404.

[115] Yuiki Takahashi et al. "Engineered Molecular Clock Transitions for Symmetry Violation Searches". In: *Phys. Rev. X* (2026). Accepted in Phys. Rev. X. DOI: 10.1103/4t7q-d58r. arXiv: 2508.06787 [physics.atom-ph].

[116] Huidong Kim, Hyok Sang Han, and D. Cho. "Magic Polarization for Optical Trapping of Atoms without Stark-Induced Dephasing". In: *Phys. Rev. Lett.* 111.24 (Dec. 2013), p. 243004. ISSN: 0031-9007. DOI: 10.1103/PhysRevLett.111.243004.

[117] Ichiro Ushijima, Masao Takamoto, and Hidetoshi Katori. "Operational Magic Intensity for Sr Optical Lattice Clocks". In: *Phys. Rev. Lett.* 121 (26 Dec. 2018), p. 263202. DOI: 10.1103/PhysRevLett.121.263202.

[118] K. H. Leung et al. "Terahertz Vibrational Molecular Clock with Systematic Uncertainty at the 10^{-14} Level". In: *Phys. Rev. X* 13 (1 Mar. 2023), p. 011047. DOI: 10.1103/PhysRevX.13.011047.

[119] Alexander Aeppli et al. "Clock with 8×10^{-19} Systematic Uncertainty". In: *Phys. Rev. Lett.* 133 (2 July 2024), p. 023401. DOI: 10.1103/PhysRevLett.133.023401.

[120] Tanya S. Roussy et al. "Experimental Constraint on Axionlike Particles over Seven Orders of Magnitude in Mass". In: *Phys. Rev. Lett.* 126 (17 Apr. 2021), p. 171301. DOI: 10.1103/PhysRevLett.126.171301.

[121] Mingyu Fan et al. *First results from a search for axionlike dark matter using octupole-deformed nuclei in a crystal*. 2024. arXiv: 2410.02218 [physics.atom-ph].

[122] Malika Denis et al. "Enhancement factor for the electric dipole moment of the electron in the BaOH and YbOH molecules". In: *Physical Review A* 99.4 (2019), p. 42512. ISSN: 0031-899X. DOI: 10.1103/PhysRevA.99.042512.

[123] Konstantin Gaul and Robert Berger. "Ab initio study of parity and time-reversal violation in laser-coolable triatomic molecules". In: *Phys. Rev. A* 101.1 (Jan. 2020), p. 012508. DOI: 10.1103/PhysRevA.101.012508.

[124] E. Kirilov et al. "Shot-noise-limited spin measurements in a pulsed molecular beam". In: *Phys. Rev. A* 88.1 (July 2013), p. 013844. ISSN: 1050-2947. DOI: 10.1103/PhysRevA.88.013844. eprint: 1305.2179.

[125] Arian Jadbabaie et al. "Enhanced molecular yield from a cryogenic buffer gas beam source via excited state chemistry". In: *New J. Phys.* 22 (Jan. 2020). ISSN: 1367-2630. URL: https://iopscience.iop.org/article/10.1088/1367-2630/ab6eae.

[126] Arian Jadbabaie. "Measuring Fundamental Symmetry Violation in Polyatomic Molecules". PhD thesis. California Institute of Technology, 2023.

[127] Robin Santra et al. "High-Accuracy Optical Clock via Three-Level Coherence in Neutral Bosonic ^{88}Sr". In: *Phys. Rev. Lett.* 94 (17 May 2005), p. 173002. DOI: 10.1103/PhysRevLett.94.173002.

[128] Thomas Zanon-Willette et al. "Cancellation of Stark Shifts in Optical Lattice Clocks by Use of Pulsed Raman and Electromagnetically Induced Transparency Techniques". In: *Phys. Rev. Lett.* 97 (23 Dec. 2006), p. 233001. DOI: 10.1103/PhysRevLett.97.233001.

[129] A. V. Taichenachev et al. "Compensation of field-induced frequency shifts in Ramsey spectroscopy of optical clock transitions". In: *JETP Letters* 90.11 (Feb. 2010), pp. 713–717. ISSN: 1090-6487. DOI: 10.1134/S0021364009230052.

[130] V. Yudin et al. "Hyper-Ramsey spectroscopy of optical clock transitions". In: *Phys. Rev. A* 82.1 (July 2010), 011804(R). ISSN: 1050-2947. DOI: 10.1103/PhysRevA.82.011804.

[131] R. Hobson et al. "Modified hyper-Ramsey methods for the elimination of probe shifts in optical clocks". In: *Phys. Rev. A* 93 (1 Jan. 2016), p. 010501. DOI: 10.1103/PhysRevA.93.010501.

[132] Zhi-Xin Duan et al. "Simple and active magnetic-field stabilization for cold atom experiments". In: *Review of Scientific Instruments* 93.12 (Dec. 2022), p. 123201. ISSN: 0034-6748. DOI: 10.1063/5.0119778. eprint: https://pubs.aip.org/aip/rsi/article-pdf/doi/10.1063/5.0119778/16567321/123201_1_online.pdf.

[133] H. Loh et al. “Precision Spectroscopy of Polarized Molecules in an Ion Trap”. In: *Science* 342.6163 (Dec. 2013), pp. 1220–1222. ISSN: 0036-8075. DOI: 10.1126/science.1243683. arXiv: 1311.3165.

[134] Luke Caldwell et al. “Systematic and statistical uncertainty evaluation of the HfF^+ electron electric dipole moment experiment”. In: *Phys. Rev. A* 108 (1 July 2023), p. 012804. DOI: 10.1103/PhysRevA.108.012804.

[135] X Wu et al. “The metastable Q3Δ2 state of ThO: a new resource for the ACME electron EDM search”. In: *New Journal of Physics* 22.2 (Feb. 2020), p. 023013. ISSN: 1367-2630. DOI: 10.1088/1367-2630/ab6a3a.

[136] Tianxiang Chen et al. “Relativistic Exact Two-Component Coupled-Cluster Study of Molecular Sensitivity Factors for Nuclear Schiff Moments”. In: *The Journal of Physical Chemistry A* 128.31 (2024). PMID: 39047199, pp. 6540–6554. DOI: 10.1021/acs.jpca.4c02640. eprint: https://doi.org/10.1021/acs.jpca.4c02640.

[137] K. Cooper Stuntz et al. “Optical cycling and sensitivity to the electron’s electric dipole moment in gold-containing molecules”. In: *Phys. Rev. A* 110 (4 Oct. 2024), p. 042807. DOI: 10.1103/PhysRevA.110.042807.

[138] Benjamin L. Augenbraun et al. “Laser-cooled polyatomic molecules for improved electron electric dipole moment searches”. In: *New J. Phys.* 22.2 (Feb. 2020), p. 022003. ISSN: 1367-2630. DOI: 10.1088/1367-2630/ab687b. arXiv: 1910.11318.

[139] X Alauze et al. “An ultracold molecular beam for testing fundamental physics”. In: *Quantum Science and Technology* 6.4 (July 2021), p. 044005. DOI: 10.1088/2058-9565/ac107e.

[140] N J Fitch et al. “Methods for measuring the electron’s electric dipole moment using ultracold YbF molecules”. In: *Quantum Science and Technology* 6.1 (Dec. 2020), p. 014006. DOI: 10.1088/2058-9565/abc931.

[141] R. A. Jenkins et al. *Spin interferometry in a beam of ultracold molecules*. 2026. DOI: 10.48550/ARXIV.2602.00713.

[142] E. Fraval, M. J. Sellars, and J. J. Longdell. “Method of Extending Hyperfine Coherence Times in $Pr^{3+} : Y_2SiO_5$”. In: *Phys. Rev. Lett.* 92 (7 Feb. 2004), p. 077601. DOI: 10.1103/PhysRevLett.92.077601.

[143] Aurélien Marc, Mickaël Hubert, and Timo Fleig. “Candidate molecules for next-generation searches of hadronic charge-parity violation”. In: *Phys. Rev. A* 108 (6 Dec. 2023), p. 062815. DOI: 10.1103/PhysRevA.108.062815.

[144] Michał Śmiałkowski and Michał Tomza. “Highly polar molecules consisting of a copper or silver atom interacting with an alkali-metal or alkaline-earth-metal atom”. In: *Phys. Rev. A* 103 (2 Feb. 2021), p. 022802. DOI: 10.1103/PhysRevA.103.022802.

[145] Maximilian Löw et al. “Coherence of Symmetry-Protected Rotational Qubits in Cold Polyatomic Molecules”. In: *Phys. Rev. Lett.* 134 (11 Mar. 2025), p. 113402. DOI: 10.1103/PhysRevLett.134.113402.

[146] Chi Zhang et al. “Quantum-Enhanced Metrology for Molecular Symmetry Violation Using Decoherence-Free Subspaces”. In: *Physical Review Letters* 131.19 (Nov. 2023), p. 193602. ISSN: 0031-9007. DOI: 10.1103/PhysRevLett.131.193602.

[147] Simon L. Cornish, Michael R. Tarbutt, and Kaden R. A. Hazzard. “Quantum computation and quantum simulation with ultracold molecules”. In: *Nature Physics* 20.5 (May 2024), pp. 730–740. ISSN: 1745-2473. DOI: 10.1038/s41567-024-02453-9.

[148] Tijs Karman, Michał Tomza, and Jesús Pérez-Ríos. “Ultracold chemistry as a testbed for few-body physics”. In: *Nature Physics* 20 (5 May 2024), pp. 722–729. ISSN: 1745-2473. DOI: 10.1038/s41567-024-02467-3.

[149] Aleksandar Radak et al. *Sensing T-violating nuclear moments of paramagnetic ions in crystals*. Mar. 2026. DOI: 10.48550/arXiv.2603.24907. arXiv: 2603.24907 [physics.atom-ph].

[150] S. M. Udrescu et al. “Precision spectroscopy and laser-cooling scheme of a radium-containing molecule”. In: *Nature Physics* 20.2 (Feb. 2024), pp. 202–207. ISSN: 1745-2481. DOI: 10.1038/s41567-023-02296-w.

[151] T. A. Isaev, A. V. Zaitsevskii, and E. Eliav. “Laser-coolable polyatomic molecules with heavy nuclei”. In: *J. Phys. B* 50.22 (Nov. 2017), p. 225101. ISSN: 0953-4075. DOI: 10.1088/1361-6455/aa8f34.